2021

# 13th International Conference on Measurement

Smolenice, Slovakia
May 17 - 19, 2021

Proceedings

# MEASUREMENT 2021

**The 13th International Conference on Measurement**

# ORGANIZERS OF THE CONFERENCE

**Organizer**

Institute of Measurement Science, Slovak Academy of Sciences, Bratislava

**Technical sponsorship**

IEEE Czechoslovakia Section

Metrological Society

Slovak National Committee U.R.S.I.

Slovak Society of Biomedical Engineering and Medical Informatics

# MEASUREMENT 2021
## ONLINE

Proceedings of the
13th International Conference on Measurement

Online Conference
Smolenice Castle, Slovakia
May 17-19, 2021

# MEASUREMENT 2021



Editors: Andrej Dvurečenskij, Ján Maňka, Jana Švehlíková, Viktor Witkovský
Cover Design: Ivan Frollo
Publisher: Institute of Measurement Science
Slovak Academy of Sciences
Dúbravská cesta 9
841 04 BratislavaSlovakia

**ISBN 978-80-972629-4-5**

# COMMITTEES

**Conference Chairman**

J. Maňka, Slovakia

**International Program Committee**

J. Švehlíková, Slovakia, Chairman
B. Antić, Serbia
I. Bajla, Slovakia
M. Bittera, Slovakia
V. Boháč, Slovakia
K. De Buysser, Belgium
E. Cocherová, Slovakia
I. Frollo, Slovakia
R. Harťanský, Slovakia
Y. V. Chugui, Russia
A. Chunovkina, Russia
P. Jurák, Czech Republic
B. Kessel, Germany
O. Kochan, Ukraine
G. Kozmann, Hungary
R. Köning, Germany
I.C. Lira, Chile
J. Markovič, Slovakia
K. Meigas, Estonia
V. Mlynarik, Austria
V. Novickij, Lithuania
M. Paluš, Czech Republic
K. Roubík, Czech Republic
Y. Serinagaoglu, Turkey
M. Soleimani, United Kingdom
Z. Starčuk, Czech Republic
M. Štork, Czech Republic
S. Takayama, Japan
M. Tarata, Romania
P. Tino, United Kingdom
D. Tyler, United Kingdom
M. Tyšler, Slovakia
J. Volaufova, USA
G. Wimmer, Slovakia
V. Witkovský, Slovakia
A. Woźniak, Poland

**Young Investigator Award Jury**

Isabel Van Driessche, Belgium
Barbora Kessel, Germany
Orest Kochan, Ukraine
Yesim Serinagaoglu-Dogrusoz, Turkey
Alexander Šatka, Slovakia

**Local Oranizing Committee**

A. Dvurečenskij, Chairman
E. Gurišová
D. Gogola
M. Chvosteková
J. Jakubík
A. Krafčík
B. Ondrušová
Z. Rošťáková
M. Škrátek
M. Teplan

## Reviewers

The submitted papers were evaluated by 53 reviewers, members of the International Program Committee and experts in the fields of measurement science and technology. Each paper was scored by two or three reviewers.

# Preface

*Measure what is measurable, and make measurable what is not so.*
*Galileo Galilei (1564 – 1642)*

This collection contains 58 original, peer-reviewed articles from renowned experts as well as young talented researchers at the beginning of their careers from universities, academic institutions and laboratories involved in the field of measurement science. These research results were presented during the 13th International Conference on Measurement, which took place on 17-19 May 2021, and are focused on the traditional topics of the MEASUREMENT conference series: Theoretical problems of measurement, measurement of physical quantities, and measurement in biomedicine. Of these, 38 papers were presented as oral presentations and 20 as posters. The submitted papers were reviewed by 53 reviewers.

Due to the ongoing pandemic of COVID-19, MEASUREMENT 2021 was not held live in the traditional conference venue in Smolenice Castle, but in the online space. It was a new challenge for the organizers to make the conference interesting, beneficial and comfortable for all participants, which was achieved with the use of modern technology. Oral presentations could be watched by an unlimited number of participants and poster presenters could present their work in separate online spaces, which provided an opportunity for in-depth discussions.

Despite the obvious disadvantages of this form of communication, there are also positives, that allowed a wider audience to participate directly from their offices or homes, join the selected sections and engage in discussion. In addition, it made it possible to attract four well-known experts as keynote speakers, namely Peter Tino (UK), Isabel van Driessche (Belgium), Gennady A. Ososkov (Russia) and Robert Hatala (Slovakia), who reported on the latest results and findings in their field of research and the modern trends in measurement methods and processing of measurement results. Moreover, ten young researchers entered the traditional Young Investigator Award competition. The awarded winners of the three best works will be invited to publish their extensive contributions in the impacted and open-access journal Measurement Science Review.

We believe that despite this difficult situation, the MEASUREMENT conference series continues to successfully fulfil its mission in the field of presentation and promotion of the latest knowledge in the field of measurement science.

We use this opportunity to express our special thanks to Associate Professor Milan Tyšler PhD, several previous years (former) conference chairman and former director of the Institute of Measurement Science, who significantly contributed to the success of the MEASUREMENT conference series. This year Milan is celebrating his important anniversary - we congratulate him and wish him all the best.

Andrej Dvurečenskij, Ján Maňka, Jana Švehlíková, Viktor Witkovský

## Contents

# *Theoretical Problems of Measurement*

# Cross-Predictions in the Search for Effective Connectivity in Brain

**Anna Krakovská**

Institute of Measurement Science, Slovak Academy of Sciences, Bratislava, Slovak Republic
Email: krakovska@savba.sk

***Abstract.*** *Complex networks are ubiquitous in the real world. Brain activity, represented by multi-channel electroencephalographic (EEG) signals, is one of the most topical examples. Modern methods are beginning to successfully detect effective connectivity (meaning causal interactions, not structural or functional relations) in the brain. In this study, cross-predictions in reconstructed state spaces are used for bivariate causal detection and also for exploring dynamical networks whose nodes are characterized by time series. The method is applied to EEG signals recorded from six positions on the head during an experiment with visual stimulation (VS) of the brain. An intense causal influence from the back to the frontal parts of the same hemisphere, most pronounced in the occipital areas of the cortex, is detected. The observed causal effect persists for a short time even after VS is switched off.*

*Keywords: Cross-Predictions, Effective Connectivity, EEG, Causality*

## 1. Introduction

Causality, as a relation between cause and effect, is a complex research problem of many scientific disciplines, with neuroscience being one of the most important. The study of connectivity in the human brain is important for the investigation of neurophysiological processes associated with cognitive functions and possibly neurological disorders (see [1] and references therein). The topic involves various concepts. One is structural connectivity (anatomical and synaptic connections), the other functional connectivity (usually referring to significant statistical dependence between brain regions). However, what we will be interested in here, is the youngest branch of research, which is effective connectivity (meaning directed or causal interactions).

The brain connectivity estimators are usually evaluated from brain activity recordings, such as electroencephalographic signals, for example. For the detection of driving connections between the signals, the well-known Granger's test, which evaluates the causal relations by a study of predictability in autoregressive models [2], remains the most popular first choice. However, if the investigated observables cannot be viewed as straightforward multivariate autoregressive (AR) processes with white-noise residuals, then the Granger causality test is not applicable.

In this study, we consider the possibility that processes in the brain could be better modelled by complex nonlinear dynamical systems than by AR processes. If that were true, then methods operating in reconstructed state spaces should be preferred to the Granger test. The method we will use works with cross-predictions (CP) - predictions of the system based only on historical data from the other system. The method has been proposed and tested on causal connections of artificial complex nonlinear systems in [3]. In this study, CP will be applied to EEG signals recorded during an experiment with visual brain stimulation [4]. These types of experiments are good candidates for investigating effective brain connections. Intense brain wave entrainment under the influence of VS can be expected and has been confirmed through an increase of spectral power and interhemispheric coherence around the stimulating frequency bands. The changes were most significant in the occipital areas, directly associated with visual inputs, but they also spread to the central and frontal regions [4].

In this study, we would like to go a step further and examine whether the data also reveal effective connectivity, i.e., that driving and driven cortical areas can be detected.

## 2. Subject and Methods

*Data from visual stimulation (VS) experiment*

Over the course of two months, 20-25 repetitions of training of a 20-minute visual stimulation program provided by a commercially available light synthesizer were applied to 6 volunteers. During the sessions, the subjects were lying in a darkened, electrically shielded room. Flashing light stimulus at frequencies of 17, 9, 4, and 2 Hz was mediated through glasses with red light-emitting diodes. During VS and also 3 minutes before and after the sessions, EEG was recorded from 6 scalp locations (fronto-central, centro-parietal and parieto-occipital of both hemispheres), with the reference electrode at Cz and the ground electrode at Fpz position (according to the International 10-20 system). The signals were high-pass- and low-pass-filtered (0.07 - 234 Hz). The recording frequency was 500 Hz, which means that we have 600000 points available from the VS phase of the session and 90000 from each relaxation phase.

We subject the measured data to bivariate causal analysis. With EEGs from 6 positions, this means testing 15 pairs of signals for each training.

*Cross-prediction method (CP)*

The CP causal method we are going to use here was introduced in [3]. It is a bivariate method concerning two potentially coupled dynamical systems $X$ and $Y$, represented by a single time series, $x$, and $y$, respectively. CP is based on predictions of the evolution of the systems in state spaces. If a system is represented by only one time series, the multi-dimension1al state space has to be reconstructed first. Namely, a $d_X$-dimensional manifold $M_X$ is built from lags of series $x$: $(x(t), x(t-\tau_X), x(t-2\tau_X), \ldots, x(t-(d_X-1)\tau_X))$, and a $d_Y$-dimensional manifold $M_Y$ is built analogously using appropriate $\tau_Y$ and $d_Y$.

According to Takens' theorem [5], the reconstruction is equivalent, in the sense of diffeomorphism, to the original manifold. One of the important consequences is that reconstruction is useful for predicting the system's evolution.

In the reconstructed spaces, the self-predictions (denoted $xX, yY$) and cross-predictions $(xY, yX)$ will be computed using the method of analogues [6]. The method finds previous points, close to the current state, and assumes that the system will continue analogously to what it did in the past. In this way, we obtain the self-prediction of $y$ in $M_Y$ and the self-prediction of $x$ in $M_X$.

The way of cross-predicting (predicting the first system based on the history of the second system) is a bit different. To get the cross-prediction of $y$, for example, the indices of the neighbours of $Y_t$ are taken from the neighbours of $X_t$ found in $M_X$.

After completing the predictions, based on statistical testing of the mean absolute errors $\mathscr{E}$, we get the next four possible causal relations between $X$ and $Y$:

- *$X$ and $Y$ are causally independent*
  $X$ cannot be predicted from $Y$ and vice versa. The normalized (by the mean absolute deviation) errors $n\mathscr{E}xY$ and $n\mathscr{E}yX$ of cross-predictions are expected to be close to 1.
- $X \leftrightarrow Y$
  For fully synchronized or bidirectionally coupled systems, the driver and the response are indistinguishable from each other and we can predict them equally well in $M_X$ as in $M_Y$.
- $X \rightarrow Y$
  If either of the two previous cases was ruled out, then the remaining option is a one-way relationship. If $n\mathscr{E}xY < n\mathscr{E}yX$, then $Y$ contains more information about $X$ than vice versa, which is a sign of a unidirectional link from $X$ to $Y$.
- $Y \rightarrow X$
  $n\mathscr{E}yX < n\mathscr{E}xY$ is the last option - a unidirectional coupling, opposite to the previous case.

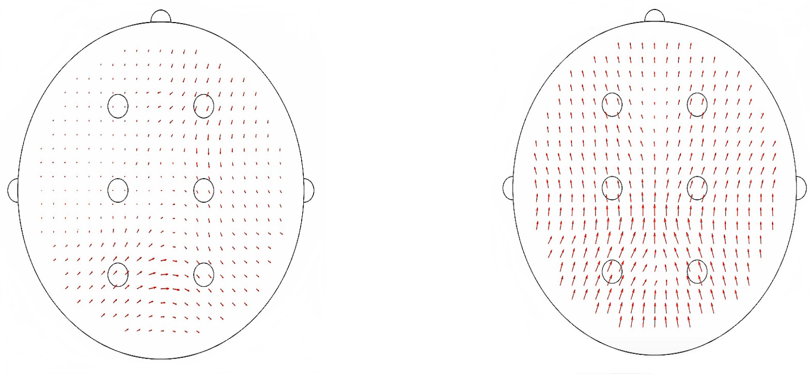

Fig. 1: Two typical examples of effective connectivity visualization - without (on the left) and during (on the right) visual stimulation. Arrow sizes and orientations are derived from the detected causal links.

## 3. Results

We divided the EEG signals into 4000 points (6 seconds) intervals. For each interval, after reconstructing the manifolds $M_X$ and $M_Y$, we computed the self-predictions and cross-predictions. In each case, 1000 points were predicted, with the help of 3000 historical points of the reconstructed trajectory.

After testing for significant differences between the prediction errors, we got the following results:

- In a pre-VS record, causality often changed orientation, intensity, and duration, without any obvious pattern.
- During the VS, there was an intense increase in causal influence from the back to the frontal parts of the same hemisphere, most pronounced in the posterior areas of the cerebral cortex. In the second half of the VS, the prediction errors were so reduced that, according to our rules, a bidirectional connection was often detected (probably a manifestation of the onset of synchronization of cortex regions).
- Intense causal effect from back to front was observable even after switching off the VS. However, the effect disappeared within 1-2 minutes, and during the rest of the 3-minute post-VS relaxation, the situation was similar to that before VS with causal effects often and unpredictably changing in direction.
- During VS, the left and right hemispheres resembled subsystems working in unison, but they were in fact causally independent. A causal connection between hemispheres was almost never detected.

As part of a recent master thesis project [7], we also made software that extrapolates local results to the entire cortex and shows the course of changes in the form of a video presentation. We created a 625 point grid and extrapolated the intensity and direction of causality between adjacent grid points based on the cross-prediction errors of the records from nearby positions. Fig. 1 shows two typical examples of effective connectivity visualization - without and during visual stimulation.

## 4. Discussion

Although neuroscience has been trying to understand connectivity for some time, we believe that only now the causality research is reaching a stage that allows a reliable evaluation of the directional (effective) type of connectivity in brain activity.

In this study, we used cross-predictions in reconstructed state spaces for bivariate causal detection and exploring dynamical networks whose nodes are characterized by time series. In this context, our EEG data are viewed as a network of six nodes. We must, however, be aware that the best we can hope for when reconstructing a causal dynamical network is finding the strongly connected components (sets of mutually reachable vertices) which represent distinct subsystems coupled through one-way driving links. We cannot recover self-loops or distinguish between direct driving, indirect driving, or correlate of direct or indirect driving.

Moreover, we still cannot be sure whether the dynamical network concept on the cortex is justified at all. The opposing standpoint in its extreme form presupposes the global nature of the brain with a cyclical information flow. Then, in the spirit of Takens' theorem, a single-channel EEG recording would suffice for encoding information about the entire dynamics of the system. Considerations of the relative autonomy of smaller brain regions, with changeable causal relationships, would be groundless.

Even the character of the EEG signal itself is still largely a mystery. In principle, if autoregressive models are suitable for modelling the EEGs, then Granger's methodology should be the right choice for causality detection. However, if deterministic dynamics dominate the data or a newer concept of EEG as a power-law noise combined with oscillating activity applies, then a qualified choice of some more recent causal method, such as CP, is required. Blind use of a causal method can easily result in contradictory conclusions and false detections.

In this study, a modern causal method based on cross-predictions detected a significant directional effect from the occipital to the frontal regions of the cerebral hemispheres during visual stimulation. The results look promising and interesting. But we are only at the beginning, and much remains unresolved. In further research, we must first compare our results with those obtained from the Granger test and draw conclusions from the comparison. We will also look at and discuss the differences in the results between the individual participants in the experiment. Finally, interpreting the results in a broader context can also be a complicated task that will require a lot of attention in the future.

**Acknowledgements**

Supported by the Slovak Grant Agency for Science (Grant 2/0081/19).

**References**

[1] Chicharro, D., Panzeri, S. (2014). Algorithms of causal inference for the analysis of effective connectivity among brain regions. *Frontiers in Neuroinformatics*, 8 (64).

[2] Granger, C. W. (1969). Investigating causal relations by econometric models and cross-spectral methods. *Econometrica: Journal of the Econometric Society*, 424–438.

[3] Krakovská, A., Jakubík, J. (2020). Implementation of two causal methods based on predictions in reconstructed state spaces. *Physical Review E*, 102 (2), 022203.

[4] Teplan, M., Krakovská, A., Štolc, S. (2011). Direct effects of audio-visual stimulation on EEG. *Computer Methods and Programs in Biomedicine*, 102 (1), 17–24.

[5] Takens, F. (1981). Detecting strange attractors in turbulence. In *Dynamical Systems and Turbulence*. Springer, 366–381.

[6] Lorenz, E. N. (1969). Atmospheric predictability as revealed by naturally occurring analogues. *Journal of the Atmospheric Sciences*, 26 (4), 636 – 646.

[7] Pócoš, Š. (2020). *Optimalization of state space predictions and their use for causality detection*. Master's thesis, Comenius University, Bratislava.

# A Measure of Prediction Precision for Granger Causality Analysis

**Martina Chvosteková**

Institute of Measurement Science, Slovak Academy of Sciences, Bratislava, Slovakia
Email: martina.chvostekova@savba.sk

***Abstract.*** *Identification of causal interactions from time-series data is an emerging issue in many fields of science. The causal connection between two variables is detected by the Granger causality if the prediction of one variable based on a linear combination of its past values can be improved by incorporating past values of another. The mean squared deviation is usually used to measure prediction for the Granger causality analysis. In this contribution, it is shown on an example that the mean squared deviation strictly decreases by adding a past value even from a causally independent variable and, due to this behaviour, it is unusable for such causal analysis. On the other hand, the adjusted squared deviation does not collide with the Granger causality definition in this way. The presented results imply that the confidence of the commonly used $F$-test of prediction improvement in the Granger causality analysis depends on the number of past values of the predicted variable included in a linear prediction. The adjusted squared deviation can be used to determine the proper number of past values.*

*Keywords: Granger Causality, Variance Estimator, Linear Prediction*

## 1. Introduction

Identification of causal interactions from time-series data is an emerging issue in many fields of science; for example, in neuroscience [1] this identification allows the characterization of functional circuits underpinning perception, cognition, behaviour, and consciousness. Granger [2] has defined a concept of causality which, under suitable conditions, is fairly easy to deal with in the context of linear autoregressive models. Therefore it has become quite popular in recent years. The Granger causality is based entirely on the predictability of some variable, say $X$. Thus, if the past of some other variable $Y$ contains information that helps predict $X$, and this information is contained in no other variable, then $Y$ is said to Granger cause $X$.

The important issue related to the foregoing definition is the measure of prediction precision. The variance of predictive error represents a prediction precision measure. The mean squared deviation (MSD) is often used to estimate the variance of predictive error. However, in regression with nonstochastic regressors, MSD is a biased estimator of the variance, and an adjustment for degrees of freedom is desired. The adjusted squared deviation (ASD) is such an unbiased estimator of the variance of predictive error. In this contribution, we analyze the relevance of MSD and ASD for the Granger causality analysis. The statistical significance of a prediction improvement in the Granger causality analysis is commonly assessed by the $F$-test for regression coefficients (i.e., the coefficients on the past values) significance. The behaviour of MSD, ASD, and the confidence of the $F$-test of prediction improvement is studied on an example of two causally independent variables.

## 2. Subject and Methods

Let variables $X$, $Y$ are represented by two zero-mean stationary time series $\{x_t\}_{t=1}^{T}$, $\{y_t\}_{t=1}^{T}$. Firstly, the precision of the prediction of a signal $x_t$ based only on its past values, and the precision of the prediction of $x_t$ containing also the past values of $Y$, as well has to be determined for analyzing if $Y$ Granger causes $X$, denoted $Y \to X$. Let $\tilde{X}_t$ represent the set of past values of

$X$ since time $t-1$, and let $\tilde{Y}_t$ represent the set of past values of $Y$ since time $t-1$. According to Granger, the linear prediction of $x_t$ using only the past of $X$ is of the form

$$P_t(x|\tilde{X}) = \sum_{j=1}^{p} a_j x_{t-j} \tag{1}$$

and linear prediction of $x_t$ using past of $X$ and past of $Y$ is of the form

$$P_t(x|\tilde{X},\tilde{Y}) = \sum_{j=1}^{p} b_j x_{t-j} + \sum_{j=1}^{q} c_j y_{t-j}. \tag{2}$$

Then, the predictive error series for the predictions (1) and (2) are defined as

$$\varepsilon_t(x|\tilde{X}) = x_t - P_t(x|\tilde{X}) \quad \text{and} \quad \varepsilon_t(x|\tilde{X},\tilde{Y}) = x_t - P_t(x|\tilde{X},\tilde{Y}), \tag{3}$$

respectively. The orders $p,q$ of the linear autoregressive models (1, 2) can be determined using a model selection criterion. The estimates of the regression coefficients $a_j$, $b_j$, $c_j$ are usually obtained with the least squares method by minimizing the sum of the squared predictive errors. It is worth noting that autoregressive modelling is suitable to fit a data, if $\varepsilon_t(x|\tilde{X})$ and $\varepsilon_t(x|\tilde{X},\tilde{Y})$ can be treated as zero mean white noise vector processes with time invariant variances. Let $\sigma_x^2$ and $\sigma_{xy}^2$ be the variance of $\varepsilon_t(x|\tilde{X})$ and $\varepsilon_t(x|\tilde{X},\tilde{Y})$, respectively.

It is said that $Y$ Granger-causes $X$ if we are better able to predict a value of $X$ using the past values of $Y$ than only the past values of $X$ are used. Thus, it holds $Y \to X$, if $\sigma_x^2 > \sigma_{xy}^2$. Unless there is no significant difference between the variances $\sigma_x^2$ and $\sigma_{xy}^2$, it is said that $Y$ does not Granger-cause $X$, denoted $Y \nrightarrow X$.

The prediction precision can be measured with the mean squared deviation (MSD), given as

$$^{MSD}\hat{\sigma}_x^2 = \frac{1}{T-p^{'}} \sum_{i=1}^{T-p^{'}} \varepsilon_t^2(x|\tilde{X}), \tag{4}$$

where $T$ is length of time series, $p^{'} = max(p,q)$ and $T-p^{'}$ is the number of model's data. For determination of $^{MSD}\hat{\sigma}_{xy}^2$, $\varepsilon_t^2(x|\tilde{X})$ is replaced by $\varepsilon_t^2(x|\tilde{X},\tilde{Y})$. MSD in regression with non-stochastic regressors is a biased estimator of the variance of predictive errors. It means that the expected value of $^{MSD}\hat{\sigma}_x^2$ is equal to the difference of a true value $\sigma_x^2$ and $p^{'}/(T-p^{'})\sigma_x^2$. Since the bias is equal to $-p^{'}/(T-p^{'})\sigma_x^2$, MSD slightly underestimates the variance of a predictive error on average.

Therefore, an adjustment for degrees of freedom is often desired to obtain an unbiased estimator of the variance. The adjusted squared deviation is given as

$$^{ASD}\hat{\sigma}_x^2 = \frac{1}{T-p^{'}-p} \sum_{i=1}^{T-p^{'}} \varepsilon_t^2(x|\tilde{X}). \tag{5}$$

For determination of $^{ASD}\hat{\sigma}_{xy}^2$, $p$ is replaced by $p+q$ and $\varepsilon_t^2(x|\tilde{X})$ is replaced by $\varepsilon_t^2(x|\tilde{X},\tilde{Y})$ in (5). MSD and ASD are asymptotically equivalent and are consistent estimators of variance if the predictive errors are the standard white noise [3].

The definition of Granger-non-causality implies that all regression coefficients $c_j$ are zero iff $Y$ fails to Granger-cause $X$. The significance of $q$ linear coefficient restrictions implied by the Granger non-causality may be assessed by the $F$-test for regression coefficients significance. If the null hypothesis about $Y \not\to X$ is rejected by the $F$-test, than it is concluded that $Y \to X$ [4]. Note that the opposite direction of causal influence (i.e., $X \to Y$) is analyzed analogously.

In the next part, we will demonstrate that MSD, a commonly used measure of the prediction precision for Granger causality analysis (e.g., [5]), does not fit the definition of Granger non-causality. In particular, we will demonstrate that MSD, due to its bias, is reduced using past of $Y$ in the case $Y \not\to X$, and this can lead to incorrect causal detection $Y \to X$. The behaviour of both estimators of variance (4, 5) and of the $F$-test for Granger non-causality will be studied for a model of causally independent variables.

## 3. Numerical Experiment

We consider two causally independent variables $X, Y$ (i.e., $X \not\to Y$ and $Y \not\to X$) represented by time series $\{x_t\}_{t=t^*+1}^{t^*+T}, \{y_t\}_{t=t^*+1}^{t+*T}$ generated by autoregressive model of order four and three

$$\begin{aligned} x_t &= \alpha_1 x_{t-1} + \alpha_2 x_{t-2} + \alpha_3 x_{t-3} + \alpha_4 x_{t-4} + \varepsilon_t(x) \\ y_t &= \beta_1 y_{t-1} + \beta_2 y_{t-2} + \beta_3 y_{t-3} + \varepsilon_t(y), \end{aligned} \tag{6}$$

respectively. The analysis of causal interaction between the variables was performed with generated time series of length $T = 1000$ after the initial $t^* = 10^4$ iterations were discarded. The regression parameters $\alpha_i$, $i = \{1,2,3,4\}$, $\beta_j$, $j = \{1,2,3\}$ were drawn from a uniform distribution $U(-1,1)$ with bounds $a = -1$ and $b = 1$. The errors $\varepsilon(x)$, $\varepsilon(y)$ were independent normally distributed random variables with zero mean and with the same deviation $\sigma_x = \sigma_y = 0.1$. The experiment was repeated $10^4$ times. We determined MSD and ASD of $\sigma_x^2$ with $p = \{3,4,5\}$ and of $\sigma_y^2$ with $p = \{2,3,4\}$, where the middle value in both sets of values $p$ represents the true order of the model. For each run, MSD and ASD of $\sigma_{yx}^2, \sigma_{xy}^2$ were calculated for $q = \{1,2,\ldots,10\}$ and two separate $F$-tests were performed (one for $X \to Y$, one for $Y \to X$) at the significance level $\alpha/2$ with $\alpha = 0.05$.

The averaged MSD and the averaged ASD estimates of variances are depicted in Figure 1. MSD estimate decreases as $p$ increases for $q = 0$ and decreases as $q$ increases for a fixed $p$. However, ASD estimate decreases by increasing $p$ until the value of $p$ is not equal to the true order of the model. After that, the ASD estimate does not change for larger values $p$. ASD estimate for a fixed value $p$ does not change significantly by increasing $q$.

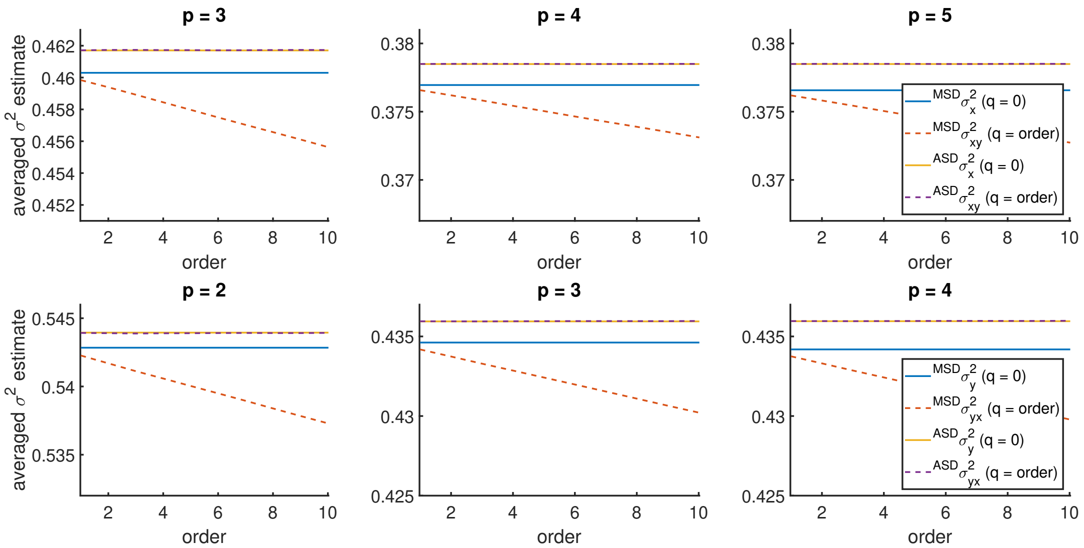


Fig. 1: The averaged MSD and ASD estimates of variance calculated on $10^4$ samples of time series with length $T = 10^3$ corresponding to causally independent variables $X, Y$ for various values of $p$ and $q$.

The empirical confidence level of the $F$-test is presented in Figure 2. The confidence level of the $F$-test strongly depends on the used order $p$. The presented empirical confidence level is below the chosen confidence level for the order $p$ smaller than the true order of the autoregressive model, i.e., $p = 4$ for variable $X$ and $p = 3$ for $Y$, and it decreases as $q$ increases. On the other hand, the presented empirical confidence levels equal to the theoretical confidence level independently of order $q$ for the orders $p$ equal or greater than the true order of the autoregressive model.

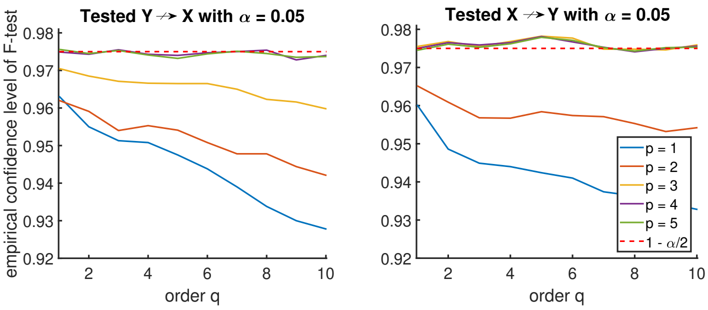


Fig. 2: The empirical confidence level is based on $10^4$ samples of time series with $T = 10^3$ corresponding to causally independent variables $X, Y$ for various values of $p$ and $q$.

## 4. Conclusions

We found out that MSD is not an appropriate measure of the prediction precision for the Granger causality analysis. MSD spuriously decreases when a past value is added to a prediction model, no matter it is its own past value of the predicted variable or the past value of the other causally not connected variable. The use of MSD in the context of Granger causality can lead to incorrect conclusions, as happened in [5]. Although ASD does not collide with the definition of the Granger causality in this way, we recommend, under the condition that linear autoregressive modelling is suitable to fit data, to assess the significance of causal connection by the $F$-test for regression coefficients significance. The confidence of the $F$-test depends on the number of past values of the predicted variable used in a linear prediction. It seems that the number of own past values for which ASD does not change substantially by adding more own past values can be recommended as a suitable one.

## Acknowledgements

Supported by the Scientific grant agency of the Ministry of Education of the Slovak Republic and of Slovak Academy of Sciences (Grant 2/0081/19, Grant 2-0096-21).

## References

[1] Seth, A.K., Barrett, A.B., Barnett, L. (2015) Granger causality analysis in neuroscience and neuroimaging. *The journal of neuroscience*, 35(8), 3293–3297.

[2] Granger, C.W.J. (1969) Investigating causal relations by econometric models and cross-spectral methods. *Econometrica*, 37, 424–438.

[3] Lütkepohl, H. (2005) *New Introduction to Multiple Time Series Analysis*, Springer-Verlag.

[4] Barnett, L., Seth, A.K. (2014) The MVGC multivariate Granger causality toolbox: A new approach to Granger-causal inference. *Journal of neuroscience methods*, 223, 50–68.

[5] Grassmann, G. (2020). New considerations on the validity of the Wiener-Granger causality test. *Heliyon*, 6, e05208.

# Handling Fluctuating Observability of the Rössler System

**Jozef Jakubík**

Institute of Measurement Science, Slovak Academy of Sciences, Bratislava, Slovakia
Email: jozef.jakubik.jefo@gmail.com

***Abstract.*** *Fluctuating observability of the Rössler system may lead to inconsistent prediction accuracy and that may influence causality detection of methods based on predictability improvement. Fluctuating observability is caused by an ill-conditioned numerical problem when drastically changing the magnitude of the observed variable. In this paper, we will show that this problem causes difficulties mainly in cases with a smaller number of data and when using an insufficient model. With enough data and "effort" to find the right model, we can achieve good accuracy of prediction from all variables.*

*Keywords: Rössler System, Observability, Neural Networks*

## 1. Introduction

Consider Rössler dynamical systems [1] (Fig. 1):

$$\begin{aligned} \dot{x} &= -1.015y - z \\ \dot{y} &= 1.015x + 0.15y \\ \dot{z} &= 0.2 + z(x - 10) \end{aligned} \tag{1}$$

where $(a, b, c)$ are parameters. We observe the Rössler system as time series. We denote the time series generated by variable $x$ as $X(t) = [x(1), x(2), \dots]$, and similarly for the other variables. We consider the original manifold $M$ - the set of points: $[x(t), y(t), z(t)]$ for $t \in \{1, \dots, T\}$ and $d_x$-dimensional reconstructed manifold $M_x$ - the set of points: $[x(t), x(t-1), \dots, x(t-d_x)]$ for $t \in \{1, \dots, T\}$. Similarly for the other variables.

The reconstructed manifolds $M_x, M_y$ and $M_z$ can be a good representation of the original manifold $M$ as a consequence of the Takens' theorem [2] which in simplified, slightly inaccurate version from [3] says:

> Suppose the $d$-dimensional state vector $x_t$ evolves according to an unknown but continuous and (crucially) deterministic dynamic. Suppose, too, that the one-dimensional observable $y$ is a smooth function of $x$, and "coupled" to all the components of $x$. Now at any time we can look not just at the present measurement $y(t)$, but also at observations made at times removed from us by multiples of some lag $\tau : y_{t-\tau}, y_{t-2\tau}$, etc. If we use $k$ lags, we have a $k$-dimensional vector. One might expect that, as the number of lags is increased, the motion in the lagged space will become more and more predictable, and perhaps in the limit $k \to \infty$ would become deterministic. In fact, the dynamics of the lagged vectors become deterministic at a finite dimension; not only that, but the deterministic dynamics are completely equivalent to those of the original state space (More exactly, they are related by a smooth, invertible change of coordinates, or diffeomorphism.) The magic embedding dimension $k$ is at most $2d + 1$, and often less.

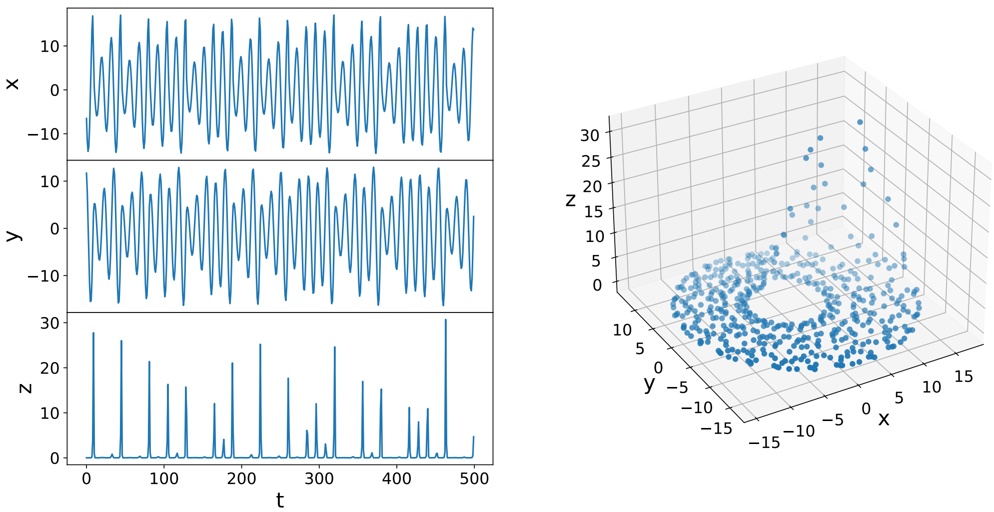


Fig. 1: Visualization of 500 points of variables $x$, $y$ and $z$ from the Rössler system (left) and 500 points of the original manifold $M$ of the Rössler system (right).

This means that we should be able to predict all variables (time-series) of the given system based on one given variable (time-series). This theoretical assumption is disturbed with numerical complications as mentioned for example in papers [4, 5, 6, 7]. The authors state that from some variables it is more difficult to obtain good predictions of the other variables and they attribute it to so-called observability. The paper [4] expands the term observability from linear systems to non-linear systems and define the local observability index. The paper also claims that variable $z$ in the Rössler system has lower values of observability around values close to 0 and therefore it would be more difficult to predict variables $x$ and $y$ from variable $z$ mainly if $z$ is close to 0. A simplified explanation of this phenomenon: Consider two real numbers $A$ and $B$. Consider that we know values $A$, $A \times B$ and the value $B$ is unknown. If $A \neq 0$ than based on the value $A \times B$ we can exactly identify the value $B$. But if $A = 0$ we cannot determine the value $B$. This may lead to an ill-conditioned numerical problem (for a small change in the inputs there is a large change in the answer) when predicting variables $x$ and $y$ from variable $z$ which is often moving around 0 as you can see in the Fig. 1.

In this paper, we will show that low observability may not be a problem with enough data and effort in searching for the model. Then the predictions of variables $x$ and $y$ from variable $z$ in the Rössler system may be as good as from variables $x$ and $y$.

## 2. Data and Methods

We generated 11000 data points from the Rössler system, Eq. 1. 10000 points were used for training our models and 1000 points for evaluating the trained models. We normalize all variables to mean zero and variance one. For the evaluation of prediction error, we use mean square error (MSE). Our model is a 3-layer neural network with 10 nodes on every layer and the hyperbolic tangent activation function (except for the output layer). As a loss, we used MSE and we used an iterative optimising method stochastic gradient descent - SGD (unless otherwise stated, with 1000 iterations).

## 3. Results

As is shown in Table 1, baseline predictions of variables $x$ and $y$ from variable $z$ are not as accurate as from variables $x$ and $y$.

Table 1: Mean of 100 MSE of baseline predictions (using 1000 optimisation steps) of predicted variables based on the explanatory variable.

| | | explanatory variable | | |
|---|---|---|---|---|
| | | $x$ | $y$ | $z$ |
| predicted variable | $x$ | $5.7777\times10^{-4}$ | $8.398\times10^{-4}$ | $1.073292\times10^{-2}$ |
| | $y$ | $5.7477\times10^{-4}$ | $3.1525\times10^{-4}$ | $1.070302\times10^{-2}$ |
| | $z$ | $3.43108\times10^{-3}$ | $1.158321\times10^{-2}$ | $3.989074\times10^{-2}$ |

Figure 2 shows the rising accuracy on the test set with the rising number of optimisation steps.

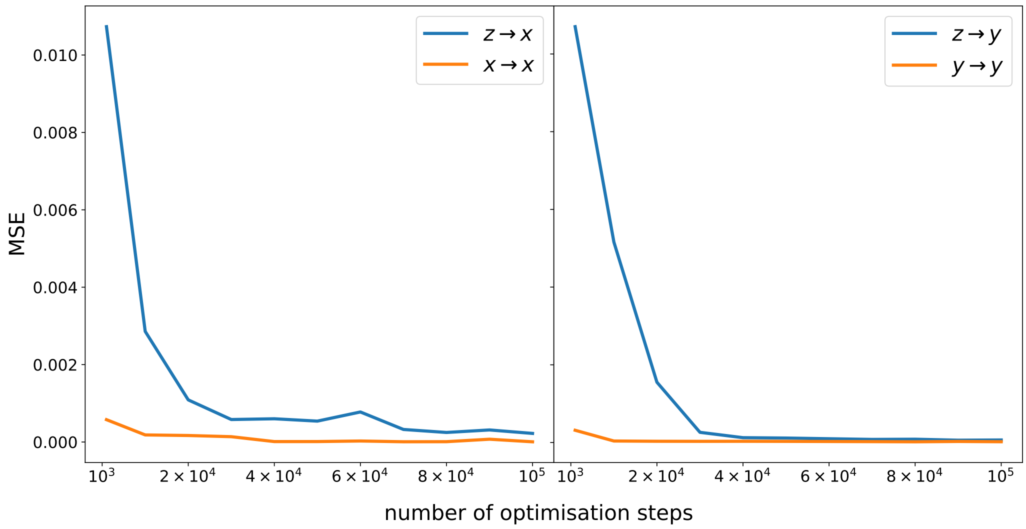


Fig. 2: Rising accuracy of predictions of variables $x$ and $y$ from variable $z$ compared with predictions from itself.

Moreover, Table 2 shows that the accuracy of prediction of variable $y$ from variable $z$ rises faster than the accuracy from the other two variables.

Table 2: Mean of 100 MSE of improved predictions (using 100000 optimisation steps) of predicted variables based on the explanatory variable.

| | | explanatory variable | | |
|---|---|---|---|---|
| | | $x$ | $y$ | $z$ |
| predicted variable | $x$ | $5.48400117\times10^{-6}$ | $3.01541549\times10^{-5}$ | $2.22069189\times10^{-4}$ |
| | $y$ | $1.46055823\times10^{-5}$ | $1.99560227\times10^{-5}$ | $6.54280003\times10^{-5}$ |
| | $z$ | $1.09350026\times10^{-5}$ | $1.51071907\times10^{-5}$ | $7.81030053\times10^{-4}$ |

## 4. Conclusions

The initial results from Table 1 may be interpreted as a violation of Takens's theorem because the result from a small number of iterations may lead to around 20× worse results of prediction of variables $x$ and $y$ from variable $z$. The main difficulty is the ill-conditioned problem of prediction from the "jumping" variable $z$. As we showed in Fig. 2 and Table 2 this problem may be solved with more available data or a better, more accurate model, which can be achieved (in the case of neural network) with more optimisation steps. Ill-conditioned prediction from the variable $z$ may still be a problem in the case of low training data availability, therefore these cases should be interpreted carefully.

For example, consider the discrete Rössler system [8]. Every variable can be expressed as a function of any given variable, which relates to Takens's theorem. Therefore for the discrete variant of the Rössler system, you can estimate those functions from data. With a larger dataset, the estimated functions will fit the original functions better. This may be complicated with the bad numerical behaviour of those functions. This is the case when we use the variable $z$ in the Rössler system. This is not a theoretical problem, just a complication that can be overcome with more data and better estimation models.

## Acknowledgements

The work was supported by the Scientific Grant Agency of the Ministry of Education of the Slovak Republic and the Slovak Academy of Sciences, projects VEGA 2-0096-21 and VEGA 2-0081-19.

## References

[1] Rössler, O.E. (1976). An equation for continuous chaos. *Physics Letters A* 57(5), 397–398.

[2] Takens, F. (1981). Detecting strange attractors in turbulence. In: *Dynamical systems and turbulence, Warwick 1980*. Springer, 366–381.

[3] Shalizi, C.R. (2006). Methods and techniques of complex systems science: An overview. *Complex systems science in biomedicine*, 33–114.

[4] Aguirre, L.A., Letellier, C. (2005). Observability of multivariate differential embeddings. *Journal of Physics A: Mathematical and General* 38(28), 6311.

[5] Aguirre, L.A., Bastos, S.B., Alves, M.A., Letellier, C. (2008). Observability of nonlinear dynamics: Normalized results and a time-series approach. *Chaos: An Interdisciplinary Journal of Nonlinear Science* 18(1), 013123.

[6] Aguirre, L.A., Portes, L.L., Letellier, C. (2018). Structural, dynamical and symbolic observability: From dynamical systems to networks. *PLoS One* 13(10), e0206180.

[7] Krakovská, A., Jakubík, J. (2020). Implementation of two causal methods based on predictions in reconstructed state spaces. *Physical Review E* 102(2), 022203.

[8] Selvam A, G., Roslin, D., Rajendran, J. (2014). A discrete model of rossler system. *International Journal of Advanced Technology in Engineering and Science*, Volume No.02, August 2014, ISSN (online): 2348–7550.

# Computational Study of Magnetic Particle Alignment in External Magnetic Field Under the Influence of Viscous and Brownian Torques

**[1]Andrej Krafcik, [2]Peter Babinec, [1]Ivan Frollo**

[1]Institute of Measurement Science, Slovak Academy of Sciences, Bratislava, Slovakia,
[2]Faculty of Mathematics, Physics and Informatics, Comenius University, Bratislava, Slovakia
Email: andrej.krafcik@savba.sk

***Abstract.*** *Dynamics of rotational magnetic particle alignment, an inverse process to Brownian relaxation, has been studied theoretically. It was found that arbitrary viscous torque with history term due to inertia and friction of surrounding water ambient has significant effect in strong magnetic field limit. On the other hand, for weak fields it can be neglected and stochastic Brownian torque induced by random collisions of surrounding fluid molecules is dominant.*

*Keywords: Magnetic Particle Alignment, Arbitrary Viscous Torque, Stochastic Brownian Torque, Stochastic Integro-Differential Equation, Simulation*

## 1. Introduction

Magnetic particle alignment, as Brownian rotation of the whole particle or rotation of its magnetic moment, are inverse processes to the Brownian or Néel relaxation. Their mechanism is today well known, although description of their dynamics is often simplified. In this paper we would like to address the description of dynamics of the first one—Brownian rotation of the magnetic particle during magnetic alignment.

Magnetic particle in external magnetic field feels magnetic torque, which generates its rotational movement. If the particle is located in viscous fluid ambient viscous torque due to friction breaks its rotation. There is often used quasi-steady limit ($\gamma\omega = 8\pi\eta R^3\omega$) to evaluate of this viscous torque, which use is correct only for constant angular velocity during particle rotation. For arbitrary angular velocity, addition of history term to the viscous term is necessary, as it was shown [1]. Origin of this term is based on inertia and friction of fluid around the arbitrary rotating particle. In further, denote quasi-steady viscous torque and its history term simply as arbitrary viscous torque.

Also in fluid ambient, particle small enough feels stochastic effect of Brownian motion of surrounding molecules [2] with intensity dependent on temperature. Denote this contribution to the overall torque on magnetic particle as stochastic Brownian torque.

In most papers [3] [4] only quasi-steady viscous torque is concerned and the history torque, inertia torque and stochastic Brownian torque are completely neglected, as well as consider only the latter and simple quasi-steady viscous term [2], or looks on thermal disturbance of rotational magnetic alignment with Brownian motion through the rotational diffusion model [5]. Therefore, we aimed to develop complex model of dynamics of rotational magnetic particle alignment in external homogeneous magnetic field and fluid ambient, coming out of the arbitrary viscous torque and stochastic Brownian torque. This approach brings to the studied problem solution of stochastic integro-differential equation, which is not trivial.

## 2. Subject and Methods

Lets consider quiescent spherical magnetic particle with radius $R$, mass density $\rho_p$, and magnetic moment $\mu_p$ originally oriented in perpendicular direction to the external homogeneous magnetic flux density $B_0$, and water as viscous fluid ambient with mass density $\rho$, dynamic

Table 1: Parameters used in simulations.

| Parameter | Symbol | Value | Unit |
|---|---|---|---|
| Finite time step | $h$ | $10^{-8}$ | s |
| Thermodynamic temperature | $T$ | 293.15 | K |
| Magnetic flux density norm | $B_0$ | $5\times 10^{-6}, \ldots, 0.5, 5$ | T |
| Water dynamic viscosity | $\eta$ | $10^{-3}$ | Pa.s |
| Water mass density | $\rho$ | $10^3$ | kg/m$^3$ |
| MyOne particle diameter | $2R$ | $10^{-6}$ | m |
| MyOne particle mass density | $\rho_p$ | 1 792 | kg/m$^3$ |
| MyOne particle magnetic moment[a] | $\mu_p$ | $2.25\times 10^{-14}$ | A.m$^2$ |

[a] Calculated as $\mu_p = M_{sp}V_p$, where $M_{sp} = 43\times 10^3$ A/m and $V_p = \frac{4}{3}\pi R^3$.

and kinematic viscosity $\eta$ and $\nu = \eta/\rho$, respectively, and thermodynamic temperature $T$. Rotational magnetic alignment of such particle can be described with the system of differential equations and initial conditions:

$$I_p \frac{\mathrm{d}\omega}{\mathrm{d}t} = \mu_p B_0 \sin\varphi + T_\mathrm{v}(t) + T_\mathrm{B}(t), \qquad \frac{\mathrm{d}\varphi}{\mathrm{d}t} = -\omega, \qquad \varphi(0) = \frac{\pi}{2}\,\mathrm{rad}, \qquad \omega(0) = 0\,\mathrm{rad/s} \tag{1}$$

where $\varphi \equiv \measuredangle(\vec{B}_0, \vec{\mu}_p)$ and $\omega$ are angle and angular velocity of magnetic particle, and $I_p = \frac{2}{5} m_p R^2$ and $m_p = \frac{4}{3}\pi R^3 \rho_p$ are its moment of inertia and mass, respectively. Arbitrary viscous torque is according [1]:

$$T_\mathrm{v}(t) \equiv -\gamma\omega(t) - \frac{\gamma}{3\sqrt{\pi}} \int_{-\infty}^{t} K(t-\tau) \frac{\mathrm{d}\omega(\tau)}{\mathrm{d}\tau}\,\mathrm{d}\tau, \tag{2}$$

where $\gamma \equiv 8\pi\eta R^3$ is Stokes drag coefficient and kernel function is:

$$K(t-\tau) \equiv \frac{R}{\sqrt{\nu(t-\tau)}} - \sqrt{\pi}\exp\left(\frac{\nu(t-\tau)}{R^2}\right)\mathrm{erfc}\left(\frac{\sqrt{\nu(t-\tau)}}{R}\right). \tag{3}$$

History integral term in (2) of whole time evolution of angular acceleration is denoted as "acceleration torque". Fluctuating Brownian torque is stochastic term generated with random impulses from the neighboring fluid molecules, which can be mathematically represented as Gaussian white noise with zero mean ($\langle W(t)\rangle = 0$) and with assumption of un-correlation ($\langle W(t)W(t+\tau)\rangle = \delta(\tau)$) [6]. Then, stochastic Brownian torque can be expressed as:

$$T_\mathrm{B}(t) \equiv \sqrt{2k_\mathrm{B}T\gamma}W(t), \tag{4}$$

where $k_\mathrm{B}$ is Boltzmann constant, $\langle\ldots\rangle$ represents an ensemble average and $\delta(\tau)$ is the Dirac delta function. This Gaussian white noise in stochastic Brownian torque in discrete sense has variance $\frac{1}{h}$, where $h$ is the time step.

For solution of the system of integro-differential equations (1)–(4) we have used first-order integration method generalizing Euler method to stochastic differential equation (finite difference approach) [6] and order one quadrature scheme to evaluation of history viscous acceleration torque integral term similar to those presented in [7], however using different kernel function, i.e. (3).

Parameters used in simulations are shown in Table 1. As the particle we have considered commercially available MyOne 1 $\mu$m (ThermoFischer Scientific, Dynabeads$^{\mathrm{TM}}$ MyOne$^{\mathrm{TM}}$).

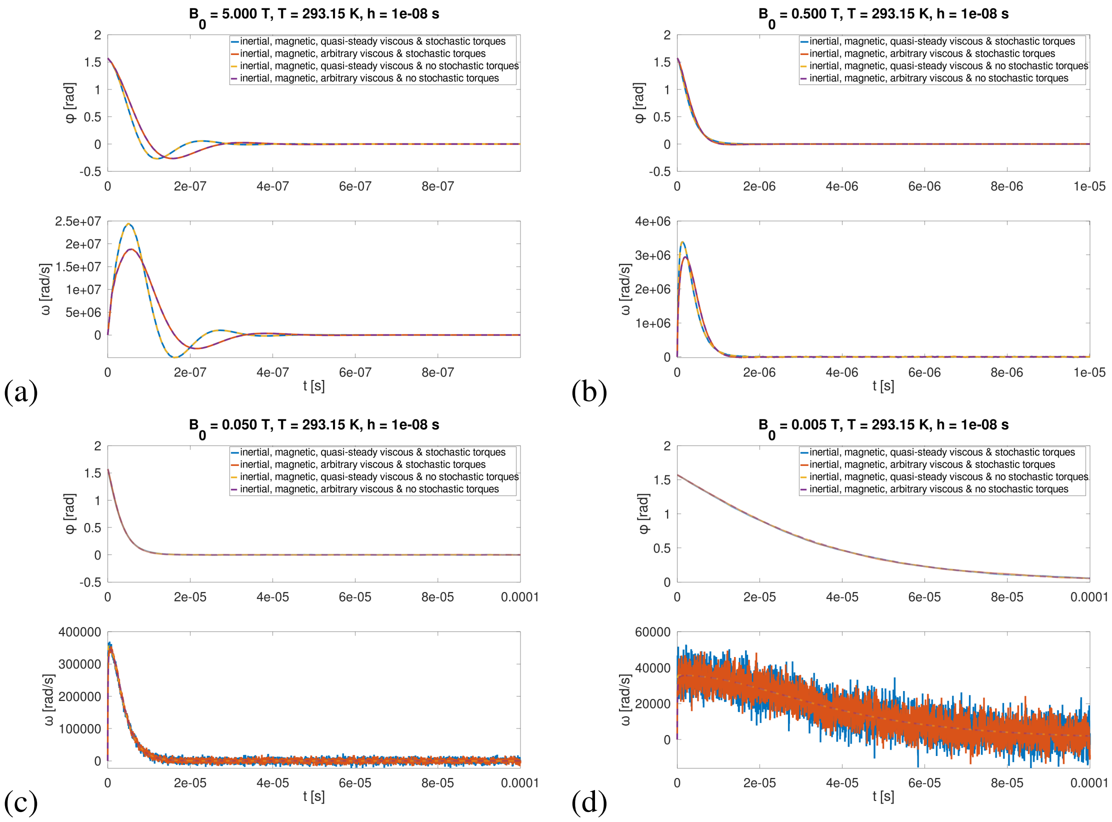


Fig. 1: Rotational magnetic particle alignment. Comparison of models for $B_0 = 5, 0.5, 0.05, 0.005\,\mathrm{T}$ (a)–(d), respectively.

## 3. Results and Discussion

We have simulated magnetic particle alignment in external homogeneous magnetic field with $B_0 = 5, 0.5, 0.05, 0.005\,\mathrm{T}$ and originally quiescent water as fluid ambient for four different models involving: (i) magnetic, quasi-steady viscous and stochastic Brownian torque, (ii) magnetic, arbitrary viscous and stochastic Brownian torque, (iii) magnetic, quasi-steady viscous and no stochastic Brownian torque, and (iv) magnetic, arbitrary viscous and no stochastic Brownian torque (for comparison see Fig. 1). Significant effect of history acceleration torque (arbitrary viscous torque) is visible only for the strongest magnetic fields when reduction of amplitude of $\omega$, and elongation of period due to inertia of fluid surrounding magnetic particle is obvious. On the other hand, affect of stochastic Brownian torque rises with weakening of magnetic field, when magnetic particle feels stochastic Brownian motion collisions of surrounding fluid molecules. Stochastic behavior for shown $B_0$ in Fig. 1 is well visible only for $\omega(t)$, however, with further weakening of $B_0$, stochasticity will be well visible also for $\varphi(t)$, and for fields with $B_0 \leq 50\mu\mathrm{T}$ its affect starts to be significant.

From simulations we have estimated characteristic time of rotational magnetic particle alignment for each $B_0$, and found its dependence on magnitude of $B_0$ as a least-square minimization fit: $\tau_{\mathrm{char}}(B_0) = \frac{C}{B_0}$ with obtained parameter $C = 1.655 \times 10^{-7}\,\mathrm{s.T}$. Here has to be mentioned limitation of numerical evaluation of history acceleration torque using kernel function (3) due to presence of $\exp(t\nu/R^2)$ function in its definition, which is for used values of parameters numerically reachable only for $t \leq 10^{-4}\,\mathrm{s}$. Therefore we have to omit models (ii) and (iv) with arbitrary viscous torque for weaker magnetic fields simulations, i.e. for $B_0 \leq 0.5\,\mathrm{mT}$ (see Fig. 2). Although, it does not matter, while, its affect for the weak magnetic fields can be neglected, as it was mentioned in discussion for Fig. 1. Also, there is an another limitation of our model: Due to history acceleration torque, stochastic Brownian torque should be not mathematically

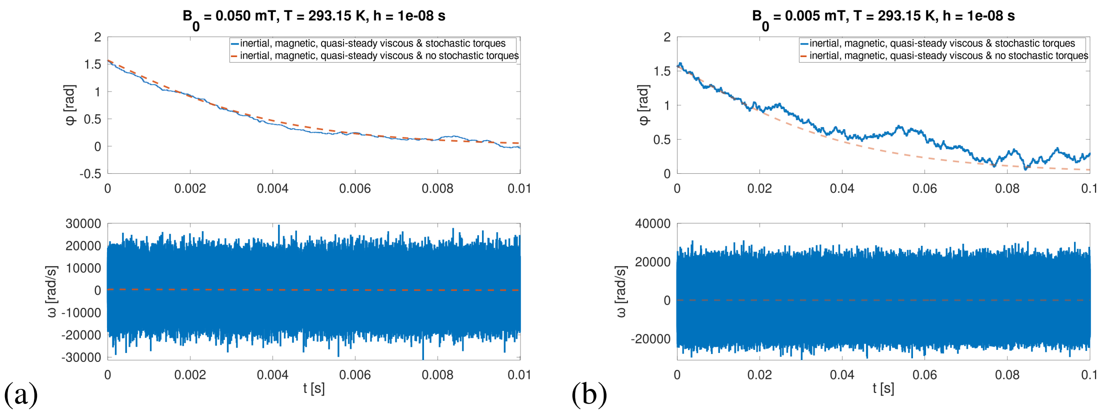


Fig. 2: Rotational magnetic particle alignment. Comparison of models for $B_0 = 0.05, 0.005\,\mathrm{mT}$.

represented as Gaussian white random process in Langevin theory, but "colored" one [8]. On the other hand, correlation in time of random process due to neglecting of history term in weak magnetic flux density field limit diminishes.

## 4. Conclusions

Complex model of rotational magnetic particle alignment dynamics has been presented for the scale of homogeneous magnetic flux densities $B_0$ from $5\,\mu\mathrm{T}$ to $5\,\mathrm{T}$. Significance of the history arbitrary viscous torque term rises in strong magnetic flux density field limit. On the other hand, in weak $B_0$ limit it diminishes and stochastic Brownian torque affect starts to manifest. Also characteristic time of rotational magnetic particle alignment for the whole scale of $B_0$ has been estimated.

## Acknowledgements

This work was supported with grants No. APVV-19-0032 and VEGA 2/0003/20.

## References

[1] Lei, U., Yang, C., Wu, K. (2006). Viscous torque on a sphere under arbitrary rotation. *Applied Physics Letters*, 89(18), 181908.

[2] Romodina, M., Lyubin, E., Fedyanin, A. (2016). Detection of Brownian torque in a magnetically-driven rotating microsystem. *Scientific Reports*, 6, 21212.

[3] Helgesen, G., Pieranski, P., Skjeltorp, A. (1990). Nonlinear phenomena in systems of magnetic holes. *Physical Review Letters*, 64(12), 1425–1428.

[4] Tierno, P., Claret, J., Sagues, F., Cabers, A. (2009). Overdamped dynamics of paramagnetic ellipsoids in a precessing magnetic field. *Physical Review E - Statistical, Nonlinear, and Soft Matter Physics*, 79(2), 021501.

[5] Yamaguchi, M., Ozawa, S., Yamamoto, I. (2009). Rotational diffusion model of magnetic alignment. *Japanese Journal of Applied Physics*, 48(6), 063001.

[6] Volpe, G., Volpe, G. (2013). Simulation of a Brownian particle in an optical trap. *American Journal of Physics*, 81(3), 224–230.

[7] Daitche, A. (2013). Advection of inertial particles in the presence of the history force: Higher order numerical schemes. *Journal of Computational Physics*, 254, 93–106.

[8] Tothova, J., Lisy, V. (2015). Generalized Langevin theory of the Brownian motion and the dynamics of polymers in solution. *Acta Physica Slovaca*, 65(1), 1–64.

# Methodology for Measuring Phase Shifts of Signals Using Discrete Hilbert Transform

**[1]Yurii Kuts, [2,3]Orest Kochan, [1]Iuliia Lysenko, [3]Ruslana Huminilovych**

[1]Igor Sikorsky Kyiv Polytechnic Institute, Kyiv, Ukraine
[2]School of Computer Science, Hubei University of Technology, Wuhan, China
[3]Lviv Polytechnic National University, Lviv, Ukraine
Email: j.lysenko@kpi.ua

***Abstract.*** *The phase methods for measuring physical quantities and the phase measuring equipment are widely used in various fields of science and technology. Improving the metrological characteristics of phase measuring equipment, which is intended for use in a wide range of signal-to-noise ratio, involves the development of a methodology for phase measurements and the presentation of their results based on the harmonization of the material and physical measures of phase shifts. The paper proposes a signal processing methodology based on a combination of the discrete Hilbert transform and deterministic as well as statistical methods of phase measurement. Circular statistics such as circular mean, circular variance and the resulting vector length are proposed for use in the phase measurements.*

*Keywords: Signal Processing Methodology, Hilbert Transform, Circular Statistics*

## 1. Introduction

The concept of the internet of things [1, 2] together with the progress in measurement science [2, 3] led to the exponential growth of measurement data. The rise of the computational power of computers created the opportunity to develop the methods for measurement data processing to improve the accuracy of measurement and their noise immunity [1-3]. This paper is devoted to the development of such a technique in phase shift measurements.

Phase methods of measuring physical quantities, transformation, and transfer of information allow effectively solving many problems in diverse fields of science and technology, e.g. in experimental physics, radiophysics, radio and radar navigation, telecommunications, geodesy, non-invasive testing, and so on. Based on the phase methods, many important scientific and technical problems related to the precise measurement of distances, time intervals, angles, analysis of the characteristics of signal fields of different physical nature have been solved.

The application of the methods required the creation of appropriate phase measuring equipment. At the initial stage of the development of the phase measuring equipment, the measurement transformation of signals' phase shifts to either the rotation angle of the electromechanical device' arm or constant voltage or time intervals was used [4, 5]. There had already been accurate measures of voltage and time intervals that allowed simplifying the phase measuring equipment. Then later, the two-phase generators [5], which generated two coherent signals with a fixed phase shift between them, began to be used as signals' phase shift measures. That approach determined the further direction of development of the phase measurement techniques for a long time. It also determined the use of methods for processing random quantity in the algorithms of phase measurements and during the error estimation of that measurements. But the transfer of statistical analysis methods of random quantity into the field of processing the measurements of signals' phase shifts has its limitations. This is because the phase of periodic signals has a natural periodicity of $2\pi$, which has to be taken into account when justifying the algorithms for processing phase data, and when forming the result of phase measurements and choosing the probability measure [6]. In the case of low signal-to-noise ratios in the additive mixture of harmonic signal and noise, all of these are especially important. In general, the abovementioned signals belong to periodic signals. The property of periodicity is manifested in the repetition of certain parts or states of processes and signals. In the case of estimating the parameters of harmonic signals, which are the components of the additive mixture with noise, the problem of processing random phase shifts occurs. Since the models of random angles are similar to the models of random phase shifts [7], the methods of statistical processing of angular data can be applied to them [8, 9]. It should be noted that advances in computer technology and digital signal processing created the preconditions for improving the methodology of processing the phase measurements, more extensive use of complex algorithms for the statistical processing of angular data. All of these allow significantly improving the metrological characteristics of the phase measuring equipment.

The paper considers the features of the proposed methodology for processing the phase measurements based on the use of the discrete Hilbert transform (DHT) [10, 11] and methods of statistical processing of angular data.

## 2. Basic of the Phase Measurements Methodology

The signals can be presented as follows:

$$u(t) = U\cos[2\pi ft + \varphi] + n(t),\ u_r(t) = U_r\cos[2\pi ft],\ t \in T\,, \tag{1}$$

where $U$, $U_r$ are the trains of the signal $u(t)$ and the reference signal $u_r(t)$, respectively; $\varphi$ the phase shift between the harmonic signal component $u(t)$ and the reference signal $u_r(t)$; $t$, $T$ are time and time interval of signal observation, respectively; $f$ is the frequency of the harmonic signals; $n(t)$ is the implementation of white noise with zero expectation and $\sigma^2$ variance.

There is a Fourier transform for signals from Eq. 1. After transformation to the digital signals, they are represented by samples $\{u[j],\ j=\overline{1,J}\}$, $\{u_r[j],\ j=\overline{1,J}\}$, where $J = \mathrm{int}(T/T_s)$, where $T_s$ is a sampling interval. It is necessary to consider the methodology for determining the phase shift estimate based on combining the usage of the DHT and methods of statistical processing of angular data.

*Discrete Hilbert Transform and Its Application for Signal Phase Calculation*

The DHT and the concept of "analytical signal" introduced on its basis are widely used for theoretical researches of periodic processes and phenomena [7, 8]. The discrete analytical sequence is determined as $\dot{z}[j] = u[j] + i\tilde{u}[j]$, where $\tilde{u}[j]$ is a DTH of $u[j]$. The simplest method of DHT calculating is the spectral method. It can be found in [12]. From the definition of a discrete analytical sequence, one can find the discrete instantaneous phase of the sequence $x[n]$:

$$\hat{\varphi}[j] = \tan^{-1}\frac{\tilde{u}[j]}{u[j]} + \frac{\pi}{2}\left\{2 - \mathrm{sign}\,\tilde{u}[j]\left(1 + \mathrm{sign}\,u[j]\right)\right\}. \tag{2}$$

Function in Eq. 2 has a sawtooth shape and changes periodically within the range of $[0, 2\pi)$. The discrete instantaneous unwrapped phase could be obtained from Eq. 2:

$$\hat{\Phi}[j] = \hat{\varphi}[j] + 2\pi g\left(\hat{\varphi}[j]\right), \tag{3}$$

where $g\left(\hat{\varphi}[j]\right)$ is a step function, which increases by one when the phase changes from $2\pi$ to 0.

The discrete instantaneous phase shift is determined according to the equation as follows:

$$\hat{\varphi}_j = \hat{\Phi}_j - 2\pi fT_s j,\ j = \overline{1,J}\,. \tag{4}$$

One can apply the methods of statistical processing of angular data to the sample from Eq. 4 and calculate several circular statistics.

*Circular Statistics for the Use in Phase Measurement*
The most important circular statistics in phase measurement are given in Table 1.

Table 1. Some circular statistics defined for the sample $\hat{\varphi}_j,\ j=\overline{1,J}$.

| Name of circular statistical characteristic | Definition, formula |
|---|---|
| Sampling trigonometric moment of order u relatively to the direction α (u is an integer) | $T_u(\alpha)=\frac{1}{J}\sum_{j=1}^{J}e^{iu(\hat{\varphi}_j-\alpha)}=a_u(\alpha)+ib_u(\alpha)=r_u(\alpha)e^{im_u(\alpha)}$ <br> $a_u(\alpha)=\frac{1}{J}\sum_{j=1}^{J}\cos\left[u\left(\hat{\varphi}_j-\alpha\right)\right]=a_u(0)\cos(u\alpha)+b_u(0)\sin(u\alpha)$ <br> $b_u(\alpha)=\frac{1}{J}\sum_{j=1}^{J}\sin\left[u\left(\hat{\varphi}_j-\alpha\right)\right]=-a_u(0)\sin(u\alpha)+b_u(0)\cos(u\alpha)$ |
| Sampling circular mean | $\varphi_c=\tan^{-1}\frac{S}{C}+\frac{\pi}{2}\left[2-(signS)\times(1+signC)\right]$ <br> $C=\frac{1}{J}\sum_{j=1}^{J}\cos\hat{\varphi}_j;\quad S=\frac{1}{J}\sum_{j=1}^{J}\sin\hat{\varphi}_j$ |
| Sampling length of the resultant vector | $r=\sqrt{C^2+S^2}$ |
| Sampling circular variance | $V=1-r$ |

*Probability Distributions of Random Angles for the Use in Phase Measurements*
The measurement result consists of one measured value and the measurement uncertainty with the stated probability of coverage [6]. The probability can be evaluated from probability density functions. The probability distribution functions of random phase shifts are the same as those of random angles. One of the characteristic features of the circle as space, on which sets of phase shifts are formed, is the periodicity (with the period 2π) property of the laws of the probability density distribution of random phase shifts.

The von Mises probability distribution for a random angle is determined by the formula:

$$p_M\left(\theta\,|\,\mu,k\right)=\exp\left\{k\cos\left(\theta-\mu\right)\right\}\big/2\pi I_0\left(k\right),\ |\mu|<\infty,\ k>0\,, \tag{5}$$

where $I_0$ is the modified Bessel function of the first kind and zero-order; $\mu$ is the circular average direction of a random angle; $k$ is the concentration parameter of a random angle in the vicinity of μ.

The von Mises distribution is one-vertex and symmetric according to the value of μ, which is the mathematical expectation of this distribution. Some other typical circle distributions such as uniform, triangular, wrapped normal are presented in [5]. For the wrapped normal distribution, the central limit theorem holds on the circle: for independent random angles, which have the same probability distribution function, the probability distribution of the normalized sum of angles approaches to the wrapped normal distribution [5]. An appropriate choice of the parameters of the wrapped normal distribution allows giving a reasonable approximation for it by von Mises distribution.

## 3. Using the Offered Methodology in Some Applied Problems of Phase Measurement

The research confirms the effectiveness of the proposed methodology for phase measurements in the following applications: (i) precise phase shifts measurement when a signal-to-noise ratio close to unity; (ii) estimation of the signal period by its discrete instantaneous unwrapped phase [13]; (iii) detection of ultrasonic testing signals at a low signal-to-noise ratio using the sampling length of the resultant vector, which is calculated in the sliding mode; (iv) determination of the signal-to-noise ratio in case of the sum of the harmonic signal and Gaussian noise through sampling trigonometric moments.

## 4. Conclusions

The DHT allows determining the signal phase through the tan-1 function without a physical measure of phase. Since the signal samples are obtained with the sampling interval, it allows studying their change even within one period of the carrier signal in the case of modulation of the phase and amplitude of the harmonic signal. It also allows obtaining samples of phase shifts of large volumes to which the methods of statistical processing of angular data can be applied. Thus, it increases the measurement accuracy. The probability distribution of random phase shifts is proposed to determine the probability of coverage, coverage factor, and extended measurement uncertainty for the phase measurements.

## References

[1] Jun, S., Przystupa, K., Beshley, et all. (2020). A Cost-Efficient Software Based Router and Traffic Generator for Simulation and Testing of IP Network. *Electronics*, *9*(1), 40.

[2] Pytka, J., Budzyński, P., Józwik, J., et all. (2019). Application of GNSS/INS and an Optical Sensor for Determining Airplane Takeoff and Landing Performance on a Grassy Airfield. *Sensors*, 19(24), 5492.

[3] Wang, J., Kochan, O., Przystupa, K., and Su, J. (2019). Information-measuring system to study the thermocouple with controlled temperature field. *Measurement Science Review*, 19(4), 161-169.

[4] Dorozhovets, M., Motalo, V., Stadnyk, B., Vasyliuk, V., Borek, R. and Kovalchyk, A. (2005). *Fundamentals of metrology and measuring techniques*, vol. 2, “Measuring techniques”. Lviv Polytechnic National University Press. *(In Ukrainian).*

[5] Kuts, Y., Shcherbak, L. (2009). *Statistical phase measurement*. Ternopil Ivan Puluj National Technical University Press. *(In Ukrainian).*

[6] *International Vocabulary of Metrology*: Basic and General Concepts and Associated Terms, JCGM 200:2012 (2012).

[7] Babak, V., Yeremenko, V., Kuts, Y., Myslovych M. amd Shcherbak L. (2019). *Models and measures in measurements*. Naukova Dumka Publishing. *(In Ukrainian).*

[8] Mardia K. (2000). *Directional Statistics*. John Willey & Sons.

[9] Fisher N. (2000). *Statistical Analysis of Circular Data*. Cambridge University Press.

[10] Bendat, J., Piersol, A. (2010). *Random Data. Analysis and Measurement Procedures*. John Willey & Sons.

[11] Poularikas, A. (2010). *Transforms and Applications Handbook*. CRC Press LLC.

[12] Lawrence Marple, S. (1999). Computing the Discrete-Time ”Analytic” Signal via FFT. *IEEE Transactions on Signal Processing*, 47 (9), 2600-2603.

[13] Kuts, Y., Protasov, A., Lysenko, I., Bliznuk, O. and Uchanin, V. (2017). *Using multidifferential transducer for pulsed eddy current object inspection*. 2017 IEEE 1st Ukraine Conference on Electrical and Computer Engineering, 826–829.

# Exact Confidence Intervals for Parameters in Linear Models With Parameter Constraints

[1]Viktor Witkovský, [2]Gejza Wimmer

[1]Institute of Measurement Science, Slovak Academy of Sciences, Bratislava, Slovak Republic
[2]Mathematical Institute, Slovak Academy of Sciences, Bratislava, Slovak Republic
Email: witkovsky@savba.sk

***Abstract.*** *We consider the exact distribution of the best linear unbiased estimator (BLUE) of a linear combination of the unknown model parameters in linear models with possible parameters constraints. Here, we present a method for computing the exact confidence intervals for the considered linear combinations of the model parameters under the assumption that the errors are linear combinations of independent random variables with known probability distributions. This is a typical situation in measurement and metrology. It is often necessary to consider systematic errors or uncertainties determined by Type B evaluation (i.e., based on expert knowledge). The proposed method for calculating the confidence intervals uses the characteristic function approach (CFA) and suitable algorithms for numerical inversion of the characteristic function.*

*Keywords: Linear Regression Model, Parameter Constraints, Best Linear Unbiased Estimator, Exact Distribution, Confidence Interval, Characteristic Function Approach (CFA)*

## 1. Introduction

In measurement and metrology, it is often necessary to consider a complex combination of influencing effects caused by classical measurement errors and the effects of systematic errors or other possible sources of uncertainty determined by the Type A and Type B evaluation methods. These complex effects can significantly affect the accuracy of the uncertainty analysis of measurement results based on standard assumptions about the normality of the distribution of measurement errors, see [1].

Here, we present a general method for computing the exact confidence intervals for the linear combinations of the model parameters under the assumption that the input errors can be formally identified and expressed as linear combinations of independent random variables with known probability distributions.

## 2. Subject and Methods

The most simple statistical model for modeling measurement process and making further inference about the model parameters is the model of direct measurements specified as

$$\boldsymbol{Y}^* = \boldsymbol{\mu} + \boldsymbol{\varepsilon}, \tag{1}$$

where $\boldsymbol{Y}^* = (Y_1^*, \ldots, Y_n^*)'$ is the $n$-dimensional random vector representing the (uncorrected) measurements, $\boldsymbol{\mu} = (\mu_1, \ldots, \mu_n)'$ is the $n$-dimensional parameter vector representing the unknown (expected) values of the measurements $\boldsymbol{Y}^*$, and $\boldsymbol{\varepsilon} = (\varepsilon_1, \ldots, \varepsilon_n)'$ is the $n$-dimensional random vector of measurement errors with zero-mean and known covariance matrix $\boldsymbol{\Sigma}$.

However, frequently we have a more specific knowledge about the structure of the mean vector $\boldsymbol{\mu}$ as well as about the error vector $\boldsymbol{\varepsilon}$, with possible constraints on the parameters. This leads to the general linear regression model, here also interpreted as the model of indirect measurements,

$$\boldsymbol{Y}^* = \mathbf{X}\boldsymbol{\beta} + \mathbf{Z}(\boldsymbol{\delta} + \boldsymbol{\epsilon}) \quad \& \quad \mathbf{A}\boldsymbol{\beta} + \mathbf{B}\boldsymbol{\gamma} + \mathbf{c} = \mathbf{0}. \tag{2}$$

or, after correction of the known systematic effects, to the model

$$\boldsymbol{Y} = \mathbf{X}\boldsymbol{\beta} + \mathbf{Z}\boldsymbol{\epsilon} \quad \& \quad \mathbf{A}\boldsymbol{\beta} + \mathbf{B}\boldsymbol{\gamma} + \mathbf{c} = \mathbf{0}. \tag{3}$$

Here, $\mathbf{X}\boldsymbol{\beta} + \mathbf{Z}\boldsymbol{\delta}$ is used instead of $\boldsymbol{\mu}$ and $\mathbf{Z}\boldsymbol{\epsilon}$ is used instead of $\boldsymbol{\varepsilon}$ in (1). The vector $\boldsymbol{\delta} = (\delta_1, \ldots, \delta_m)'$ represents the $m$-dimensional vector of known mean values of the included influencing random effects (known systematic effects or biases) which should be applied as a necessary corrections to the original vector of measurements, i.e. leading to the corrected vector of measurements $\boldsymbol{Y} = \boldsymbol{Y}^* - \mathbf{Z}\boldsymbol{\delta}$ . $\mathbf{X}$ is a known $(n \times k)$-dimensional matrix of coefficients (frequently denoted as a design matrix or as a matrix of regressors) and $\boldsymbol{\beta} = (\beta_1, \ldots, \beta_k)'$ is an unknown $k$-dimensional vector of regression parameters (fixed effects), with $k \leq n$. Similarly, $\mathbf{Z} = [\mathbf{Z}_1, \ldots, \mathbf{Z}_r]$ is a known $(n \times m)$-dimensional design matrix (with $m = \sum_{i=1}^{r} n_i$) of the input stochastic effects (errors or other random effects) and $\boldsymbol{\epsilon} = (\boldsymbol{\epsilon}_1', \ldots, \boldsymbol{\epsilon}_r')'$ is $m$-dimensional stochastic vector ($m \geq n$) with mutually independent components, where the $n_i$-dimensional sub-vectors $\boldsymbol{\epsilon}_i = (\epsilon_{i,1}, \ldots, \epsilon_{i,n_i})'$ consist of mutually independent random variables with known probability distributions, for all $i = 1, \ldots, r$.

The possible constraints on the model parameters are specified by a set of $q$ linear restrictions $\mathbf{A}\boldsymbol{\beta} + \mathbf{B}\boldsymbol{\gamma} + \mathbf{c} = \mathbf{0}$, where $\mathbf{A}$ is a known $(q \times k)$-dimensional matrix of coefficients related to the $k$-dimensional vector parameter $\boldsymbol{\beta}$, $\mathbf{B}$ is a known $(q \times p)$-dimensional matrix of coefficients related to the $p$-dimensional vector parameter $\boldsymbol{\gamma}$ (the additional parameters specifying the restrictions), and $\mathbf{c}$ is a known $q$-dimensional vector of coefficients. Here we assume that the standard regularity conditions are fulfilled (see below).

Note that if $\mathbf{A}$, $\mathbf{B}$ and $\mathbf{c}$ are zero matrices, then (2) is a linear regression model (alternatively understood as a linear mixed effects model) without parameter restrictions. If $\mathbf{A}$ is a non-zero matrix and $\mathbf{B}$ is a zero matrix then we say that (2) is a linear regression model with *Type I* restrictions. Otherwise, we say that (2) is a linear regression model with *Type II* restrictions. Depending on particular specification of the design matrices $\mathbf{X}$, $\mathbf{Z}$, and the restriction matrices $\mathbf{A}$, $\mathbf{B}$, and $\mathbf{c}$, we get the specific type of the used linear regression model, e.g., the model of direct (or indirect) measurements with (or without) constraints (linear restrictions of *Type I* or *Type II*) on the model parameters. For further details see [3].

Frequently, the vector of measurement errors is simply denoted as a random vector $\boldsymbol{\varepsilon}$, however, here we shall assume that $\boldsymbol{\varepsilon} = \mathbf{Z}\boldsymbol{\epsilon} = \mathbf{Z}_1\boldsymbol{\epsilon}_1 + \cdots + \mathbf{Z}_r\boldsymbol{\epsilon}_r$ where, typically, $\mathbf{Z}_1$ is $(n \times n)$-dimensional identity matrix, i.e. $\mathbf{Z}_1 = \mathbf{I}_{n,n}$ and $\boldsymbol{\epsilon}_1$ is $n$-dimensional random vector with independent and identically distributed (i.i.d.) components.

Hence, the covariance matrix of the error vector, $\mathrm{cov}(\boldsymbol{\varepsilon})$, as well as the covariance matrix of the measurement vector, $\mathrm{cov}(\boldsymbol{Y})$, is specified by $\boldsymbol{\Sigma} = \mathbf{Z}_1\boldsymbol{\Sigma}_1\mathbf{Z}_1' + \cdots + \mathbf{Z}_r\boldsymbol{\Sigma}_r\mathbf{Z}_r'$, where $\boldsymbol{\Sigma}_i = \mathrm{cov}(\boldsymbol{\epsilon}_i)$ are the known $(n_i \times n_i)$-dimensional diagonal covariance matrices of the random vectors $\boldsymbol{\epsilon}_i$, $i = 1, \ldots, r$.

Let $\boldsymbol{\vartheta} = (\boldsymbol{\beta}', \boldsymbol{\gamma}')'$ denotes the vector of parameters in the model (2). In this paper, our parameter of interest is a scalar function of the model parameters, say $\theta$, defined as

$$\theta = \mathbf{d}'\boldsymbol{\vartheta} = \mathbf{d}_\beta'\boldsymbol{\beta} + \mathbf{d}_\gamma'\boldsymbol{\gamma} = \sum_{i=1}^{k} d_{\beta_i}\beta_i + \sum_{j=1}^{p} d_{\gamma_j}\gamma_j, \tag{4}$$

which is an estimable linear combination of the model parameters $\boldsymbol{\beta}$ and $\boldsymbol{\gamma}$, where $\mathbf{d} = (\mathbf{d}_\beta', \mathbf{d}_\gamma')' = (d_{\beta_1}, \ldots, d_{\beta_k}, d_{\gamma_1}, \ldots, d_{\gamma_p})$ is the specific (given) vector of coefficients. Please note that for each estimable function of the parameters $\boldsymbol{\beta}$ and $\boldsymbol{\gamma}$ the vector of coefficients $\mathbf{d}_\beta$ is to be of the form $\mathbf{d}_\beta = \mathbf{X}'\mathbf{d}_\mu$ for some specific $\mathbf{d}_\mu$.

Then, the exact $(1-\alpha)\%$-confidence interval for the parameter $\theta$ is defined as the (random) interval

$$\left\langle \hat{\theta} - \tilde{\theta}_{upp}, \hat{\theta} - \tilde{\theta}_{low} \right\rangle, \tag{5}$$

where $\hat{\theta}$ is the best linear unbiased estimator (BLUE) of $\theta$ and $\tilde{\theta} = \hat{\theta} - \theta$ denotes a zero-mean random variable with $\tilde{\theta}_{low}$, and $\tilde{\theta}_{upp}$ being the specific quantiles of the probability distribution of the random variable $\tilde{\theta}$, such that the following holds true

$$\Pr\left(\tilde{\theta}_{low} \leq \hat{\theta} - \theta \leq \tilde{\theta}_{upp}\right) = 1 - \alpha, \tag{6}$$

and hence,

$$\Pr\left(\hat{\theta} - \tilde{\theta}_{upp} \leq \theta \leq \hat{\theta} - \tilde{\theta}_{low}\right) = 1 - \alpha, \tag{7}$$

which proves the exactness of the confidence interval defined in (5).

In the next section we present explicit form of the best linear unbiased estimator $\hat{\theta}$ and a method to derive the exact distribution (and the quantiles) of the random variable $\tilde{\theta}$. As explained below, BLUE is a linear function of the (random) measurement vector $\boldsymbol{Y}$. Given its observed value, say $\mathbf{Y}^{(obs)}$, we get the (observed) estimate, $\hat{\theta}^{(obs)}$, as well as the estimated (observed) confidence interval, $\left\langle \hat{\theta}^{(obs)} - \tilde{\theta}_{upp}, \hat{\theta}^{(obs)} - \tilde{\theta}_{low} \right\rangle$.

## 3. Results

Let $\hat{\boldsymbol{\vartheta}}$ denotes the BLUE of the vector parameter $\boldsymbol{\vartheta}$. Formally, as the name suggests, BLUE is *linear* (as a function of $\boldsymbol{Y}$) and *unbiased* estimator. That is, we have

$$\hat{\boldsymbol{\vartheta}} = \mathbf{h} + \mathbf{H}\boldsymbol{Y}, \tag{8}$$

for suitable $(k+p)$-dimensional vector of known coefficients $\mathbf{h}$ and known $[(k+p)\times n]$-dimensional matrix $\mathbf{H}$ (see below). Its mean value (expectation) satisfies the following relations: $E\left(\hat{\boldsymbol{\vartheta}}\right) = E(\mathbf{h} + \mathbf{H}\boldsymbol{Y}) = \mathbf{h} + \mathbf{H}E(\boldsymbol{Y}) = \mathbf{h} + \mathbf{H}E(\mathbf{X}\boldsymbol{\beta} + \mathbf{Z}\boldsymbol{\epsilon}) = \mathbf{h} + \mathbf{H}\mathbf{X}\boldsymbol{\beta} = \boldsymbol{\vartheta}$.

Hence, the best linear unbiased estimator $\hat{\theta}$ of the parameter of interest $\theta$ is given by

$$\hat{\theta} = \mathbf{d}'\hat{\boldsymbol{\vartheta}} = \mathbf{d}'\mathbf{h} + \mathbf{d}'\mathbf{H}\boldsymbol{Y}, \text{ and } \theta = E\left(\hat{\theta}\right) = \mathbf{d}'\mathbf{h} + \mathbf{d}'\mathbf{H}\mathbf{X}\boldsymbol{\beta}. \tag{9}$$

Finally, the zero-mean random variable $\tilde{\theta} = \hat{\theta} - \theta$ is distributed as

$$\tilde{\theta} = \hat{\theta} - \theta = \mathbf{d}'\mathbf{H}\mathbf{Z}\boldsymbol{\epsilon} = \mathbf{g}'\boldsymbol{\epsilon} = \sum_{i=1}^{r}\sum_{j=1}^{n_i} g_{i,j}\epsilon_{i,j}, \tag{10}$$

where $\mathbf{g}' = \mathbf{d}'\mathbf{H}\mathbf{Z}$ with $\mathbf{g}' = (\mathbf{g}_1, \ldots, \mathbf{g}_r)$ where $\mathbf{g}_i' = (g_{i,1}, \ldots, g_{i,n_i}) = \mathbf{d}'\mathbf{H}\mathbf{Z}_i$ for all $i = 1, \ldots, r$. Notice that the random variable $\tilde{\theta}$ is expressed as a linear combination of mutually independent zero-mean random variables $\epsilon_{i,j}$ with known probability distributions.

Let $\mathrm{cf}_{\epsilon_{i,j}}(t)$ is the characteristic function (CF) of the random variable $\epsilon_{i,j}$. Then the characteristic function of the random variable $\tilde{\theta}$, say $\mathrm{cf}_{\tilde{\theta}}(t)$, is given by

$$\mathrm{cf}_{\tilde{\theta}}(t) = \prod_{i=1}^{r}\prod_{j=1}^{n_i} \mathrm{cf}_{\epsilon_{i,j}}\left(g_{i,j}t\right), \tag{11}$$

Then, the probability density function (PDF) and the cumulative distribution function (CDF) of the random variable $\tilde{\theta}$ can be evaluated by numerical inversion of its characteristic function (11), and further, we can compute the required quantiles $\tilde{\theta}_{low}$ and $\tilde{\theta}_{upp}$, see [4] and [5].

According to [2] (Theorem IV.4.1, page 129), if the model (3) is regular (i.e. $\mathrm{rank}(X) = k \leq n$, $\mathrm{rank}([A, B]) = q \leq k + p$, $\mathrm{rank}(B) = p \leq p$, and $\boldsymbol{\Sigma}$ is positive definite matrix), then the best linear unbiased estimator $\hat{\boldsymbol{\vartheta}}$ of the vector parameter $\boldsymbol{\vartheta} = (\boldsymbol{\beta}', \boldsymbol{\gamma}')'$, introduced in (8), is given by

$$\hat{\boldsymbol{\vartheta}} = \mathbf{h} + \mathbf{H}\boldsymbol{Y} = \left[ -\begin{pmatrix} \left(\mathbf{X}'\boldsymbol{\Sigma}^{-1}\mathbf{X}\right)^{-1}\mathbf{A}'\mathbf{Q}_{1,1} \\ -\mathbf{Q}_{2,1} \end{pmatrix} \mathbf{c} \right] + \left[ \begin{pmatrix} \mathbf{I} - \left(\mathbf{X}'\boldsymbol{\Sigma}^{-1}\mathbf{X}\right)^{-1}\mathbf{A}'\mathbf{Q}_{1,1}\mathbf{A} \\ -\mathbf{Q}_{2,1}\mathbf{A} \end{pmatrix} \left(\mathbf{X}'\boldsymbol{\Sigma}^{-1}\mathbf{X}\right)^{-1}\mathbf{X}'\boldsymbol{\Sigma}^{-1} \right] \boldsymbol{Y}, \tag{12}$$

where

$$\begin{pmatrix} \mathbf{Q}_{1,1} & \mathbf{Q}_{1,2} \\ \mathbf{Q}_{2,1} & \mathbf{Q}_{2,2} \end{pmatrix} = \begin{pmatrix} \mathbf{A}\left(\mathbf{X}'\boldsymbol{\Sigma}^{-1}\mathbf{X}\right)^{-1}\mathbf{A}' & \mathbf{B} \\ \mathbf{B}' & \mathbf{0} \end{pmatrix}^{-1}. \tag{13}$$

Hence, the required vector of coefficients **g**, specified in (10) and used in (11), is evaluated as

$$\mathbf{g}' = \mathbf{d}' \begin{pmatrix} \mathbf{I} - \left(\mathbf{X}'\boldsymbol{\Sigma}^{-1}\mathbf{X}\right)^{-1}\mathbf{A}'\mathbf{Q}_{1,1}\mathbf{A} \\ -\mathbf{Q}_{2,1}\mathbf{A} \end{pmatrix} \left(\mathbf{X}'\boldsymbol{\Sigma}^{-1}\mathbf{X}\right)^{-1}\mathbf{X}'\boldsymbol{\Sigma}^{-1}\mathbf{Z}. \tag{14}$$

## 4. Conclusions

Here we have presented a method to compute the exact distribution of the best linear unbiased estimator (BLUE) of a linear combination of the unknown model parameters in linear models with possible parameters constraints. This is important in measurement and metrology, where is often necessary to consider different sources of measurement uncertainty, including the systematic errors or uncertainties determined by Type B evaluation. The presented approach specify in details how to evaluate the characteristic function of the BLUE (shifted to zero mean) of the scalar parameter of interest, which is expressed as a linear combination of independent random variables with know probability distributions. For illustration of the approach see [3].

## Acknowledgements

The work was supported by the Slovak Research and Development Agency, project APVV-18-0066, and by the projects VEGA 2/0081/19 and VEGA 2/0096/21.

## References

[1] JCGM 100:2008 (GUM) (2008). *Evaluation of measurement data – Guide to the expression of uncertainty in measurement* (GUM 1995 with minor corrections), ISO, BIPM, IEC, IFCC, ILAC, IUPAC, IUPAP and OIML.

[2] Kubáček, L., Kubáčková, L. (2000). *Statistics and Metrology* (In Czech), Published by Palacký University Olomouc.

[3] Wimmer, G., Witkovský, V. (2021). Determination of the exact confidence intervals for parameters in a model of direct measurements with independent random errors. In *Proceedings of MEASUREMENT 2021*.

[4] Witkovský, V. (2016). Numerical inversion of a characteristic function: An alternative tool to form the probability distribution of output quantity in linear measurement models. *ACTA IMEKO*, 5(3), 232–244.

[5] Witkovský V. (2021). *CharFunTool: The Characteristic Functions Toolbox (MATLAB).* `https://github.com/witkovsky/CharFunTool`.

# *Measurement of Physical Quantities I*

# Nondestructive Evaluation of Conductive Biomaterials Using SFECT Method

**Filip Vaverka, Milan Smetana, Daniela Gombarska, Ladislav Janousek**

Department of electromagnetic and biomedical engineering
Faculty of electrical engineering and information technology
University of Zilina, Univerzitna 1, Zilina, Slovakia,
Email: filip.vaverka@feit.uniza.sk

***Abstract.*** *The aim of this work is to perform the electromagnetic nondestructive evaluation on conductive material using sweep frequency eddy current testing. The potential for this technique to be used for more complex defect detection is being investigated. Three types of eddy current probes are used to examine the three specimens with the presence of artificial notches. Gained signals are processed and discussed.*

*Keywords: Sweep Frequency Eddy Current Testing, Material Inhomogeneities, Eddy-Current Probe, Harmonic Excitation, Lock-Inn Amplifier.*

## 1. Introduction

Defects within the materials that are used in the field of industry are widespread. It is necessary to monitor the quality of the material at all manufacturing and services phases to manufacture defect-free products. In recent years, the need for precise crack and flaw evaluation while maintaining the material undamaged has given nondestructive evaluation worldwide prominence [1], [2]. One of the most used nondestructive testing methods for conductive materials is eddy current testing, ECT. This method is based on the phenomenon of electromagnetic induction in conductive material. A time-varying electric current drives the probe. Consequently, a time-varying electromagnetic field is formed around the current conductor. A time-varying field is produced in the conductive material when the coil is close to it. Eddy currents flow in closed loops through the material because of the induced EM field. It also generates a secondary electromagnetic field. This EM field opposes the coil's main EM field. The distribution of the current field in the material is disturbed by the presence of a defect in the material. The EM field generated by the eddy currents changes as a result and affect the primary EM field. The probe impedance will change as the EM field changes. Knowledge indicating the presence of a defect in the material can be gained by analyzing these changes [1], [2], [3]. The sweep frequency method, SFECT, is a variation of the conventional ECT approach. The principle is based on the generation of an excitation signal with harmonic frequencies that covers a wide frequency range. The excitation frequency varies within a given range while the probe is fixed at a specific point of interest [4]. As a result, this approach is particularly well suited to continuous and long-term product tracking. The SFECT method is used for various purposes, including evaluating the material's physical and electromagnetic properties, measuring coating thickness etc. [5], [6]. This approach has a great potential for nondestructive identification and evaluation of surface and near sub-surface defects.

## 2. Experimental set-up

This research work aims to verify the use of the sweep frequency eddy current method to detect defects of various geometry. Three different types of ECT probes are used for the measurement and investigation. Based on the measurements, we will select the most appropriate one for further examination.

*Specimen Under Examination*

The measurement is performed on three conductive non-magnetic stainless steel AISI316L plates. The thickness of the plates is $h$=10mm, and the electric conductivity is $\sigma$ = 1.35 MS/m$^{-1}$. Five artificially produced surface defects in the form of a cuboid were present on each plate, respectively. The electric discharge machining method was used to create artificial flaws. Plate defects come in a variety of dimensions. Each specimen contains five defects. Specimen No.1 contains defects with the length of $l$ = 10 mm, and the width of $w$ = 0.25 mm, the same for each defect. The defect's depth varies from 1 mm to 9 mm with the step of 2 mm: $d$ = 1, 3, 5, 7, and 9 mm. The depth of defects of specimen No.2 is $d$ = 5 mm, the width is $w$ = 0.25 mm, and the length varies between $l$ = 10, 15, 20, 25, and 30 mm. The defects on the third specimen vary in each direction (except the width parameter), simulating real defects. All dimensions of the third plate are summarized in Table 1.

Table 1. Dimensions of defects of third material sample - specimen

| Dimensions | Defect n.1 | Defect n.2 | Defect n.3 | Defect n.4 | Defect n.5 |
|---|---|---|---|---|---|
| Depth [mm] | 1 | 3 | 5 | 7 | 9 |
| Length [mm] | 3 | 9 | 15 | 21 | 27 |
| Width [mm] | 0.2 | 0.2 | 0.25 | 0.25 | 0.25 |

*Eddy Current Probes*

As previously mentioned, defects are evaluated by using three different probes. These ECT probes consist of two coils, transmitting (Tx) and receiving (Rx). The first test probe is coreless (air-core probe), and the measured inductances of its coils are $L_{Tx1}$ = 11 µH. and

$L_{Rx1}$ = 4,7 µH. The measured inductances for the second probe, which has a ferrite core, are $L_{Tx2}$ = 25 µH. and $L_{Rx2}$ = 64 µH. The third coil is identical to the second coil, with the exception that it is covered by an aluminium shield. The dimensions of the coils are the same (see Fig. 1).

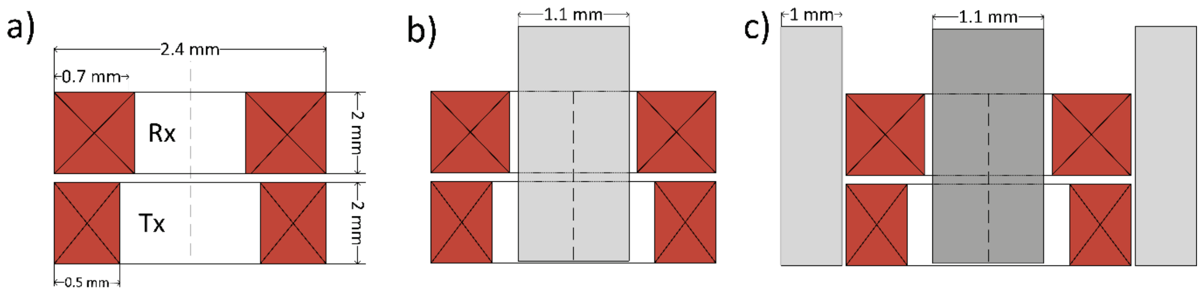


Fig. 1. Configuration and dimensions of ECT probes: a) coreless probe, b) probe with ferrite core, c) probe with ferrite core and aluminium shield

*Measurement*

The sweep frequency method is based on the excitation of a signal within a given frequency interval. A frequency generator is needed, as well as the ability to generate signals in discrete steps. To detect the response signal, the digital lock-in amplifier is used (Signal Recovery 7280 DSP). The generated harmonic signal has a frequency range of $f$ = 1 kHz to $f$ = 1.5 MHz, with a $\Delta f$ = 10 kHz step. A period of $T$ = 2 s is set as the sweep time for one frequency. The total period of one full-sweep measurement is $T$ = 300 s. A value $U_{pp}$ = 0.1 V is the peak-to-peak amplitude of the excitation signal. The measuring and data-acquisition card with analog and digital inputs and outputs is used to link the Lock-in amplifier's output to a PC. The LabVIEW software is used for the processing of measured data. The observed single frequency signal is acquired with parameters: $S$ =10 ks/s and sampling frequency $f_s$ =10kHz. The algorithm is set up in such a way that, for each frequency, a suitable synchronization ensures that only the specified amount of data is obtained. The averaged sample values for the real and imaginary components of the induced voltage are saved in specific files. The resulting values are plotted in the form of graphs after math post-processing. These graphs are performed by use of MATLAB software.

*Experimental Results*

In this section, the measured values are presented and discussed. All the experiments were performed under the same conditions as described in this article. The measurements were performed in three different probe positions. Probe in the air, reference measurement of probe over defect-free material, and the probe above the defect. The probe above the defect was located axially symmetrically to the center of the defect. Lift-off of the probe above the material and above the defect was set to $lf$ = 0.5 mm. The value of the measured voltage on the probe above the defects was subtracted from the value of the measured voltage in the air. The value $\Delta U$ was then normalized to the coil in the air. From the normalized values, the absolute value is calculated ($|\Delta U|$), and the resulting values are plotted in graphs (see Fig. 2, Fig. 3, Fig. 4).

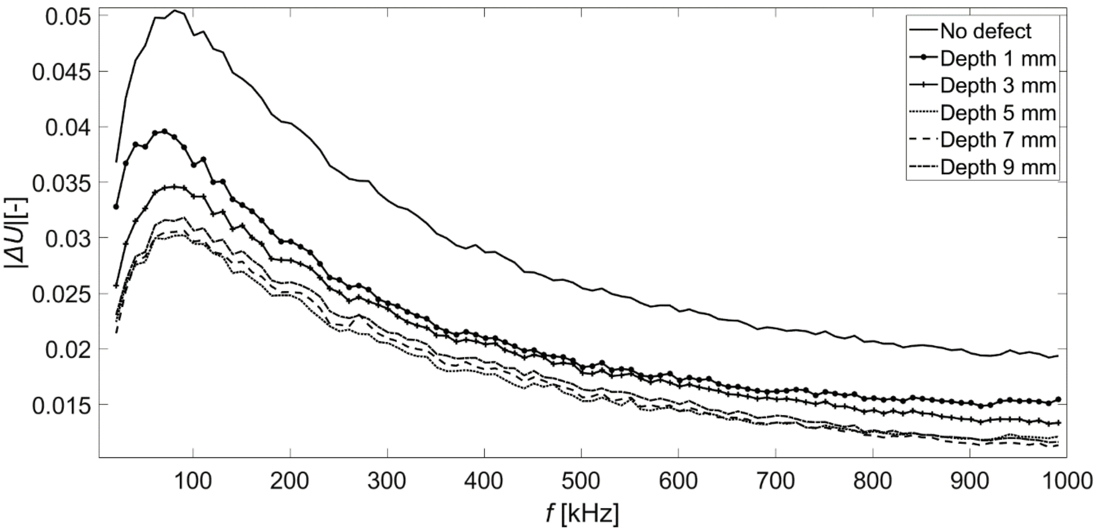


Fig. 2. Experiment results: Probe No.2, Specimen No. 1, different depth of the defects.

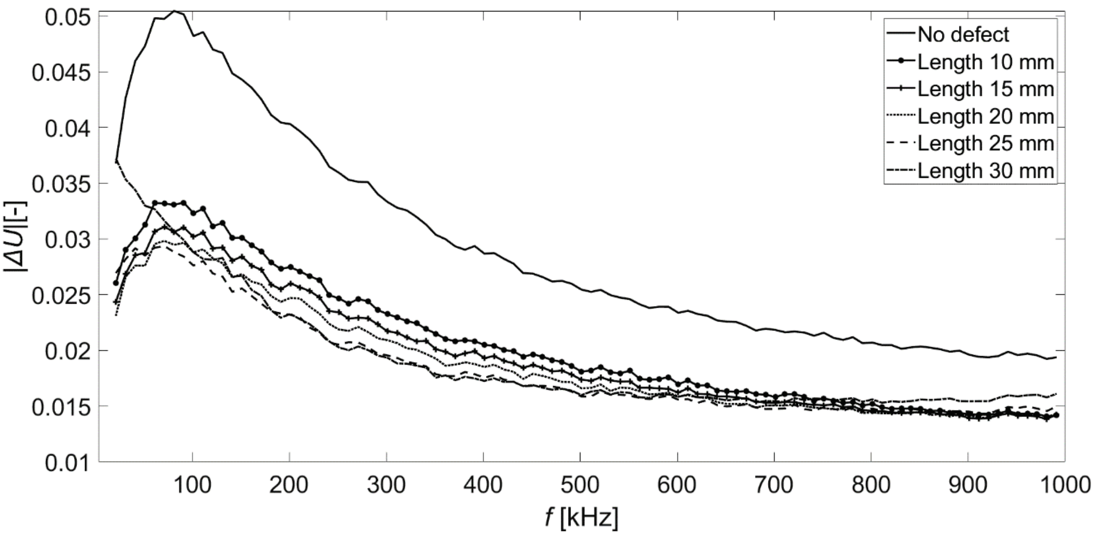


Fig. 3. Experiment results: Probe No.2, Specimen No. 2, different length of the defects.

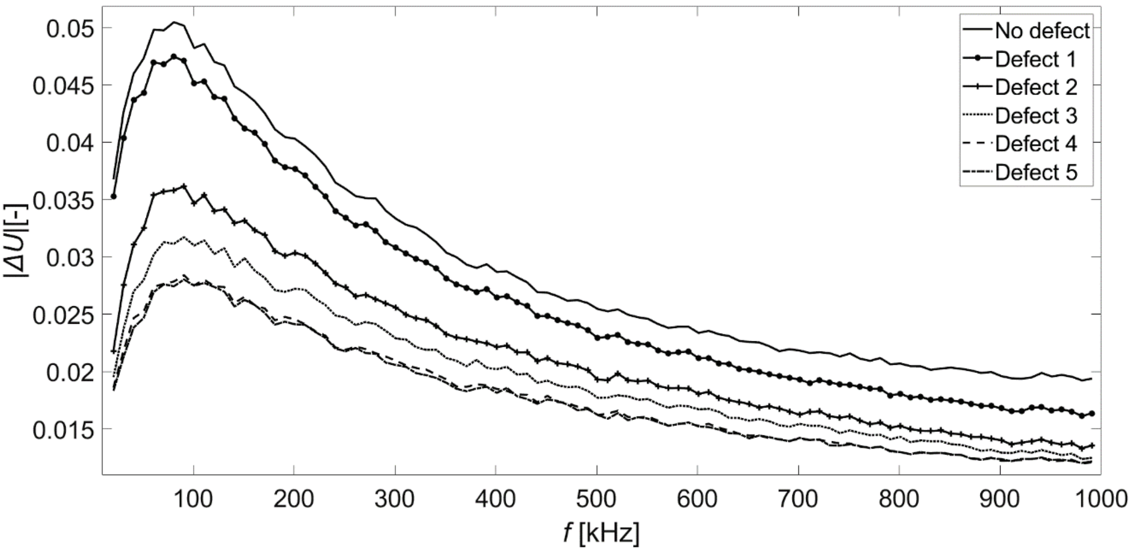


Fig. 4. Experiment results: Probe No.2, Specimen No. 3, the different depth, and length of the defects.

Individual curves are well-differentiated, as seen in the graphs. It means that by use of the SFECT method, it is possible to recognize different defect geometry.

## 4. Discussion

This work aimed to verify the use of the sweep frequency eddy current method to detect defects of various sizes. By comparing the results, we found that a probe with a ferrite core has the highest sensitivity, and thus this one brought results with the highest information content. Another result was that the defect's dimension has a correlation with the signal in the resonant frequency area. These novel findings shed light on how the SFECT with fixed sensors could be used to evaluate cracks. Further work will be focused on the investigation of real stress-corrosion and fatigue cracks.

## Acknowledgements

This work was supported by the project APVV-19-0214.

## References

[1] Rao, B.P.C. (2007). Practical Eddy Current Testing. *Alpha industries International Ltd*.

[2] García-Martín, J., Gómez-Gil,J., Vázquez-Sánchez*,* E. (2011). Non-destructive techniques based on eddy current testing. *Sensors*, 11, 2525-2565.

[3] Bowler, N. (2017). *Eddy-Current Nondestructive Evaluation*. Springer.

[4] Janousek, L., Stubendekova, A., Smetana, M. (2017). Novel insight into swept frequency eddy-current nondestructive evaluation of material defects. *Measurement,* 116, 246-250.

[5] Takahashi, Y., Urayama, R., Uchimoto, T., Takagi, T., Naganuma, H., Sugawara, K., Sasaki, Y. (2012). Thickness evaluation of thermal spraying on boiler tubes by eddy current testing. *International Journal of Applied Electromagnetics and Mechanics*, 39(1–4), 419–425.

[6] Cheng, W. (2017). Thickness measurement of metal plates using swept-frequency eddy current testing and impedance normalization. *IEEE Sensors Journal*, 17(14), 4558–4569.

# Determination of Physical Properties of Bi-Doped $CaO-Al_2O_3-SiO_2$ Glasses

**[1]Melinda Majerová, [2,3]Anna Prnová, [3]Jozef Kraxner, [3]Beata Pecušová, [4]Simona Randáková, [3]Alfonz Plško, [2,3]Dušan Galusek**

[1]Institute of Measurement Science, Slovak Academy of Sciences, Bratislava, Slovakia
[2]Vitrum Laugaricio – Joint Glass Center of the IIC SAS, TnU AD, FChPT STU, Bratislava, Slovakia
[3]Centre for functional and surface functionalized glass, Alexander Dubček University of Trenčín, Trenčín, Slovakia
[4]Laboratoř rentgenové difraktometrie, VŠCHT Praha – Centrální laboratoře, Praha, Czech Republic
Email: melinda.majerova@savba.sk

***Abstract.*** *Bi-doped calcium aluminosilicate glass materials (CAS), with the concentration of $Bi^{3+}$ ions 0.5, 1.0 and 3.0 mol %, were prepared by conventional melting. The basic properties and thermal behavior were studied by X-ray diffraction (XRD), He-pycnometry, X_Ray Fluorescence (XRF) and differential thermal analysis (DTA). XRD analysis showed the presence of crystalline gehlenite traces in samples with the highest Bi content. Crystallization of gehlenite in all prepared samples and crystallization of $Bi_2O_3$ in case of samples with 1 and 3 mol.% $Bi^{3+}$ content was observed by a combination of DTA and XRD analysis. The increasing ability to crystallize was correlated with the increasing Bi content in the samples.*

*Keywords: Bi-Doped Silicates, Gehlenite, Conventional Melting Method*

## 1. Introduction

Gehlenite ($2CaO-Al_2O_3-SiO_2$), which belongs to the melilite silicates, has been intensively studied as a suitable host for optically active ions, mainly rare-earth (RE) elements [1]. The sharp increase in the prices of RE as well as their limited raw material resources threatens the production of inorganic phosphors. Bi-doped oxide glasses are therefore of significant interest because they exhibit luminescence both in the ultraviolet-visible and near-infrared wavelength range [2, 3]. Nowadays, Bi-doped materials have been intensively researched and find potential applications in different areas (e.g. medicine, and optical communication systems) [4, 5].

For possible applications, it is essential to study the thermal behavior of these glasses. Differential scanning calorimetry (DSC) and DTA are commonly used to study the thermal properties of the studied system [3, 6]. XRD and scanning electron microscopy are commonly used methods to supplement the results of thermal analysis, to obtain more accurate information about thermal properties [7, 8]. The thermal properties of oxide glasses depend on various parameters: glass composition [9, 10], glass preparation condition [11], presence of dopant(s) [6], the particle size of glasses [12]. In this work, we investigated the basic properties and thermal properties of Bi-doped gehlenite glasses prepared by conventional melting.

## 2. Subject and Method

Bi-doped gehlenite glasses were prepared by mixing powdered oxides ($Al_2O_3$, $SiO_2$, $Bi_2O_3$) and $CaCO_3$ of analytical grade purity. Table 1 summarizes the nominal compositions of the prepared glasses. The glasses were melted for 2-3 h at 1600 °C in the Pt-20%Rh crucible in a super-kanthal furnace in an ambient atmosphere. During the preparation, the melts were poured onto a stainless-steel plate. For further analysis, the prepared pieces of samples were crushed, ground, and then sieved through a 32 μm sieve. The density of prepared bulk glass was measured by He-pycnometry (QuantachromeUltrapyc 1200e).

Table 1. The nominal composition of the prepared powder precursors and the chemical compositions of prepared systems.

| Sample | Nominal composition [mol.%] | | | | Chemical composition (XRF) [mol.%] | | | |
|---|---|---|---|---|---|---|---|---|
| | SiO2 | Al2O3 | CaO | Bi2O3 | SiO2 | Al2O3 | CaO | Bi2O3 |
| GBi0.5 | 24.87 | 24.87 | 49.76 | 0.50 | 23.2±0.2 | 26.0±0.1 | 50.8±0.2 | 0.10±0.01 |
| GBi1.0 | 24.75 | 24.75 | 49.50 | 1.00 | 23.3±0.2 | 26.1±0.1 | 50.4±0.2 | 0.26±0.01 |
| GBi3.0 | 24.25 | 24.25 | 48.50 | 3.00 | 23.0±0.2 | 25.9±0.1 | 50.1±0.2 | 0.96±0.02 |

Mastersizer 2000 (Malvern Instruments) instrument was used to check the diameter size distribution after grinding and sieving. The chemical compositions of prepared samples were determined by XRF (ARL 9400 XP spectrometer, Thermo ARL). Intensities of elements were converted to concentrations using semiquantitative non-standard software UniQuant 4. XRD analysis was used to verify the amorphous (glassy) nature of prepared samples and to determine the phase composition of the crystallized samples after DTA analysis. Diffraction analysis was performed using a powder diffractometer Panalytical Empyrean (CuKα radiation, at ambient temperature in the $2\theta$ range 10-80°). The basic thermal characteristics of prepared glasses (glass transition temperature – $T_g$, the onset of crystallization temperature – $T_x$ and the peak temperature of crystallization – $T_p$) were estimated from the DTA records. DTA analysis was carried out in the temperature range 30 – 1200 °C, heating rates 2°C.min$^{-1}$ and 10°C.min$^{-1}$, and in a nitrogen atmosphere, with the use of simultaneous Netzsch STA 449 F1 Jupiter thermal analyzer in TG / DTA mode. The measured DTA records were evaluated by Netzsch Proteus Thermal Analysis Version 6.0.0 program.

## 3. Results

The density of prepared glasses ranged in the interval 2.9092 to 3.0192 ± 0.0005 g.cm$^{-3}$ and increases with the increase of the Bi content (Fig. 1). Particle size measurement results of screened fractions ≥32 μm (intended for thermal analysis and XRF analysis) show very fine monomodal distribution with Span values in the interval 1.7-2.0. The major portion of these samples (50 vol.%) was created by particles with a diameter from 19.2±0.6 μm (sample GBi3.0) to 24.4±0.5 μm (sample GBi0.5). The results of XRF analysis show only negligible differences between the theoretical and real composition of prepared glasses (Table 1). XRD analysis confirmed that the GBi0.5 and GBi1.0 samples are X-ray amorphous (without discrete diffraction maxima and a broad band in the 2 θ range 24°-36°). In the case of GBi3.0 samples, the XRD patterns contained low-intensity diffractions of crystalline gehlenite (Fig. 2). In all DTA curves (measured at both heating rates 2 and 10°C.min$^{-1}$), an exothermic effect in the temperature interval 910-982°C was observed. A similar exothermic effect corresponding to the crystallization of the gehlenite phase was observed in work [6].

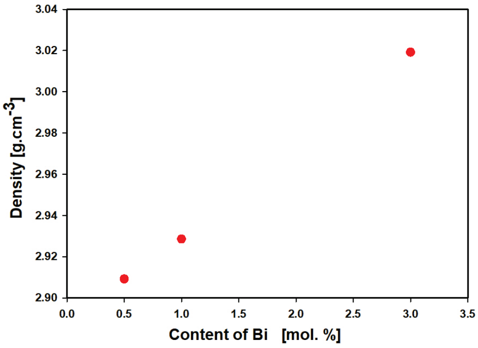


Fig. 1. Density of prepared Bi doped glasses.

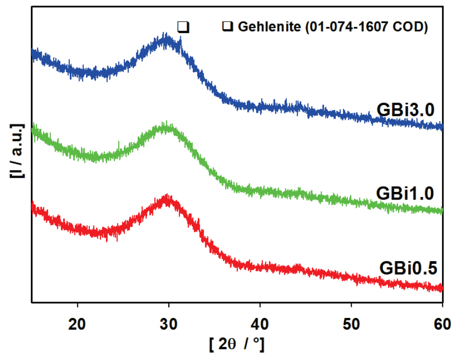


Fig. 2. XRD patterns of the Bi doped glasses.

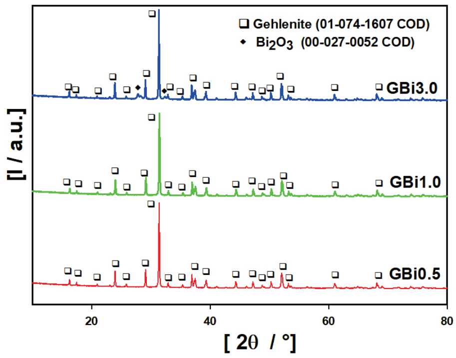


Fig. 3. XRD patterns of the studied system after DTA analysis (10 °C.min$^{-1}$).

Whereas the XRD patterns of samples GBi0.5 and GBi1.0 after DTA analysis measured at a heating rate of 10°C.min$^{-1}$ contains only the gehlenite phase (01-074-164 COD), the XRD pattern of sample GBi3.0 measured at the same conditions also contains $Bi_2O_3$ (00-027-0052 COD) phase (Fig. 3). Also, XRD patterns of the GBi1.0 sample measured at the heating rate of 2°C.min$^{-1}$ contains both gehlenite (as major phase) and traces of $Bi_2O_3$. Based on these findings, it can be concluded that the observed exothermic effect can be attributed to the crystallization of gehlenite and a slow (more time-consumable) crystallization of $Bi_2O_3$. The characteristic temperatures of prepared glasses (for both heating rates) are summarized in Table 2. Significant reduction of the characteristic temperatures was observed in the DTA curves of GBi3.0 glass with the highest content of Bi dopant, which could indicate a role of $Bi^{3+}$ cation as a nucleating agent. A similar decrease of $T_g$ and $T_p$ temperatures was observed by Reddy et al. in the case of Bi-doped melilite glasses and by Maleczki et al. in the case of gehlenite glasses doped with $Co^{2+}$, $Eu^{3+}$ and $Th^{4+}$ [6, 7]. Also, in the GBi3.0 sample, the presence of traces of the gehlenite crystalline phase could serve as crystallization centers and accelerate crystallization. However, to confirm these assumptions and for a more detailed examination of the crystallization mechanism, additional isothermal experiments in combination with XRD, high-temperature XRD, and DTA analysis will be necessary.

Table 2. Characteristic temperatures of studied glasses from DTA determined at 10 °C.min$^{-1}$ and 2 °C.min$^{-1}$ (glass transition temperature – $T_g$, the onset of crystallization temperature – $T_x$ and the peak temperature of crystallization – $T_p$).

| Sample | 10 °C.min$^{-1}$ | | | 2 °C.min$^{-1}$ | | |
|---|---|---|---|---|---|---|
| | $T_g$ [°C] | $T_x$ [°C] | $T_p$ [°C] | $T_g$ [°C] | $T_x$ [°C] | $T_p$ [°C] |
| GBi0.5 | 858±3 | 963±3 | 982±3 | 836±3 | 935±3 | 953±3 |
| GBi1.0 | 852±3 | 954±3 | 975±3 | 823±3 | 921±3 | 943±3 |
| GBi3.0 | 838±3 | 918±3 | 925±3 | 815±3 | 889±3 | 910±3 |

## 4. Conclusions

Three Bi-doped glasses of gehlenite composition were prepared by the conventional melting method. For the study of thermal behavior, finely powdered glasses (the powder particle size ranging between 19-24 ± 0.6 μm) were used. The measured density values of prepared glasses range from 2.9092 to 3.0192 ± 0.0005 g.cm$^{-3}$. The density of all prepared samples increases with the increase of the Bi content. The effect of Bi addition was also reflected in the thermal behavior of prepared samples, while the increase of Bi content was correlated with the decrease of the characteristic crystallization peak temperatures. The role of Bi as a nucleating agent during the crystallization of the glasses will be further investigated.

## Acknowledgements

This paper is a part of the dissemination activities of project FunGlass. The financial support of this work by the projects APVV 19-0010, APVV 17-0049, VEGA 1/0527/18, VEGA 2/0028/21, and VEGA 2/0141/21 is gratefully acknowledged. The idea of studying the transition metal doped compounds with melilite structure was based on discussions with prof. Lothar Wondraczek from the Otto-Schott Institute, Friedrich Schiller University of Jena, Germany.

## References

[1] Shih, S.J. et al. (2016). Preparation and characterization of Eu-doped gehlenite glassy particles using spray pyrolysis. *Ceramics International*, 42, 11324-11329.

[2] Xu, W. et al. (2012). A new study on bismuth doped oxide glasses. *Optics Express*. 20, 15692-15702.

[3] Majerova, M., et al. (2018). Crystallization and VIS-NIR luminescence of Bi-doped gehlenite glass. *Royal Society Open Science*, 5:181667.

[4] Wang, W., Jiang, Ch. (2020). Anomalous photoemission in bismuth-doped amorphous solid via selective reduction and energy transfer mechanism investigation. *Journal of Alloys and Compounds*. 820, 153169

[5] Wang, L. et al. (2018). Multi-functional bismuth-doped bioglasses: combining bioactivity and photothermal response for bone tumor treatment and tissue repair. *Light: Science & Applications*, 7:1.

[6] Malecki, A. et al. (1997) Kinetics and mechanism of crystallization of gehlenite glass pure and doped with $Co^{2+}$, $Eu^{3+}$, $Cr^{3+}$ and $Th^{4+}$. *Journal of Non-Crystalline Solids*. 212, 55-58.

[7] Reddy, A.A. et al. (2012). Study of melilite based glasses and glass-ceramics nucleated by $Bi_2O_3$ for functional applications. *RSC Advances*. 2, 10955-10967.

[8] Kim, B.S., Lim, E.S., Lee, J.H., Kim, J.J. (2007). Effect of $Bi_2O_3$ content on sintering and crystallization behavior of low-temperature firing $Bi_2O_3$- $B_2O_3$-$SiO_2$ glasses. Journal of the European Ceramic Society. 27, 819-824

[9] Monterio, R.C.C., et al. (1989). Crystallization of CaO-$Al_2O_3$-$SiO_2$ and CaO-MO-$Al_2O_3$-$SiO_2$ (M = Mg, Zn) glasses. *Journal of Material Science.* 24, 2839-2844.

[10] Kingery, W.D., Vandiver, P.B., Huang, I.W. (1983). Liquid-liquid immiscibility and phase separation in the quaternary systems $K_2O$-$Al_2O_3$-CaO-$SiO_2$ and $Na_2O$-$Al_2O_3$-CaO-$SiO_2$. *Journal of Non-Crystalline Solids* . 54, 163-171

[11] Duan, R.G., Linag, K.M. (1998). A study on the crystallization of CaO-$Al_2O_3$-$SiO_2$ system glasses. *Journal of Materials Processing Technology*. 75, 235-239.

[12] Ray, C.S., Day, D.E. (1996). Identifying internal and surface crystallization by differential thermal analysis for the glass-to-crystal transformation. *Thermochimica Acta*. 280/281, 163-174.

# *Measurement of Physical Quantities - Posters I*

# The Application of Lab VIEW Environment in Light Flicker Severity Studies Using Optotypes

**Przemysław Otomański**

Poznan University of Technology, Institute of Electrical Engineering and Electronics, Piotrowo street 3A, 60-965 Poznań, Poland
Email: przemyslaw.otomanski@put.poznan.pl

***Abstract.*** *The results of experimental research concerning a dependence of light flickering on voltage fluctuations were presented in the paper. The research was realized on a design measuring position that included the examined light source, a voltage generator with amplitude modulation supplying the light source with control software, and a positioning system of the observer regarding the observed surface. The research results, permitting us to formulate a conclusion concerning the description of the influence of the flicker intensity for a number of correctly recognized optotypes for selected light sources, were described in the paper. An application in the form of a virtual instrument dedicated to determining the values of measurement errors was developed for the purpose of measurement inaccuracy evaluation during the counting of optotypes.*

*Keywords: Voltage Fluctuation, Flicker, Optotype, Virtual Instrument*

## 1. Introduction

Voltage fluctuations affect the operation of powered loads. Light sources are particularly susceptible to such fluctuations. Flicker is caused by voltage fluctuations. Flicker is a sensation of instability in visual perception caused by a light beam $\Phi$ whose luminance or spectral distribution changes over time [1]. Depending on the variability and type of light source, flicker can be sensible and visible. Visual perception is a complex process composed of the following stages: voltage fluctuations–light source–eye–brain. The intensity of observed flicker depends on the type of light source and on the construction parameters. The results of long-term research point to the fact that different optical radiation sources behave differently at the same values of voltage fluctuations. The effect of light flicker on the observer is a complex process depending on the individual features and the condition of the observer [2], [3]. Available publications describe research dedicated exclusively to a selected source of optical radiation or for the relatively limited frequency range of modulating signal variation.

This publication presents the results of a laboratory study concerning the relationship of the visual intensity of flickering light and the number of correctly counted optotypes. The following light sources were used in the study: halogen lamps, so-called energy saving fluorescent lamps of different manufacturers, and, for comparison purposes, incandescent.

The research results obtained for those light sources allow us to evaluate the effect of modulation depth and the colour of the illuminated surface onto the number of Landolt rings correctly counted by the test participants. The results made it possible to determine the error values between the values counted during the study and the correct number of optotypes. To determine those values, a virtual measurement instrument was designed.

## 2. Experimental Research

The research was conducted in a designed measurement system shown in Fig.1., which included the tested light source, a voltage generator of amplitude modulation supplying the light source, and a system of positioning the observer in relation to the observed surface illuminated with the tested light source.

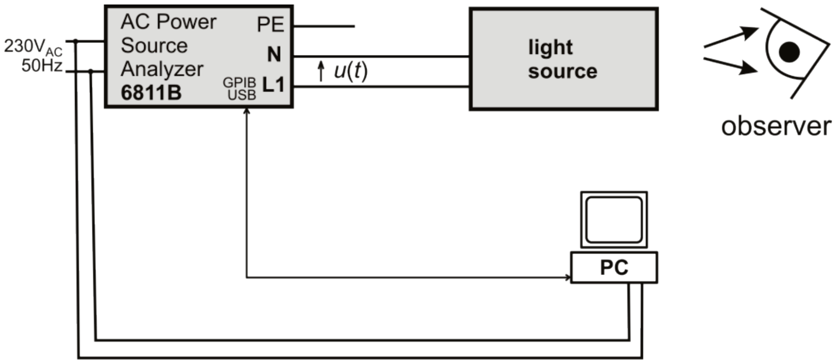


Fig. 1. Block diagram of the measurement system to examine flicker severity

The results of the work of many authors on the study of the effects of light flicker on the observer prove that the in the $\Delta U/U=f(f_m)$ characteristic – where $\Delta U/U$ means the modulation depth, and $f_m$ is the modulation frequency – there are three local minima and a supremum for the value $f_m$ = 8,8 Hz. It was decided, therefore, to perform the measurements for a sinusoidal signal with an rms value of 230 V, amplitude modulated with a sinusoidal signal with a frequency of 8,8 Hz. The research was done for three constant values of the amplitudes of the sinusoidal modulating signal $\Delta U$, equal, respectively, to 0.5 V, 4 V and 10 V. The purpose of the research was to find a relationship between the intensity of flicker caused by the fluctuations in voltage supplying the light source and the number of errors made when the optotypes – Landolt rings placed in charts of different colours – were counted. Fig. 2 presents examples of test charts with the optotypes used in the measurements.

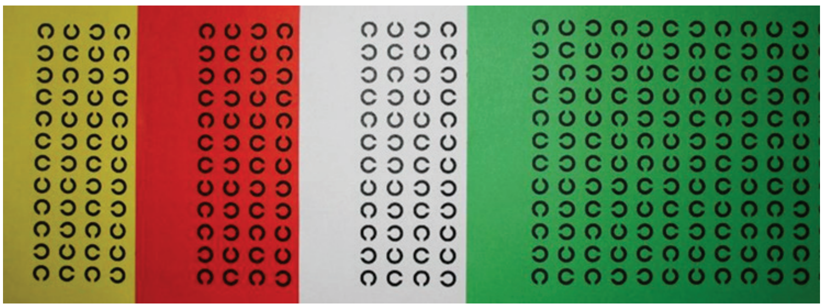

Fig. 2. Test charts used in measurements.

The designed charts (Fig. 2) contain 156 Landolt rings, equally spaced and of equal size. The arrangement of rings was designed randomly. It was done so in order to improve the research reliability – the test person could not memorize the number of rings in the next measurements. The tests were conducted in a cyclic manner, i.e., after the first measurement series, for example, the examined incandescent source, the amplitude of modulating signal $\Delta U$=4 V, red sheet, counted ring in position Ɔ, the test person went to rest. Then another person started the test. The purpose of such a measurement method was to eliminate an adverse effect of fatigue shown in the test persons. The number of errors made by the observers was measured for all the examined sources of optical radiation. For example, Fig. 3a and Fig. 3b present the measurement results for a halogen source and for modulating signal amplitudes equal to $\Delta U$=0.5 V and $\Delta U$ =10 V.

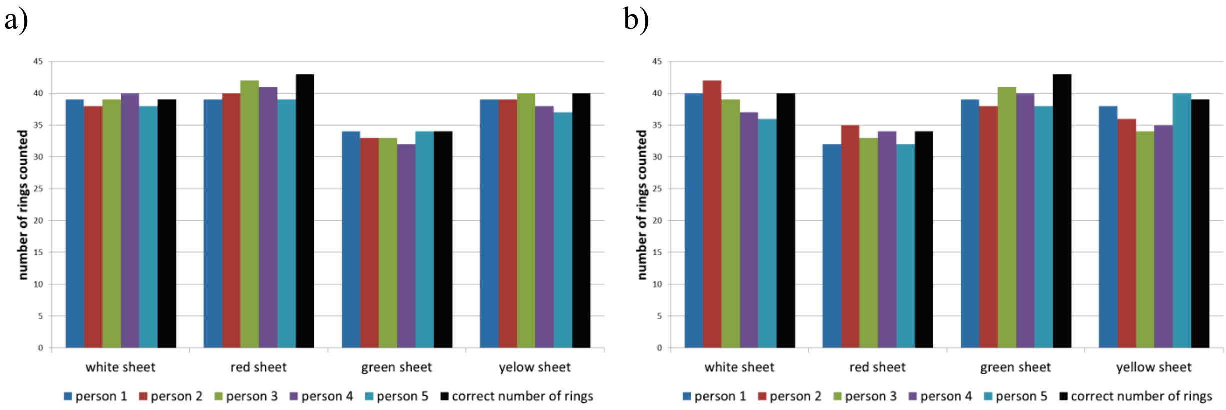


Fig. 3. The number of counted rings for a) $\Delta U$=0.5 V and b) $\Delta U$=10 V – halogen source.

## 3. Virtual Instrument

In practice, virtual measuring instruments are often used to determine the values of measurement errors. Examples of such instruments are presented in works [4], [5]. To evaluate measurement inaccuracy during optotype counting, a program in the form of a virtual instrument has been developed for the determination of measurement errors.

The application designed in the LabVIEW environment consists of three separate stages. At each of these stages, a certain parameter must be selected. During the first stage, called the data input stage, the sex and age of the person participating in the experiment is selected. The element of the chart with the number zero is the sex of the person performing the test: a woman is assigned value 1, a man– value 0. Another element of the chart, number one, corresponds to the age of the test person, which can be set in the appropriate field of the program. A green light on informs the program user that a given window is active.

After selecting the sex and the age of the test person, the entered data should be confirmed by pressing the indicator button "confirm". Then, the program proceeds to the second stage called experiment setup; the application user is informed about that by the green indicator light on. The indicator from the first stage is deactivated. At this point, it is necessary to select further elements. Chart element number 2 concerns the selection of the special location of Landolt rings. The following values: 0 – , 1 – , 2 – , 3 – were assigned to the appropriate positions of rings. Chart element number 3 is the colour of the illuminated surface. The following values were assumed for this criterion: 0 – blue, 1 – yellow, 2 – green, and 3 – red. At the stage of experiment setup, it is necessary to enter the fourth chart element, the amplitude of modulating signal. Three possible values, which may be modified in the designed application, were entered for this element. The value 0 corresponds to the amplitude $\Delta U$ equal to 0.5 V; value 1 to $\Delta U$ = 4 V; and value 2 to $\Delta U$ = 10 V. Entering the above-described data completes the experiment setup stage. Then, all the data necessary to perform the experiment have been entered into the designed application. The experiment involves counting the number of Landolt rings for complex initial conditions: the spatial position of rings, the colour of the illuminated surface and the modulating signal amplitude.

The setup stage is followed by a measurement experiment, which determines the relationship between flicker vision intensity and the number of correctly counted optotypes. After that experiment, in stage three, called "results", it is necessary to enter the number of counted optotypes and confirm the entered data by pressing the "confirm" indicator light.

Then, the value of relative error is determined and displayed in the "relative error value" indicator. Fig. 4 shows the display of the virtual instrument panel. The active state of the window is indicated by the diode on in the top right corner during each of the experimental stages.

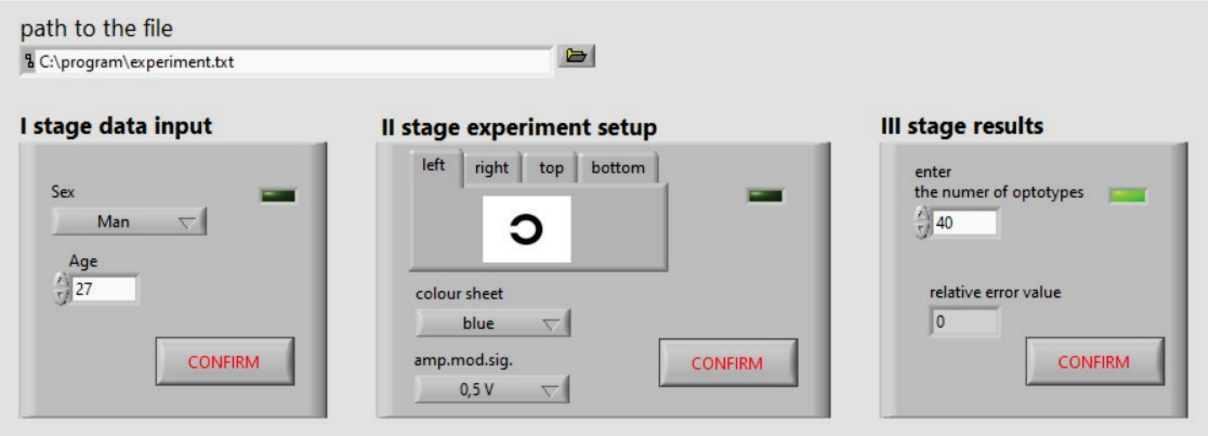


Fig. 4. The panel of the designed virtual instrument.

After each research stage, the results obtained by particular individuals are saved in a text file. Then the results are transferred to an Excel spreadsheet. The compiled file allows the recording of the measurement results. After performing the measurements for all the participants, for all the measurement series, it is possible to develop summaries according to an arbitrary criterion.

## 4. Conclusions

The paper presents the experimental results of a study on flicker severity of selected optical radiation sources. The measurements were performed for modulation frequency $f_m$ equal to 8.8 Hz, for which the flicker is particularly severe for the human eye. The relationship between flicker vision intensity and the number of correctly counted optotypes was determined. With the obtained measurement results, it was possible to evaluate how the modulation depth and the colour of the illuminated surface influenced the number of Landolt rings correctly counted by the experiment participants. This evaluation allows the determination of error values between the values counted during the measurement and the correct number of optotypes. The virtual instrument presented in the paper was designed for the purpose of determining the values of those errors.

## References

[1] IEV number 845-02-49, flicker.

[2] Emanuel A.E., Peretto L. (2004). A simple Lamp-Eye_Brain model for flicker observations, *IEEE Transaction on Power Delivery*, 19 (3), 1308-1313.

[3] Peretto L., Pivello E., Tinarelli R., Emanuel A.E. (2007). Theoretical Analysis of the Physiologic Mechanism of Luminous Variation in Eye-Brain System, *IEEE Transaction on Instrumentation and Measurement*, 58 (9), 164-170.

[4] Otomański P., Szlachta A. (2008), The evaluation of expanded uncertainty of measurement results in direct measurements using the LabVIEW environment, *Measurement Science Review*, 8 (6), 147-150.

[5] Otomański P., Krawiecki Z., Odon A. (2010). The application of the LabVIEW environment to evaluate the accuracy of alternating voltage measurements, *Journal of Physics: Conference Series*, 238, 1-6.

# The Dependence of the $P_{st}$ Indicator on the Rectangular Modulating Signal Frequency for Sinusoidal Voltage in the Power Grid

**Grzegorz Wiczyński**

Poznań University of Technology, Poznań, Poland,
Email: grzegorz.wiczynski@put.poznan.pl

***Abstract.*** *The paper presents the test results of the flickermeters installed in AMI energy meters. The research involved modulation of the sinusoidal voltage amplitude with a rectangular signal. The frequency of the modulating signal was being preset from 0.17 Hz to 126 Hz. It has been shown that testing within the properly selected frequency range of the modulating signal is crucial in assessing the quality of a flickermeter implementation.*

*Keywords: Flickermeter, AMI Energy Meters, AM Modulation*

## 1. Introduction

Voltage fluctuations are common disturbances in the power grids. The $P_{st}$ indicator is used to evaluate the effects of voltage fluctuation. It is measured by a flickermeter. The flickermeter principle operation and design requirements are defined in standard IEC 61000-4-15 [1]. The flickermeter signal chain is so complex that to describe its operation it is necessary to use characteristics connecting the $P_{st}$ indicator with the input voltage with a specific variability [2, 3]. Most often, the fluctuations are recreated by amplitude modulation with a square signal without the attenuated carrier wave. Such recreated voltage fluctuations can be described as:

$$u(t) = \sqrt{2}U_c \cos(2\pi f_c t) \left[ 1 + \frac{1}{2} \left( \frac{\Delta U}{U} \right) \operatorname{sign}\{\cos(2\pi f_m t)\} \right], \tag{1}$$

where: $U_c$ – rms voltage value, $f_c$ – power frequency (carrier frequency), $\left(\frac{\Delta U}{U}\right)$ – modulation depth, $f_m$ – frequency of the modulating signal.

The basic characteristic used to describe the flickermeter operation are the dependence of the $P_{st}$ indicator on the modulating signal frequency $f_m$ for $\left(\frac{\Delta U}{U}\right) = \text{const}$ and the dependence $\left(\frac{\Delta U}{U}\right) = \mathrm{f}(f_m, P_{st} = \text{const})$. Table 1 shows the set of seven points of the characteristic for $P_{st} = 1$ (presented in [1]) allowing testing flickermeter. The set is limited to $f_m \leq 33.3(3)\,\text{Hz}$. This is an unjustified limitation, because the characteristic $P_{st} = \mathrm{f}(f_m)$ for the sinusoidal voltage in the power grid contains the $f_m$ up to the value of approx. $3f_c \approx 150\,\text{Hz}$.

Figure 1 presents the characteristic $\left(\frac{\Delta U}{U}\right) = \mathrm{f}(f_m, P_{st} = 1)$ (with the marked points from Table 1) and the characteristic $P_{st} = \mathrm{f}\left(f_m, f_c = 50\,\text{Hz}, \left(\frac{\Delta U}{U}\right) = 0.2805\%\right)$. The scale of the horizontal axis is log-linear for better clarity of characteristics.

The characteristics from Figure 1 confirm that the local extremes of the $P_{st}$ indicator are present for $f_m > f_c$. This means that flicker severity can be caused by voltage variation for $f_m > f_c$. It is worth noting, that for such voltage variation the flicker frequency is smaller than $f_c$.

Table 1: The set of points of the characteristic $\left(\frac{\Delta U}{U}\right) = \mathrm{f}(f_m, P_{st} = 1)$ from [1]

| No. | 1 | 2 | 3 | 4 | 5 | 6 | 7 ($f_c = 50\,\text{Hz}$) |
|---|---|---|---|---|---|---|---|
| $f_m$ [Hz] | 0.0083(3) | 0.016(6) | 0.0583(3) | 0.325 | 0.916(6) | 13.5 | 33.3(3) |
| $\left(\frac{\Delta U}{U}\right)$ [%] | 2.715 | 2.191 | 1.45 | 0.894 | 0.722 | 0.407 | 2.343 |

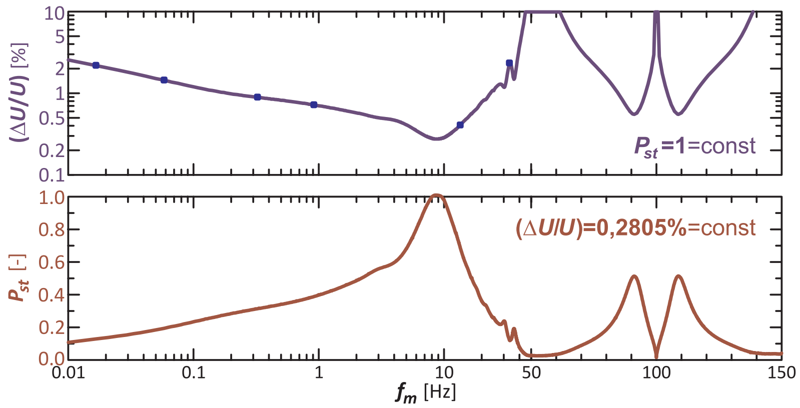


Fig. 1: The characteristic $\left(\frac{\Delta U}{U}\right) = \mathrm{f}\left(f_m, P_{st} = 1\right)$ (with marked points from Table 1) and the characteristic $P_{st} = \mathrm{f}\left(f_m, f_c = 50\,\mathrm{Hz}, \left(\frac{\Delta U}{U}\right) = 0.2805\%\right)$.

Including fact that the flicker severity can occur for $f_m > f_c$, the flickermeter testing should consider the appropriate frequency range of the modulating signal. The testing can be performed by setting the values according to the dependence $P_{st} = \mathrm{f}\left(f_m, \left(\frac{\Delta U}{U}\right)_{P_{st}=\mathrm{const}}\right)$ for the assumed value of the $P_{st}$ indicator. For such testing conditions, the $P_{st}$ measurement result should be constant and consistent with the conditions of the given voltage variation. The differences between the measurement results and the adopted $P_{st}$ value allow determining the flickermeter signal chain implementation imperfections. A separate problem is the insufficient efficiency of the $P_{st}$ indicator in the voltage variation severity assessment as well as the $P_{st}$ indicator limited diagnostic capabilities. It is a measure that estimates the flicker severity for a specific type of light source (incandescent bulb 60 W). Therefore, there are also alternative measures of voltage fluctuations considering the voltage variation and allowing identification of disturbance loads [4, 5, 6, 7, 8, 9].

Flickermeters that comply with [1] are usually implemented in the following devices: power quality analyzers, energy meters (the most common in use) and (software) simulators. More and more of the available AMI energy meters have built-in power quality functionalities. Power quality analyzers are considered the reference power quality parameter meters while AMI energy meters are treated as auxiliary power quality parameter meters. However, the still development (qualitative and quantitative) of AMI energy meters makes them very important diagnostic information sources (including the information about voltage fluctuations) results in the necessity to carry out metrological research of energy meters (including the implemented flickermeter in energy meters).

The paper presents the results of laboratory tests of three AMI energy meters with built-in flickermeters. The power quality analyzer [10] measurements also were performed to verify the correctness of the voltage fluctuation generation.

## 2. Laboratory Tests of Energy Meters With Built-in Flickermeters

The studies of three energy meters with built-in flickermeters were carried out in the circuit presented in Figure 2. Nine AMI energy meters were used for measurements (i.e. three units from three different types of meters) to obtain representative test results. Single-phase voltage (1) was applied to the three phase-voltage measurement inputs. Nine $P_{st}$ measurement results were obtained for each type of meter as a result. The simple statistical operations (determining of maximum, minimum and median values) were performed for obtained measurement results. The voltage (1) was generated according to the dependence $\left(\frac{\Delta U}{U}\right) = \mathrm{f}\left(f_m, P_{st} = \mathrm{const}\right)$ for $P_{st} = 1$ and 10. This allowed for the experimental determination of the characteristic $P_{st} =$

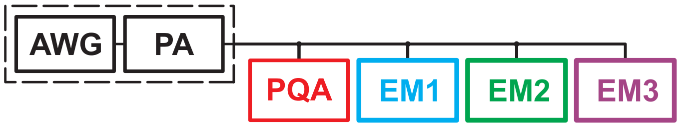


Fig. 2: The diagram of the testing circuit for AMI energy meters; PQA – power quality analyzer, EM1 – energy meter no. 1, EM2 – energy meter no. 2, EM3 – energy meter no. 3, PA – power amplifier, AWG – arbitrary waveform generator.

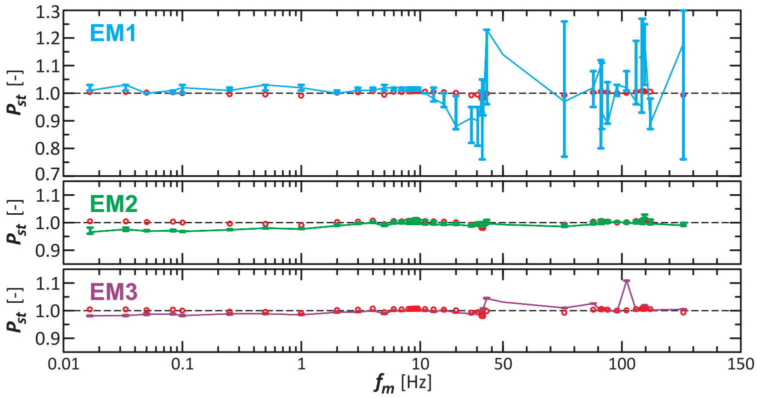


Fig. 3: Measurement results of $P_{st} = \mathrm{f}\left(f_m, \left(\frac{\Delta U}{U}\right)_{Pst=1}, f_c = 50\,\mathrm{Hz}\right)$ for energy meters EM1-EM3 and the power quality analyzer (red circles).

$\mathrm{f}\left(f_m, \left(\frac{\Delta U}{U}\right)_{Pst=\mathrm{const}}\right)$. Figure 3 shows the test results for three types of energy meters (EM1-EM3) with marked maximum and minimum values. The lines in Figure 3 connect the median values. The measurement results of the power quality analyzer are marked with red circles.

The power quality analyzer measurement results coincide with the line for $P_{st} = 1$ (Figure 3). This confirms the correctness of the voltage fluctuations generation. The measurement results are consistent with the adopted value of $P_{st} = 1$ for $f_m < 10\,\mathrm{Hz}$ for the three energy meters. There are discrepancies for higher $f_m$ values. It is especially visible for energy meter EM1 – the difference between the measurement results and the adopted value for some $f_m$ values exceeds 0.2. For EM3 it can be noticed that for three $f_m$ values there is a greater difference than for the other measuring points.

Figure 4 presents the measurement results for $P_{st} = 10$. The measurement results of the power

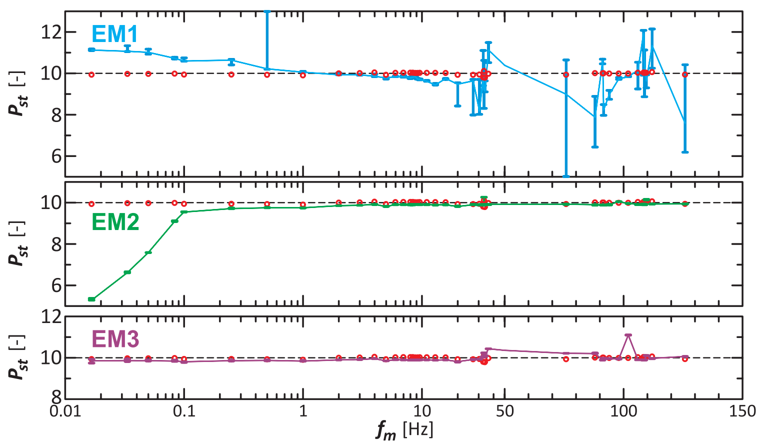


Fig. 4: Measurement results of $P_{st} = \mathrm{f}\left(f_m, \left(\frac{\Delta U}{U}\right)_{Pst=10}, f_c = 50\,\mathrm{Hz}\right)$ for energy meters EM1-EM3 and the power quality analyzer (red circles).

quality analyzer from Figure 4 coincide with the line for $P_{st} = 10$. There is a greater discrepancy in the measurement results compared to Figure 3. It is difficult to indicate the $f_m$ frequency range in which the three types of energy meters are consistent with the adopted value of $P_{st} = 10$. The best agreement is for the EM3 – the shape of $P_{st} = \mathrm{f}\left(f_m, \left(\frac{\Delta U}{U}\right)_{Pst=10}\right)$ is similar to the shape of $P_{st} = \mathrm{f}\left(f_m, \left(\frac{\Delta U}{U}\right)_{Pst=1}\right)$. For EM2 the agreement can be found at $f_m > 0.1\,\mathrm{Hz}$. For $f_m < 0.1\,\mathrm{Hz}$, the $P_{st}$ measurement result decreases with the decrease of the $f_m$ values. It is most difficult to describe the dependence of the $P_{st}$ indicator measurement result on the $f_m$ frequency for the EM1. For $f_m < 20\,\mathrm{Hz}$, a trend is visible in which the $P_{st}$ value decreases with an increasing $f_m$. For $f_m > 20\,\mathrm{Hz}$, the dependence of $P_{st}$ indicator on the $f_m$ frequency is non-monotonic. It should be noticed that for the EM1, regardless of the adopted $P_{st}$ value, there is a large dispersion of the measurement results for $f_m > 20\,\mathrm{Hz}$.

## 3. Conclusions

AMI energy meters are advanced measuring and recording systems. Some of them have built-in power quality assessment functionalities, including the IEC 61000-4-15 compliant flickermeter. Flickermeter testing is a complex procedure requiring the use of appropriate testing signals. The common voltage fluctuation model for testing flickermeter is the amplitude modulated sinusoidal voltage by a square signal. The test involves setting modulation parameters (the frequency of the modulating signal $f_m$ and the modulation depth $\left(\frac{\Delta U}{U}\right)$) and comparing the $P_{st}$ measurement results with reference values. The paper assumes the modulation parameters that allow construction of the characteristic $P_{st} = \mathrm{f}\left(f_m, \left(\frac{\Delta U}{U}\right)_{Pst=\mathrm{const}}\right)$. The tests were carried out over the full $f_m$ frequency range in which there is a significant variation in the $P_{st}$ indicator.

## References


[1] (2010). IEC 61000-4-15: Testing and measurement techniques – Flickermeter – Functional and design specifications.

[2] Majchrzak, J., Wiczyński, G. (2012). Basic characteristics of IEC flickermeter processing. *Modelling and Simulation in Engineering*.

[3] Wiczyński, G. (2010). Analysis of flickermeter's signal chain for input signal with two sub/interharmonics. *Przegląd Elektrotechniczny*, 86(4), 328–335.

[4] Piątek, K., *et al.* (2021). Optimal selection of metering points for power quality measurements in distribution system. *Energies*, 14(4), 1–18.

[5] Wiczyński, G. (2009). Voltage-fluctuation-based identification of noxious loads in power network. *IEEE Transactions on Instrumentation and Measurement*, 58(8), 2893–2898.

[6] Michalski, M. (2018). Introductory results of tests of algorithms for recreation of voltage variation with voltage fluctuation indices. In: *Proceedings of* $18^{th}$ *ICHQP*. Ljubljana, 1–5.

[7] Kuwałek, P. (2020)a. Increase of diagnostic capabilities of voltage fluctuation indicies. In: *Proceedings of* $19^{th}$ *ICHQP*. Dubai, 1–6.

[8] Kuwałek, P. (2020)b. AM modulation signal estimation allowing further research on sources of voltage fluctuations. *IEEE Trans. Ind. Electron.* 67(8), 6937–6945.

[9] Kuwałek, P. (2021). Estimation of parameters associated with individual sources of voltage fluctuations. *IEEE Transactions on Power Delivery*, 36(1), 351–361.

[10] (2011). Power quality analyser PQ-Box 100 (Manual). A. Eberle GmbH & Co. KG.

# Description of Voltage Variation in Power Grids on the Basis of Voltage Fluctuation Indices

**Grzegorz Wiczyński**

Poznań University of Technology, Poznań, Poland,
Email: grzegorz.wiczynski@put.poznan.pl

***Abstract.*** *The paper describes voltage variation based on voltage fluctuation indices. The presented example of voltage variation analysis makes use of the results of measurements recorded in the LV power grid. As a result of the analysis, the information on voltage changes related to the occurrence of* $P_{st} > 0.8$ *has been obtained. Their* $f$ *rate and* $\delta U$ *magnitude have been determined, making it possible to estimate the parameters of the voltage variation source.*

*Keywords: Voltage Variation, Voltage Fluctuations Indices,* $P_{st}$ *Indicator*

## 1. Introduction

build our knowledge about the voltage fluctuations that cause the obnoxious flicker. The assessment of flicker obnoxiousness is most commonly based on the $P_{st}$ indicator. It is a measure aimed at assessing the effects of voltage fluctuation but not describing voltage variation. Since it is characterized by low diagnostic capabilities, other measures are also used to describe voltage variation. Frequently used are the maximum and minimum values (determined based on rms voltage refreshed each half-cycle) and the voltage fluctuation indices [1]. It should be noted that the voltage fluctuation indices are still under development [2] and new methods for obtaining voltage variation information [3, 4, 5, 6] are being proposed. Therefore, one should expect an increase in the diagnostic capabilities of these measures. The paper presents an example of using the maximum and minimum values and voltage fluctuation indices to describe the voltage variation. The results of measurements recorded in the LV power grid have been selected for the analysis. The selected data do not have any features that would facilitate the analysis process. In many cases, when the real power grids are tested, there are measurement results are obtained that do not facilitate the diagnostic process.

## 2. Flicker Severity Assessment

The measurement results for the analysis have been recorded in the circuit which simplified structure has been shown in Figure 1. In order to assess the obnoxiousness of the voltage fluctuation, the $P_{st}$ indicator for phase voltages has been used. The measurement results in Figure 2 have been presented in the form of a time waveforms and a histogram.

The time waveforms of $P_{st} = \mathrm{f}(t)$ and the histogram imply that $P_{st} > 1$ exists in three phases. However, the most severity voltage fluctuations occur in the phase marked L1. Therefore, in further analysis, this phase has been considered. During the measurements, simultaneous records of the following values have been made: voltages (including the $U_{\max}$ maximum values, the $U_{\mathrm{avg}}$ average values, and the $U_{\min}$ minimum values of phase voltages) at points P0 and P1 and currents (including the $I_{\max}$ maximum values and the $I_{\mathrm{avg}}$ average values of phase currents) at

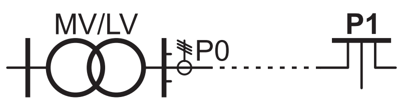


Fig. 1: Scheme of the analyzed power grid.

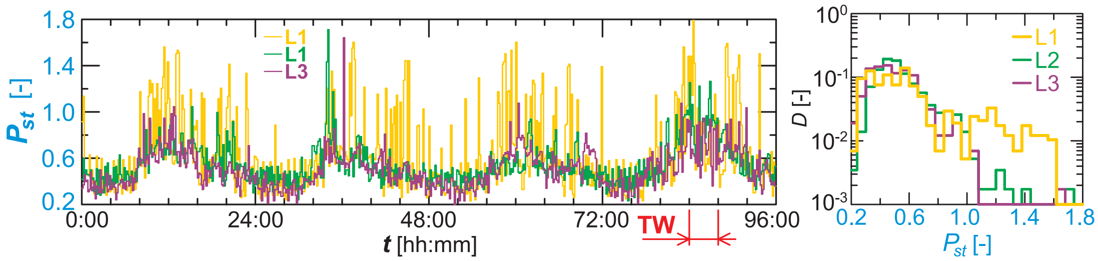


Fig. 2: $P_{st} = \mathrm{f}(t)$ time waveforms and $D = \mathrm{f}(P_{st})$ histogram for phase voltages at point P1 (recording interval 10 min).

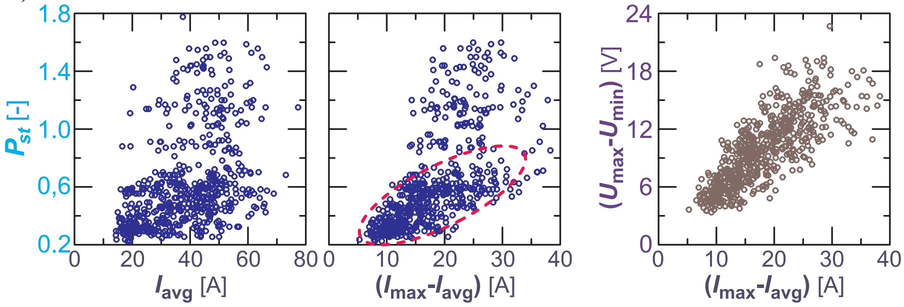


Fig. 3: $P_{st} = \mathrm{f}\left(I_{\mathrm{avg}}\right)$, $P_{st} = \mathrm{f}(I_{\max} - I_{\min})$ and $(U_{\max} - U_{\min}) = \mathrm{f}\left(I_{\max} - I_{\mathrm{avg}}\right)$ characteristics for currents at point P0 and phase voltages at point P1 (recording intervals 10 min).

point P0. Unfortunately, the currents at point P1 have not been recorded. Taking into account the available data, an attempt has been made to define the voltage variation parameters in conjunction with the flicker severity. Figure 3 presents the dependency of the $P_{st}$ indicator and the difference $(U_{\max} - U_{\min})$ at point P1 on the $I$ current and the difference $(I_{\max} - I_{\mathrm{avg}})$ at point P0.

Visual analysis of the Figure 3 characteristics allows for the following conclusions: a) there is no connection between the flicker severity at point P1 and the average value of the current $I_{\mathrm{avg}}$ at point P0; b) for $P_{st} < 0.8$ there is a visible increase of flicker severity at point P1 associated with an increase in the difference of currents $\left(I_{\max} - I_{\mathrm{avg}}\right)$ at point P0, for $P_{st} \geq 0.8$ there is no visible relationship; c) the increase of the voltage difference $(U_{\max} - U_{\min})$ at point P1 is related to the increase of the current difference $\left(I_{\max} - I_{\mathrm{avg}}\right)$ at point P0.

## 3. Description of Voltage Variation

The characteristics from Fig 3 have not provided explicit diagnostic information. On their basis it can be assumed that for $P_{st} > 0.8$ the value of this indicator is influenced by the values which are not included in Figure 3. A more precise description of voltage variation requires the use of voltage fluctuation indices [7]. The results obtained with this measure consist of a set of $\delta U$ magnitude and $f$ rates of fluctuation. The values of these indices are derived from the detected voltage changes $\delta V$. Figure 4 shows the $P_{st} = \mathrm{f}(f_{1.0-0.4})$, $P_{st} = \mathrm{f}(\delta U)$ and $\delta U = \mathrm{f}(f_{1.0-0.4})$) for the voltage at P1. The $f_{1.0-0.4}$ symbol means that when determining the $f$ rate, the $\delta V$ voltage changes within the range $\langle \delta U, 0.4\delta U)$ have been taken into account.

The characteristics from Figure 4 provide direct information about the voltage fluctuation inducing an elevated flicker severity. The characteristic $\delta U = \mathrm{f}(f_{1.0-0.4})$ shows the measurement points located above the permissible voltage fluctuation borderline (PVFB). Most of these points are concentrated along the line $\delta U = 3.5\%$ for the rate values of $f_{1.0-0.4}$ from 0.3 cpm to 30 cpm. This is consistent with the distribution of the measurement points on the $P_{st} = \mathrm{f}(f_{1.0-0.4})$ and $P_{st} = \mathrm{f}(\delta U)$ characteristics.

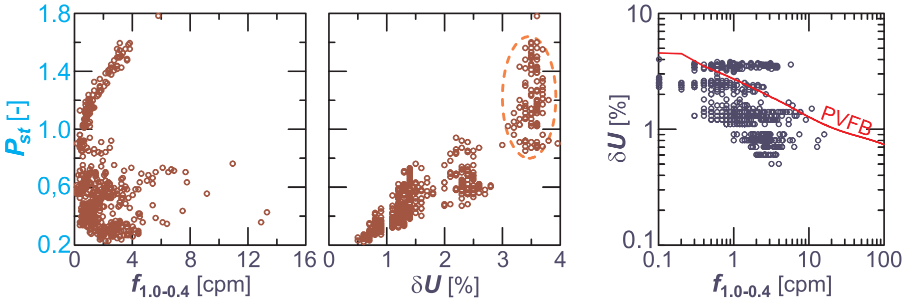


Fig. 4: $P_{st} = \mathrm{f}(f_{1.0-0.4})$, $P_{st} = \mathrm{f}(\delta U)$ and $\delta U = \mathrm{f}(f_{1.0-0.4})$ for voltage at point P1 (recording intervals 10 min).

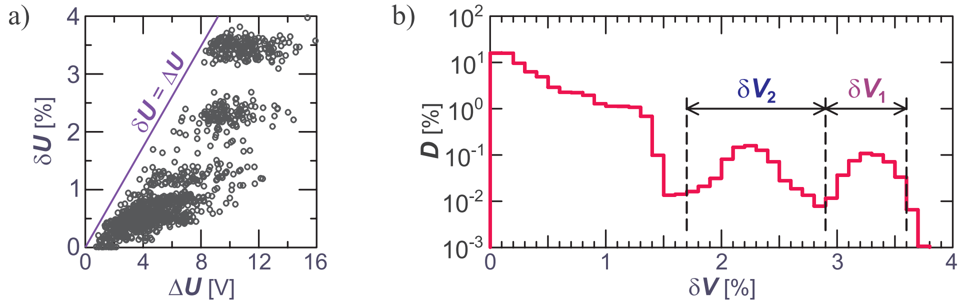


Fig. 5: $\delta U = \mathrm{f}(\Delta U)$ characteristics with a marked line that meets the $\delta U = \Delta U$ condition and the $D = \mathrm{f}(\delta V)$ histogram for recording intervals meeting the $P_{st} > 0.8$ condition; measurement results at point P1 for 1 min recording intervals in the TW time horizon (from Figure 2).

For an in-depth description of the voltage changes Figure 5 consist of two characteristics. The time horizon of the presented data was limited to 6 hours (period TW from Figure 2). Figure 5a shows the $\delta U = \mathrm{f}(\Delta U)$ characteristic with the marked line which satisfies the condition $\delta U = \Delta U$. The dispersion of points on this characteristic indicates a complex voltage fluctuation structure. The structure of voltage variation cannot be determined from the $\delta U$ magnitude alone. In order to broaden the knowledge about obnoxious voltage fluctuations on the basis of the $\delta U$ and $f$ indicators, the $\delta V$ voltage changes have been recreated. Data recorded every 1 min and the rates of fluctuations counted in seven ranges ($f_{1.0-0.9}$, $f_{0.9-0.8}$, $f_{0.8-0.7}$, $f_{0.7-0.6}$, $f_{0.6-0.5}$,$f_{0.5-0.4}$ and $f_{0.4-0.0}$) have been used for the reconstruction. Figure 5b presents the histogram of $\delta V$ voltage changes for the recording intervals in which the $P_{st} > 0.8$.

The $D = \mathrm{f}(\delta V)$ histogram has provided the information about the structure of voltage variation. Two local extremes are visible in this histogram. Taking into account the shape of the histogram, two $\delta V$ magnitude ranges have been marked: $\delta V_1 = (2.9\%, 3.6\%\rangle$ and $\delta V_2 = (1.7\%, 2.9\%\rangle$. For these $\delta V$ ranges, based on the voltage fluctuation indices, the rates $f_1$ for $\delta V_1$ and $f_2$ for $\delta V_2$ have been reconstructed. Time waveforms for $f_1 = \mathrm{f}(t)$ and $f_2 = \mathrm{f}(t)$ against the $P_{st} = \mathrm{f}(t)$ waveform have been shown in Figure 6.

The analysis of the time waveforms from Figure 6 leads to the following conclusions: a) $P_{st} > 1.1$ is related to the voltage changes $\delta V_1 = (2.9\%, 3.6\%\rangle$; b) $P_{st} > 0.8$ is associated with the voltage changes $\delta V_2 = (1.7\%, 2.9\%\rangle$ (with or without $\delta V_1$); c) the longest continuous occurrence of the $\delta V_1 = (2.9\%, 3.6\%\rangle$ voltage changes has been found in period T1, during this time horizon, the $f_1$ and $f_2$ rates change; d) rates $f_1$ and $f_2$ of the occurrences of $\delta V_1$ and $\delta V_2$ voltage changes are from 1 cpm to 7 cpm.

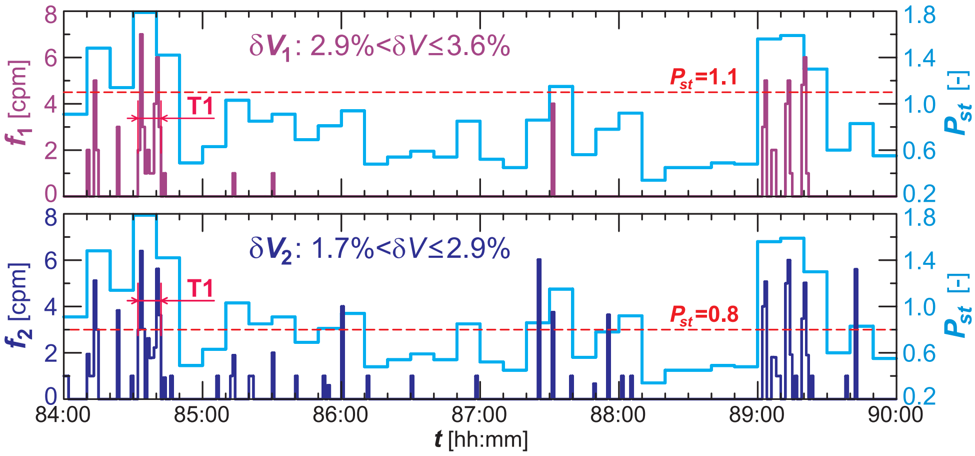


Fig. 6: Time waveforms of $P_{st} = \mathrm{f}(t)$ (recording intervals 10 min), $f_1 = \mathrm{f}(t)$ and $f_2 = \mathrm{f}(t)$ (recording intervals 1 min) over TW time period (from Figure 2) at point P1.

## 4. Conclusions

The paper presents an example of a description of voltage variation based on voltage fluctuation indices. For the examplary voltage fluctuation analysis, the results of measurements recorded in the LV power grid have been selected. This data is not characterized by specific information facilitating the location of the disturbing load. For example, no relationship has been observed between the flicker severity and the voltage variation expressed by the difference $(U_{\max} - U_{\min})$ and the current variability expressed by the difference $\left(I_{\max} - I_{\mathrm{avg}}\right)$. As a result of the presented analysis of voltage fluctuation indices, information about $\delta V$ voltage changes related to the occurrence of $P_{st} > 0.8$ has been obtained. The knowledge of the $f_1$ and $f_2$ rates makes it possible to estimate the frequency of changes in the state of the obnoxious load. In turn, the position of $\delta V_1$ and $\delta V_2$ voltage changes on the timeline informs when the load searched for is active. The values of $\delta V_1$ and $dV_2$, with the knowledge of the supply line parameters, make it possible to estimate the variability of the current which causes the voltage changes.

## References


[1] Michalski, M., Wiczyński, G. (2015). Determination of the parameters of voltage variation with voltage fluctuation indices. In: *Proceedings of 2015 Int. School on Nonsinusoidal Currents and Compensation (ISNCC),*. Łagów, Poland, 1–6.

[2] Michalski, M. (2018). Introductory results of tests of algorithms for recreation of voltage variation with voltage fluctuation indices. In: *Proceedings of* $18^{th}$ *ICHQP*. Ljubljana, 1–5.

[3] Kuwałek, P. (2020)a. Increase of diagnostic capabilities of voltage fluctuation indicies. In: *Proceedings of* $19^{th}$ *ICHQP*. Dubai, 1–6.

[4] Kuwałek, P. (2020)b. AM modulation signal estimation allowing further research on sources of voltage fluctuations. *IEEE Transactions on Industrial Electronics*, 67(8), 6937–6945.

[5] Piątek, K., *et al.* (2021). Optimal selection of metering points for power quality measurements in distribution system. *Energies*, 14(4), 1–18.

[6] Kuwałek, P. (2021). Estimation of parameters associated with individual sources of voltage fluctuations. *IEEE Transactions on Power Delivery*, 36(1), 351–361.

[7] Wiczyński, G. (2009). Voltage-fluctuation-based identification of noxious loads in power network. *IEEE Transactions on Instrumentation and Measurement*, 58(8), 2893–2898.

# Radiation Pattern Antenna System Measurement

**[1]Michal Dzuris, [2]Norbert Grilli, [3]Imrich Szolik, [3]Jozef Hallon**

[1]MWTC, s.r.o.,S. Straku 46, 914 01 Trencianska Tepla, Slovakia
[2]Towercom, a.s., Cesta na Kamzík 14, 831 01 Bratislava, Slovakia
[3]FEI STU, Ilkovicova 3, 812 19 Bratislava, Slovakia
Email: mwtc@mwtc.tech

***Abstract.*** *The article deals with measuring the radiation characteristics of the antenna system in conditions of very high electromagnetic fields and the presence of other interfering signals.*

*Keywords: Antenna Systems, Electromagnetic Compatibility, Shielding*

## 1. Introduction

Transmitters that are terminated by antenna systems (AS) are used for the terrestrial transmission of analog or digital signals. In order to make the transmission range as large as possible, ASs are mounted on tall objects - buildings, mono pipes, etc. There can be many such ASs on one object. After installing the antenna system, when verifying its functionality, it is necessary to measure its basic property - the radiation characteristic when replacing it. Measurement is problematic [1] because the measuring device must be installed on a quadcopter. It must be selectively sensitive to the measured frequency band and resistant to radiation of other systems installed nearby.

## 2. Subject and Methods

As mentioned before, the antenna array's radiation pattern and electrical characteristics may be changed when a sudden failure occurs. These changes can usually be identified by field receiving probe or by high-frequency measurement on feeder lines of each element / antenna of antenna system. Monitoring individual elements is usually not possible if the AS has a common branched transmission line.

Therefore, direct measurement of faulty elements from the main feeder is not possible on the power supply. The most promising and versatile method to confirm radiation pattern and detect faulty elements is by direct measurement of radiation pattern somewhere near the antenna system.

Electromagnetic field professional strength meter and spectrum analyzer *Promax HD Ranger 3* [2] has been chosen to evaluate this method, as it is portable and can measure/record all required frequencies. The instrument is capable to measure in most of the digital standards, such as DBV-T, DAB, DAB+, LTE, GPS, WiFi and many other satellite/terrestrial services, and it can perform various analysis like merogram, spectrogram, etc. The instrument was equipped with an external receiving antenna and external GPS module [3], to be able to capture the position in flight. Measurement was realized by Promax analyzer, fixed on a drone. Then the unit proceeded in measuring the strength of the electromagnetic (EM) field of a single frequency. The drone was flying around the antenna system while keeping a distance of ~200m from the tower at constant altitude. Measured flight data was processed and visualized for clarity of measurement (see Fig. 1).

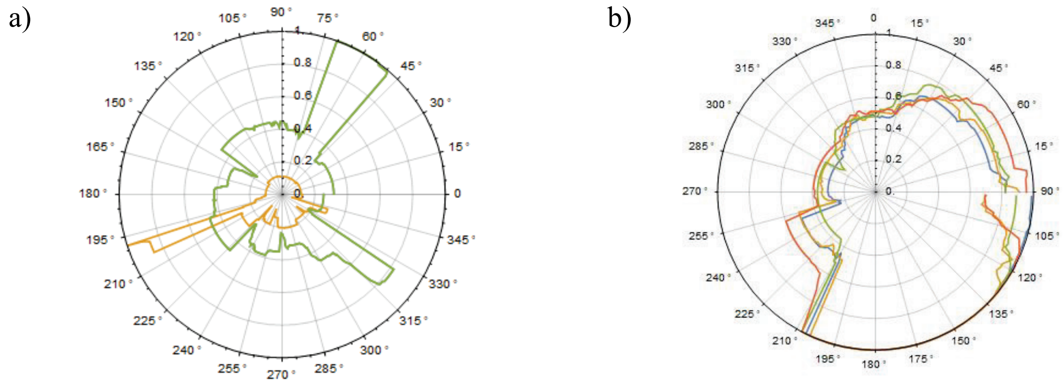


Fig. 1. Processed data that was measured by "Promax HD Ranger 3" a) without shielding (left) b) with added shielding (right).

As seen in Fig. 1a, we can clearly say that part of the measured data is invalid due to sharp and sudden spikes, which are in saturated values for a long time.

*Investigation*

Measured data seen on Fig.1a was unusable, and also, the device itself had operational problems. Therefore, the Promax analyzer was examined. To investigate this state of saturation and the cause for a faulty instrument reading, self rebooting, and freezing, we have performed several electromagnetic compatibility (EMC) susceptibility tests to determine the EM susceptibility of the device for high EM fields. EMC testing was also an easy and fast way to find an effective method to improve parameters in high EM fields.

*Test n.1*

First of all, we have put our device under test (DUT) (*Promax HD Ranger 3*) in a semi-anechoic chamber. Then without any external antenna/device connected, we have terminated antenna input and set the device frequency span to be from 80MHz to 1000MHz [4], [5], [6]. As expected, without any external EM fields in the chamber, the instrument displays only the noise background of analyzer -80 dBm.

*Test n.2 & n.3*

Next test n.2 was performed without changes in settings (no devices connected on I/O ports and antenna input was terminated), but gradually changing EM field with the strength of 50V/m was generated, with a frequency span from 80MHz to 1000MHz according to requirements of the standard EN 61000-4-3. Picture Fig. 2 shows the error of electrical spectrum from generated EM field in the shielded chamber, which was caused by the penetration of the EM field through the housing of the device and the creation of an additional error.

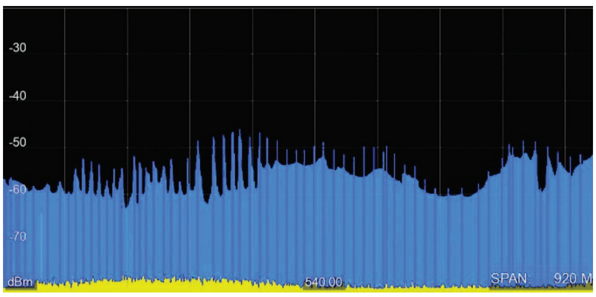


Fig. 2. Record of measurement - test n.2.

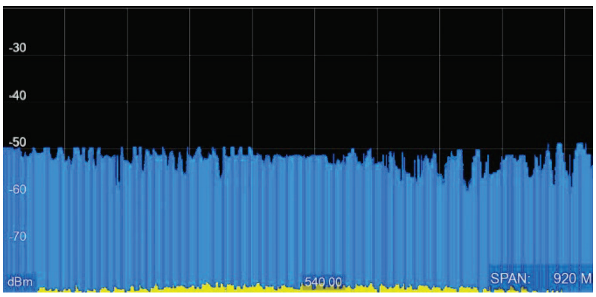


Fig. 3. Record of measurement - test n.3.

*Test n.3*
The test was done with the previous setup and with an external GPS antenna connected via a USB port. Fig. 3 shows that mentioned arrangement increased the disturbance level of the instrument in such a way that the instrument displays noise at level -50 dBm (in this configuration).

*Test n.4 & n.5*
During the test n.4, we have finally included an external measuring antenna to the arrangement of the DUT. The external antenna was connected via 26 dB attenuator and connector adapters into DUT. As expected, due to the external antenna, we can eventually see some of the "useful" signals that are seeping through the noise (see Fig. 4). Now that we know that the problem is in EM susceptibility of the instrument chassis and also GPS with USB cable interface, we tried to eliminate or at least reduce these problems. Test n.5 proved that overall better measurement results could be achieved simply by adding ferrite clamps on the USB cable coming from an external GPS antenna. As we can see in Fig. 5, "background noise" is now less than -60 dBm (10 dB improvement).

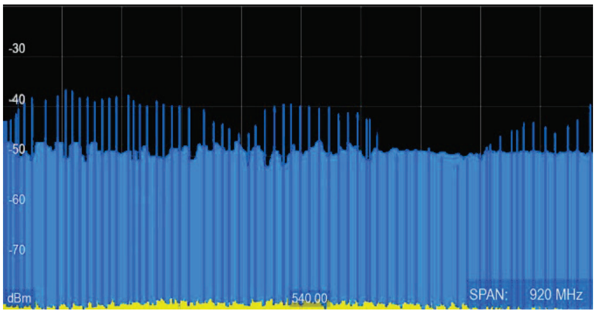


Fig. 4. Record of measurement - test n.4.

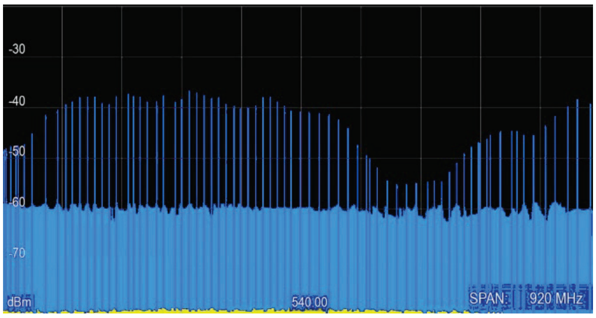


Fig. 5. Record of measurement - test n.5.

*Test n.6*
The last test also included EMC conductive fabric. The instrument was carefully wrapped with the fabric in a way that the fabric completely surrounded the instrument and also ferrite clamp on USB cable, so the only way for EM interference was via input antenna or the USB cable entering ferrite clamp (see Fig. 6).

Fig. 6. Setup for - test n.6.

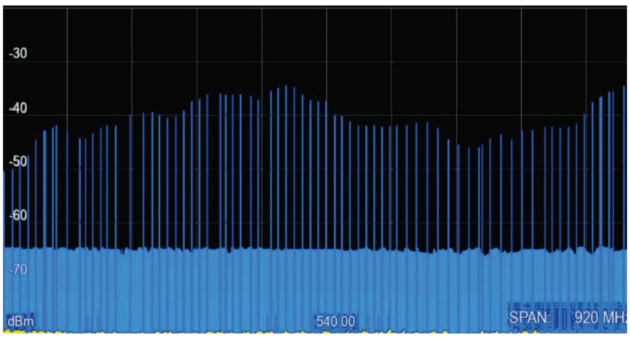


Fig. 7. Record of measurement - test n.6.

Finally, in Fig. 7, we can see a clear measurement record, where background noise dropped under -65 dBm (15dB improvement from the original measurement record from test n. 3).

## 3. Results

Various tests in the EMC chamber and at nearby AS confirmed that the problem with the measuring instrument is low EMC susceptibility. The consequence of which is either poor performance of signal to noise ratio, faulty readings with saturated values or complete failure of the instrument due to additional error of the measurement - this device is not designed to be operated at such a high-level EM field. Based on EMC tests, measures were taken using *Promax HD Ranger 3* (shielding, blocking of signal wires), which improved the dynamic range of the setup by more than 15dB in a given environment. A re-measurement of the radiation pattern was required, Fig.1b. The measurement results are usable after statistical adjustments, but the elements of interference still show.

## 4. Conclusions

To solve this problem and find a way how to measure a specific radiation pattern of a broadcasting tower, we can either modify our instrument to increase its rating for EMC susceptibility or find a better instrument for the task. The first option is not the best because of the complicated instrument setup in the field as opposed to the lab environment. Better instruments that would fit the description are usually military-grade instruments, and these instruments are not physically fit to operate with a civil drone. Therefore, to stay in a low-cost measuring system for measuring large antenna systems, the best option is to build a single-purpose device that would be highly customized for this type of measurement.

## Acknowledgements

This work was supported by APVV-15-0062 "Electromagnetic compatibility ensuring of monitoring systems of the abnormal operating condition of the nuclear power plant".

## References

[1] Slížik, J., Harťanský, R. (2013). Metrology of Electromagnetic Intensity Measurement in Near Field. In Kvalita Inovácia Prosperita = Quality Innovation Prosperity. Vol. 17, Iss. 1 (2013), s.57-66. ISSN 1335-1745 (2013: 0.121 - SJR, Q4 - SJR Best Q).

[2] [online(1.3.2021)] https://www.orbitadigital.com/en/satellite-terrestrial/meter-satfinder/2051-promax-hd-ranger-3-professional-field-meter-dvb-t-t2-c2-s-s2-h265.html

[3] [online(1.3.2021)]https://www.orbitadigital.com/en/satellite-terrestrial/meter-satfinder/13424-promax-ag-101-gps-for-ranger-neo-234-and-hd-ranger-3.html.

[4] Harťanský, R., Smieško, V., Rafaj, M. (2017). Modifying and accelerating the method of moments calculation. In Computing and Informatics. Vol. 36, No. 3 (2017), s. 664-682. ISSN 1335-9150 (2017: 0.410 - IF, Q4 - JCR Best Q, 0.198 - SJR, Q3 - SJR Best Q). In database: CC: 000404850000008.

[5] Harťanský, R., Slížik, J., Maršálka, L.(2013). Dipole Near Field Analysis - A Closed Form Calculation in Cartesian Coordinates. In Journal of Electrical Engineering. Vol. 64, No. 5 (2013), s.327-330. ISSN 1335-3632 (2013: 0.420 - IF, Q4 - JCR Best Q, 0.221 - SJR, Q3 - SJR Best Q).

[6] Harťanský, R., Halgoš, J.(2017). The problem of RF radiator with force detector. In Measurement 2017 : 11th International conference on measurement. Smolenice, Slovakia, May 29-31, 2017. Bratislava : Slovak academy of sciences, 2017, S. 139-142. ISBN 978-80-972629-0-7. V databáze: IEEE ; WOS: 000428658900032.

# Measurement of Parameters for Transformer Insulating System Oil-Paper by Frequency Method

**Miroslav Gutten, Peter Brncal, Daniel Korenciak, Jozef Kudelcik**

Faculty of Electrical Engineering and Information Technology,
University of Žilina, Univerzitná 1, 010 26 Žilina, Slovakia
Email: miroslav.gutten@feit.uniza.sk

***Abstract.*** *Experimental analysis and diagnostics of insulating system oil-paper for traction transformer by frequency method is presented in the paper. In the first part of the paper, the base theory about measurement and diagnostics insulating part (oil and paper) of transformers is described. In the other part of the paper, experimental results of the diagnostic measurement for the traction transformer at a constant temperature using to diagnostic method - frequency domain spectroscopy (FDS) are presented. This method is used for the analysis of insulating conditions of high-voltage equipment with insulating oil paper. Quality of paper moisture and oil conductivity of the transformer - before and after its drying was compared.*

*Keywords: Transformer, Insulating system, Frequency dielectric spectroscopy*

## 1. Introduction

Effects of operating current lead to deterioration of solid and liquid insulating parts of power transformers with insulations of oil and paper. Electrical diagnostics significantly contributes to the condition check, which main task is to find a clear relationship between the change of functional characteristics of the equipment and some measurable values. The purpose of equipment diagnostics is to verify whether the machine meets the specified condition using standards IEC and research [1].

Diagnostics of insulating properties is one of the main requirements for the safe operation of power transformers. Basic diagnostic methods for assessing the insulation condition of a transformer are the measurements of loss factor, insulation resistance, partial discharge, etc. These methods, however, provide only a partial picture of the polarization processes in insulating material [2]. To prevent damage to the electric machines, we perform various types of diagnostic measurements, which should illustrate the actual condition of the measuring equipment. Therefore, it is important to choose the appropriate diagnostics for the correct prediction of such conditions [3], [4].

## 2. Analysis of the Transformer Insulation by Frequency Domain Spectroscopy

Previous research in the monitoring area of insulating properties indicated that the frequency domain spectroscopy (FDS) could the most effective estimate of the deterioration in oil-paper insulation in power transformer. Because the low frequencies (up to 0.1 Hz) reflect the moisture concentration in the paper, their measurement is of utmost importance for reliable data analysis. Besides a frequency sweep, a dielectric response to a voltage sweep is experimentally investigated and discussed [5], [6]. Particular focus is given on comparing available dielectric spectroscopy methods to traditional measurement techniques, as dielectric dissipation factor (tg $\delta$) tests at power frequency and 0.1 Hz, dielectric absorption ratio, and the polarization index [7].

For example, if increased losses appear, it is complicated to distinguish whether they are caused by the insulating oil or the cellulose paper insulation. By applying a sinusoidal frequency over a wide range, it is possible to separately analyze the paper moisture and the oil conductivity. Response of the insulating system in power transformer depends on the properties of insulating paper, quality of transformer oil, and its geometrical insulating parties.

For power transformers with oil-paper insulating, the dielectric response is affected by three components. They are the response of the cellulose insulation (paper, pressboard), the response of the transformer oil, and the interfacial polarization effect. Moisture, temperature, insulation geometry, oil conductivity, and conductive ageing of the products influence the dielectric response.

## 3. Experimental Measuring Apparatus for Analysed Transformer

Based on theoretical analysis realized in the first phase of solution in this paper, the latest diagnostic insulating methods - frequency method of measurement were determined. As measuring equipment, the traction oil transformer 25/0.6 kV before repair, during drying, and after the repair was used.

Measurement of a response in the frequency domain consists of finding out the current response to the harmonic voltage with a variable frequency in whole and a particular part of the insulating transformer system. The MEGGER IDAX 350 instrument performed measurement of the frequency response of the isolation system or measurement by the FDS method. The measured parameters in this method were - the percentage loss factor, capacities, and permittivity depending on the frequency of 10 kHz up to 1 MHz at the sinusoidal power supply 140 Vef. Since the device separately distinguishes measurement of individual capacities, it is necessary thoroughly to clean the location for connection of the ground conductor of the device [8].

The disadvantage of the FDS method is the need to measure very small currents. It is necessary to use shaded measuring cables.

## 4. Results and Discussion

The developments in Fig. 1a correspond to the measured characteristics of the loss factor (tg $\delta$) depending on the frequency of the harmonic voltage before repair, during drying, and after repair of the measured traction transformer. We left such a traction transformer in a vacuum oven for a long time - 3 days.

From the entered values of temperature, moisture, and transformer parameters, the modelling curves are calculated by the IDAX 350 program. Depending on the deviation of the measured waveforms from the model, the parameters of the transformer insulating system are subsequently determined. A column comparison of the loss factor (tg $\delta$), moisture in paper, and oil conductivity of the measured transformer is shown in Fig.1. Calculated values of paper moisture, oil conductivity, and the results of a measured transformer are shown in Table 1. Since the object's temperature is measured and the surrounding area is the same, another conversion error is not taken into account.

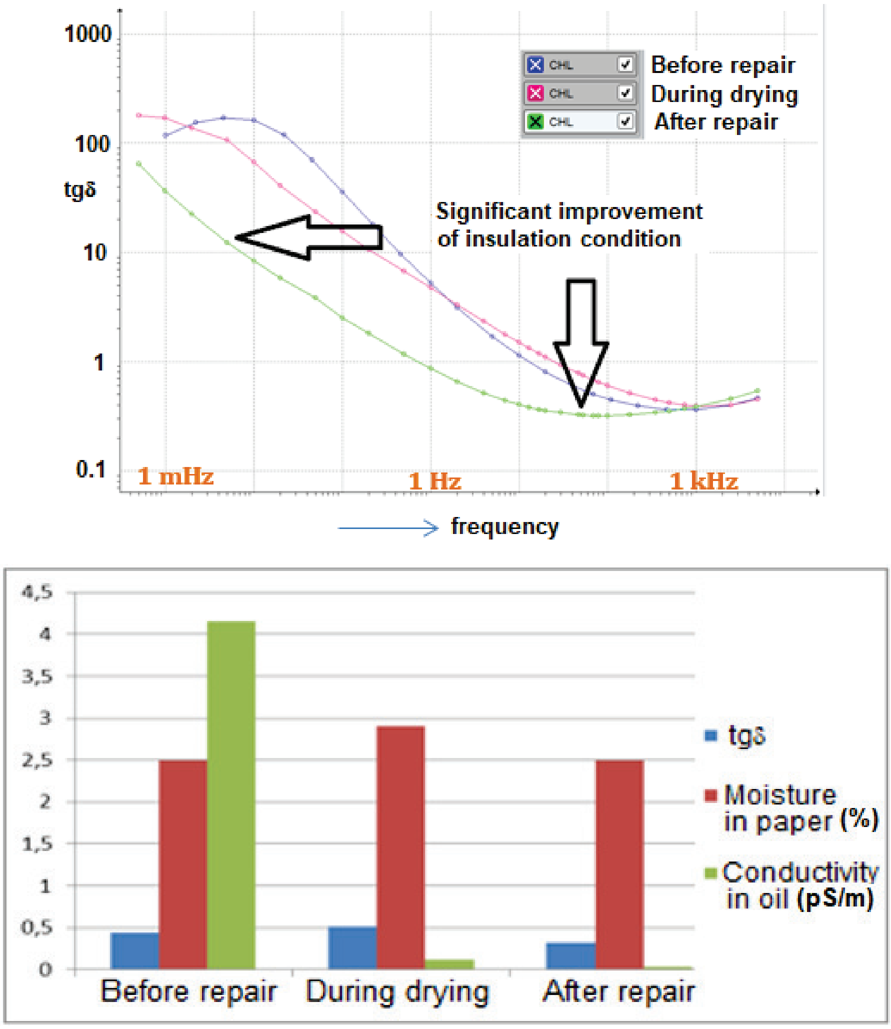


Fig. 1. Values of the measured transformer before repair, during drying, and after repair: Upper: Frequency depending on the loss factor (tg δ), Lower: Columns comparison of the loss factor (tg δ), moisture in paper, and oil conductivity.

Table 1. Measured parameters of transformer insulating system before its drying

| Condition | Transformer temperature °C | Loss factor tg δ at 20 °C | Moisture in paper % | Conductivity of oil pS/m |
|---|---|---|---|---|
| a) before its drying | 21.2 | 0.40 | **2.5** | 4.15 |
| b) after its drying | 21.2 | 0.30 | **2.5** | 0.356 |

As it is shown in Table 1 - before drying of measured transformer - despite relatively high oil conductivity (4.15 pS/m), the insulating system of the tested transformer is considerably impaired. The measured values of the loss factor, moisture in paper, and oil conductivity comprehensively indicate a poor state of the insulation system of the tested transformer.

As it is shown in Table 1 - after drying of measured transformer - the value of oil conductivity was better (0.356 pS/m), and the insulating system of the tested transformer is considerably better. The values of the loss factor, moisture in paper, and oil conductivity comprehensively indicate the very good state of the insulating system of the measured transformer.

## 5. Conclusions

This paper presents an experiment for diagnostics and measurement of insulating parameters of high-voltage traction transformer using frequency-domain spectroscopy. This diagnostic method is unique in terms of the analysis of the insulating system of oil traction transformers.

FDS method can evaluate the moisture condition of the insulation paper of the power transformer with high accuracy. The value of conductivity in transformer oil was very high (4.15 pS/m) before its drying. After drying this transformer was the value of oil conductivity 0.356 pS/m. Moisture in transformer paper after drying was the same value as before drying.

**Acknowledgements**

This work was supported by the Grant Agency VEGA from the Ministry of Education of the Slovak Republic under contract 1/0471/20.

## References

[1] Brandt, M. (2016). Identification failure of 3 MVA furnace transformer. In: *DEMISEE 2016*, Papradno, SR, pp. 6-10.

[2] Monatanari, G. C. (2000). Polarization and space charge behavior of unaged and electrically aged crosslinked polyethylene. In: *IEEE Trans. Dielectr. Electr. Insul.,* vol. 7, pp. 474-479.

[3] Heatcote, M. J. (2007). The J & P Transformer Book 13th edition. In: *Chennai: ELSEVIER*. p. 989.

[4] Kucera, M., Sebok, M. (2012). Electromagnetic compatibility analysis of electric equipments. In: *Przegląd elektrotechniczny = Electrical review*, vol. 88, No. 9a pp. 296-299.

[5] Koch, M., Krueger, M., Puetter, M. (2011). Advanced Insulation Diagnostic by Dielectric Spectroscopy. In: *Omicron Electronics Austria*.

[6] Koch, M., Tenbohlen, S., Krüger, M., Kraetge, A. (2007). A Comparative Test and Consequent Improvements on Dielectric Response Methods. In: *Proceedings of the XVth International Symposium on High Voltage Engineering*, ISH, Ljubljana, Slovenia.

[7] Koch, M. (2008). Reliable Moisture Determination in Power Transformers. In: *PhD thesis*, Institute of Energy Transmission and High Voltage Engineering, University of Stuttgart, Sierke Verlag Göttingen, Germany.

[8] Gutten, M., Korenciak D., Brncal P., Jarina R. (2020). Frequency diagnostics of insulating system of power transformers. In: *Electrical Control and Communication Engineering*, Vol 16, No. 1, pp. 1-7.

# High-Speed Digital Signal Integrator

[1,2,3]Oleg Chernoyarov, [4]Alexey Glushkov, [2]Kaung Myat San, [5]Vladimir Litvinenko, [5]Yuliya Litvinenko

[1]National Research Tomsk State University, Tomsk, Russia,
[2]National Research University “MPEI”, Moscow, Russia,
[3]Maikop State Technological University, Maikop, Russia,
[4]Voronezh Institute of the Ministry of Internal Affairs of the Russian Federation, Voronezh, Russia,
[5]Voronezh State Technical University, Voronezh, Russia,
Email: chernoyarovov@mpei.ru

***Abstract.*** *High-speed digital signal integrators operating over a specified time interval are introduced. They implement a moving (current) integration of the sampling of a specified size using the rectangle or the Simpson's rules requiring a minimum number of simple arithmetic operations for each subsequent sample of the received signal. The block diagrams and characteristics of integrators are considered, as well as the requirements to their parameters are studied and specified.*

*Keywords: Digital Integration, Rectangle Rule, Simpson's Rule, Fast Processing*

## 1. Introduction

The integration of a signal in the time domain is widely used in various devices and systems. Analog integrators are of little use while measuring the integral within a specified time interval [1]. Digital integrators can be designed using digital averaging filters [2]. Their disadvantage is the complexity of implementation in the case when a large signal sampling is to be processed. The method of direct digital integration [3] focuses on the accumulation of signal samples and allows the implementation of the computing units with continuous integration over a specified time interval. However, in this case, to ensure high accuracy, high computational and time costs are required. Below, the fast digital algorithm is introduced for the real-time processing of a large signal sampling.

## 2. Signal Integration

The input signal $s(t)$ is quantized by an analog-to-digital converter (ADC) with the frequency $f_s = 1/\tau$ forming a sampling of size *N*. Here τ is the time interval between the adjacent samples $s_i$ while *i* is a sequence number. At the current moment $t_i$ ($i > N$), according to the quadrangle formula (rectangle rule) [4], the value of the integral over the time interval from $t_i - N\tau$ to $t_i$ is equal to

$$g1_i = \int_{t_i - N\tau}^{t_i} s(t)\,\mathrm{d}t \approx \tau \sum_{j=0}^{N-1} s_{i-j} \ . \tag{1}$$

The absolute error *R* of this approximation is determined as $R \le (N\tau)^2 F / 2N$, where $F = \max_{t \in [t_i - N\tau, t_i]} \left| \mathrm{d}s(t)/\mathrm{d}t \right|$. A fast computational procedure (1) can be implemented by choosing $N = 2^n$, where *n* is an integer.

The same integral can be calculated using the parabola formula (Simpson's rule) [4] as follows:

$$g2_i = \int_{t_i-(N-1)\tau}^{t_i} s(t)\,\mathrm{d}t \approx \frac{\tau}{3}\left( s_i + 4\sum_{j=1}^{2^{m+1}} s_{i-2j+1} + 2\sum_{j=1}^{2^{m+1}-1} s_{i-2j} + s_{i-N+1} \right) = \\ = \frac{\tau}{3}\left( s_i + 4\sum_{j=1}^{2^{m+1}} s_{i-2j+1} + 2\sum_{j=1}^{2^{m+1}} s_{i-2j} - s_{i-N+1} \right), \tag{2}$$

while the calculation error does not exceed $R \le (N\tau)^5 A/180\left[2(N-1)\right]^4$, where $A = \max_{t\in[t_i - N\tau, t_i]} \left| \mathrm{d}^4 s(t)/\mathrm{d}t^4 \right|$, and the sample size is equal to $N = 2^{m+2} + 1 > 9$. In (2), $m$ is an integer and is calculated as $m = \log_2(N-1) - 2$.

For a specified integration interval $N\tau$, under increasing $N$, the error $R$, in accordance with Simpson's rule (2), decreases significantly faster than in the case when the rectangle rule (1) is applied. In this way, increasing integration accuracy is provided, but, at the same time, the number of computational operations also involved increases.

In the field of digital signal processing, the sums in (1) and (2) are averaging FIR filters. To ensure a small integration error $R$, it is necessary to use large sample sizes $N >> 100$. However, direct calculation of the sums (1) or (2) requires high costs. Thus, it is urgent to produce the fast computational averaging algorithms that would require the minimum number of addition operations. It would allow simplifying the software or hardware implementation of the integrator.

## 3. Fast Integrator Designed Based on the Rectangle Rule

To determine the integral (1) by the current sample from $N$ discrete signal samples $s_i$, the value $z_i$ is calculated as follows $z_i = \sum_{j=0}^{N-1} s_{i-j}$. Then, referring to (1), one gets

$$g1_i = \tau z_i . \tag{3}$$

The block diagram of the integrator designed in view of the rectangle rule is shown in Fig. 1.

The samples of the input signal $s_i$ are formed by ADC under the control of a clock generator (CG), and then they are fed to the first unit for the accumulation of samples $UAS_1$. This unit includes multibit one cell shifter $MR_1$ in which the previous sample $s_{i-1}$ has been previously saved and the summator $SUM_1$. To the inputs of the summator, $SUM_1$ the samples $s_i$ and $s_{i-1}$ are passed, while at its output sum $s_i + s_{i-1}$ is generated. After that, the next value $s_i$ is poked into $MR_1$. The sums of the pairs of samples are moved to $UAS_2$, in the multibit two cell shifter of which the sums $s_{i-1} + s_{i-2}$ and $s_{i-2} + s_{i-3}$ have been previously sequentially saved. The last value enters the input of the summator $SUM_2$, where it is added to the value $s_i + s_{i-1}$ forming the sum of the four samples $s_i + s_{i-1} + s_{i-2} + s_{i-3}$ at the $UAS_2$ output. Further, the data stored in $MR_2$ are shifted while the value $s_i + s_{i-1}$ is poked into its vacated first cell. Similarly, the sum of the eight samples is formed in $UAS_3$ that includes four cell shifter $MR_3$.

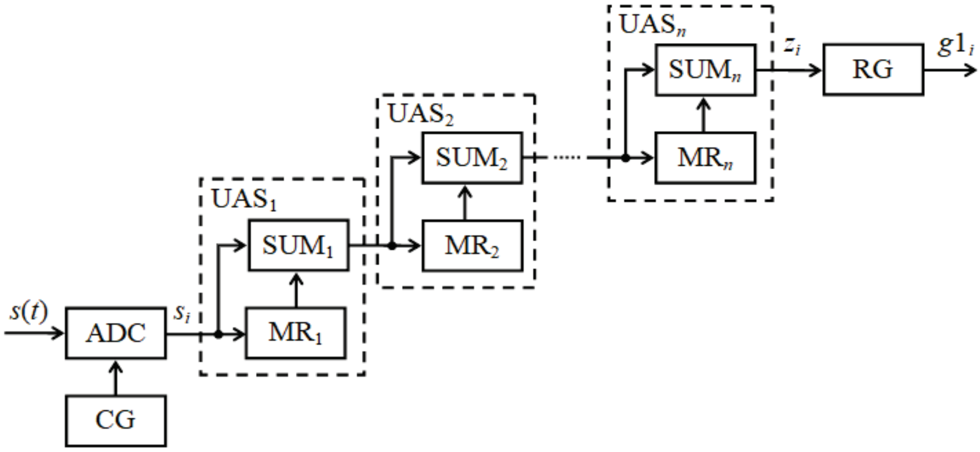


Fig. 1. The block diagram of the integrator designed based on the rectangle rule.

In the last UAS$_n$, the sum $\sum_{j=0}^{N/2-1} s_{i-j}$ and the value $\sum_{j=N/2}^{N-1} s_{i-j}$ from $N/2$ cell shifter MR$_n$ are fed to the first and second inputs of the summator SUM$_n$ and thus the value (3) is formed at its output. The obtained code enters the result generator RG and then arrives to the integrator output in a specified form.

Thus, to calculate the sum of $N$ signal samples, a minimum number of $n = \log_2 N$ summators and shifters of multidigit codes are required, and that can be conveniently implemented on the basis of $N$ cell main memory unit.

## 4. Fast Integrator Designed Based on the Simpson's Rule

The block diagram of the integrator designed based on Simpson's rule is shown in Fig. 2.

According to (2), it is necessary to calculate the two sums

$$z1_i = \sum_{j=1}^{2^{m+1}} s_{i-2j+1}, \qquad z2_i = \sum_{j=1}^{2^{m+1}} s_{i-2j} \tag{4}$$

then add them, and after that add the current received sample $s_i$ and subtract the last sample $s_{i-N+1}$ in the processed sampling. As a result, one gets $z_i = s_i + 4\sum_{j=1}^{2^{m+1}} s_{i-2j+1} + 2\sum_{j=1}^{2^{m+1}} s_{i-2j} - s_{i-N+1}$. Thus, the value of the desired integral is determined as

$$g2_i = \tau z_i / 3, \tag{5}$$

In order to generate the value (5), the signal samples $s_i$ from the ADC output are poked into the multibit shifter MR5, in which the last 5 received samples $s_1 = s_i$, $s_2 = s_{i-1}$, $s_3 = s_{i-2}$, $s_4 = s_{i-3}$ and $s_5 = s_{i-4}$ are stored. The pair of samples $s_2$ and $s_4$ is added in the summator SUM1 and then accumulated in $m$ cascade-connected UAS$_{11}$, UAS$_{12}$, ..., UAS$_{1m}$ in the same way as it is performed in the circuit shown in Fig. 1. As a result, the value $z1_i$ (4) is formed at the UAS$_{1m}$ output. Similarly, the pair of samples $s_1$ and $s_3$ is added in the summator SUM2 and then it is accumulated in UAS$_{21}$, UAS$_{22}$, ..., UAS$_{2m}$ forming the value $z2_i$ (4) at the output of the last unit.

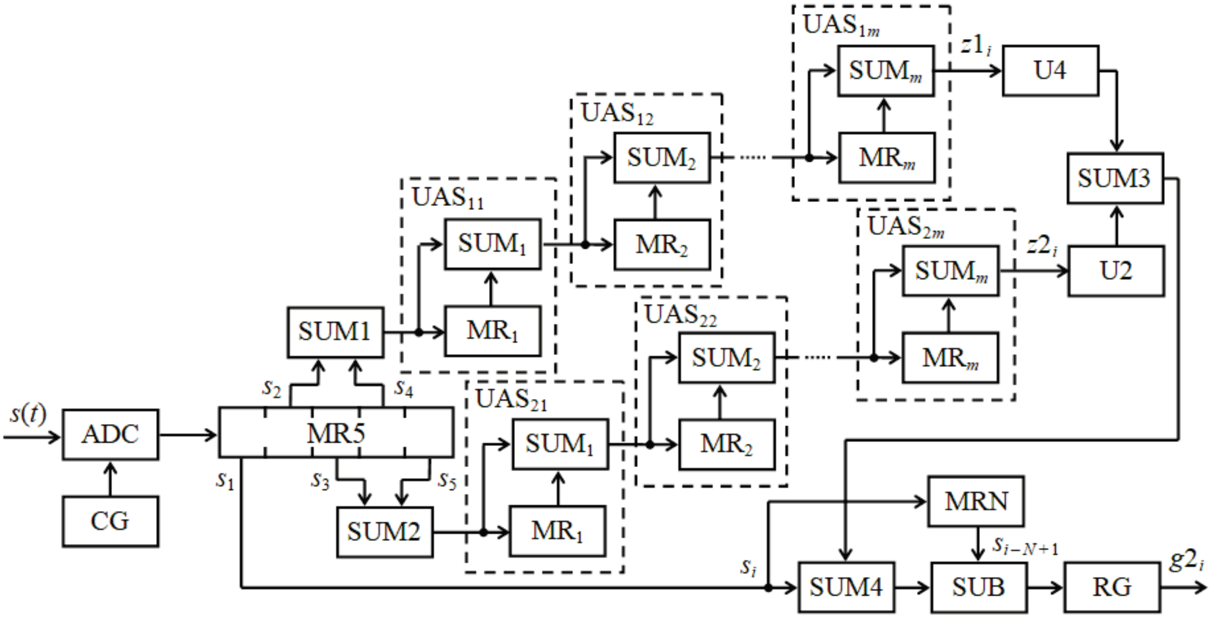


Fig. 2. The block diagram of the integrator designed based on the Simpson's rule.

The values $z1_i$ are multiplied by 4 in the unit U4 (by shifting the code by 2 bits), while the values $z2_i$ – by 2 in the unit U2 (by shifting the code by 1 bit), respectively. Then they are added in the summator SUM3 and thereafter the current sample $s_1 = s_i$ is added to this last obtained sum in the summator SUM4 while the last sample $s_{i-N+1}$ stored in multibit $N$ cell shifter MPN is removed in the subtractor SUB. The resulting code is passed to the result generator RG and appears at the output of the integrator.

## 5. Conclusion

Digital signal integrators designed based on the rectangle and Simpson's rules are considered. The characteristics of the introduced integrators are determined. The numerical integration error is estimated and the influence on it of the signal and integrator parameters is studied. It is shown that the integrator using Simpson's rule provides the error that is several orders of magnitude lower than the one based on the rectangular rule, but its structure is more complex.


### Acknowledgements

This study was financially supported by the Russian Science Foundation (research project No. 20-61-47043).


### References


[1] Peyton, A., Walsh, V. (1993). *Analog Electronics with Op-amps: A Source Book of Practical Circuits*. Cambridge University Press.

[2] Van de Vegte, J. (2001). *Fundamentals of Digital Signal Processing*. Pearson.

[3] Batrakov, A.M., Il'yin, I.V., Pavlenko, A.V. (2015). Precision digital signal integrators with accurate synchronization. *Optoelectronics, Instrumentation and Data Processing*, 51(1), 51-57.

[4] Burden, R.L., Faires, J.D. (2010). *Numerical Analysis*. Cengage Learning.

# *Measurement of Physical Quantities - Posters II*

# Advanced Hardware and Software for the Upgrade of Mirror/Prisma Monochromator SPM-2 *(Carl Zeiss Jena)* for the Measurements of Basic Spectroscopic Properties of Atoms in Near VUV, Far UV, UV Spectral Region

**Arman Bzhishkian, Arnolds Ubelis**

National Science Platform FOTONIKA-LV at the University of Latvia, Riga, Latvia
armans.bziskjans@lu.lv

***Abstract.*** *Today's digital electronics and fast computers allow the efficiently processing of large volumes of spectroscopic information, which means the opportunity to reuse and upgrade monochromator with sophisticated optical and mechanical systems being designed and used in the middle of the last century. Particular interest is towards high-resolution prism monochromator. We used such an approach to computerize manual operations of universal mirror monochromator SPM-2, which has changeable quartz, glass, NaCl and KBr crystal prisms. SPM-2 was produced by VEB Carl Zeiss JENA in the early sixties of the last century (in former GDR), and its advanced features were widely used [1]. The current interest is to use upgraded double pass SPM-2 (with quartz prisma) for atomic spectroscopy measurements in broad intensity range in near VUV, far UV, UV. Alongside standard measurements, cooled photomultipliers, photon counting mode can be used to ensure the fixing of very weak spectroscopic lines. We are using the instrument to investigate resonance spectra of atomic iodine, bromine, arsenic, selenium, tellurium, boron. Particularly duplet of atomic boron resonance lines 249.6769/249.7722 nm is easily resoluble. The approach has a high value for money because of the absence of handy monochromators for high-resolution atomic spectroscopy in the identified spectral region on the market.*

*Keywords:* Measurement of Atomic Spectra in Near VUV, Far UV, UV Spectral Region, Double Pass Mirror, Quarz Prisma Monochromator, Computerized SPM-2+

## 1. Introduction

The universal double-pass mirror monochromator SPM-2 [1] is exclusively distinguished by its high resolution in near VUV, far UV, UV spectral range between 190 nm – 300 nm when high-quality quartz prisma is used. Using weak nitrogen flow measurements could start from 180nm easily. Therefore, SPM-2 is still attractive for various spectroscopic measurements, but manual operation mode is currently a serious disadvantage.

## 2. Subject, Methods and Results

The following steps were made to get the computerized version of SPM-2 called SPM-2+ (see Fig. 1 below) :

- The wavelength knob of the monochromator is driven by a gear wheel connected to the step motor by the use of a ribbon belt. The Stepper motor is controlled by a microcontroller (MCU) which receives commands sent from the PC using USB. Stepper motor driver and rotary encoder eliminate micro-step skipping issues.
- Amplified and filtered PMT signal is converted into digital data with the help of fast and high-resolution ADC *(analog-digital converter)*. These data are read by ARM MCU and then sent to the PC using the USB port.

- Data visualization is done by software, which is designed especially for the SPM-2+ system. It represents a diagram with two axes. The horizontal axis is wavelength in angstroms or nanometers, and the vertical one is a relative unit of PMT signal amplitude.
- It is well known that the ratio of the quartz refractive index/wavelength is not linear. To ensure comfortable visualization of recorded spectra on the screen, specifically designed SPM-2+ software algorithm automatically transforms data into a linear scale.


Fig. 1. Upgraded monochromator SPM-2+ : 1-PMT chamber (1a – adjusting mechanism of optimization of the positioning of PMT against the slit, 1b – cooling jacket for PMT), 2- stepper motor power supply,

Fig. 2. 3-stepper motor driver, 4-stepper motor, 5- SPM-2+ gear wheel, 6 - gear wheel belt, 7 - SPM-2, 8 –PC cable.

## 3. Discussion

We are using the instrument to investigate resonance spectra of atomic iodine, bromine, arsenic, selenium, tellurium and boron. Particularly duplet of atomic boron resonance lines 249.678/249.678 nm is easily resoluble. The approach has a high value for money because of the absence of handy monochromators for high-resolution atomic spectroscopy in the identified spectral region on the market.

Need to be mentioned that SPM-2 was developed as a universal spectrometer. Having a changeable set of quartz, glass, NaCl and KBr crystal prisms, the measurements spectral range caver the range from 20µm till 180 nm. Using the described approach, the SPM-2+ monochromator could be upgraded and used for a variety of purposes.

### Acknowledgements

This work was supported by ERDF project No. 1.1.1.5/19/A/003.

### References

[1] Schiek, O., Winter, E. (1965). Two New Mirror Monochromators, Applied Optics 4(2), 195-199.

# Test Equipment for Measurement of Current Waveforms of Fuel Systems in Petrol Vehicles

**Matej Kubis, Miroslav Gutten, Daniel Korenciak**

Faculty of Electrical Engineering and Information Technology,
University of Žilina, Univerzitná 1, 010 26 Žilina, Slovakia
Email: miroslav.gutten@feit.uniza.sk

***Abstract.*** *The article is focused on measuring the current flowing through the injector with subsequent detection of faults in the fuel system. The claims are based on measurements and residue generation (differences between reference and fault current). Faults of movement of the injector needle valve and fuel pressure changes were simulated.*

*Keywords: Injector, Fuel System, Measurement, Diagnostics*

## 1. Introduction

The fuel system of a petrol car consists mainly of a fuel tank, fuel pump, piping, fuel filter, fuel injectors, and a fuel pressure regulator. The most important element of the fuel system is the fuel injector. Thanks to the monitoring of its operation, it is possible to verify the functionality of the fuel pump, filter, fuel line, fuel tank, and injector itself [1-2].

The reduced fuel pressure supplied to the injectors and, ultimately, the reduced volume supply of fuel is most often caused by the clogged fuel filter, damage to the fuel pump and pressure regulator. Such a failure results in a reduction in the car's power and, in worse cases, inactivity of the engine [2-3].

## 2. Test Equipment

To test the operation of the injection system and monitor the required signals, a device was designed that allows the control of the injection valves of the petrol engine. Fig. 1 shows the electrical arrangement of the device.

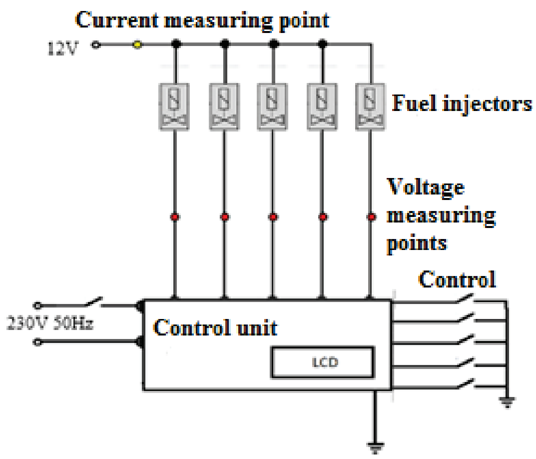


Fig. 1. Wiring diagram of the injection system in the test equipment

Control electronics replace the engine control unit in a simplified form. It is a programmed 8-bit microprocessor DC9S08QE. Using the buttons, it is possible to activate the generator and change the time intervals during which energy is accumulated on the primary side of the ignition coils. The generator also contains an LCD display with information about the set mode of signal generation.

The signal generator allows generating a time ton in the range from 0 to 9 ms and a time $t_{off}$ in the interval 10 to 500 ms in steps of 1 ms. Generation is performed for five channels. The display unit shows the mentioned times, the activation status of the generator, and the estimated speed of the four-stroke engine. The generator produces 5-volt voltage levels. The output contains optocouplers supplemented by power transistors. It can be seen from the diagram that the injectors are connected in the collector side of the transistors.

Pressure vessel allows creating a fluid pressure (replaces the fuel pump) in the range from 0 to 300 kPa, which corresponds to the fuel pressure in the car. The liquid is led to a common pipe from the pressure vessel to which all injectors are connected.

Vessels for measuring the flow of injectors are located under the individual injectors. They make it possible to determine the differences in the amount of fuel injected by the individual injectors and the flow rate of the injectors.

## 3. Measurement and Simulation of Injection System Failures

Fig. 2 shows the current and voltage of the fuel injector for a set interval of 4 ms. From the monitoring of the measured time courses, it is possible to observe the influence of the movement of the injector needle valve on the change of inductance, which ultimately also affects the change of the measured time characteristics. At approximately 1.2 ms after opening the respective transistor, the injector is fully open (interval B).

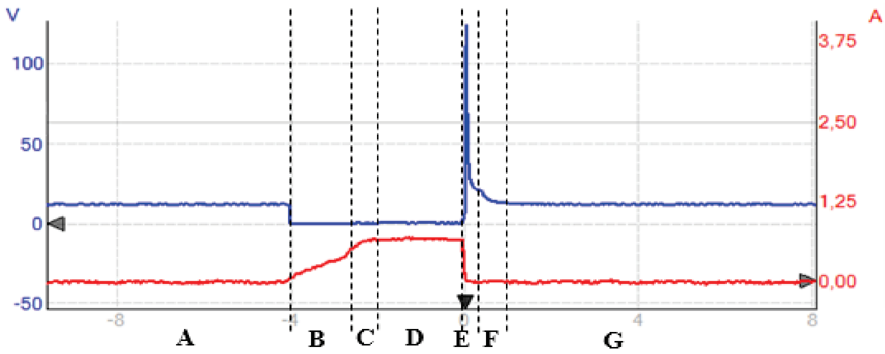


Fig. 2. Fuel injector current and voltage profile

After the fuel injection time (interval C and D), after closing the semiconductor switching element, there is an overvoltage caused by the inductance of the injector, it is also the interval of moving the needle valve to the original position. During time E, it is possible to observe the decay of the overvoltage.

Fig. 3a is an idealized time interval of the current during the operation of the injector with the sampling times shown, which would be performed in the mode of evaluating the state of the injection system. By monitoring the time $t_x$, we can evaluate the duration of the opening time of the injector. This time is influenced by the pressure ratios of the injected fuel and the design of the injector. By evaluating these times, we can determine fuel pressure failures, damage to the injector return spring, stopping or slowing down the movement of the needle valve. If we perform measurements at times $t_{m1}$ and $t_{m2}$, we get the maximum current. A change in the maximum current can be caused, by a change in the series resistance of the winding caused, for example, by a short circuit.

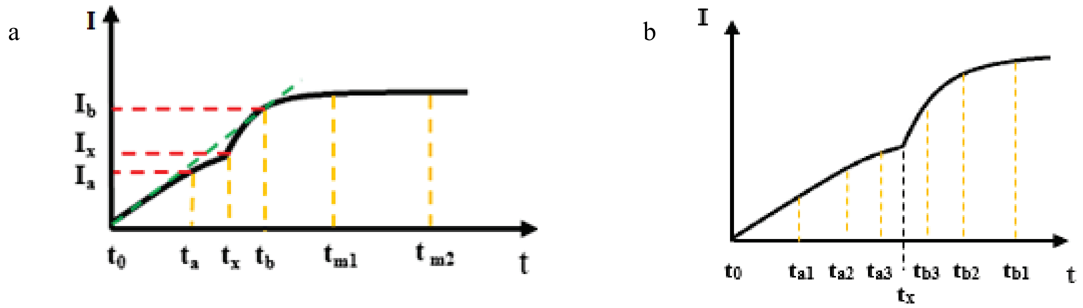


Fig. 3. (a) Ideal injector flow shape; (b) Signal sampling during injector needle valve movement

A linear green dashed line can be used to simplify the input parameters for possible simulation and further analysis. This linearization is performed between time points $t_a$ and $t_b$. Time point $t_x$ is in the middle of these points.

How to make as few samples of the tested signal as possible and with the possibility of obtaining as much information as possible is a significant problem for every measurement. Based on the experiments, it is possible to determine the point $t_x$. During the acquisition of $t_x$, it is necessary to maintain the required fuel pressure of 250-300 kPa and at a voltage of 13.5 to 14.4 V.

Fig. 3b shows the time course of the flow during the movement of the needle valve of the injector with logarithmic measurement in seven-time intervals. Such a measurement is most advantageous for detecting a change in time $t_x$. Monitoring the voltage characteristic can also provide a lot of information about the state of the injector and the fuel system. However, an overvoltage interval of more than one hundred volts is problematic in evaluating the injector needle valve seating. When the fuel pressure changes, there is no significant change in the voltage profile.

The characteristic in Fig. 4a shows the measured current and fault current profile. The reference time course is composed of five measurements at a fluid pressure of 2.5 bar. Oscilloscope sampling was set to 100 kS/s (time between samples is 10 µs). The injection time was set by the control circuit to 5 ms. Another current on the characteristic is a fault when the needle valve is stopped in the open position.

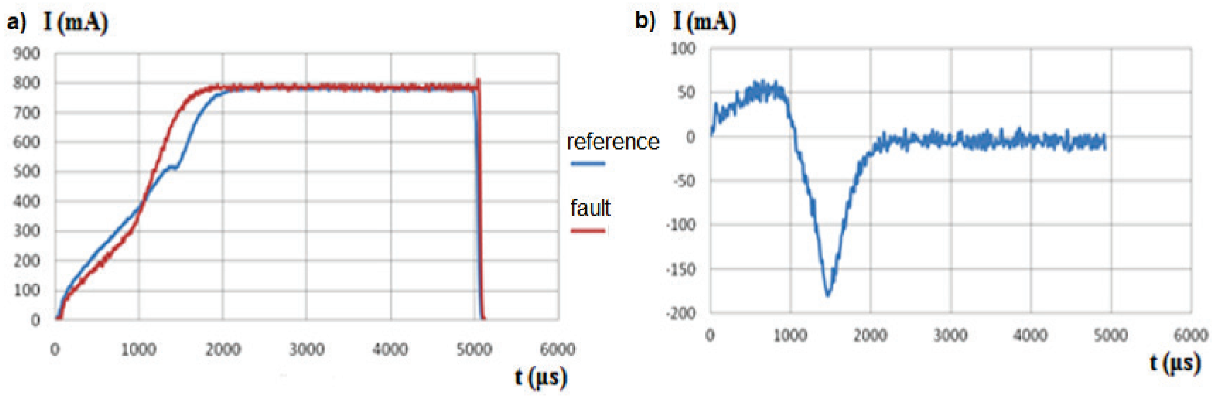


Fig. 4. (a) Injector reference current and needle valve stop current in the open position; (b) Deviation from the reference current when the needle valve is stopped in the open position

The difference between the reference and fault current is shown in Fig. 4b. See two extremes on the characteristic. One is at 650 µs (64 mA), and the other is at 1460 µs (-180 mA). Reducing the fluid pressure also shortens the time required to open the injector. The measurement in Fig. 5a also confirms this statement.

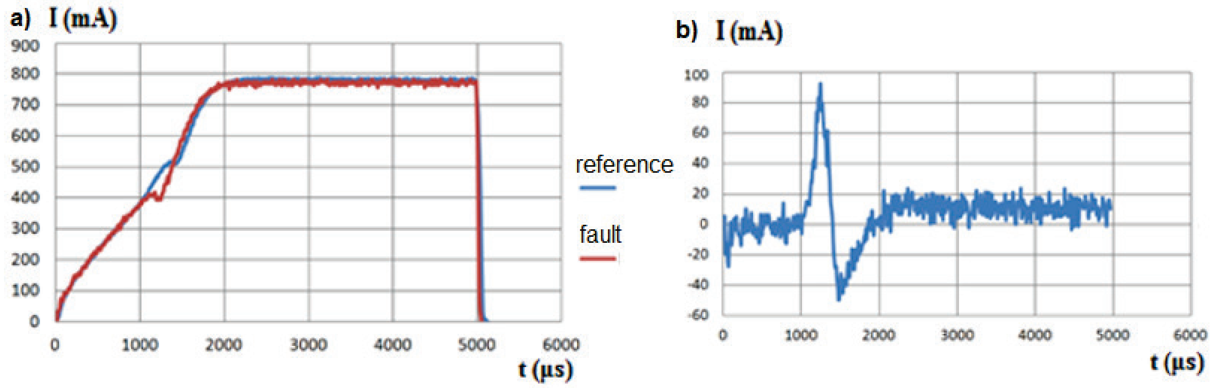


Fig. 5. (a) Injector reference flow and zero fluid pressure flow; (b) Deviation from reference flow at zero fluid pressure

Based on the different processing according to Fig. 5b, it is possible to obtain a deviation in the form of two extremes at time 1250 μs (92.5 mA) and at time 1480 μs (-50 mA).

## 4. Conclusion

The measurements elucidated the phenomena and effects that affect the duration of the opening of the injectors. By reducing the fluid pressure, the time required to open the injector was also reduced.

A new design of the test device will be used for test and analysis of individual components of the injection systems and monitoring their functionality. On the device, we can simulate various errors in the fuel system and analyze them for further development. In addition, we will create a database of fault conditions that can be compared with current waveforms measured directly in the car.

## Acknowledgements

This work was supported by the Grant Agency VEGA from the Ministry of Education of the Slovak Republic under contract 1/0471/20.

## References

[1] Kucera, M., Sebok, M. (2012). Electromagnetic compatibility analysis of electric equipments. In: *Przegląd elektrotechniczny*, 88 (9a), 296-299.

[2] Svard, C., Nyberg, M. (2010). Residual Generators for Fault Diagnosis using Computation Sequences with Mixed Causality Applied to Automotive Systems. Systems, Man and Cybernetics, Part A: Systems and Humans. In: *IEEE Transactions on*, 40, (6), 1310 - 1328.

[3] Kerkhoff, H. G, Wan, J., Zhao, Y. (2012). Hierarchical Modeling of Automotive Sensor Front-Ends for Structural Diagnosis of Aging Faults (2012). In: *18th International Conference of the Mixed-Signals, Sensors and Systems Test Workshop (IMS3TW)*, , 91-96.

[4] Chen, L., Zhang, Z. (2011). Study on the measurement of dynamic characteristics for automotive electronic fuel injector. In: *International Conference of the Transportation, Mechanical, and Electrical Engineering (TMEE),* 511 - 514.

# Measuring and Diagnostic System of Distribution Transformers

**Peter Brncal, Miroslav Gutten, Daniel Korenciak**

Faculty of Electrical Engineering and Information Technology,
University of Žilina, Univerzitná 1, 010 26 Žilina, Slovakia
Email: miroslav.gutten@feit.uniza.sk

***Abstract.*** *This article focuses on the analysis of the mechanical and insulating state of repaired distribution transformers through the diagnostic system of transformers (DST). Transformer manufacturers use the system at the quality check of their products, repair companies for repairing adventurousness evaluation and further for transformer new parameters measurement after the repair. Suppose DST is included in the entrance firm control. In that case, it is possible by means of it to verify the parameters given in the transcript of the new transformer measurement supplied by its manufacturer. The last part of the article describes how it is possible to increase the reliability of short-circuit voltage measurement thanks to a highly accurate automated diagnostic measuring system DST.*

*Keywords: Transformer, Diagnostics, Diagnostic system, Measuring methods*

## 1. Introduction

Maintenance diagnostics of transformers considering to the influence of short-circuit currents during the operation should be carried out to increase the reliability in a real trouble-free process.

In the event of an accidental outage caused by a faulty device, the economic and technical damage can be very extensive. Currently, there are several online and offline diagnostic and monitoring methods with which we can measure and detect possible malfunctions arising on the transformers or rotating machines during their operation. In this case, the high ability of the methods used, the time consuming of the measurements, the difficulty of identifying and detecting the type of failure, and last but not least, the expertise and practical experience of the technicians [1].

For example, short-circuits in operation are commonly created by different line faults, mechanical damage of insulation, electric insulation, electric insulation breakdown on over-voltage, faulty operation, and the next case row. [2]

## 2. Diagnostic System of Transformer in Laboratory Test Room

The measuring system of the transformer (DST) developed at the University of Zilina, in cooperation with the firm Lambda Control Ltd. Liptovsky Hradok and with the delivery of apparatuses from EN-CENTRUM Ltd. Praha, is certain for transformer manufacturers and for organizations working at transformers maintenance. Transformer manufacturers use the system at the quality check of their products, repair companies for repairing advantageous evaluation, and further transform transformer new parameters measurement after the repair. Suppose DST is included in the entrance firm control. In that case, it is possible by means of it to verify the parameters given in the transcript of the new transformer measurement supplied by its manufacturer.

The measuring system of transformer DST can be used for complex measuring different types and dimensions of transformers [3]:

a) for resistances and insulating tests (insulation resistance, winding resistance with time analysis of voltage, induced voltage test, separate-source test),
b) for AC analysis (no-load, voltage ratio, short-circuit measurement with analysis of short-circuit voltage, SFRA method).

## 3. Automated Measurement of Short-Circuit Test

As an example of increasing the reliability of the analysis and the accuracy of the mechanical state of the transformer winding using the DST system, the article describes the short-circuit measurement and its use in determining the relative short-circuit voltage.

Using short-circuit measurement, it is possible to analyze and identify losses in the winding and the so-called relative voltage (impedance) of the short-term transformer. The power supply is connected to the distribution transformers to the primary winding (on the higher voltage side) at a frequency of 50 Hz, while the secondary winding (lower voltage side) is short-circuited. According to the IEC standard, it is permitted to measure from 100 to 50% of the rated value of the nominal primary current of the distribution transformer.

By means of the DST - the diagnostic and measuring system, the transformer powered of 70 kVA-oil autotransformer 40 0V and 50 kVA-dry ratio transformer 0.4/1 kV were measured. By the system DST the measuring current is reduced to 54 % of the current rating of the primary winding of the distribution transformer and subsequently converted to 100 % of the rating.

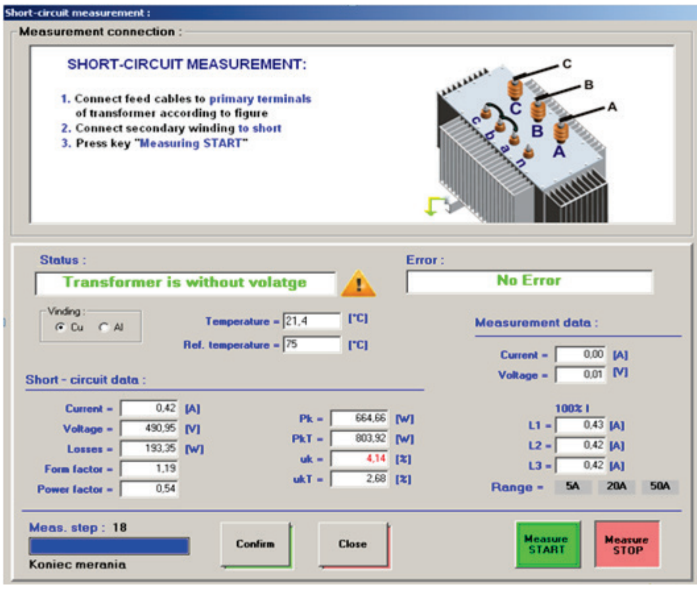


Fig. 1. Measurement opening window for measurement of short-circuit.

Fig. 1 shows the software opening window for the measurement of short-circuiting. In every dialog window of measurement there are control buttons for the starting and stopping of measurement (Measure START, Measure STOP), buttons for closing dialog window of measurement (Confirm, Close), the scheme of connection of individual measuring cables (Measurement connection) and text boxes of measured data in which after ending of measurement will be displayed measured values and measuring results.

By selecting boxes situated in the measurement window, it is possible to choose desired measuring parameter. By clicking on the selection box, this box will be marked by choosing of parameter which has to be measured.

In every box, there is the Measurement button which starts the measurement dialog window. After measuring, the measured values are transferred to the measurement box.

The state of change of the relative voltage (impedance) for a short time uk is usually an actual image of the geometric displacement of the windings and their construction in the transformer (with the change of its impedance parameters). This state can vary depending on the thermal and mechanical effects of short-circuit currents. Such a short-circuit voltage reduction can provide information not only about the deterioration of the electrical properties of the winding (change of scattering reactance), but also about the decrease in mechanical strength and quality of winding insulation due to thermal effects of short-circuit currents.

Due to the severity of the determination of the short-circuit relative voltage and its difference from the transformer label data, it is necessary to define the influences on the measurement and its accuracy. In addition, the gear ratios of the current transformers pi and the voltage pu must be taken into account.

The determined accuracy of the short-circuit voltage reduction result in the above measurement is important for accurate measuring instruments and instrument transformers. It is, therefore, necessary to precisely determine the conditions under which it is possible to reliably and accurately diagnose the windings of transformers concerning the effects of short-circuit currents and thus eliminate the adverse effects on the measurement.

When determining the short-circuit voltage, it is necessary to use an accurate ammeter and voltmeter with a final accuracy of up to 0.2 %. In the case of short-circuit measurements on transformers in the OTC, s.r.o. The LEM D4000 digital power analyzer (Fig. 2) was used in Hlohovec within the complex diagnostic system of DST transformers. A newer model, the Fluke Norma 4000 Power Analyzer, is currently used in other DST measurement systems.

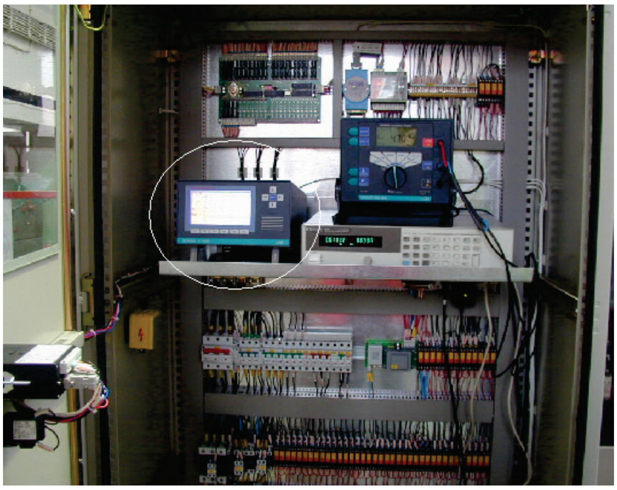

Fig. 2. LEM D4000 power analyzer as part of the DST system.

## 4. Experimental analysis

As an example of measurement in practice for analyzing the effects of short-circuit currents using short-circuit relative voltage, the following measurement is given on 22 randomly used 22 / 0.4 kV transformers in operation in the high-voltage laboratory test room. The power of the measured distribution transformers ranged from 30 to 1,000 kVA. The percentage short-circuit voltage was determined by short-circuit measurement using the DST transformer diagnostic system.

As the windings were not replaced before the test, the measurement results were a partial picture of the short-circuit stresses of the transformers during operation. From the resulting graph of random transformers, according to Fig. 3, is the average measured short-term voltage difference of 2.56 % compared to the label reading.

According to Fig. 3, transformer No. 22 (30 kVA) had this difference up to 9.27 %. Such a high difference may indicate a relatively large geometric displacement of the winding, which was subsequently visually shown to deform the side of the transformer vessel.

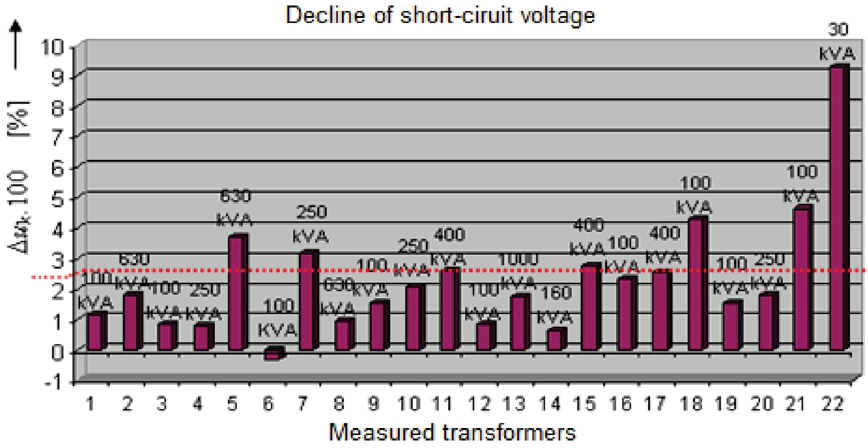


Fig. 3. Graphical representation of short-circuit voltage decline in transformers in operation.

## 5. Conclusion

During the development of the measuring and diagnostic system, knowledge from diagnostics, measuring technology, high-voltage technology, information technology, automation and safety of equipment and personal protection was used. In addition, all requirements from the customer and the operator of the high-voltage test room were included in the system.

Thanks to the diagnostic and measuring system, it is possible to increase the reliability of diagnostics and analyze repaired and subsequently tested distribution transformers.

To analyze the mechanical state of the transformer windings, we have increased the reliability of short-circuit voltage measurement thanks to a highly accurate automated diagnostic measuring system.

### Acknowledgements

This work was supported by the Grant Agency VEGA from the Ministry of Education of the Slovak Republic under contract 1/0471/20.

### References

[1] Petráš, J., Kurimský, J., Balogh, J. Cimbala, R., Džmura, J., Dolník, B., Kolcunová, I. (2016). Thermally stimulated acoustic energy shift in transformer oil. In: *Acta Acoustica United with Acoustica*, 102 (1), 16-22.

[2] Brandt. M. (2016). Identification failure of 3 MVA furnace transformer, In: *Proceedings of international conference Diagnostic of electrical machines and insulating systems in electrical engineering*, Papradno, SR.

[3] Gutten, M., Korenčiak, D., Zahoranský, R. (2012). Measuring system of transformers for Palestine, In: *Proceedings of the 29th international conference 2018 Cybernetics & Informatics,* Lazy pod Makytou, SR.

# Evaluation of Distance Sensor for Length Measurement Device

**[1]Tatiana Kelemenová, [1]Miroslav Dovica, [1]Tomaš Stejskal, [1]Teodor Tóth, [1]Ivana Koláriková, [2]Ondrej Benedik**

[1]Technical University of Kosice, Faculty of Mechanical Engineering, Kosice, Slovakia
[2]Kybernetes, Košice, Slovakia
Email: miroslav.dovica@tuke.sk

***Abstract.*** *The main goal is to assess the metrological characteristics of the distance sensor, whether it is suitable for the modernization of the Length Metroscope. The sensor is tested in the application stand using a set of length gauge blocks. The result is the determination of the maximum permissible error of the sensor with the evaluation unit.*

*Keywords: Length Measurement, Uncertainty, Measurement Error, Sensor, Gauge*

## 1. Introduction

Measurement of length dimensions is the most frequently performed measurement in mechanical engineering. The measurement is used to assess the quality of the result of the production process or to evaluate the production process continuously. Any deviations from the required dimensions are then reflected in the intervention in the production process. For example, a continuous inspection of the dimensions of the part being manufactured may indicate a worn tool on the machine tool or another failure of the machine tool. The primary goal is to ensure trouble-free production of components in the required quality. Measurement plays a dominant role in this process and thus has a major impact on product quality. However, an improperly selected or incorrect meter can damage this entire production process. The Length Metroscope covered in this article is an older instrument with reliable and stable operation, but its operation is lengthy. To speed up the measurement process, the aim is therefore to apply a suitable sensor with an evaluation unit. Increasing the measuring process's productivity will reduce the price of the measuring process and thus the final price of the product produced [1].

## 2. Length Metroscope

Abbe Length Metroscope (Fig. 1) is a measurement device for measuring length dimensions. The device includes a measuring table for placing the measured object. The device consists of a stand with a measuring table and a movable measuring touch (Fig. 1). The movable measuring stylus is connected to an abbe measuring microscope on which the position of this measuring stylus can be read. The measured dimension of the object is determined by the distance of the defining surfaces of the measured object. The zero position of the measuring contact is when it is placed on the measuring table. The measuring contact is pressed against the measured object using an additional weight, which ensures a constant measuring pressure.

The measured object is placed on one of the measured surfaces on the measuring table (Fig. 1), and a movable measuring touch is placed on the other surface of the measured dimension. The Abbe measuring microscope (Fig. 1) is part of the Abbe length metroscope and is used to determine the indication of the measured dimension. The Abbe measuring microscope makes it possible to determine the measured dimension with a resolution of one tenth of a micrometer. The manufacturer of this measuring device identified systematic errors in the evaluation that are less than one micrometer in absolute value. The manufacturer has determined the maximum permissible error (which includes systematic and random errors) and defined it by the relation:

$$MPE = \pm\left(1.5 + \frac{L}{100}\right), \tag{1}$$

where $MPE$ - maximum permissible error (μm), $L$ - measured dimension (mm).

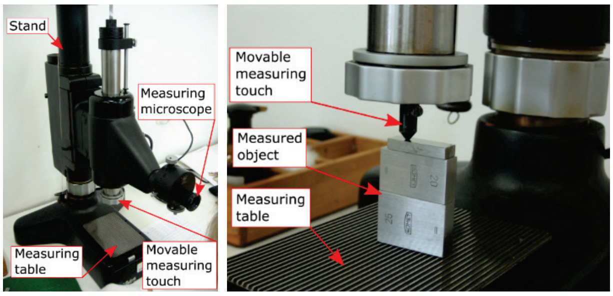


Fig. 1. Abbe Length Metroscope – overall arrangement and measurement of the gauge block.

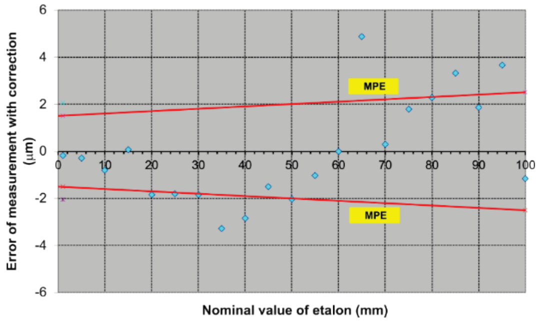


Fig. 2. Verification of Abbe Length Metroscope – measurement error obtained using the gauge blocks.

Verification of the Abbe Length Metroscope was performed using a set of length gauge blocks without calibrated coefficient of thermal expansion (CTE) of grade “0” in a thermally controlled room. Measurement errors (Fig. 2) were found to be outside the maximum permissible errors declared by the manufacturer. This means that the device is not suitable for further use for measuring dimensions. This problem can be solved by implementing a suitable sensor for measuring the position of the movable contact.

## 3. Experimental Verification of sensor for Measuring of the Movable Contact

Three pieces of optical linear encoder length sensor were selected to verify the suitability for installation on a Length Metroscope. Sensors have a range of 100 mm, resolution 0.1 μm, low measuring force less than 10N and low maximum permissible error MPE = (2+L/100). These sensors are connected to the display unit. The measured values from the sensors were compared with the standard - length gauge blocks (Fig. 3). The detected deviations from the set of measurements for sensor 2 are approximated by the mean value. From the course of the determined deviations, it can be found that the measured values are shifted in one direction, and thus it can be assumed that a systematic measurement error is included in this deviation. This systematic error can be used to correct the measured values from the sensor and thus reduce the deviations in further measurements using this sensor. This correction can be realized because the average values of the measurement errors keep the tendency approximately at the same level with respect to the reference value of the standard. After this correction (Fig. 4) only random errors remained (this is due to the very physical principle of the sensor and the random scale division errors that accumulate with increasing distance), which can be compared with the manufacturer given by the interval for the maximum permissible measurement error, where it can be seen that the sensor shows deviations within the limit interval defined by the manufacturer. The systematic errors of the standard - length gauge blocks are two decimal places smaller than the detected deviations, so we do not have to consider them for further evaluation. All measurements were performed in a thermally controlled room with a temperature stabilized sensor and length gauges. The room temperature was (20 ±1) °C, and the thermal expansion coefficient was also considered when evaluating the measured data.

Standard deviations $s$ were determined from a series of measurements $L_j$ performed under the same conditions. Standard deviations are relevant because they have been compared for different numbers of measurements, including the arithmetic average. The aim was to determine the optimal number of measurements under the same conditions. Fig. 5 shows the estimated standard deviations with a gradual increase in the number of measurements performed:

$$s^2 = \frac{\sum_{j=1}^{n}\left(L_j - \bar{L}\right)^2}{n(n-1)} \tag{2}$$

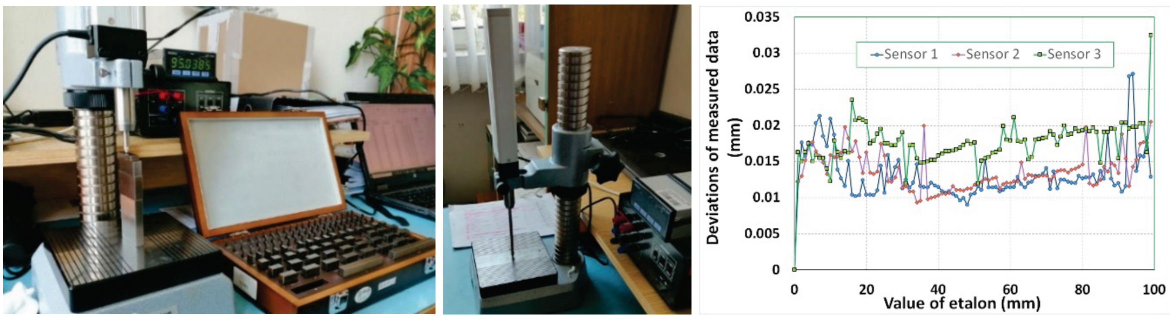


Fig. 3. Verification of selected length sensor using the gauge blocks and measured deviations.

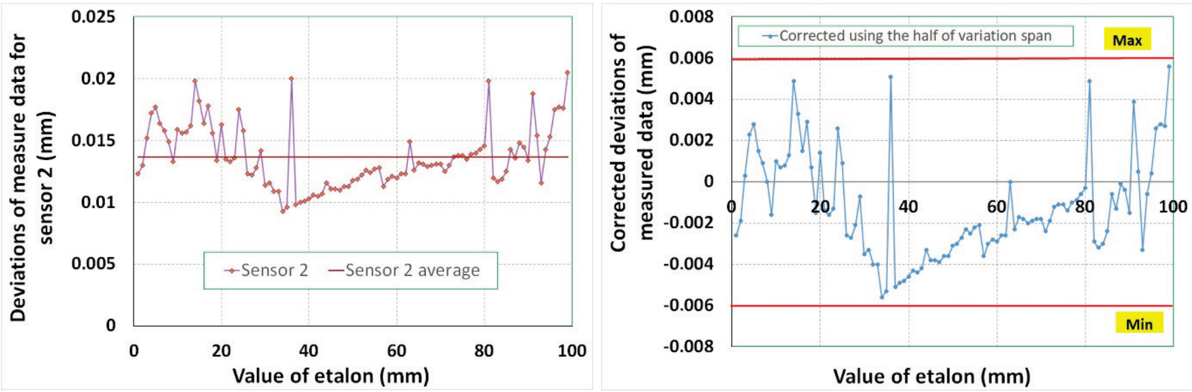


Fig. 4. Verification of selected length sensor using the gauge blocks.

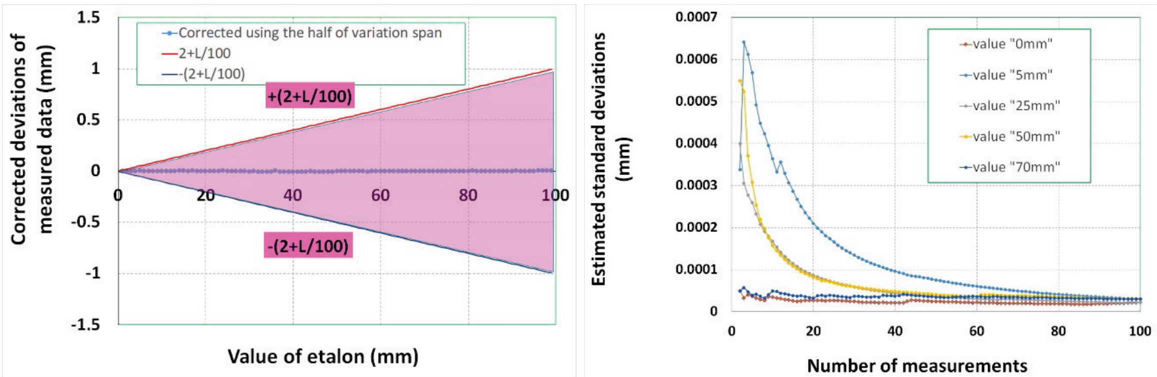


Fig. 5. Comparison of measurement deviations with limits defined by producer - permissible measurement error and dependence of the estimated standard deviation on number of measurements.

Although the variance $s^2$ is the more fundamental quantity, the standard deviation $s$ is more convenient in practice because it has the same dimension as quantity $L_j$ and a more easily comprehended value than that of the variance. From these measurements, it is possible to determine the standard uncertainty of the corrected length measurement indication using the tested sensor $u_s = s$ of the performed measurements depending on the number of measurements [2, 3, 4].

The obtained average deviations determined by measurement on the standard can be used as systematic errors and with the help of them to correct the measured values. However, deviations are known only for specific values. The average deviations can be approximated by a polynomial function and used for any measured data in the sensor range.

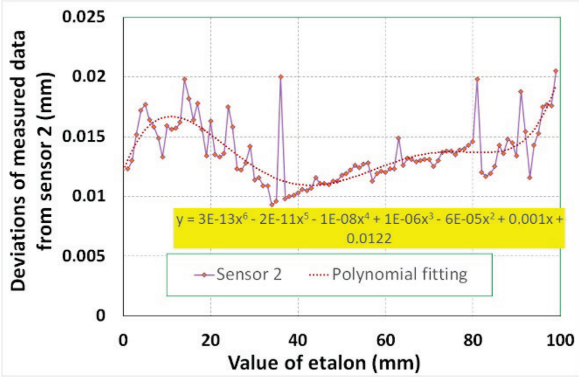


Fig. 6. Polynomial fitting of measurement deviations.

## 4. Conclusions

By correcting the measured data using the detected average deviations, measurement errors can be reduced partly. However, random errors cannot be completely eliminated and are thus included in the measurement uncertainty. The dependence of the estimated standard deviation (Fig. 5) shows that the standard uncertainty decreases significantly with repeated measurements. Even with ten measurements, the standard uncertainty is 50% lower, and with twenty measurements, the standard measurement uncertainty decreases by 60%. The aim was to determine the optimal number of measurements with respect to the resulting measurement uncertainty. This means how many measurements it still makes sense to reduce measurement uncertainty so that many measurements are not performed unnecessarily.

### Acknowledgements

The work has been accomplished under the research project VEGA 1/0168/21, 016TUKE-4/2021 financed by the Slovak Ministry of Education. This paper was published in cooperation with company KYBERNETES s.r.o. within the project “Research and development of the ECOGI product at KYBERNETES”, ITMS Code of Project: 313012Q955.

### References

[1] Chudý, V., Palenčár, R., Kureková, E., Halaj, M. (1999). *Measurement of technical quantities* (in Slovak). Edition of STU, 1st. ed., 1999. ISBN 80-227-1275-2.

[2] EA-4/02 M:2013 *Evaluation of the Uncertainty of Measurement In Calibration*. Publication Reference. European Accreditation Laboratory Committee. September 2013 rev 01. cited August, 8th, 2019. Available online: https://european-accreditation.org/wp-content/uploads/2018/10/ea-4-02-m-rev01-september-2013.pdf. EA-4/02 is a mandatory document belongs to Category: Application documents and Technical Advisory documents for Conformity Assessment Bodies.

[3] JCGM 100 – *Evaluation of measurement data – Guide to the expression of uncertainty in measurement* (ISO/IEC Guide 98-3). First edition September 2008. Available online: http://www.iso.org/sites/JCGM/GUM-JCGM100.htm.

[4] Wimmer, G., Palenčár, R., Witkovský, V. *Stochastic models of measurement*. (In Slovak) Graphic Studio Ing. Peter Juriga, Ľ. Fullu 13, 841 05 Bratislava. 1st. ed., 2001. ISBN 80-968449-2-X.

# Modeling the Process of Testing the State of Thermocouple Legs During Operation

**[1,2,3]Orest Kochan, [4]Jiwei Hu, [1]Jun Su, [5]Krzysztof Przystupa, [1]Mykola Beshley, [1]Ivan Demydov, [1,6]Mariana Levkiv, [2]Ihor Likhnovskyi, [2]Pavlo Hamula**

[1]School of Computer Science, Hubei University of Technology, Wuhan, China
[2]Lviv Polytechnic National University, Lviv, Ukraine
[3]Institute of Thermoelectricity of the NAS and MES of Ukraine, Chernivtsi, Ukraine
[4] Fiberhome Telecommunication Technologies Co.,Ltd, Wuhan, China
[5]Lublin University of Technology, Lublin, Poland
[6]I. Horbachevsky Ternopil National Medical University, Ternopil, Ukraine
Email: orestvk@gmail.com

***Abstract.*** *The method of testing virtual sections of inhomogeneous thermocouple legs by changing the temperature field along the legs is considered in this paper. The modeling showed that the error of determination of Seebeck coefficients of the virtual sections strongly depends on the errors of the temperature measurements on the endpoints of virtual sections.*

*Keywords: Thermocouple, Selftesting, Thermocouple with Controlled Temperature Field*

## 1. Introduction

The thermocouple (TC) is a popular sensor for measuring temperatures within the range of 600-1100°C [1]. Its advantages are: a wide measuring range, simplicity, and mechanical robustness. The TC disadvantages are low accuracy and metrological reliability due to the degradation of its legs at high temperatures [2]. The degradation manifests itself as: (i) error due to the gradual change of the TC conversion characteristics (CC) (drift) [2]; (ii) error due to thermoelectric inhomogeneity of TC legs acquired during operation, i.e. the change of TC thermoelectromotive force (thermo-e.m.f.) when changing the temperature field along its legs [2]. The method for correcting the instantaneous error during the operation was developed in [3, 4]. Its use increases the accuracy of inhomogeneous TCs. However, the period when the residual error of the TC is small grows. That is, the need for replacing the TC does not arise, however, degradation processes continue running. Thus there is a danger of sudden destruction of TC legs. Therefore it is necessary to test TC legs periodically.

## 2. State of the Art

The general criterion of the state of TC legs is the error. However, it does not always adequately describe the state of the sections of TC legs. Error due to degradation of the most common type K TC is not proportional to the operation temperature [1, 2]. At the same time, specific impurities can speed up the degradation of some sections of the legs at certain temperatures. Therefore, in general, the error of the TC weakly characterizes the state of its legs. The study of the TC error in different temperature fields [4] and the construction of the model of error of TC sections facilitate the analysis of the state of the TC legs. However, the method [5] is complex due to the need for periodic laboratory studies of the TC in different temperature fields. A more convenient and less time-consuming method of testing the state of TC legs during operation without its dismantling was proposed in [6]. The goal of this work is to model the process of testing the state of TC legs by this method.

## 3. Method of Thermocouple Selftesting.

The idea of the method of testing TC legs proposed in [6, 7] lies in the gradual shift of the zone of temperature gradient along the legs towards the reference junction of the main TC of the thermocouple with a controlled temperature field (TCTF) [8, 9]. The developed thermo-e.m.f. in each temperature field is measured and processed. The procedure of testing has to be carried out when the temperatures of the measuring and reference junctions are constant.

The method [8, 9] is illustrated in Fig. 1. The temperature field of the tested TC gradually changes from ABCD to AB2C2D. Intermediate temperature fields are indicated by dashed lines. In each temperature field, each virtual section of the TC legs (in Fig. 1, they are denoted as 1, 2 - k) makes its contribution to error due to drift of TC CC $\Delta E_1^{DR} ... \Delta E_{k+1}^{DR}$. When changing the temperature field of sections 1, 2 - adjacent to B… B2, they one by one leave the gradient zone (and thus cease, according to the fundamental law of thermoelectric thermometry [1], to develop thermo-e.m.f., and therefore their errors $\Delta E_1^{DR} ... \Delta E_{k+1}^{DR}$ cease to influence the net TC thermo-e.m.f.). In place of the sections that left the gradient zone, it includes the sections adjacent to the ones C… C2 (they do not undergo the degradation because they are operated at the temperature close to that of the reference junction).

The thermo-e.m.f. developed by each TC section in a certain temperature field can be given as

$$\begin{aligned} E_i^{PROF} &= \left(e_i + \Delta e_i\right) \cdot \left(T_{Ei} - T_{Ei+1}\right) = \\ &= e_i \cdot \left(T_{Ei} - T_{Ei+1}\right) + \Delta e_i \cdot \left(T_{Ei} - T_{Ei+1}\right) = E_i^{POCH} + \Delta E_i^{DR} \end{aligned} , \qquad (1)$$

where $i$ is a certain TC section; $E_i^{PROF}$ is the thermo-e.m.f. developed by a certain section in a certain temperature field; $e_i$, $\Delta e_i$ are Seebeck coefficient and its deviation of a TC section; $T_{Ei}$, $T_{Ei+1}$ are the temperatures of section endpoints; $E_i^{POCH}$, $\Delta E_i^{DR}$ are the initial (before operation) thermo-e.m.f. of a certain section and its deviation due to drift of its CC.

From measurements of thermo-e.r.f. developed in different temperature fields we can write

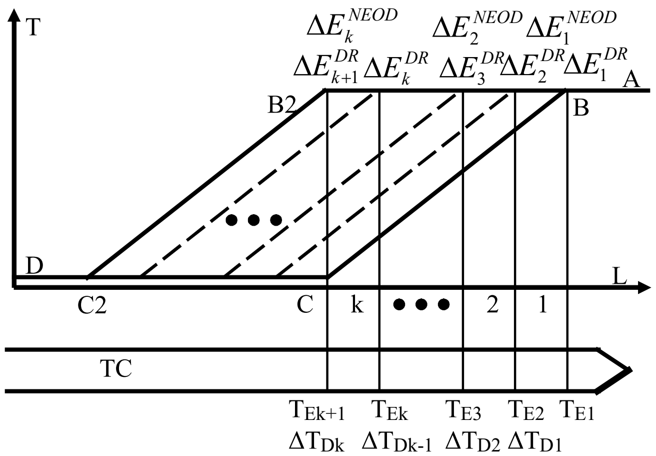

Fig. 1. Temperature fields when testing TC legs.

$$\begin{cases} \sum_{i=1}^{k} \left(E_i^{POCH} + \Delta E_i^{DR}\right) = E_1^{VYM} \\ \sum_{i=1}^{k} \left(E_i^{POCH} + \Delta E_i^{DR}\right) = E_2^{VYM} \\ \bullet\bullet\bullet\bullet\bullet\bullet\bullet\bullet\bullet\bullet\bullet\bullet\bullet\bullet\bullet\bullet \\ \sum_{i=1}^{k} \left(E_i^{POCH} + \Delta E_i^{DR}\right) = E_k^{VYM} \end{cases}, \qquad (2)$$

where $E_1^{VYM}$ ... $\Delta E_k^{VYM}$ are the thermo-e.m.f.s measured in all k temperature fields. The system of equations (2) illustrates the process of testing by changing the temperature field. The sections are subjected to different temperature gradients and, according to fundamental law of thermoelectric thermometry [1], their contribution to the total e.m.f. changes in each temperature field. In particular, some sections do not contribute at all because they are not subjected to a temperature difference. The solution of (2) allows determining the deviation *$\Delta E^{DR}$* of the e.m.f. of each TC section from the initial value due to drift and subsequently the change of the Seebeck coefficient $\Delta e_i$. Comparing the values $\Delta e_i$ obtained from solving (2) with the ones obtained from studies of like TCs in similar conditions, it is possible to identify the sections that undergo greater degradation than the others. When some sections of the TC approach a critical value, it is necessary to substitute this TC with a new one because of a big probability of damage. However, even in this case, the error of the old TC can be lesser than that of the other TCs in similar conditions as the TCTF [8] adjusts its temperature field to minimizes its error.

## 4. Modeling Technique

The technique of modeling of the method of developed TC testing is performed for the prototype of the TCTF [8, 9]. It consists of the measuring junction, 8 zones of temperature control and the reference junction. The technique is as follows:

1. Enter the temperatures of operation and seven temperature fields of testing for the measuring junction, temperatures of endpoints of 8 zones (their state is tested), and the temperature of the reference junction.

2. Generate 1000 realizations of the matrix of measurement errors $\Delta T_{8x8}$ (the dimensions are 8 rows and columns) of temperature differences across these 8 zones in each out of 8 fields.

3. Calculate the operating temperatures of $T_{EXPi}$ as the average of endpoint temperatures.

4. Enter the nominal Seebeck coefficients $e_{N8x1}$ and the law of their change on the operating temperature $\Delta e = f\,(T_{EXP})$, and use it to calculate the change of Seebeck coefficients of the TC sections $\Delta e_{8x1}$ and actual specific Seebeck coefficients of each section $e_{8x1}=(e_{N8x1} + \Delta e_{8x1})$.

5. Find the temperature differences across each section in the temperature field of operation and write the differences in the matrix $dT_{8x8}$. Do the same for 7 fields of testing from point 1.

6. Find the thermo-e.m.f. developed by the TC in 8 fields from point 1 as $E_{8x1}=\Delta T_{8x8}\times e_{8x1}$.

7. Add the temperature differences across the sections $dT_{8x8}$ to the errors of their measurement $\Delta T_{8x8}$ for 1000 implementations ($\Delta T_{8x8} + dT_{8x8}$).

8. Set the amplitude of the random error of measurements of thermo-e.m.f. of the TC and generate 1000 implementations of the measurement error matrix $\Delta E_{8x1}$.

9. Add thermo-e.m.f. of the TC in all 8 temperature fields $E_{8x1}$ to errors $\Delta E_{8x1}$ of their measurements $(E_{8x1} + \Delta E_{8x8})$.

10. Solve the system of equations $(\Delta T_{8x8} + dT_{8x8})\ \bar{e}_{8x1} = (E_{8x1} + \Delta E_{8x1})$ with respect to Seebeck coefficients $\bar{e}_{8x1}$, which are obtained when testing for 1000 implementations of $\Delta E_{8x1}$ and temperature differences across the sections $(\Delta T_{8x8} + dT_{8x8})$ (see point 7).

11. Find the errors in determining the Seebeck coefficients of the TC sections $\bar{e}_{8x1}$ - $e_{8x1}$ for all values of $\bar{e}_{8x1}$. Calculate the mean and variance for these errors. The simulation shows that the deviation of the average value of $(\bar{e}_{8x1}$- $e_{8x1})$ from zero for 1000 implementations is not more than 0.05 µV, thus the method has no systematic error.

12. Carry out the modeling of error of TC sections difference measurements $\overline{0...10°C}$ and thermo-e.m.f. for all combinations of errors of temperature measurements $\overline{0...20\mu V}$. As a result, the plot (Fig. 2) of standard deviation of the error of Seebeck coefficients (Z axis) versus random error of measuring thermo-e.m.f. (X axis) and error of temperature differences across TC sections (Y axis) is constructed. The plot reveals the main source of error of testing is caused by the error temperature differences across TC sections, so accurate control of the temperature field across the TCTF [10] is needed.

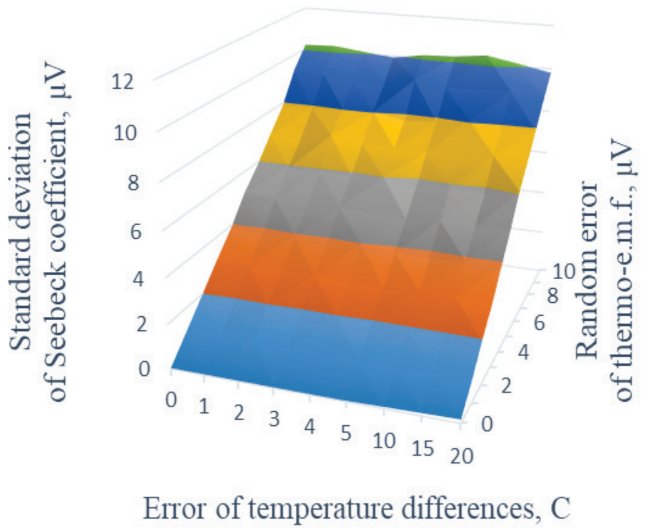


Fig. 2. Standard deviation of the error of Seebeck coefficients versus errors of e.m.f. and temerature differences across TC sections.

## 5. Conclusions

The advantage of the method of testing the state of TC legs is its simplicity of implementation, no use of standard equipment, the ability to determine and predict the state of TC sections during operation, as well as the forecast of the developed thermo-e.m.f. and TC error in different temperature fields.

## Acknowledgements

This work was support by the Technological innovation project of Hubei Province 2019(2019AAA047).

## References

[1] Park, R.M. (ed.) (1993). *Manual on the Use of Thermocouples in Temperature Measurement*. ASTM International.

[2] Su Jun, Kochan O. (2015). The mechanism of the occurrence of acquired thermoelectric inhomogeneity of thermocouples and its effect on the result of temperature measurement. *Measurement Techniques*, 57 (10), 1160-1166.

[3] Shu, C., Kochan, O. (2013). Method of thermocouples self verification on operation place. *Sensors & Transducers*, 160(12), 55-61.

[4] Jun, S., Kochan, O., Levkiv, M. (2017). Metrological software test for studying the method of thermocouple error determination during operation. In *2017 11th International Conference on Measurement*. IEEE, 171-174.

[5] Jun, S., Kochan, O. V., Vasylkiv, N. M., Kochan, R. V. (2015). A method of correcting the error of temperature measurements due to acquired inhomogeneity of the electrodes of thermocouples. *Measurement techniques*, 58(8), 904-910.

[6] Kochan, O. Method of self-testing of thermocouples ain situ and the device for its implementation. Patent of Ukraine 104952. G01K13 / 00.

[7] Jun, S., Kochan, O., Kochan, R. (2016). Thermocouples with built-in self-testing. *International Journal of Thermophysics*, 37(4), 37.

[8] Wang, J., Kochan, O., Przystupa, K., Su, J. (2019). Information-measuring system to study the thermocouple with controlled temperature field. *Meas. Sci. Rev.* 19(4), 161-169.

[9] Jun, S., Kochan, O., Chunzhi, W., Kochan, R. (2015). Theoretical and experimental research of error of method of thermocouple with controlled profile of temperature field. *Measurement science review*, 15(6), 304-312.

[10] Jun, S., Kochan, O., et al. (2016). Development and investigation of the method for compensating thermoelectric inhomogeneity error. *Int. J. Thermophys*, 37(1), 10.

# *Young Investigator Award Session I*

# Eliminating Speckle Noises for Laser Doppler Vibrometer Based on Empirical Wavelet Transform

[1]Yang Jin, [1]Zili Li

[1]Railway Engineering, Delft University of Technology, The Netherlands
Email: J.Jin-3@tudelft.nl

***Abstract.*** *This paper presents a novel approach for eliminating speckle noises in Laser Doppler Vibrometer signals based on empirical wavelet transform (EWT). The moving root-mean-square thresholds are utilized to cut off signal drop-outs and produce noise discontinuity that EWT can identify. The extremum ratio behaves as the criterion to reject or accept the EWT decomposed components. While processing simulated signals, the EWT-based approach outperforms others and presents de-speckle robustness. In experiments, EWT reveals the actual vibration despite low signal-to-noise ratios, which indicates de-speckle efficiency.*

*Keywords: Laser Doppler Vibrometer, Speckle Noise, Empirical Wavelet Transform*

## 1. Introduction

Vibration measurement is playing an increasingly significant role in modal analysis and mechanical system diagnosis. Laser Doppler Vibrometer (LDV) is a non-contact and non-destructive vibration detector, which can acquire the signals remotely (e.g., from high-temperature objects) and avoid mass loading that light structures are sensitive to, superior to attached transducers. The speckle noise arising from coherent laser components over the rough surface is an extremely troublesome issue restricting the LDV application extension [1]. Two kinds of the speckle noise distort the actual signal, as the signal drop-outs can reach over 30 times of the vibration amplitudes and the dominant noises with normal amplitudes can reduce the signal-to-noise ratio (SNR) to -15 db. The characteristics of speckle noises are far different from those of the white noises, thereby former de-noise strategies becoming inapplicable. Developing novel approaches for mitigating speckle noises has aroused recent research concerns, such as energy analysis [2], polishing target surface [3], cutting off outliers [4] and moving-averaging signals [5]. These methods are not suitable for extensive practices, e.g., those that require complete time-series analysis, large-scale measurements, or high-speed scanning. Calculating the signal energy is effective in damage inspection but overlooks the waveforms significant for modal analysis; attaching retroreflective tapes can reduce the surface roughness and further the noise amplitude, but not applicable in large-scale measurements; utilizing thresholds can cut off signal drop-outs but preserves the dominant noises with normal amplitudes; the moving average approach requires cyclical measurements with the scanning period far lower than the vibration period. Therefore, an effective post-processing approach for eliminating speckle noises remains to be developed. Empirical wavelet transform (EWT) [6] is an adaptive signal decomposition approach with wavelets adapted to the processed signal. It has the potential to handle speckle noises and mitigate related distortions due to the naturally determined bandwidths and the continuity of decomposed signal components.

In this paper, we develop an EWT-based approach to extract actual vibrations from noisy LDV signals. The moving root-mean-square (MRMS) thresholds are utilized to cut off signal drop-outs and produce noise discontinuity that EWT can identify. The extremum ratio behaves as the criterion to reject or accept the EWT decomposed components. The developed de-speckle approach is evaluated in both numerically simulated and experimentally acquired signals.

## 2. Subject and Methods

*Empirical Wavelet Transform*

Since the actual vibration is time-frequency variant and the speckle noise is not uniformly distributed in the frequency domain, traditional signal decomposition approaches with certain bandwidths, including band-pass filters (BPF) [7] and wavelet transform (WT) [8], become inadequate for analysis. EWT overcomes this disadvantage by adaptively determining the wavelet bandwidths around the maxima of the Fourier spectrum. Therefore the empirical wavelets are adapted to the processed signal and have the potential to naturally extract the actual vibrations. Besides, EWT can avoid artifacts from high-frequency components, specifically the signal drop-outs, superior to empirical mode decomposition that presents similar adaptive properties. The mathematical construction of the wavelet group and scaling functions is described in [6].

*De-speckle Algorithm*

A specific algorithm is designed to eliminate the speckle noises. The first procedure is to calculate the MRMS thresholds $T_r(t)$ of the signal $v(t)$ with the moving window $w$, utilizing Eq. 1. It replaces signal amplitudes outlying the thresholds by the MRMS values, thereby reducing drop-outs amplitudes and producing discontinuities that represent the noise locations. Cutting off the signal drop-outs can mitigate the effect of large amplitude distortions in low-frequency components.

$$T_r(t) = v(t) \otimes e_w/w \pm \sqrt{v^2(t) \otimes e_w/w}, \tag{1}$$

where

$\otimes$ convolution calculation

$e_w$ all ones vector with length $w$

The following procedures are to decompose the signal by EWT and then reconstruct the actual vibration by chosen components. EWT can acquire diverse approximate and detail coefficients that contain noises or actual vibrations. The extremum-number ratio between the decomposed components and the original signal is predefined as a criterion to determine the component belongings. An actual-vibration component should achieve an extremum-number ratio ranging below the frequency ratio (2 times the target frequency divide by sampling frequency).

*Simulation and Experiment*

The numerical simulation of speckle noises is based on the LDV measurement principle, Doppler frequency shifts. The time variance of the modulated laser phase, which dominantly contributes to the speckle noises, arises from the varying surface roughness. Therefore, the scanning surface is divided into speckle elements that have been assigned optical intensities and phases according to statistical distributions. The mathematical calculations of speckle noises are derived in [9].

In numerical simulations, a nonstationary signal is adopted as the actual vibration, polluted by simulated speckle noises. In order to evaluate the de-speckle robustness, the initial SNR varies in (-5 db, -10 db, -15 db). Other approaches including BPF and WT are compared, and the correlation coefficient between the de-speckle signal and actual vibration can evaluate the accuracy. In experiments, a $540 \times 40$ mm$^2$ cantilever strip is artificially excited at 500 Hz. The LDV system acquires vibration signals along the strip surface with the scanning speed 0.1 m/s and the sampling frequency 102400 Hz.

## 3. Results

Figure 1a presents the simulated vibration polluted by speckle noises, with initial SNR = -10 db. The signal drop-outs can reach 100 times the smallest vibration amplitude and the dominant noises significantly distort the vibrations. The corresponding de-speckle results achieved by our developed approach is illustrated in Figure 1b. The de-speckled curve agrees well with the actual vibration, with the post SNR = 17.24 db and the correlation coefficient 0.98. Table 1 outlines the comparison results. The EWT-based approach outperforms others in the de-speckle procedure. BPF and WT approaches fail to achieve promising results with intensive speckle noises. The correlation coefficients of EWT results retain over 0.95 and the post SNRs retain over 13 db with decreasing initial SNRs, which indicates the robustness of the developed approach.

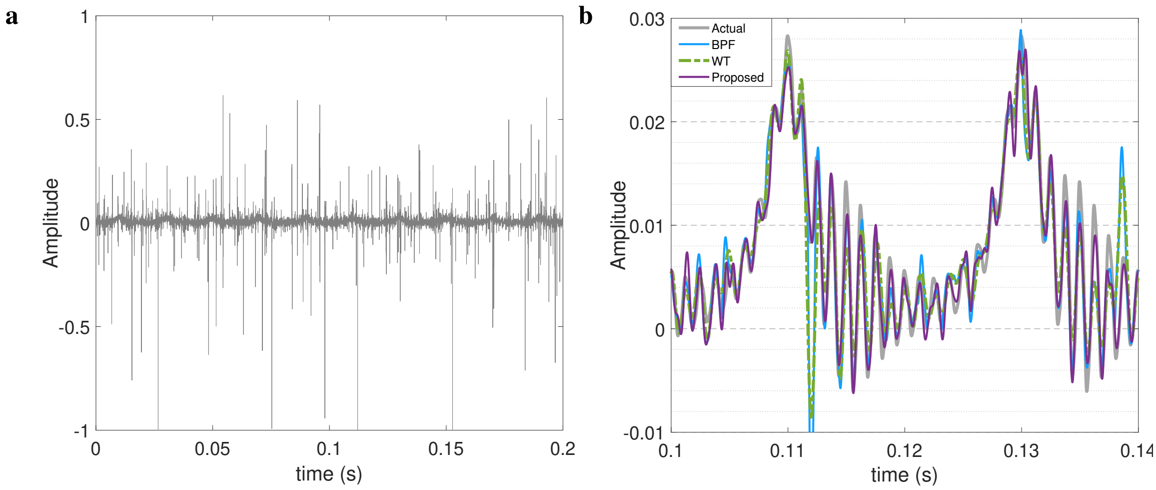


Fig. 1: a. Simulated signal polluted by speckle noises; b. De-speckle results versus actual vibration.

| Initial SNR | Post SNR | | | Correlation | | |
|---|---|---|---|---|---|---|
| | EWT | BPF | WT | EWT | BPF | WT |
| -5 db | 21.65 db | 12.55 db | 9.66 db | 0.99 | 0.95 | 0.94 |
| -10 db | 17.24 db | 6.97 db | 4.50 db | 0.98 | 0.85 | 0.82 |
| -15 db | 13.11 db | 2.78 db | 0.44 db | 0.95 | 0.71 | 0.66 |

Table 1: Post SNRs and correlation coefficients of diverse comparison results.

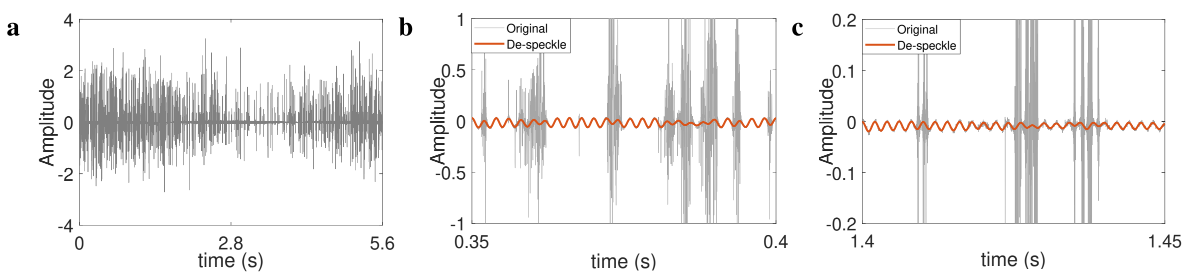


Fig. 2: a. Experimental LDV signal; b. De-speckle results with relatively large vibrations; c. De-speckle results with weak vibrations.

Figure 2a presents the scanning LDV signal from experiments. The 500 Hz vibration amplitude varies from 0.005 to 0.05, lower than 1/40 of the signal drop-out amplitude. The estimated initial SNR is -14 db, which means intensive speckle noises have dramatically polluted the actual vibrations. Figure 2b shows the de-speckle result between 0.35 s and 0.4 s (intensive noise duration), where the 500 Hz vibration amplitudes are around 0.05 and the estimated initial SNR is -24 db. The developed EWT-based approach has revealed the 500 Hz vibrations despite some amplitude deformations. Figure 2c illustrates the de-speckle results between 1.4 s and 1.45 s (intensive noise duration), where the 500 Hz vibration amplitudes are around 0.05 and the estimated initial SNR is -25 db. The de-speckle curve presents promising 500 Hz waveforms even at intensively noisy locations. Therefore, the developed approach is applicable in eliminating speckle noises.

## 4. Conclusions

This paper develops an EWT-based approach for eliminating speckle noises in LDV vibration signals. The MRMS thresholds are utilized to cut off signal drop-outs and the extremum-number ratio behaves as the criterion to reject or accept the EWT decomposed components. In numerical simulations, the EWT-based approach can effectively reconstruct the actual vibrations despite intensive noises, outperforming BPF and WT. The post SNR and correlation coefficient retain promising with the decreasing initial SNR, thereby indicating the de-speckle robustness. In experiments, the speckle noises are intensive in the acquired LDV signals with the estimated initial SNR -14 db. The developed approach can reveal the actual 500 Hz vibrations regardless of how weak the vibration responses are. Therefore, our approach is applicable in eliminating speckle noises.

Further investigations can concern the applicability in mitigating speckle noises acquired from different materials by different scanning strategies. In addition, the de-speckle approach will be applied to process LDV signals for modal analysis and damage inspection.

## References


[1] Rothberg, S., Allen, M., Castellini, P., Di Maio, D., Dirckx, J., Ewins, D., Halkon, B.J., Muyshondt, P., Paone, N., Ryan, T., et al. (2017). An international review of laser doppler vibrometry: Making light work of vibration measurement. *Optics and Lasers in Engineering*, 99, 11–22.

[2] Chiariotti, P., Martarelli, M., Revel, G. (2017). Delamination detection by multi-level wavelet processing of continuous scanning laser doppler vibrometry data. *Optics and Lasers in Engineering*, 99, 66–79.

[3] Xu, Y., Chen, D.-M., Zhu, W. (2020). Modal parameter estimation using free response measured by a continuously scanning laser doppler vibrometer system with application to structural damage identification. *Journal of Sound and Vibration*, 485, 115536.

[4] Vass, J., Šmíd, R., Randall, R., Sovka, P., Cristalli, C., Torcianti, B. (2008). Avoidance of speckle noise in laser vibrometry by the use of kurtosis ratio: Application to mechanical fault diagnostics. *Mechanical Systems and Signal Processing*, 22(3), 647–671.

[5] Zhu, J., Li, Y., Baets, R. (2019). Mitigation of speckle noise in laser doppler vibrometry by using a scanning average method. *Optics Letters*, 44(7), 1860–1863.

[6] Gilles, J. (2013). Empirical wavelet transform. *IEEE Transactions on Signal Processing*, 61(16), 3999–4010.

[7] Shenoi, B. A. (2006). *Introduction to digital signal: Processing and filter design*. Wiley Online Library.

[8] Pathak, R. S. (2009). *The wavelet transform*, Vol. 4. Springer Science & Business Media.

[9] Rothberg, S. (2006). Numerical simulation of speckle noise in laser vibrometry. *Applied Optics* 45(19), 4523–4533.

# Factor Number Selection in the Tensor Decomposition of EEG Data: Mission (Im)Possible?

**Zuzana Rošťáková, Roman Rosipal**

Institute of Measurement Science, Slovak Academy of Sciences, Bratislava, Slovakia
Email: zuzana.rostakova@savba.sk

***Abstract.*** *A number of factors is an essential parameter in the tensor decomposition methods. It significantly influences not only the decomposition quality but also its interpretation. Many approaches and heuristics were proposed for this purpose. However, their performance is usually demonstrated on data with a simplified structure, and therefore they can produce inferior results when applied to more complex real data. In this study, on a generated dataset closely mimicking the nature of a human multichannel electroencephalogram (EEG), we compared the performance of five methods for selecting the number of factors. We identified the best performing method, but not even this method led to sufficiently acceptable results.*

*Keywords: Number of Factors, Electroencephalogram, Tensor Decomposition, PARAFAC*

## Introduction

Tensor decomposition is a powerful tool for detecting hidden structure in higher-order arrays (tensors), for example, in chemometrics, psychometrics, or neurophysiology [1]. An important parameter, which influences the decomposition quality, is the number of hidden factors $F$. To determine $F$, we have to apply a suitable method. Several approaches for selecting the number of factors or heuristics with different assumptions and computational complexity were proposed, but none of them became a state-of-the-art approach. Then, which one to use?

This study aims to help answer this question by comparing five methods for selecting $F$ in the parallel factor analysis (PARAFAC) tensor decomposition [2] on artificial data that mimics the multichannel EEG signal character. We have two main reasons for choosing this particular type of data. First, our long-term research focuses on EEG tensor decomposition by PARAFAC. We often face the problem of correctly determining $F$. Second, existing methods' performance is usually compared on artificially generated data with a simplified structure that does not follow the real data character. For example, the factors are often generated as mutually orthogonal or independent and identically distributed random sample from a normal or uniform distribution [1, 3, 4]. However, EEG data are more complex, and both orthogonality and normality properties miss their neurophysiological interpretation. Consequently, methods used to determine $F$ can produce inferior results when applied to such data.

## Data and Methods

*Data*

We applied an anatomical forward model consisting of 2,004 dipoles placed in gray matter to generate one minute of scalp 64-channel EEG data [5]. The generated signal comprises a broadband brain activity (BBA) and four narrow-band oscillations – 5 Hz oscillation located in the frontal region, 8 Hz and 14 Hz oscillations in the central region and 11 Hz oscillation in the occipital region. The activity (presence) of each oscillation was generated as non-overlapping with any other in time. To simulate BBA, we used a realization of the fractional Brownian motion with the Hurst exponent $H = 0.6$. According to the amplitude of BBA, we define noiseless data ($N_0$), data with low ($NBBA_{low}$) and high ($NBBA_{high}$) levels of BBA [5]. Moreover, we added

Gaussian noise to each scalp EEG channel of the $N_0$ data. To mimic the signal-to-noise ratio at the occipital EEG electrodes of the $NBBA_{low}$ and $NBBA_{high}$ data, we considered two levels of the noise variance denoted as $NG_{low}$ and $NG_{high}$. These data are less in line with the character of a real EEG signal (missing BBA), but follow the theoretical assumptions of methods described below. For each type of data, we generated 20 datasets/realisations. Before applying PARAFAC, the simulated EEG signal was segmented into two-second time windows with 1900 ms of overlap. The oscillatory part of the amplitude spectrum for each time window and each electrode was transformed into a three-way tensor, representing the time-space-frequency modes [5].

*Parallel Factor Analysis*

The PARAFAC model [2] decomposes a three-way tensor $\mathbb{X} \in \mathbb{R}^{I_1 \times I_2 \times I_3}$ into three matrices $A^{(n)} \in \mathbb{R}^{I_n \times F}, n = 1,2,3$, where $F$ represents the number of factors, and follows the equation

$$x_{i_1 i_2 i_3} = \sum_{f=1}^{F} a^{(1)}_{i_1 f} a^{(2)}_{i_2 f} a^{(3)}_{i_3 f} + e_{i_1 i_2 i_3}, \qquad i_n = 1,\ldots,I_n, \quad n = 1,2,3.$$

The tensor $\mathbb{E} \in \mathbb{R}^{I_1 \times I_2 \times I_3}$ represents the error term. Similar to our previous studies [5, 6], we assume nonnegativity of $A^{(1)}$ and $A^{(2)}$ together with unimodality of $A^{(3)}$ columns to follow neurophysiology of data and simplify the interpretation of decomposition.

*Factor Number Selection Methods*

The approaches for factor number selection can be divided into five sets according to their character. By selecting the best performing candidate from each set, we focus on:

i) **core consistency diagnostics (CCD)** [7]: The CCD values are plotted against the number of factors $F$ and a rapid change in the graph is visually detected.

ii) **non-redundant model order estimator (NORMO)** [8]: The method searches for the lowest $F$ with any redundant factor in PARAFAC. But at least one redundancy occurs for $F+1$. The algorithm considers either all $F$ (NORMO$_E$) or a subset of them (NORMO$_B$).

iii) **numerical convex hull (NCH)** [3]: The method focuses on the maximal change in fit between models belonging to the fit convex hull boundary.

iv) **minimal description length (MDL)** [4]: The approach analyses eigenvalues of matricized forms of a tensor.

v) **automatic relevance determination (ARD)** [1]: ARD begins with a large $F$ and continuously prune out factors with a small weight in PARAFAC by using Bayesian statistics. The algorithm follows either the sparse (ARD$_S$) or ridge (ARD$_R$) version.

To avoid convergence to a local optimum, the PARAFAC algorithm was run five times for each $F$ and the model with the lowest error was chosen.

We set the maximal number of factors $F$ to 10. A method was considered successful if it selected $F = 4$. Moreover, the estimated factors as a by-product of CCD, NORMO or ARD were checked for consistency with the generated oscillations. Free parameters of each method were carefully tuned to achieve the best possible output. We set the threshold $\alpha > 0.9$ for $F$ selection in NCH and MDL. For NORMO, we set $\alpha = 0.7$.

The original ARD does not allow us to apply the unimodality constraint, and therefore we had to modify the algorithm. Moreover, the tolerance $tol$ for pruning out the unnecessary factors, as suggested by authors, could not decrease the maximal allowed $F = 10$. Different $tol$ values led to different $F$, and without a priori knowledge about the true $F$ (which is always unknown in practice), we could not set optimal $tol$ value. Therefore, we propose the following modification. In each iteration step, we ordered the factors according to their increased norms, and we skipped the first few factors with cumulative normalized norms under 0.1.

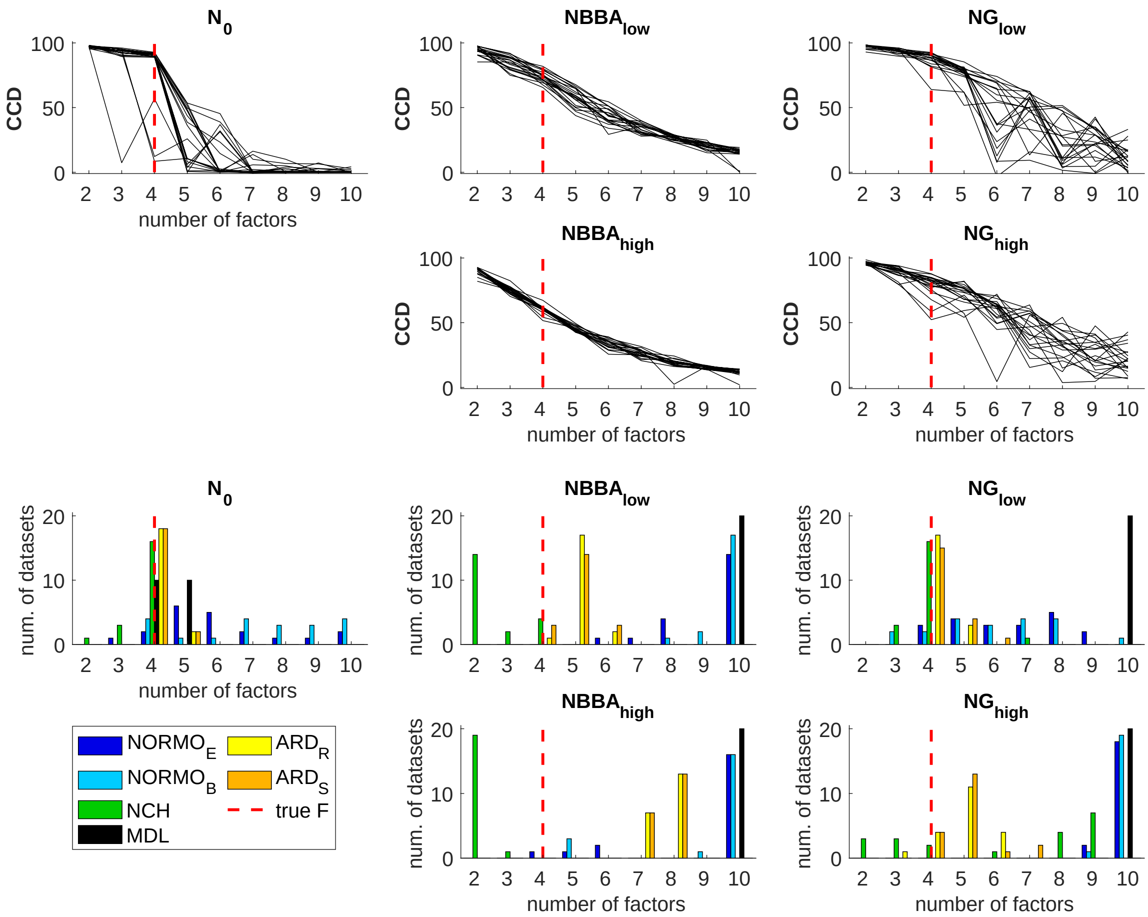


Fig. 1: *First and second row:* The core consistency diagnostics (CCD) of PARAFAC with two to 10 factors. *Third and fourth row:* Histograms of selected factor number in 20 datasets by the non-redundant model order estimator (NORMO$_B$, NORMO$_E$), numerical convex hull (NCH), minimal description length (MDL) and automatic relevance determination (ARD$_S$, ARD$_R$). Red dashed vertical lines represent the correct factor number $F = 4$. Three columns represent data with no noise ($N_0$), low and high broadband brain activity ($NBBA_{low}, NBBA_{high}$) or Gaussian noise ($NG_{low}, NG_{high}$).

## Results and Discussion

A visible rapid drop in CCD (Fig. 1, first and second row) allowed us to select $F = 4$ only for $N_0$. For $NG_{low}$ data, the number of factors was overestimated ($F = 5$). The CCD values decrease relatively linearly for the other data types, and it was not possible to visually select the best $F$.

Both NORMO versions detected the correct $F$ for $N_0$ and $NG_{low}$ in less than one-third of datasets (Fig. 1, dark and light blue). Due to BBA or Gaussian noise, the estimated factors showed numerically weak correlation ($< 0.5$) despite many physiological similarities detected by visual inspection. Consequently, NORMO resulted in $F$ close to the maximal allowed value 10 for $NBBA_{low}$, $NBBA_{high}$ and $NG_{high}$.

The correct $F = 4$ was detected by NCH in 16 $N_0$ and $NG_{low}$ datasets (Fig. 1, green). However, $F = 4$ was chosen in only four cases for $NBBA_{low}$ and two factors were incorrectly chosen in all $NBBA_{high}$ datasets. For $NG_{high}$, the selected $F$ varied between two and 10.

MDL failed to select the correct $F$ in one-half of $N_0$ datasets (Figure 1, black). BBA or Gaussian noise's presence forced the $F$ selection to the maximal allowed value equal to 10.

ARD$_R$ and ARD$_S$ performed well for $N_0$ and $NG_{low}$, the correct $F = 4$ was selected in at least 15 of 20 datasets (Figure 1, yellow and orange). For $NBBA_{low}$ and $NG_{high}$ the performance had decreased and led to $F = 5$ or $F = 6$. However, only 14 Hz oscillation was present in the estimated five or six factors. The other factors represented higher oscillations or noise. The ARD method was not able to recover the correct number of factors for $NBBA_{high}$.

## Conclusions

We compared the performance of five methods for selecting the number of factors in PARAFAC on generated multichannel EEG data. MDL and NORMO methods fail to choose the correct number of factors already for noiseless data. Increasing the level of broadband brain activity (BBA) or Gaussian noise deteriorates the other methods' performance. The best, but still far from ideal, results were obtained by ARD. We can conclude that none of the considered methods provides satisfactory results.

Moreover, we observed inferior results in data with BBA compared to data with Gaussian noise. We hypothesise, that this is due to the methods' assumption of the tensor trilinear structure and presence of Gaussian noise. This assumption is not met in the data with BBA.

In real EEG data, BBA and a measurement noise make detecting narrow-band scalp oscillations harder. Due to the investigated methods' failure to determine correct $F$ in well-controlled generated data, we expect similar sub-optimal performance when applied to real EEG data. In [6], we addressed the problem of the factor number selection differently. We ran PARAFAC models with different $F$ and applied the cluster analysis on obtained decompositions. This allows us to identify the most dominant clusters representing the subject-specific narrow-band scalp EEG oscillations.

Nevertheless, selecting the number of factors in the PARAFAC model remains an open problem, and new approaches are needed.

## Acknowledgements

This research was supported by the Slovak Research and Development Agency (grant APVV-16-0202) and by the VEGA grant 2/0081/19.

## References

[1] Mørup, M., Hansen, L.K. (2009). Automatic relevance determination for multi-way models. *Journal of Chemometrics*, 23(7-8), 352–363.

[2] Harshman, R.A. (1970). Foundations of the PARAFAC procedure: Models and conditions for an "explanatory" multimodal factor analysis. *UCLA Working Papers in Phonetics*, 16, 1–84.

[3] Ceulemans, E., Kiers, H. A.L. (2006). Selecting among three-mode principal component models of different types and complexities: A numerical convex hull based method. *British Journal of Mathematical and Statistical Psychology*, 59(1), 133–150.

[4] Liu, K., da Costa, J., So, H.C., Huang, L., Ye, J. (2016). Detection of number of components in CANDECOMP/PARAFAC models via minimum description length. *Digital Signal Processing*, 51, 110–123.

[5] Rosipal, R., Rošťáková, Z., Trejo, L.J. (2021). Tensor decomposition of human oscillatory EEG activity in frequency, space and time. *PsyArXiv*.

[6] Rošťáková, Z., Rosipal, R., Seifpour, S., Trejo, L.J. (2020). A comparison of non-negative Tucker decomposition and Parallel Factor Analysis for identification and measurement of human EEG rhythms. *Measurement Science Review*, 20(3), 126–138.

[7] Bro, R., Kiers, H. A.L. (2003). A new efficient method for determining the number of components in PARAFAC models. *Journal of Chemometrics*, 17(5), 274–286.

[8] Fernandes, S., Fanaee-T, H., Gama, J. (2020). NORMO: A new method for estimating the number of components in CP tensor decomposition. *Engineering Applications of Artificial Intelligence* 96.

# Significance of Multi-Lead ECG Electrodes Derived from Patient-Specific Transfer Matrix

[1,2]Beata Ondrusova, [1]Jana Svehlikova,[1]Milan Tysler,[3]Peter Tino

[1]Institute of Measurement Science, Slovak Academy of Sciences, Bratislava, Slovakia,
[2]Faculty of Electrical Engineering and Information, Slovak University of Technology, Bratislava, Slovakia,
[3]School of Computer Science, University of Birmingham, Birmingham, UK
Email: umerondb@savba.sk

***Abstract.*** *During multi-lead ECG recording, some electrodes can be identified as broken and thus information from those electrodes cannot be used for the inverse problem of electrocardiography. The objective of this study is to explore the significance of individual ECG electrodes derived from the patient-specific transfer matrix for homogeneous volume conductor. Four multi-lead ECG measurement datasets with corresponding geometries were used for this study. The transfer matrices were computed using the boundary element method. The significance of individual torso electrodes for a given position of the dipole as the equivalent heart generator was assessed by the singular value decomposition of the transfer matrices for the forward and inverse problem of electrocardiography, respectively. The study showed that the position of the most significant electrodes depends on the position of the heart within the chest and the position of the dipole as an equivalent heart generator. The positions of the first 20% of the most significant electrodes for the forward and inverse problem differ from 0% to 16%.*

*Keywords: Inverse Problem of Electrocardiography, Transfer Matrix, Singular Value Decomposition*

## 1. Introduction

The forward problem of electrocardiography describes the electric potential field on the torso surface generated by the electrical activity of the heart. On the other hand, the inverse problem of electrocardiography reconstructs the origin of the electrical activity of the heart using multi-lead ECG measurement and the patient's specific geometry models. Often, this method is used to noninvasively identify the origin of a premature ventricular contraction (PVC) [1]. In clinical practice, the application of many electrodes on the patient's torso is challenging. Sometimes, information from some electrodes is missing in the recording and thus current research is focused to identify the influence of individual electrodes on the inverse localization of the PVC origin. This influence was evaluated from the parameters obtained from the measured signals on the patient's torso such as potential gradient [2] and signal power [3]. A transfer matrix is another necessary input for the inverse solution in addition to the measured ECG signals. Therefore, the objective of this study is to identify important electrodes for the forward and inverse problem using the singular value decomposition (SVD) of the patient-specific transfer matrix.

## 2. Subject and Methods

This study explores four multi-lead ECG datasets recorded during ventricular pacing available via the EDGAR database [4], specifically animal torso tank experiments (Utah tank 1, Utah tank 2, Bordeaux tank) and measurement on human (Bratislava human). For this study, available geometry models of the torso and heart as well as the defined positions of the torso electrodes and ventricular pacing electrodes were used. Bratislava human geometry data were constructed

Table 1: Number of torso electrodes, number of nodes on heart and torso mesh and size of the transfer matrix.

| Dataset | Num. of torso electrodes [-] | Num. of nodes Heart [-] | Num. of nodes Torso [-] | Transfer matrix size [-] |
|---|---|---|---|---|
| Utah tank 1 | 192 (12 x 16) | 247 | 771 | 192 x 741 |
| Utah tank 2 | 192 (12 x 16) | 337 | 771 | 192 x 1011 |
| Bordeaux tank | 128 (irregular) | 894 | 4002 | 128 x 2682 |
| Bratislava human | 128 (8 x 16) | 1528 | 1773 | 128 x 4584 |

from available CT scans by using TomoCon PACS® software. The number of torso electrodes as well as the number of nodes of the individual torso and heart geometries are shown in Table 1. From available geometries, corresponding transfer matrices were calculated.

Let us consider a homogeneous volume conductor bounded by body surface $S_B$ and equivalent heart generator $H_G$. Solution of the forward problem enables to compute electric potentials on the body surface $S_B$ generated by the equivalent heart generator $H_G$ and is expressed as a linear equation

$$\Phi_B = TH_G, \tag{1}$$

where $\Phi_B$ is a vector of electric potentials calculated on the body surface, $T$ is a transfer matrix and $H_G$ is a vector of heart electric sources. A single dipole is used as an elementary heart source. The transfer matrix $T$ is computed using the boundary element method and reflects the geometrical and electrical properties of the torso volume conductor. It can be viewed as a linear operator transferring the data from the heart to the torso. The size of the transfer matrix $T$ is $m \times 3 * n$ where $m$ represents the number of electrodes attached to the torso and $n$ represents the number of heart dipoles with the three orthogonal components of dipole moment. Let $A$ be a submatrix of the transfer matrix $T$ corresponding to a single heart dipole with size $m \times 3$. The SVD of the matrix $A$ is written as

$$A = U\Sigma V^T, \tag{2}$$

where $U$ (size $m \times m$) and $V$ (size $3 \times 3$) are orthogonal matrices and $\Sigma$ (size $m \times 3$) is a rectangular matrix with zeros outside of the diagonal and nonnegative singular values on the diagonal where $\sigma_i$ is the $i$th diagonal entry of $\Sigma$ [5]. The rank $r$ of the matrix $A$ is at most 3 and it is determined by the number of positive singular values. To determine the observability of the corresponding source on the torso surface, columns of matrix $U$ will be used. For a lead $k$ ($1 \le k \le m$) its weighted observability $w_k$ for the forward problem is calculated as follows

$$w_k = \sum_{i=1}^{3} |u_{k_i}| \sigma_i, \tag{3}$$

where $u_{k_i}$ is the $k$th element of the $i$th column vector of $U$. Weighted observabilities $w_k$ calculated for all leads $k = 1, 2, \ldots, m$, are then sorted in the descending order to identify leads with the highest observability for the given position of the heart generator.

Solution of the inverse problem estimates equivalent electric heart generator $H_G$ on the heart surface/volume from the measured body surface potentials $\Phi_B$ as

$$H_G = T^+ \Phi_B, \tag{4}$$

where $T^+$ is a pseudoinverse of the transfer matrix $T$ [1]. Let $A$ be a submatrix of the transfer matrix $T$ representing one heart dipole with size $m \times 3$, then the pseudoinverse $A^+$ is written as

$$A^+ = V\Sigma^{-1}U^T, \tag{5}$$

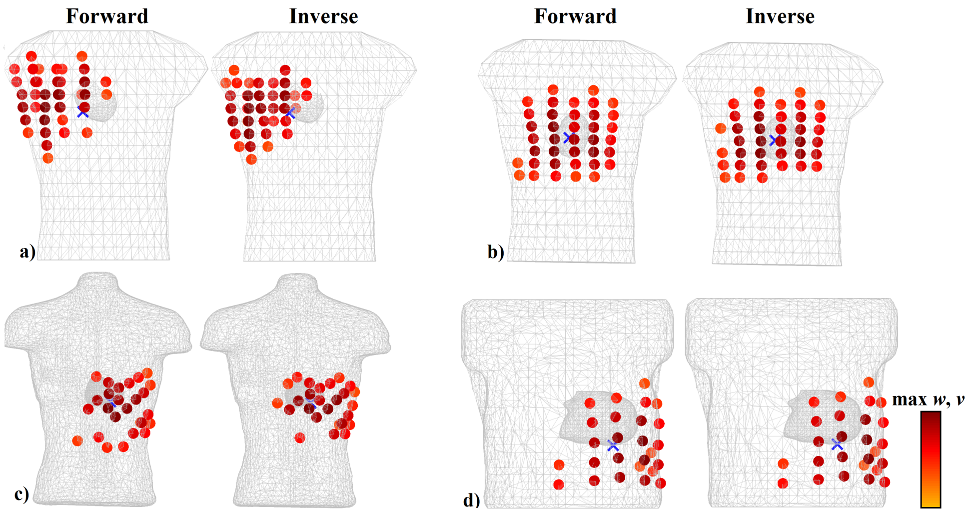


Fig. 1: The 20% of the most significant leads for the forward and inverse solution and real pacing electrode position (blue mark) - a) Utah tank 1, b) Utah tank 2, c) Bordeaux tank, d) Bratislava human.

considering that matrices $U$ and $V$ are orthogonal and $U^{-1} = U^T$ and $V^{-1} = V^T$ [5]. Reciprocals of the non-zero entries in the diagonal are taken to obtain $\Sigma^{-1}$. As before, the columns of $U$ (rows of $U^T$) will be used to evaluate the weighted contribution of a specific lead to the inverse solution. For a lead $k$ ($1 \leq k \leq m$) its weighted contribution $v_k$ to the inverse problem is calculated as

$$v_k = \sum_{i=1}^{3} \frac{1}{\sigma_i} |u_{k_i}|. \tag{6}$$

Again, the weighted contributions calculated for all leads are sorted in the descending order to identify the most significant leads for the inverse solution.

## 3. Results

We investigated the most significant ECG electrodes derived from the SVD of the transfer matrix i.e., leads with the highest observability on the torso for the forward problem and leads with the highest contribution to the inversely computed equivalent heart generator. First, we examined the position of the most significant leads on the torso for the known position of the ventricular pacing electrode. In Figure 1 we depict the first 20% of the most significant leads for the forward and inverse solution (38 leads for Utah tank 1 and Utah tank 2 and 26 leads for Bordeaux tank and Bratislava human) in a red colour scale. As can be seen from Figure 1, the positions of the most significant leads on the torso vary between datasets and depend on the placement of the heart in the chest as well as on the position of the pacing site. The positions of the first 20% of the most significant electrodes for the forward and inverse problem differ by 0% for Bratislava human, 5% for Utah tank 2, 15% for Bordeaux tank and 16% for Utah Tank 2.

Further, we used Bratislava human data for a more detailed examination of the position of significant leads for the inverse solution with respect to different positions of the origin of ventricular activity (dipole positions). The results are shown in Figure 2. The positions of the most significant leads strongly depend on the position of the dipole as an equivalent heart generator. Figure 2 shows that the most significant leads for the inverse solution could be located also on the patient's back if the dipole is located on the left ventricular free wall.

## 4. Discussion and Conclusion

The study explores the positions of significant leads on the torso for the solution of the forward and inverse problem. The significance of the leads was determined using the SVD of the transfer

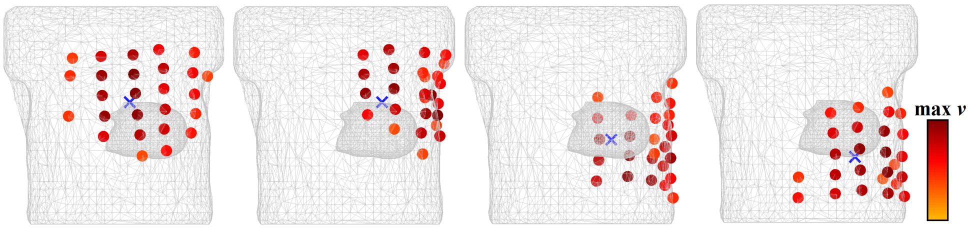


Fig. 2: The 20% of the most significant leads (Bratislava human data) for the inverse solution and different positions of dipole (blue mark) - from left: right ventricle superior, left ventricle superior, left ventricle inferior, right ventricle inferior.

matrix. The results demonstrate that the positions of the most significant leads depend on the heart position in the chest and differs between patients. Moreover, the study demonstrates that the positions of the most significant leads depend on the position of the dipole as an equivalent heart generator which can represent the origin of the PVC.

The results confirm the importance of using multi-lead ECG with a patient-specific geometry for the inverse solution since the heart-torso geometry and the position of the origin of ventricular activity are not known in advance. This study showed that the positions within 20% of the most significant electrodes for the forward and inverse problem differ from 0% to 16%. These differences could be caused by the non-regularity of the transfer matrix. The results of the study should be considered when some electrodes in the recordings are missing. In future studies, we will investigate how the significant electrodes influence the inverse localisation of the PVC origin.

## Acknowledgements

Data for this study were obtained via the EDGAR database and provided by the CVRT and CSI Institute at the University of Utah, by the IHU-LIRYC Institute at the Université de Bordeaux and by the Institute of Measurement Science, SAS in cooperation with the National Institute for Cardiovascular Diseases, Bratislava, Slovakia. This work was supported by the research grant 2/0125/19 from the VEGA Grant Agency in Slovakia and by the grant APVV-19-0531 from the Slovak Research and Development Agency.

## References

[1] Svehlikova, J., Teplan, M., Tysler, M. (2018). Geometrical constraint of sources in noninvasive localization of premature ventricular contractions. *Journal of Electrocardiology*, 51 (3), 370-377.

[2] Rababah, A.S., Bond, R.R., Rjoob, K., Guldenring, D., McLaughlin, J., Finlay D.D. (2019). Novel hybrid method for interpolating missing information in body surface potential maps. *Journal of Electrocardiology*, 57, S51–S55.

[3] Svehlikova, J., Ondrusova, B., Zelinka, J., Tysler, M. (2020). The influence of the most powerful signals on the pacing site localization by single dipole. In *Computing in Cardiology*, IEEE, 1–4.

[4] Aras, K., Good, W., Tate, J., Burton, B., Brooks, D., Coll-Font, J., Doessel, O., Schulze, W., Potyagaylo, D., Wang, L., van Dam, P., MacLeod, R. (2015). Experimental data and geometric analysis repository-EDGAR. *Journal of Electrocardiology*, 48 (6), 975–981.

[5] Ford, W. (2015). *Numerical Linear Algebra with Applications*, Academic Press.

# Problems of Estimating Fractal Dimension by Higuchi and DFA Methods for Signals That Are a Combination of Fractal and Oscillations

**Hana Krakovská, Anna Krakovská**

Institute of Measurement Science, Slovak Academy of Sciences, Bratislava, Slovakia
Email: hana.krakovska@savba.sk

***Abstract.*** *Stochastic fractals of the 1/f noise type are an important manifestation of the brain's electrical activity and other real-world complex systems. Fractal complexity can be successfully estimated by methods such as the Higuchi method and detrended fluctuation analysis (DFA). In this study, we show that if, as with the EEG, the signal is a combination of fractal and oscillation, the estimates of fractal characteristics will be inaccurate. On our test data, DFA overestimated the fractal dimension, while the Higuchi method led to underestimation in the presence of high-amplitude, densely sampled oscillations.*

*Keywords: Fractal, 1/f Noise, Higuchi Dimension, Detrended Fluctuations Analysis, EEG*

## 1. Introduction

Electroencephalogram (EEG) is the recording of the electrical activity of the brain, and its analysis is of importance for improving our understanding of the human brain's functions and pathology. In addition to the apparent oscillating character, EEG is also a fractal or $1/f^{\beta}$ noise, which is an indication of scale-free underlying dynamics. It is known that fractal characteristics such as fractal dimension ($D$), spectral power-law slope $\beta$, and Hurst exponent ($H$), are nicely related:

$$D = 2 - H = \frac{5-\beta}{2}, \text{ for } 1 \leq \beta \leq 3, [1].$$

The consequence is that if you estimate one of the characteristics, you also get the others. In this study, we will estimate $D$ and the Hurst exponent.

The fractal characteristics of the EEG signal have proven to be particularly effective in recognizing the onset of epileptic seizures [2], classifying sleep stages [3], and many other applications. There are several ways to estimate $D$ from a time series. We will focus on two commonly used approaches, the Higuchi method [4] and detrended fluctuation analysis [5]. The methods are tailored for fractal signals to capture statistical self-similarity when examining signals at different scales. They are usually applied to discrete measured values, and their performance is affected by factors such as data length, sampling frequency, or measurement noise [1], [6].

In this paper, we are interested in how Higuchi dimension and DFA perform if the signal is not a pure fractal, but also has a strong rhythmic component. This is motivated by the uncertainty surrounding fractal analysis of EEGs, which are typical examples of signals that combine self-affinity with oscillations (the well-known delta, theta, alpha, beta and gamma waves). We will create synthetic signals as the sums of sine functions and fractional Brownian motion (fBm) as a representative of a stochastic monofractal. We will consider different amplitudes for oscillations and various sampling of final signals and ask under what conditions, if at all, the presence of the rhythmic part distorts the estimate of fractal complexity.

## 2. Subject and Methods

*Fractional Brownian Motion*

Fractional Brownian motion is a stochastic process, defined as:

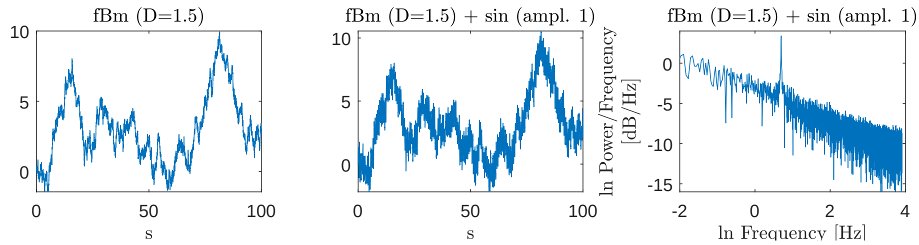


Fig. 1: 10000 points of fBm signal of $D = 1.5$ for time $[0, 100s]$ (on the left) and combination of the same fractal and sine of amplitude 1 (in the middle). The right figure shows the ln-ln representation of the power spectrum with a visible peak representing the sine frequency.

$$Z(t) \stackrel{\mathrm{d}}{=} W t^H, \quad t > 0,$$

where $W \sim \mathcal{N}(0,1)$ and $H \in (0,1)$ is called the Hurst exponent. The process is self-affine, meaning that:

$$X(\lambda t) \stackrel{\mathrm{d}}{=} \lambda^H X(t), \quad t \geq 0,$$

where $\lambda > 0$, and $\stackrel{\mathrm{d}}{=}$ denotes equality in distribution. FBm is a non-stationary process with stationary increments, which are negatively correlated for $H < 0.5$, and positively correlated for $H > 0.5$. Its fractal dimension $D$ is related to the Hurst exponent via the formula $D = 2 - H$.

*Data*

We will investigate the performance of the methods on three types of data: pure sine, fBm with varying dimensions and the conceptual synthetic EEG signal, given as their combination:

$$s_{EEG} = fBm(t) + A \times sin(2\pi f_{sin} t),$$

where the frequency $f_{sin} = 2.0063$ was randomly chosen (in order to avoid potential numerical problems with frequency exactly equal to 2). We consider two amplitudes $A = \{1, 0.2\}$ and the fBm element of the signal will have three values of dimensions $D = \{1.2, 1.5, 1.8\}$. For the purpose of this paper, we will present only the results for the variant with $D = 1.5$. We will use 10000 data points. Since the fBm is self-similar, the sampling frequency does not have an impact on the estimated dimensions of pure fBm. On the other hand, in the case of sine, we will test sampling of approximately 500, 50 and 5 points per period.

The fBm signals were generated by an exact algorithm from Davies and Harte [7]. Example of our synthetic test data is shown in Figure 1.

*Higuchi method*

Higuchi method, introduced in [4], estimates how the fluctuations of the fractal curve change with a reduced sampling of the data. More specifically, given a time series $X(1), X(2), \ldots, X(N)$, one constructs a reduced time series $X_k^m$ that includes only every $k$-th point, starting from the $m$-th ($m = 1, 2, \ldots, k$) position:

$$X_k^m : \quad X(m), X(m+k), X(m+2k), \ldots X\left(m + \left\lfloor \frac{N-m}{k} \right\rfloor k\right).$$

Then, the length of the curve $L_k^m$ is calculated:

$$L_k^m = \sum_{i=1}^{\left\lfloor \frac{N-m}{k} \right\rfloor} |X(m+ik) - X(m+(i-1)k)| \times \frac{N-1}{\left\lfloor \frac{N-m}{k} \right\rfloor k^2}.$$

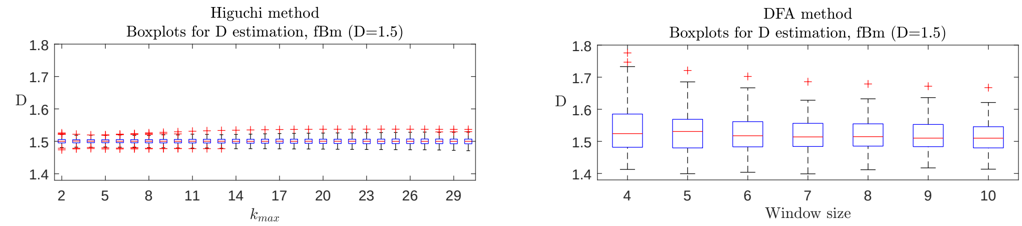


Fig. 2: Boxplots of estimates of fractal dimension $D$ for 100 fBm's of length of 10000 points, generated by Davies and Harte algorithm. Results for Higuchi method (on the left) and DFA (on the right).

From $L_k^m$, the average curve length $L(k) = \frac{1}{k}\sum_{m=1}^{k} L_k^m$ can be found. Finally, one observes the following scaling for fractal signals $L(k) \sim k^{-D}$, where $D$ is the fractal dimension.

When applying the algorithm, the range of the values of $k$ needs to be determined. We will set the range to $k = \{1, 2, \ldots k_{max}\}$ and investigated how the choice of $k_{max}$ influences the estimates.

*Detrended Fluctuation Analysis*

The DFA method, first introduced by Peng et al. [5], is a scaling analysis method that is suitable also for non-stationary signals. The output of the method is an exponent $\alpha$, which for fBm is related to the Hurst exponent through $\alpha = H + 1$ [5].

The method consists of the following steps. Let us consider a time series $X(1), X(2), \ldots, X(N)$. First, one constructs a cumulative sum with subtracted mean $\langle X \rangle = \frac{1}{N}\sum_{i=1}^{N} X(i)$:

$$Y(i) = \sum_{i=1}^{N} (X(i) - \langle X \rangle).$$

Next, the signal is divided into non-overlapping boxes of size $l$, and in them, we calculate the local trend by using the linear least-squares fit. Then, we detrend the data in each box and calculate the root mean square of the detrended time series $Y_l(i)$:

$$F(l) = \sqrt{\frac{1}{N}\sum_{i=1}^{N} Y_l(i)^2}.$$

Finally, the scaling is determined by an exponent $\alpha$: $F(l) \sim l^{\alpha}$. The considered box sizes $l$ should be $4 < l$ and $l < N/4$ [5]. To investigate this parameter, we chose various ranges of box (window) size.

## 3. Results and Discussion

The results of the application of the Higuchi method and DFA on the fBm signal with $D = 1.5$ are summarized in Figure 2. The results for the combination of fBm (D=1.5) and sine can be found in Figure 3. Window size parameter $i$ represents the considered range of box sizes in DFA, for a given $i$ we considered box sizes $\{i, i+1, \ldots, N/i\}$, where the length of the signal is $N = 10000$. We can notice that using the Higuchi method, the estimates of $D$ of pure fBm are more accurate than using DFA. The best choice for $k_{max}$ lies in the range of $5 - 10$, and for DFA, larger window sizes performed better.

In Figure 3, we can see that while DFA overestimates the dimension in the presence of densely sampled high-amplitude oscillations, Higuchi method does so in sparse sampling.

EEG signals combine both arrhythmic (fractal) and rhythmic activities that are likely to have different origins. However, both have proven useful in brain research, and it is, therefore, important to characterize them as accurately as possible. The two time-domain methods used here

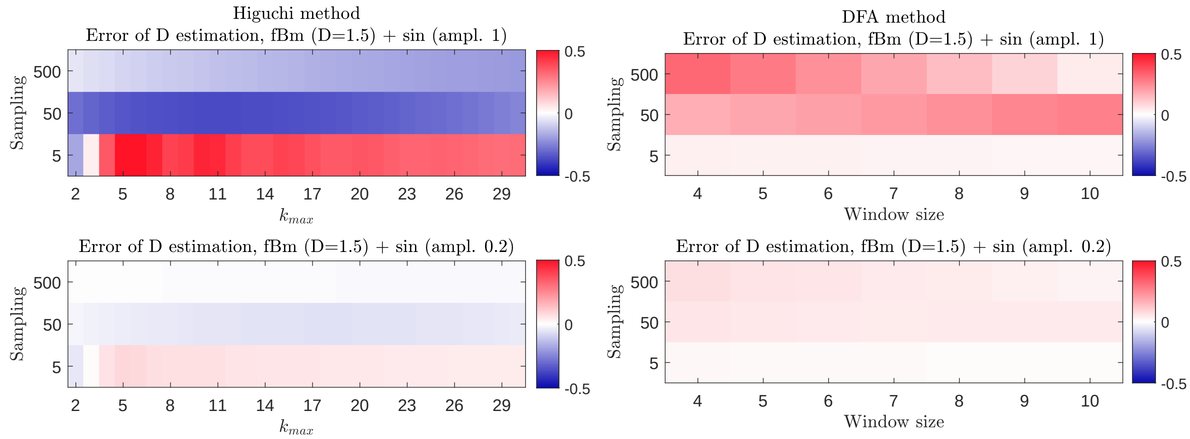


Fig. 3: Average error of dimension estimation for 100 fBm signals ($D = 1.5$)+sine signal. 500, 50 or 5 samples per period and varying parameters $k_{max}$ and window size of Higuchi and DFA methods are used. The colors indicate an underestimation (blue) or an overestimation (red) of the $D$ estimates.

approach the estimation of fractal complexity differently, and - as we found in this study - they also react differently to the presence of an oscillatory component.

The question for future research is whether we can estimate the fractal characteristics of such signals as EEG better after separating the rhythmic and arrhythmic components in the frequency domain, for example, by the method from [8]. Fractal measures are then derived from the spectral power-law slope $\beta$, which is not the most accurate method for pure fractals [6], but could become the recommended choice for fractals with added oscillations.

**Acknowledgements**

Supported by the Slovak Grant Agency for Science (Grant 2/0081/19).

**References**

[1] Eke, A., Herman, P., Kocsis, L., Kozak, L. (2002). Fractal characterization of complexity in temporal physiological signals. *Physiological Measurement*, 23(1), R1.

[2] Esteller, R., Vachtsevanos, G., Echauz, J., Henry, T., Pennell, P., Epstein, C., Bakay, R., Bowen, C., Litt, B. (1999). Fractal dimension characterizes seizure onset in epileptic patients. In: *1999 IEEE International Conference on Acoustics, Speech, and Signal Processing. Proceedings. ICASSP99 (Cat. No.99CH36258)*, Vol. 4, 2343–2346.

[3] Šušmáková, K., Krakovská, A. (2008). Discrimination ability of individual measures used in sleep stages classification. *Artificial Intelligence in Medicine*, 44(3), 261–277.

[4] Higuchi, T. (1988). Approach to an irregular time series on the basis of the fractal theory. *Physica D: Nonlinear Phenomena*, 31(2), 277–283.

[5] Peng, C.-K., Buldyrev, S.V., Havlin, S., Simons, M., Stanley, H.E., Goldberger, A.L. (1994). Mosaic organization of dna nucleotides. *Physical Review E*, 49(2), 1685.

[6] Krakovská, A., Krakovská, H. (2016). Dimension of self-affine signals: four methods of estimation. *arXiv:1611.06190*.

[7] Davies, R. B., Harte, D. (1987). Tests for hurst effect. *Biometrika* 74(1), 95–101.

[8] Wen, H., L.Z. (2016). Separating fractal and oscillatory components in the power spectrum of neurophysiological signal. *Brain Topography,* 29(1), 13–26.

# Comparison of MFDFA and Chhabra-Jensen Method on Multifractal and Monofractal Data

**Hamed Farahani**

Institute of Measurement Science, Slovak Academy of Sciences, Bratislava, Slovakia
Email: hamed.farahani@savba.sk

***Abstract.*** *Researchers of different fields attempt to characterize time series in complex systems. In this comparative study, the behaviour of two well-known complexity methods called multifractal detrended fluctuation analysis (MFDFA) and Chhabra-Jensen (CJ) method was investigated. The results showed that the width of the singularity spectrum, as the main factor of complexity, for both deterministic and stochastic binomial data could be properly estimated by MFDFA and the CJ method. The symmetric assumption about the singularity spectrum of stochastic binomial data was reflected by both methods, for deterministic data, it was more closely followed by the CJ method. Moreover, the results indicated CJ cannot track the singularity spectrum of monofractal data properly as compared with MFDFA.*

*Keywords: Multifractal Detrended Fluctuation Analysis, Chhabra-Jensen Method, Binomial Multifractal Model*

## 1. Introduction

In recent years fractal geometry has emerged as a powerful platform for describing natural phenomena. Several techniques currently exist for analyzing data drawn from fractal systems such as geophysics (river runoff), physiology and medicine (DNA sequences), and econophysics (stock prices) [2]. However, multifractal structures cannot be represented by a single exponent, thus, they require a continuous spectrum of exponents [3]. Many algorithms have been developed to represent the multifractal scaling behaviour of time series. Multifractality in time series is generally classified into two types, the first one relates to the broad probability density function and the second to different long-range correlations of the small and large fluctuations [2].

This study compares the accuracy of the CJ method and MFDFA in estimating the complexity of binomial multifractal data, Weierstrass function data, and fractional Brownian motion data. These results can be insightful in different domain areas.

## 2. Subject and Methods

One of the well-known tools for generating multifractal data is the binomial multifractal model [1] in which elements are constructed according to

$$x_k = a^{n(k-1)}(1-a)^{n_{max}-n(k-1)} \tag{1}$$

where $a$ parameter is restricted to $0.5 < a < 1$, $k$ parameter is defined as $k = 1, ..., 2^{n_{max}}$ and $n(k)$ is an operator that calculates sum of digits equal to 1 in the binary representation of $k$.

We will also use monofractals for testing, namely the Weierstrass function (Wf) and fractional Brownian motion (fBm). The Weierstrass function, as everywhere continuous and nowhere differentiable function, has been used for modelling monofractal time series. Fractional Brownian motion is also suggested to generate self-affine time series [1].

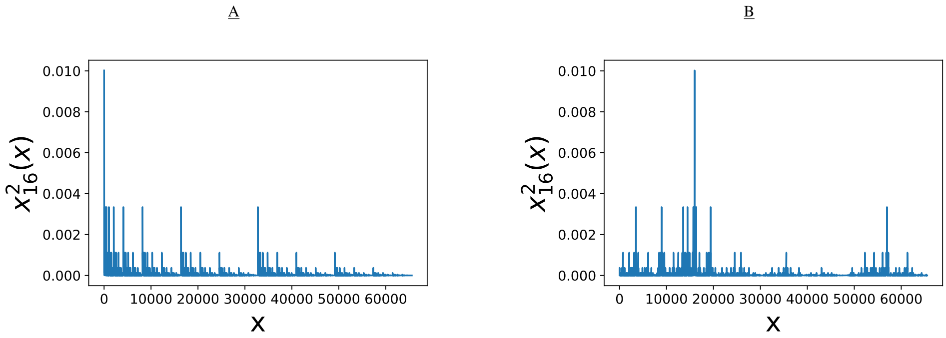


Fig. 1: (A) Deterministic binomial data with $a = 0.75$ and $n_{max} = 16$; (B) Stochastic binomial data with $a = 0.75$ and $n_{max} = 16$

Multifractal detrended fluctuation analysis is a generalization of the conventional detrended fluctuation analysis (DFA) via the standard partition function concept. It determines the singularity spectrum through the Legendre transform [2].

The Chhabra-Jensen method is utilized as a direct method which, unlike MFDFA, does not use Legendre transformations. It consists of calculating normalized probabilities and subsequently obtaining a multifractal spectrum [3]. The width of the singularity spectrum, $\Delta(\alpha) = \alpha_{max} - \alpha_{min}$, is a measure of the time series' complexity. The more complex the time series, the wider the spectrum. Very narrow width is an indication that the data are monofractal or non-fractal instead of multifractal.

## 3. Results

*Generating Binomial Cascade*

The deterministic and stochastic test data were generated by the binomial multifractal model with parameters $n_{max}$ and $a$ set to 16 and 0.75, respectively (Figure 1).

*Chhabra-Jensen Method vs. MFDFA*

For drawing comparison between MFDFA and CJ, multifractal spectrum and the $q$-order Hurst exponent were plotted (Figure 2).

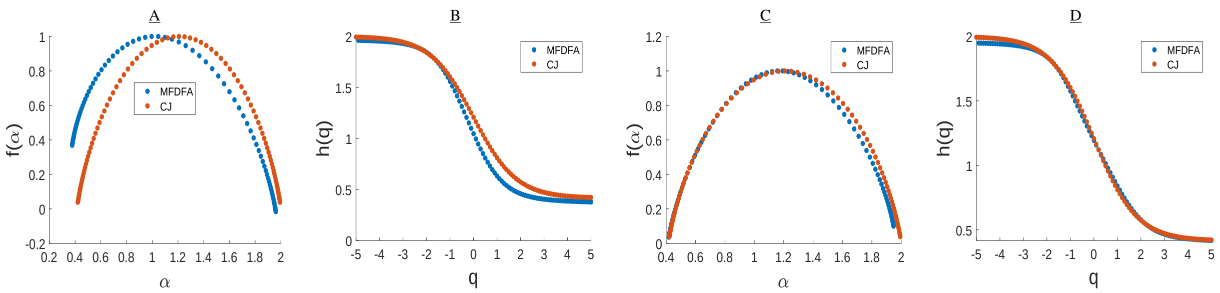


Fig. 2: MFDFA against CJ singularity spectrum of (A) the deterministic binomial multifractal data with $a = 0.75$, (C) the stochastic binomial multifractal data with $a = 0.75$, MFDFA against CJ plots of $h_q$ vs. $q$ calculated for (B) the deterministic binomial multifractal data with $a = 0.75$, (D) the stochastic binomial multifractal data with $a = 0.75$.

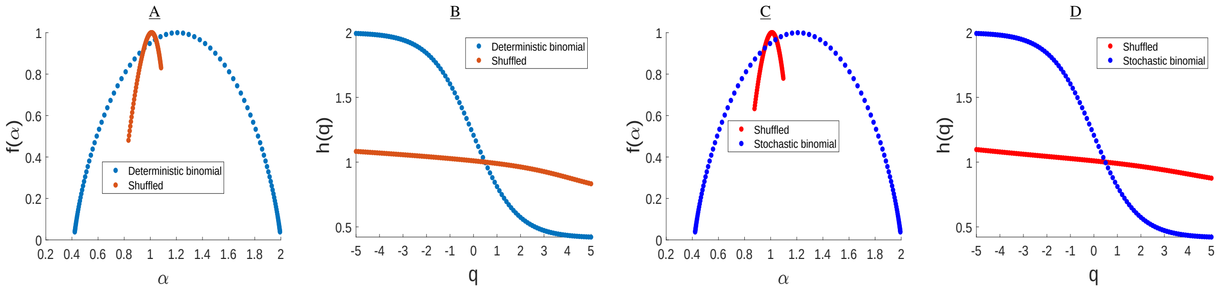


Fig. 3: CJ singularity spectrum of (A) the deterministic binomial multifractal data with $a = 0.75$ against its shuffled, (C) the stochastic binomial multifractal data with $a = 0.75$ against its shuffled. CJ plots of $h_q$ vs. $q$ calculated for (B) the deterministic binomial multifractal data with $a = 0.75$ against its shuffled, (D) the stochastic binomial multifractal data with $a = 0.75$ against its shuffled.

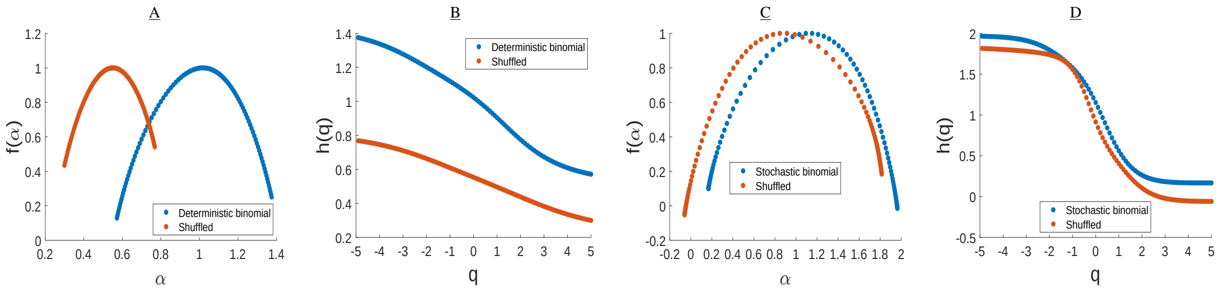


Fig. 4: MFDFA singularity spectrum of (A) the deterministic binomial multifractal data with $a = 0.6$ against its shuffled, (C) the stochastic binomial multifractal data with $a = 0.6$ against its shuffled. MFDFA plots of $h_q$ vs. $q$ calculated for (B) the deterministic binomial multifractal data with $a = 0.6$ against its shuffled, (D) the stochastic binomial multifractal data with $a = 0.6$ against its shuffled.

### *Binomial Data vs. Shuffled*

The original order of the data points was shuffled to remove correlations and measured the singularity spectrum to investigate the effect of correlation on the multifractality. Removing the correlations by shuffling influenced the singularity spectrum of the data generated with $a = 0.75$ (Figure 3), but not the singularity spectrum of the data generated with $a = 0.6$ (Figure 4).

### *Multifractal vs. Monofractal*

Figure 5 enables us to compare the width of the singularity spectra for monofractal and multifractal data. This figure shows considerable differences between the width of the singularity spectrum of binomial multifractal data and data generated with the Weierstrass function ($D = 1.4$).

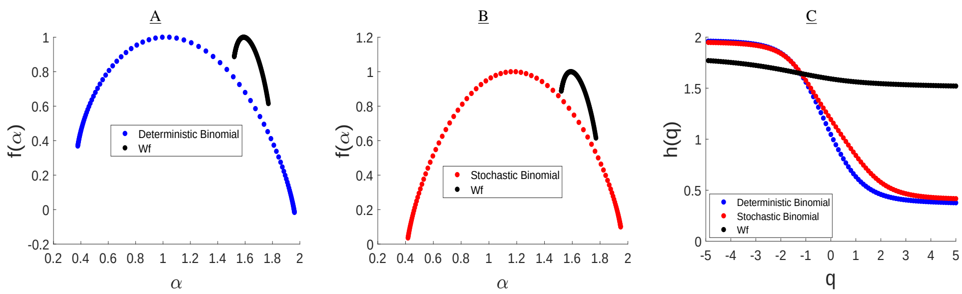


Fig. 5: MFDFA singularity spectra of (A) the deterministic binomial multifractal data with $a = 0.75$ and Wf with $D = 1.4$, (B) the stochastic binomial multifractal data with $a = 0.75$ and Wf with $D = 1.4$, (C) MFDMA plots of $h_q$ vs. $q$ calculated for both binomial multifractal data with $a = 0.75$ and Wf with $D = 1.4$.

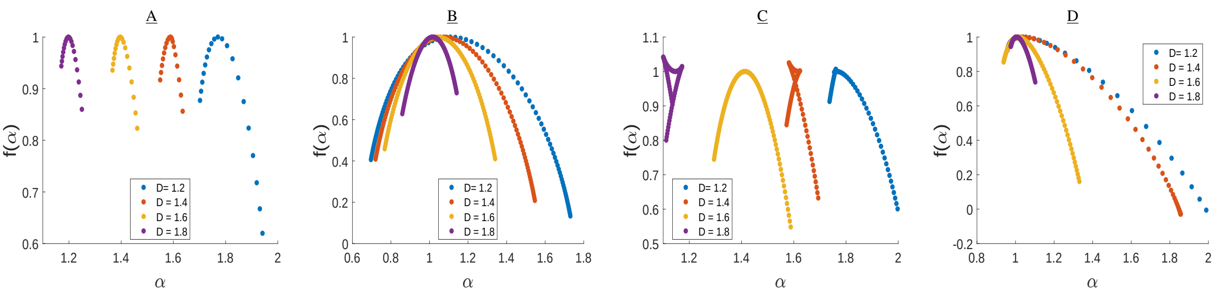


Fig. 6: MFDFA singularity spectra of (A) Wf data, (C) fBm data. CJ singularity spectra of (B) Wf data, (D) fBm data

*Monofractals*

Tables 1 and 2 report $\alpha(q=2)$, Hurst exponent and fractal dimension of Wf and fBm by MFDFA. The $\alpha(q=2)$ between 0 and 1 means that the time series is produced by a stationary process and $H=\alpha$, $\alpha(q=2)$ between 1 and 2 means non-stationary process and $H=\alpha-1$, $D=2-H$ [2]. As was mentioned earlier, it is expected that both methods estimate a very narrow width of the singularity spectrum in which MFDFA outperformed CJ.

Table 1: MFDFA dimension estimations of the Wf tested data.

| exact dimension | $\alpha(q=2)$ | Hurst exponent | fractal dimension |
|---|---|---|---|
| 1.2 | 1.7334 | 0.7334 | 1.2666 |
| 1.4 | 1.5715 | 0.5715 | 1.4285 |
| 1.6 | 1.3835 | 0.3835 | 1.6165 |
| 1.8 | 1.1845 | 0.1845 | 1.8155 |

Table 2: MFDFA dimension estimations of the fBm tested data.

| exact dimension | $\alpha(q=2)$ | Hurst exponent | fractal dimension |
|---|---|---|---|
| 1.2 | 1.7609 | 0.7609 | 1.2391 |
| 1.4 | 1.6123 | 0.6123 | 1.3877 |
| 1.6 | 1.3526 | 0.3526 | 1.6474 |
| 1.8 | 1.1700 | 0.1700 | 1.8300 |

## 4. Discussion

This study has compared MFDFA and CJ on multifractal and monofractal data. To this end, multifractal data was generated with a binomial model and monofractal data was generated with Wf and fBm. According to theoretical calculations, it is expected that both the deterministic and stochastic data are represented by $\Delta(\alpha)\approx 1.58$, $h(-\infty)=0.4$ and $h(-\infty)=2$, complexity indices, when the value of $a$ is equal to 0.75. As shown in Figure 4, both MFDFA and CJ analyses could achieve satisfactory results. The obtained results from the CJ analysis revealed that this method could mostly follow the symmetric singularity spectrum assumption, as expected. CJ can produce misleading results concerning monofractal data.

## References

[1] Feder, J. (2013). Fractals. In *Springer Science & Business Media*.

[2] Kantelhardt, J. W., Zschiegner, S. A., Koscielny-Bunde, E., Havlin, S., Bunde, A., Stanley, H. E. (2002). Multifractal detrended fluctuation analysis of nonstationary time series. In *Physica A: Statistical Mechanics and its Applications*, 1-4, 87–114.

[3] Chhabra, A., Jensen, R. V. (1989). Direct determination of the f ($\alpha$) singularity spectrum. In *Physical Review Letters*, 12, 1327.

# *Theoretical Problems of Measurement - Posters III*

# Comparison of the Estimation Errors of Parameters Associated With Individual Voltage Fluctuations Sources Using Selected Decomposition Methods

**Piotr Kuwałek**

Institute of Electrical Engineering and Electronics, Poznan University of Technology
Poznan, Poland
Email: piotr.l.kuwalek@doctorate.put.poznan.pl

***Abstract.*** *The paper presents preliminary research results on the estimation errors of parameters associated with individual voltage fluctuations sources using selected decomposition methods, i.e. Empirical Mode Decomposition (EMD), Empirical Wavelet Transform (EWT), Enhanced Empirical Wavelet Transform (EEWT). The estimated parameters are the rate of changes in the operating state of disturbing loads and the voltage changes values caused by a particular source of the disturbance. The decomposition of the voltage modulating signal, assuming that the voltage fluctuations can be identified with the amplitude modulation without the suppressed carrier wave, was used for estimation. The paper presents the results of experimental studies that allow comparing the accuracy of the estimation errors of parameters associated with individual voltage fluctuations sources using selected decomposition methods. Experimental studies were included typical sources of voltage fluctuations that cause fast voltage changes.*

*Keywords: Decomposition, Demodulation, Power Quality, Voltage Fluctuations*

## 1. Introduction

One of the typical disturbances in the power grid is voltage fluctuations, which can be defined as fast changes in the maximum or rms value of a voltage [1]. Voltage fluctuations can cause flicker and the incorrect operation of loads supplied from the power grid. Hence, it is important to locate such loads to eliminate the interference they cause [2, 3].

The change in the maximum value of the voltage at time $U_m(t)$ in a stiff power grid can be identified with the change in the envelope of the amplitude modulated (AM) voltage (without the suppressed carrier wave) [4, 5]. This assumption is used in the signal chain of flickermeter [6, 7], allowing the measurement of indicators of short-term and long-term flicker. Typically, change in the voltage envelope is the result of the impact of many sources of voltage fluctuations, so the AM modulating signal is the resultant signal. The decomposition of the AM modulating signal or the voltage envelope allows selective location sources of voltage fluctuations by assessing the propagation of voltage changes associated with the individual voltage fluctuation sources [8].

The paper presents research results, assessing the diagnostic possibilities of decomposition (Empirical Mode Decomposition (EMD) [9], Empirical Wavelet Transform (EWT) [10] or Enhanced Empirical Wavelet Transform (EEWT) [11]) for the estimation of selected parameters (the rate of changes $f_m$ in the operating state of disturbing loads and the voltage changes values $(\delta U/U_m)$ caused by a particular source of disturbance), which are associated with the individual sources of voltage fluctuations. In the experimental research, the rectangular shape with an asymmetrical duty cycle was considered, because most voltage fluctuations are caused by rapid voltage changes [12, 8, 13].

## 2. Identification of Parameters Associated With Voltage Fluctuation Sources

The identification algorithm is precisely discussed in [8], where the EEWT algorithm is used to decompose the modulating signal [14]. However, it does not discuss the impact of the decomposition method on the accuracy of identification of selected parameters. Hence, an attempt is made to evaluate the estimation errors of selected parameters depending on the selected method of decomposition in the signal chain of the identification algorithm [8]. Fig. 1 shows the waveform of the voltage envelope in case of occurring one source of voltage fluctuations, with marked considered parameters associated with its operation. In the case of independent operation of more sources of disturbance, the modulating signal or voltage envelope is the sum of signals associated with individual sources [12, 8]. Voltage fluctuations with the shape shown in Figure 1 are typical disturbance and result from cyclic switching on and off of loads [8, 13, 12].

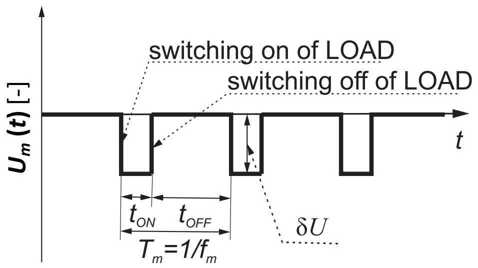


Fig. 1: The example of a voltage envelope with variation caused by cyclic switching on and off of load

## 3. Research Results

To compare the estimation error of amplitude and frequency of voltage changes associated with the specific disturbing loads, the following coefficients are assumed: $k_c/k$ and $f_{mc}/f_m$ assessing the decomposition accuracy for correct estimation of the amplitude ($\delta U/U_m$=2$k$) and frequency respectively, of voltage changes caused by individual sources of disturbance, where $k_c$ and $f_{mc}$ are respectively the amplitude and frequency of the estimated components of the modulation signal. For ideal decomposition, the $k_c/k$ and $f_{mc}/f_m$ should be equal to one.

In experimental studies, voltage fluctuations were modeled in accordance with the equation:

$$u(t) = \sqrt{2}U_c \sin(2\pi f_c t)\left[1 + u_{mod1}(t) + u_{mod2}(t)\right], \tag{1}$$

where $U_c$=230 V, $f_c$=50 Hz. In the research it was assumed that the components of modulating signal ($u_{mod1}(t)$ and $u_{mod2}(t)$) are rectangular signals with a duty cycle $\delta = t_{ON}/\left(t_{ON} + t_{OFF}\right)$, described by the equation:

$$u_{modi}(t) = \begin{cases} k_i & lT_{m_i} < t < lT_{m_i} + t_{ON} \\ -k_i & lT_{m_i} + t_{ON} \leq t \leq (l+1)\,T_{m_i} \end{cases}, \tag{2}$$

where: $i$=1,2; $k_i$ and $T_{mi}$=1/$f_{mi}$ is respectively the amplitude and period of the modulation signal associated with the $i$-th source of voltage fluctuations, and $l$ is any natural number.

To evaluate the accuracy of the estimation of selected parameters using the EMD, EWT and EEWT decomposition, the following parameters of the component signals were assumed: $k_2$=0.025 (depth of modulation of 5%), $k_1 \in$ [0.005 (depth modulation of 2%); 0.05 (depth modulation of 10%)], $f_{m2}$=2 Hz, $f_{m1} \in$ [0.01;50] Hz, $\delta_2$=50%, $\delta_1 \in \{10\%, 30\%, 50\%, 70\%, 90\%\}$.

In experimental research, using an arbitrary generator in PicoScope 5444d, a sinusoidal signal with $f_c$=50 Hz (carrier signal) was AM modulated (without suppressed carrier wave) with signal described by equation (1). Using the amplifier built into CHROMA 61502, the modulated signal was amplified to the voltage level in the low voltage network (the gain was selected in such a way that the rms value of voltage $U_c$ without modulation (carrier signal), was equal to the nominal value of voltage in the low voltage network). The amplified voltage signal was recorded using the measuring card PicoScope 5444d. For the recorded signal, the amplitude and frequency of individual components of the modulation signal (associated with individual disturbing loads), obtained from the decomposition were estimated.

Figure 2 shows an example of an given component signal $u_{mod1}(t)$ with $f_{m1}$=5 Hz, $k_1$=0,025, and $\delta_1$=90%; and its estimation obtained using EMD, EWT and EEWT. Estimated parameters $k_{1c}$ and $f_{m1c}$ associated with selected disturbing load are marked on the presented waveforms.

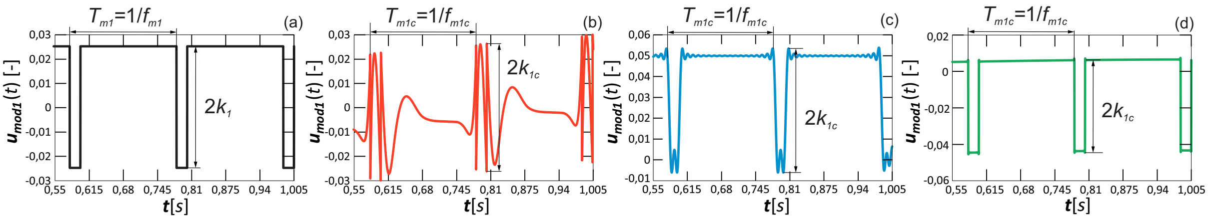

Fig. 2: The example of the given component signal $u_{mod1}(t)$ with $f_{m1}$=5 Hz, $k_1$=0,025, and $\delta_1$=90% (a); and its estimation obtained using EMD (b), EWT (c) and EEWT (d)

Figures. 3 shows the characteristics $k_{1c}/k_1$=f($f_{m1}$) and $f_{m1c}/f_{m1}$=f($f_{m1}$) for $u_{mod1}(t)$ with the amplitude of $k_1 = 0,05$ and with the duty cycle of $\delta_1 \in \{50\%, 90\%\}$. The characteristics $k_c/k$=f($f_{m1}$) and $f_{mc}/f_m$=f($f_{m1}$) for $u_{mod2}(t)$, and for $u_{mod1}(t)$ with other parameters $k_1$ and $\delta_1$, are omitted, because the tendency of error for these cases are coincided with the presented results.

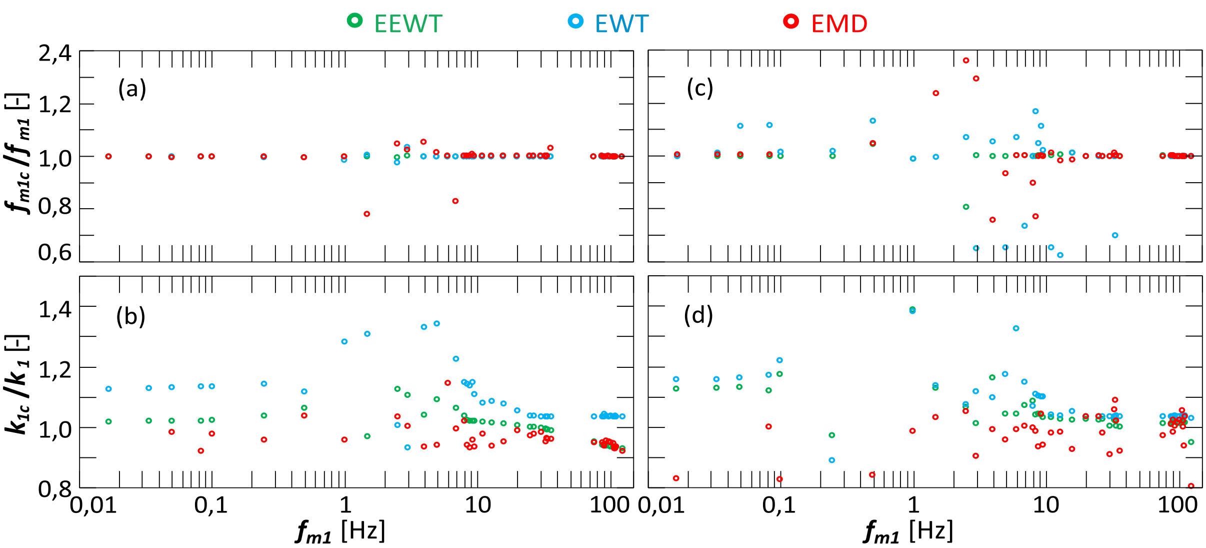

Fig. 3: (a) The characteristic $f_{m1c}/f_{m1} = \mathbf{f}(f_{m1}; k_1 = 0,05; \delta_1 = 50\%; f_{m2} = 2\,\text{Hz}; k_2 = 0,025; \delta_2 = 50\%)$; (b) The characteristic $k_{1c}/k_1 = \mathbf{f}(f_{m1}; k_1 = 0,05; \delta_1 = 50\%; f_{m2} = 2\,\text{Hz}; k_2 = 0,025; \delta_2 = 50\%)$; (c) The characteristic $f_{m1c}/f_{m1} = \mathbf{f}(f_{m1}; k_1 = 0,05; \delta_1 = 90\%; f_{m2} = 2\,\text{Hz}; k_2 = 0,025; \delta_2 = 50\%)$; (d) The characteristic $k_{1c}/k_1 = \mathbf{f}(f_{m1}; k_1 = 0,05; \delta_1 = 90\%; f_{m2} = 2\,\text{Hz}; k_2 = 0,025; \delta_2 = 50\%)$

## 4. Discussion and Conclusions

The best estimation of the selected parameters is achieved when both component signals have the duty cycle of 50%. In this case, the fundamental harmonic in the spectrum of the component signal is dominant. If the fundamental harmonic in the spectrum of the component signal is significantly lower than the higher harmonics ($\delta_1 \in \{10\%, 90\%\}$), the decomposition error increases. If additionally $f_{m1} \approx f_{m2}$, the shape of the estimated component signals is significantly distorted and maximal errors of estimation of the desired parameters occur. The maximum error mainly depends on the contribution of the fundamental harmonic in the spectrum of the component signal (duty cycle $\delta$). If the frequency of the component signals is equal ($f_{m1} = f_{m2}$), the individual component signals are not detected.

The estimation error of amplitude of the voltage changes $\delta U/U_m$=2$k$ caused by the specific disturbing loads, is greater than the frequency estimation error because of rapid changes Gibbs effect has occurred. For the EEWT and EWT methods, the error does not depend on the amplitude value of the component signal, unlike the EMD method. For the EMD method, as the value of the amplitude of the component signal decreases, the inaccuracy of the estimation of considered parameters for this component signal increases. This is dangerous because in practice the relative amplitude of the voltage changes $\delta U/U_m$ caused by the individual disturbing loads are small ($k \ll 1$). For the EWT method, the amplitude estimation error is much greater than for the EEWT method.

The EEWT method does not cause data redundancy, which is for EWT and EMD methods. The EMD decomposition creates redundant signals resulting from the operation of the algorithm, that does not have a physical interpretation. The data redundancy in EWT method results from the incorrect division of the spectrum of AM modulating signal. Thus, several EWT result signals can create one real signal associated with the source of voltage fluctuations. Furthermore, EMD and EWT causes excessive changes (Figure 2), which may result in incorrect locating of the disturbing load in the power grid.

**References**


[1] (2016) IEV number 161-08-05, Voltage fluctuation. [Online]. Available: `http://www.electropedia.org/`

[2] Wiczynski G. (2020). Determining location of voltage fluctuation source in radial power grid. *Electric Power Systems Research*, 180, art. no. 106069.

[3] Otomanski P., et al. (2011). The usage of voltage and current fluctuation for localization ofdisturbing loads supplied from power grid. *Przeglad Elektrotechniczny*, 87(1), 107–111.

[4] Wiczynski G. (2017). Estimation of $P_{st}$ indicator values on the basis of voltage fluctuation indices. *IEEE Transactions on Instrumentation and Measurement*, 66(8), 2046–2055.

[5] Wiczynski G. (2010). Analysis of flickermeter's signal chain for input signal with two sub/interharmonics. *Przeglad Elektrotechniczny*, 86(4), 328–335.

[6] Majchrzak J., Wiczynski G. (2012). Basic Characteristics of IEC Flickermeter Processing. *Modelling and Simulation in Engineering*, 2012, art. no. 362849.

[7] Wiczynski G. (2009). A Model of the Flickermeter for Frequency Modulation of the Input Voltage. *IEEE Trans. on Instrumentation and Measurement*, 58(7), 2139–2144.

[8] Kuwalek P. (2021). Estimation of Parameters Associated With Individual Sources of Voltage Fluctuations. *IEEE Transactions on Power Delivery*, 36(1), 351–361.

[9] Onal Y., Gerek O.N., Ece D.G (2016). Empirical mode decomposition application for short-therm flicker severity. *TTurkish Journal of Electrical Engineering & Computer Sciences*, 24, 499–509.

[10] Gilles J. (2013). Empirical Wavelet Transform. *IEEE Transactions on Signal Processing*, 61(16), 3999–4010.

[11] Hu Y., et al. (2017). An Enhanced Empirical Wavelet Transform for noisy and non-stationary signal processing. *Digital Signal Processing*, 60, 220–229.

[12] Wiczynski G. (2017). Estimation of Pst indicator value for a simultaneous influence of two disturbing loads. *Electric Power Systems Research*, 147, 97–104.

[13] Kuwalek P., Jesko W. (2020). Recreation of Voltage Fluctuation Using Basic Parameters Measured in the Power Grid. *Journal of Electrical Engineering & Technology*, 15(2), 601–609.

[14] Kuwalek P. (2020). AM Modulation Signal Estimation Allowing Further Research on Sources of Voltage Fluctuations. *IEEE Transactions on Industrial Electronics*, 67(8), 6937–6945.

# Determination of the Exact Confidence Intervals for Parameters in a Model of Direct Measurements With Independent Random Errors

**[1]Gejza Wimmer, [2]Viktor Witkovský**

[1]Mathematical Institute, Slovak Academy of Sciences, Bratislava, Slovak Republic
[2]Institute of Measurement Science, Slovak Academy of Sciences, Bratislava, Slovak Republic
Email: wimmer@mat.savba.sk

***Abstract.*** *Presented is a simple real-data example with analysis of direct pressure measurements by electronic pressure transducer sensors, which illustrates our new method for obtaining exact confidence intervals for the unknown parameters in linear regression models. The method assumes that the errors are expressible as linear combinations of independent random variables with known, however, not necessarily normal distributions. The suggested method for calculating the confidence intervals in linear regression models with possible parameter constraints is based on the application of the characteristic function approach (CFA).*

*Keywords: Linear Regression Model, Direct Measurements, Best Linear Unbiased Estimator, Exact Distribution of Parameter Estimator, Confidence Interval, Characteristic Function Approach (CFA)*

## 1. Introduction

In [3], we have suggested a general method for computing the exact probability distribution of the best linear unbiased estimator (BLUE) of a linear combination of the unknown model parameters in linear regression model with possible constraints. The proposed method is based on the assumption that the model errors, i.e., the measurement errors and the systematic errors or other possible sources of uncertainty determined by the Type A and Type B evaluation methods, see [1], are expressible as linear combinations of known independent random variables, which are not necessarily normally distributed. The suggested method is based on using the characteristic function approach (CFA), see [4], which has some advantages over the standard alternative approach based on using the Monte Carlo method (MCM) suggested in [2].

Here we apply the general approach to the specific situation. In this paper, we are interested in computing the exact confidence intervals for the linear combination of the model parameters in the most simple but frequently occurred statistical model of direct measurements. Using the observed data and based on using the CFA, calculated are the realizations of the exact 95% confidence intervals for all individual parameters, which represent the measurand values (the true pressures of the measured objects).

## 2. Subject and Methods

*Uncertainty Analysis of Direct Pressure Measurements*

We present a simple real-data example of uncertainty analysis of direct pressure measurements by using electronic pressure transducer sensors measurements and by using the general method for computing the exact probability distribution of a linear combination of BLUE in linear regression model. Here we study the measurement application of the Cerabar PMP51 (PMP51-2154/0, Endres and Hauser Cerbar M) digital pressure transmitter with welded metal membrane suitable for measurement in gases, steam, or liquids, typically used in process and hygiene applications for pressure, level, volume, or mass measurement in liquids or gases. PMP51 is designed for high-pressure applications up to 400 bar. The presented data (experimental measurements) were obtained at the laboratory of the Faculty of Mechanical Engineering of the Slovak University of Technology in Bratislava.

Let $\mathcal{P}_1, \mathcal{P}_2, \ldots, \mathcal{P}_7$ denote the measured objects (seven measurands) with given suitable pressure values and let $\beta_1, \beta_2, \ldots, \beta_7$ represent the true (unknown) values of these measurands. The measurements were performed by the pressure transducer PMP51-2154/0 with measuring range (0 to 10) MPa for pressure range (0 to 4) MPa with current output (4 to 10) mA. The values of the pressure transducer PMP51-2154/0 were directly measured with the multimeter Picotest M3500A.

In accordance with [3], by $\boldsymbol{Y}^* = (Y_1^*, \ldots, Y_7^*)'$ we shall denote the (random) vector of the measurements and by $\boldsymbol{\epsilon}_1 = (\epsilon_{1,1}, \epsilon_{1,2}, \ldots, \epsilon_{1,7})'$ the random vector of errors representing the variability of the transducer values, assumed to be normally distributed with zero mean and known variance $\sigma^2$, (here, the value $\sigma^2 = 0.0000071$ was specified by expert knowledge from previous repeated experiments), i.e., $\boldsymbol{\epsilon}_1 \sim N(\mathbf{0}, \sigma^2\mathbf{I})$. Further, in measuring the quantities $\beta_i$, $i = 1, 2, \ldots, 7$, the pressure transducer has systematic errors (effects specified by the manufacturer), $\delta_{2,i} + \beta_i \epsilon_{2,i}$, where $\delta_{2,i}$ denote the known biases of these systematic errors and $\epsilon_{2,i} = \epsilon_2$ for all $i = 1, 2, \ldots, 7$. Here we have $\delta_{2,i} = \delta_2 = 0$ and $\epsilon_2$ has symmetric rectangular distribution on the interval $(-0.0005, 0.0005)$, i.e., $\epsilon_2 \sim R(-0.0005, 0.0005)$. Hence, $\beta_i \epsilon_2 \sim \beta_i R(-0.0005, 0.0005)$ or $\beta_i \epsilon_2 \sim 0.0005\, \beta_i R(-1, 1)$. Similarly, in measuring the quantities $\beta_i$, $i = 1, 2, \ldots, 7$, the multimeter has systematic errors $\delta_{3,i} + \beta_i \epsilon_{3,i}$, where $\delta_{3,i} = \delta_3 = 0$ is the known biases of these systematic errors and $\epsilon_{3,i} = \epsilon_3 + \beta_i \epsilon_4$, for all $i = 1, 2, \ldots, 7$, with $\epsilon_3 \sim 0.080002 R(-1, 1)$, $\epsilon_4 \sim 0.05 R(-1, 1)$. Please notice, that the random variables $\epsilon_{1,1}, \epsilon_{1,2}, \ldots, \epsilon_{1,7}, \epsilon_2, \epsilon_3, \epsilon_4$ are mutually independent random variables with know distributions.

In order to get the model of measurement process in a compact vector-matrix notation consistent with [3], let $\boldsymbol{\beta} = (\beta_1, \beta_2, \ldots, \beta_7)'$ denotes the 7-dimensional column vector of the parameters (true unknown values of the measurands), let $\boldsymbol{\delta} = (\boldsymbol{\delta}_1', \delta_2, \delta_3, \delta_4)'$ denotes the 10-dimensional vector of the known systematic error biases (the pressure transducer systematic error biases and the multimeter systematic error biases given specified by the expert knowledge), where $\boldsymbol{\delta}_1 = (\delta_{1,1}, \ldots, \delta_{1,7})' = (0, \ldots, 0)'$, $\delta_2 = 0$, $\delta_3 = 0$, and $\delta_4 = 0$, and let $\boldsymbol{\epsilon} = (\boldsymbol{\epsilon}_1', \epsilon_2, \epsilon_3, \epsilon_4)'$ denotes the 10-dimensional vector of the input errors, where $\boldsymbol{\epsilon}_1 \sim N(\mathbf{0}, \sigma^2\mathbf{I})$ with $\sigma^2 = 0.0000071$, $\epsilon_2 \sim R(-0.0005, 0.0005)$, $\epsilon_3 \sim R(-0.080002, 0.080002)$, and $\epsilon_4 \sim R(-0.05, 0.05)$.

Then, the model of the measuring process can be written as

$$\begin{aligned} \boldsymbol{Y}^* &= \boldsymbol{\beta} + \mathbf{Z}(\boldsymbol{\delta} + \boldsymbol{\epsilon}) \\ &= \boldsymbol{\beta} + \mathbf{Z}_1(\boldsymbol{\delta}_1 + \boldsymbol{\epsilon}_1) + \mathbf{Z}_2(\delta_2 + \epsilon_2) + \mathbf{Z}_3(\delta_3 + \epsilon_3) + \mathbf{Z}_4(\delta_4 + \epsilon_4), \end{aligned} \tag{1}$$

where $\mathbf{Z} = [\mathbf{Z}_1, \mathbf{Z}_2, \mathbf{Z}_3, \mathbf{Z}_4] = [\mathbf{I}, \boldsymbol{\beta}, \mathbf{1}, \boldsymbol{\beta}]$ is a $(7 \times 10)$-dimensional matrix, where $\mathbf{I}$ denotes a $(7 \times 7)$-dimensional identity matrix and $\mathbf{1}$ denotes a 7-dimensional column vector of ones. Based on expert knowledge, the unknown vector $\boldsymbol{\beta} = (\beta_1, \beta_2, \ldots, \beta_7)'$ in $\mathbf{Z}_2$ and $\mathbf{Z}_4$ is substituted by the vector of known values, $\boldsymbol{\lambda} = (\lambda_1, \lambda_2, \ldots, \lambda_7)'$, equal to the realized (observed) values of the corrected vector of measurements $\boldsymbol{Y} = \boldsymbol{Y}^* - \mathbf{Z}\boldsymbol{\delta}$, i.e., $\boldsymbol{\lambda} = \mathbf{Y}^{obs} = (0.4623, 0.9925, 1.6046, 2.1970, 2.7950, 3.3032, 3.7653)'$. The covariance matrix of the corrected vector of measurements, $\boldsymbol{\Sigma} = \mathrm{cov}(\boldsymbol{Y})$, is given by

$$\begin{aligned} \boldsymbol{\Sigma} &= \mathrm{cov}(\mathbf{Z}_1\boldsymbol{\epsilon}_1) + \mathrm{cov}(\mathbf{Z}_2\epsilon_2) + \mathrm{cov}(\mathbf{Z}_3\epsilon_3) + \mathrm{cov}(\mathbf{Z}_4\epsilon_4) \\ &= 0.0000071\,\mathbf{I} + \frac{0.0005^2}{3}\boldsymbol{\lambda}\boldsymbol{\lambda}' + \frac{0.080002^2}{3}\mathbf{1}\mathbf{1}' + \frac{0.05^2}{3}\boldsymbol{\lambda}\boldsymbol{\lambda}'. \end{aligned} \tag{2}$$

So, our statistical model of the (corrected) direct pressure measurements is

$$\boldsymbol{Y} = \boldsymbol{\beta} + \mathbf{Z}\boldsymbol{\epsilon}, \tag{3}$$

where $\mathbf{Z}$ is a known matrix and $\boldsymbol{\epsilon}$ is a vector of independent errors with known distributions.

## 3. Results

*Computing the Exact Confidence Intervals for $\beta_i$ Using the Characteristic Function Approach*

The model (3) is a special case of the general linear regression model with constraints, i.e. model (3) specified in [3], where we set $\mathbf{X} = \mathbf{I}$, $\mathbf{A} = \mathbf{0}$, $\mathbf{B} = \mathbf{0}$, and $\mathbf{c} = \mathbf{0}$. Based on using the general formula for the BLUE of the model parameters (see the formula (12) in [3]), the BLUE of the vector parameter $\boldsymbol{\beta}$ is given by $\hat{\boldsymbol{\beta}} = \boldsymbol{Y}$. So, the BLUE of a linear combination of the unknown parameters $\sum_{i=1}^{7} d_{\beta_i}\beta_i = \mathbf{d}'_{\beta}\boldsymbol{\beta}$, say $\widehat{\mathbf{d}'_{\beta}\boldsymbol{\beta}}$, is given by $\widehat{\mathbf{d}'_{\beta}\boldsymbol{\beta}} = \mathbf{d}'_{\beta}\hat{\boldsymbol{\beta}} = \mathbf{d}'_{\beta}\boldsymbol{Y}$, and (as BLUE is an unbiased estimator) its mean value is equal to the true value $\mathbf{d}'_{\beta}\boldsymbol{\beta}$.

Based on (3), the estimation error $\widehat{\mathbf{d}'_{\beta}\boldsymbol{\beta}} - \mathbf{d}'_{\beta}\boldsymbol{\beta} = \mathbf{d}'_{\beta}(\boldsymbol{Y} - \boldsymbol{\beta})$ is expressible as a linear combination of independent random variables $\epsilon_{1,1}, \epsilon_{1,2}, \ldots, \epsilon_{1,7}, \epsilon_2, \epsilon_3, \epsilon_4$ with known distributions. In particular,

$$\widehat{\mathbf{d}'_{\beta}\boldsymbol{\beta}} - \mathbf{d}'_{\beta}\boldsymbol{\beta} = \sum_{i=1}^{7} d_{\beta_i}\epsilon_{1,i} + \left(\sum_{i=1}^{7} d_{\beta_i}\lambda_i\right)\epsilon_2 + \left(\sum_{i=1}^{7} d_{\beta_i}\right)\epsilon_3 + \left(\sum_{i=1}^{7} d_{\beta_i}\lambda_i\right)\epsilon_4. \tag{4}$$

Let $\omega_{\frac{\alpha}{2}}$ and $\omega_{1-\frac{\alpha}{2}}$ denote the $\frac{\alpha}{2}$ quantile and the $1-\frac{\alpha}{2}$ quantile, respectively, of the distribution of the random variable $\widehat{\mathbf{d}'_{\beta}\boldsymbol{\beta}} - \mathbf{d}'_{\beta}\boldsymbol{\beta}$, i.e., such that $\Pr(\omega_{\frac{\alpha}{2}} \le \widehat{\mathbf{d}'_{\beta}\boldsymbol{\beta}} - \mathbf{d}'_{\beta}\boldsymbol{\beta} \le \omega_{1-\frac{\alpha}{2}}) = 1-\alpha$. Hence, the (random) interval

$$\left(\widehat{\mathbf{d}'_{\beta}\boldsymbol{\beta}} - \omega_{1-\frac{\alpha}{2}}, \widehat{\mathbf{d}'_{\beta}\boldsymbol{\beta}} - \omega_{\frac{\alpha}{2}}\right) \tag{5}$$

is the exact $(1-\alpha)\times 100\%$-confidence interval for the parameter function $\mathbf{d}'_{\beta}\boldsymbol{\beta}$ in the model (3), that we are looking for.

Let $\mathrm{cf}_{\epsilon_{1,1}}(t), \mathrm{cf}_{\epsilon_{1,2}}(t), \ldots, \mathrm{cf}_{\epsilon_{1,7}}(t)$, $\mathrm{cf}_{\epsilon_2}(t)$, $\mathrm{cf}_{\epsilon_3}(t)$, and $\mathrm{cf}_{\epsilon_4}(t)$ denote the characteristic functions (CFs) of the random variables $\epsilon_{1,1}, \epsilon_{1,2}, \ldots, \epsilon_{1,7}$, $\epsilon_2$, $\epsilon_3$, and $\epsilon_4$. Then, CF of the random variable $\widehat{\mathbf{d}'_{\beta}\boldsymbol{\beta}} - \mathbf{d}'_{\beta}\boldsymbol{\beta}$, say $\mathrm{cf}_{\widehat{\mathbf{d}'_{\beta}\boldsymbol{\beta}} - \mathbf{d}'_{\beta}\boldsymbol{\beta}}(t)$, is given by

$$\mathrm{cf}_{\widehat{\mathbf{d}'_{\beta}\boldsymbol{\beta}} - \mathbf{d}'_{\beta}\boldsymbol{\beta}}(t) = \prod_{i=1}^{7} \mathrm{cf}_{\epsilon_{1,1}}\left(t d_{\beta_i}\right) \times \mathrm{cf}_{\epsilon_2}\left(t\sum_{i=1}^{7} d_{\beta_i}\lambda_i\right) \times \mathrm{cf}_{\epsilon_3}\left(t\sum_{i=1}^{7} d_{\beta_i}\right) \times \mathrm{cf}_{\epsilon_4}\left(t\sum_{i=1}^{7} d_{\beta_i}\lambda_i\right). \tag{6}$$

The values of PDF (probability density function) and CDF (cumulative distribution function) of the random variable $\widehat{\mathbf{d}'_{\beta}\boldsymbol{\beta}} - \mathbf{d}'_{\beta}\boldsymbol{\beta}$ can be computed by numerical inversion of its CF, which can be efficiently calculated by a simple trapezoidal quadrature:

$$\mathrm{pdf}_{\widehat{\mathbf{d}'_{\beta}\boldsymbol{\beta}} - \mathbf{d}'_{\beta}\boldsymbol{\beta}}(y) \approx \frac{\delta_t}{\pi}\sum_{j=0}^{N} w_j \Re\left(e^{-\mathrm{i}t_j y}\,\mathrm{cf}_{\widehat{\mathbf{d}'_{\beta}\boldsymbol{\beta}} - \mathbf{d}'_{\beta}\boldsymbol{\beta}}(t_j)\right), \tag{7}$$

$$\mathrm{cdf}_{\widehat{\mathbf{d}'_{\beta}\boldsymbol{\beta}} - \mathbf{d}'_{\beta}\boldsymbol{\beta}}(y) \approx \frac{1}{2} - \frac{\delta_t}{\pi}\sum_{j=0}^{N} w_j \Im\left(\frac{e^{-\mathrm{i}t_j y}\,\mathrm{cf}_{\widehat{\mathbf{d}'_{\beta}\boldsymbol{\beta}} - \mathbf{d}'_{\beta}\boldsymbol{\beta}}(t_j)}{t_j}\right), \tag{8}$$

where $N$ is sufficiently large integer, $w_j$ are the trapezoidal quadrature weights ( $w_0 = w_N = \frac{1}{2}$, and $w_j = 1$ for $j = 1, \ldots, N-1$), $t_j$ are equidistant nodes from the interval $(0, T)$, for sufficiently large $T$, and $\delta_t = \frac{T}{N}$. By $\Re(z)$ and $\Im(z)$ we denote real and imaginary part of the complex value $z$, respectively. The algorithms have been implemented into the MATLAB characteristic functions toolbox `CharFunTool` [4].

In particular, the BLUE of the measurand value $\beta_i$ is $\hat{\beta}_i = Y_i$, and the CF of $\hat{\beta}_i - \beta_i$ is

$$\begin{aligned}\mathrm{cf}_{\hat{\beta}_i - \beta_i}(t) &= \mathrm{cf}_{\varepsilon_{1,i}}(t) \times \mathrm{cf}_{\varepsilon_2}(t\lambda_i) \times \mathrm{cf}_{\varepsilon_3}(t) \times \mathrm{cf}_{\varepsilon_4}(t\lambda_i) \\ &= \mathrm{cf}_{N(0,1)}(\sigma t) \times \mathrm{cf}_{R(-1,1)}(\lambda_i 0.0005t) \times \mathrm{cf}_{R(-1,1)}(0.080002t) \times \mathrm{cf}_{R(-1,1)}(\lambda_i 0.05t). \end{aligned} \tag{9}$$

The required quantiles $\omega_{\frac{\alpha}{2}}$ and $\omega_{1-\frac{\alpha}{2}}$ can be easily obtained from the CDF which can be evaluated for arbitrary values by using (8). In particular, for given $\alpha = 0.05$, the values of the 0.025-quantile and the 0.975-quantile of the distribution of $\hat{\beta}_1 - \beta_1$ are $-0.0841$ and $0.0841$, respectively. Consequently, the observed 95%-confidence interval for $\beta_1$ is

$$\left(Y_1^{obs} - \omega_{0.975}, Y_1^{obs} - \omega_{0.025}\right) = (0.3782, 0.5464). \tag{10}$$

Similarly, the observed 95%-confidence intervals for the remaining parameters $\beta_i$, $i = 2, \ldots, 7$, are: $(0.8909, 1.0941)$ for $\beta_2$, $(1.4801, 1.7291)$ for $\beta_3$, $(2.0490, 2.3450)$ for $\beta_4$, $(2.6225, 2.9675)$ for $\beta_5$, $(3.1094, 3.4970)$ for $\beta_6$, and $(3.5518, 3.9788)$ for $\beta_7$.

Using the covariance matrix of the random vector $\boldsymbol{Y}$ specified in (2), the variance of $Y_i - \beta_i$ is $0.00214054 + 0.000833416\lambda_i^2$. So, the standard deviation (standard uncertainty) of $\hat{\beta}_1 - \beta_1 = Y_1 - \beta_1$ is $u_{\hat{\beta}_1-\beta_1} = 0.0482$. According to [1], for expressing the uncertainty in measurement, it is recommended to use the expanded uncertainty which is obtained as a multiple of the combined standard uncertainty, by a suitably chosen coverage factor $k$. Under standard assumptions, it is recommended to choose $k = 2$. So, the expanded uncertainty of $\hat{\beta}_1 - \beta_1$ is $2u_{\hat{\beta}_1-\beta_1} = 0.0963$, and hence, the interval $(-0.0963, 0.0963)$ is the uncertainty interval of the measurement. In our case, the observed exact 95%-confidence interval for $\hat{\beta}_1 - \beta_1$ is $(-0.0841, 0.0841)$, which can be equivalently written as $(-1.746\,u_{\hat{\beta}_1-\beta_1}, 1.746\,u_{\hat{\beta}_1-\beta_1})$, i.e., the coverage factor is 1.746 instead of 2. On the other hand, the uncertainty interval $(-2u_{\hat{\beta}_1-\beta_1}, 2u_{\hat{\beta}_1-\beta_1})$, recommended in [1], has coverage probability at the level of 0.9927.

## 4. Conclusions

We have presented a real-data example with uncertainty analysis of direct pressure measurements using the characteristic function approach to compute the exact confidence interval for any linear combination of the model parameters. Alternatively, for assessing the stated confidence interval, we can also use the Monte Carlo simulations, as suggested in [2]. Based on our comparisons (not presented here), the confidence intervals obtained through (5) and by the use of Monte Carlo simulations are in perfect agreement. We have also compared out exact 95%-confidence interval with the coverage interval recommended in [1] and found that the correct coverage factor should be $k = 1.746$, to get the interval that has a coverage probability of 0.95.

**Acknowledgements**

The work was supported by the Slovak Research and Development Agency, project APVV-18-0066, and by the projects VEGA 2/0081/19 and VEGA 2/0096/21.

**References**

[1] JCGM 100:2008 (GUM) (2008). *Evaluation of measurement data – Guide to the expression of uncertainty in measurement* (GUM 1995 with minor corrections), ISO, BIPM, IEC, IFCC, ILAC, IUPAC, IUPAP and OIML.

[2] JCGM 101:2008 (GUM S1) (2008). *Evaluation of measurement data – Supplement 1 to the Guide to the expression of uncertainty in measurement – Propagation of distributions using a Monte Carlo method*. ISO, BIPM, IEC, IFCC, ILAC, IUPAC, IUPAP and OIML.

[3] Witkovský V. and Wimmer G. (2021). Exact confidence intervals for parameters in linear models with parameter constraints. In *Proceedings of MEASUREMENT 2021*.

[4] Witkovský V. (2021). *CharFunTool: The Characteristic Functions Toolbox (MATLAB)*. `https://github.com/witkovsky/CharFunTool`.

# Selection of the Observation Angle in Thermography Temperature Measurements with the Use of a Macro Lens

**Krzysztof Dziarski**

[1] Institute of Electric Power Engineering, Poznan University of Technology, Piotrowo 3A, 60-965 Poznan, Poland

Email: Krzysztof.Dziarski@put.poznan.pl

***Abstract.*** *Thermography is an effective method of diagnostics of electronic components. In the case of thermography temperature measurements with the use of a macro lens, the thermography temperature measurement error increases with the increase of an observation angle. During thermography temperature measurements with the use of a macro lens of objects with a complex design of the case, it is difficult to control the value of an observation angle. This article presents theoretical considerations regarding angular emissivity and the experimentally obtained relationship between the value of the thermography temperature measurement error with the use of a macro lens and an observation angle. In addition, it presents the designed measuring system.*

*Keywords: Thermography, Electronics, Measurement Error, Observation Angle*

## 1. Introduction

The temperature of electronic components is an important parameter. A too high temperature of the electronic component case may be a sign of its malfunctioning. Functioning of the element with too high temperature may cause its malfunction (e.g. switching of transistors too long), shorter operation time and even damage. In addition, the knowledge of temperatures of selected parts of the Printed Circuit Board (PCB) facilitates to quickly identify abnormal component condition (e.g. short circuits, cold solders). Temperature measurement on the surface of the electronic component and PCB is possible thanks to thermography [1,2]. This contactless method is a safe method - the temperature sensor does not need to be in contact with the PCB. As a consequence, there is no risk of electric shock when taking this temperature measurement. The use of thermography has one more advantage: no contact of the temperature sensor with a tiny component makes there is no exchange of thermal energy between the temperature sensor and the observed element. When using an additional wide-angle lens (e.g. Close up 2x), it is possible to record temperature distributions on cases with small dimensions, such as SMD (Surface Mounted Devices) or BGA (Ball Grid Array) [3].

It is also possible to record the so-called Hot spots - such points on integrated circuits cases that are characterized by a higher temperature (compared to other parts of the case) and small dimensions of the order of micrometres. Due to the limited depth of field of thermograms, the use of an additional lens is difficult. It requires selecting the appropriate distance between the lens and the observed surface *d*. Only in this case, the value of IFOV (Instantaneous Field of View) known. The thermography temperature measurement error depends on the observation angle $\beta$ [4]. After having analyzed the data provided by the manufacturer of the lens - the Flir company, no information was found about the influence of $\beta$ on the result of a thermography temperature measurement with the use of a macro lens. For this reason, experimental work was undertaken aimed at determining the relationship between the temperature measurement result $\vartheta_{cam}$ and $\beta$. Based on the determined dependency, it was decided to conclude for which $\beta$ values the measurement error is lower than the thermography temperature measurement error declared by the manufacturer of the thermography camera $\Delta\vartheta_{cam}$.

## 2. Angular Emissivity

Angular emissivity can be expressed using the expression 1

$$\varepsilon = 1 - \rho \tag{1}$$

where ε - emissivity factor, ρ - reflectance factor.

In accordance with the Fresnel equation, ρ is half of the sum of the reflectance factor for parallel polarized radiation $\rho_{\|}$ and the reflectance factor for perpendicularly polarized radiation $\rho_{\perp}$ (2) [5].

$$\rho = \frac{\rho_{\perp} + \rho_{\|}}{2} \tag{2}$$

The values $\rho_{\perp}$ and $\rho_{\|}$ depend on the angle of radiation $\alpha$ and the refractive index $n$. The value of $n$ depends on the material from which the observed surface was made, the surface temperature and the radiation band. For materials in which electromagnetic wave is damped (e.g. for metals), the complex value of the refraction index $n' = n - \mathrm{j}k$ is assumed: where $n$ - refraction index, $k$ - damping factor ultimately, the values $\rho_{\perp}$ $\rho_{\|}$ and for lossy materials take the form (3a) and (3b) [5].

$$\rho_{\|} = \frac{[n\cos(\alpha) - 1]^2 + k^2\cos^2(\alpha)}{[n\cos(\alpha) + 1]^2 + k^2\cos^2(\alpha)} \tag{3a}$$

$$\rho_{\perp} = \frac{[n + \cos(\alpha)]^2 + k^2\cos^2(\alpha)}{[n - \cos(\alpha)]^2 + k^2\cos^2(\alpha)} \tag{3b}$$

In metals - materials that strongly absorb radiation in a given spectral range, the angle of refraction is close to 90°. For the angle equal to Brewster's angle, the reflected wave polarized in the plane parallel to the plane of incidence is being extinguished. This means that for large angles the amount of reflected energy is smaller. As a consequence, the emissivity for these angles is higher, and the value read from the thermograms is lower [5].

## 3. Measurement System

To check for which $\beta$ values the measurement error is lower than $\Delta\vartheta_{cam}$, the constructed measuring system was used. The main element of the constructed measuring system is the Flir E50 [6] thermography camera with an additional Close up 2x lens. The thermography camera was attached to the linear module with a stepper motor, which allows for selecting the distance $d$ = 33 mm. This is a distance for which the IR resolution is known. The distance $d$ was selected with a resolution of 1 mm and measured using a linear resistance displacement sensor. The linear module was attached to a tripod. The observed element was an aluminium block with dimensions of 16 mm x 16 mm x 45 mm, with an upper wall painted with a paint of known emissivity. A heater was attached to the lower wall of the block. A hole with a diameter of $\phi$ = 4 mm was drilled in the block. A Pt1000 resistance temperature sensor was placed in the hole. The space between the sensor and the block was filled with silicone thermal paste. Such a prepared block was placed on the shaft of the stepper motor. The value of $\beta$ was changed with a step equal to 0.9 °.

The whole, together with a thermography camera mounted on a tripod, was placed in a Plexiglas chamber. Placing the camera inside the chamber made it possible to stabilize the measurement conditions. The chamber's walls were lined with black polyurethane foam. Due to the similarity of a single pore of the foam to a cavity model of a black body, it was possible to optically separate the interior of the chamber from the environment. The thermovision camera was communicated with a computer via a USB interface. This made it possible to display the recorded thermograms on the computer screen. Outside the chamber also a PLC controller was placed and used to control the stepper motors. The constructed measuring system and the dimensions of the block are presented in Figure 1.

a)

b)

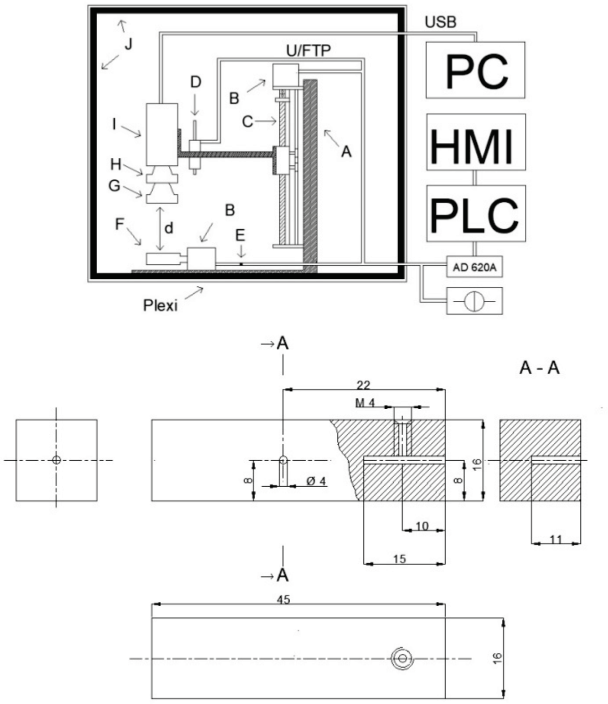


Fig. 1. a) The view of schematic of measurement system: (A) Tripod; (B) Stepper motors; (C) Linear guide; (D) Resistance linear distance sensor; (E) Connector; (F) Observed aluminium block; (G) Additional macro lens Close up lens 2x P/NT 197200; (H) Thermal imaging camera lens; (I) Thermal imaging camera; (J) Polyurethane foam; (d) WD (Work Distance) – the distance between observed object and thermal imaging camera macro lens. b) dimensions of the observed aluminium block.

## 4. Results

The laboratory stand prepared in this way made it possible to start the work aimed at determining the dependency of an error $\Delta\vartheta$ of a thermography temperature measurement on the value of $\beta$. The value of $\Delta\vartheta$ value was defined as a difference between the temperature of aluminium block $\vartheta_{Al}$ and the temperature read from the thermogram $\vartheta_{cam}$ (4). The value of $\vartheta_{Al}$ was measured with the use of Pt1000 placed in the block and considered a correct value.

$$\Delta\vartheta = \vartheta_{Al} - \vartheta_{cam} \tag{4}$$

Three series of measurements were made, during which the same point on the surface of the aluminium block was observed, which was painted with a paint of known $\varepsilon = 0.95$. The setpoints of other parameters were selected as follows: reflected temperature value $\vartheta_{refl}$ = 20°C, air temperature $\vartheta_a$ = 20°C, the temperature of the external optical system $\vartheta_l = \vartheta_a$, transmittance of the external optical system $\tau_l = 1$, relative humidity $\omega_{\%}$ = 50%. In each series, the value of $\beta$ was changed from 0 ° to 89.1 ° in steps = 0.9 °. During the measurements, $\vartheta_{Al}$ was changing from 56 °C to 58.7 °C. The obtained results are presented in Figure 2. The mean value of $\vartheta_{AlAv}$ = 57.35 °C was used to determine the value of $\Delta\vartheta$. In Figure 2, the line was applied to denote the value of $\vartheta_{AlAv}$ increased by the value of $\Delta\vartheta_{cam}$ and $\vartheta_{AlA}$ decreased by the value of $\Delta\vartheta_{cam}$. In accordance with data provided by the manufacturer, $\Delta\vartheta_{cam}$ = 2 °C.

a) b)

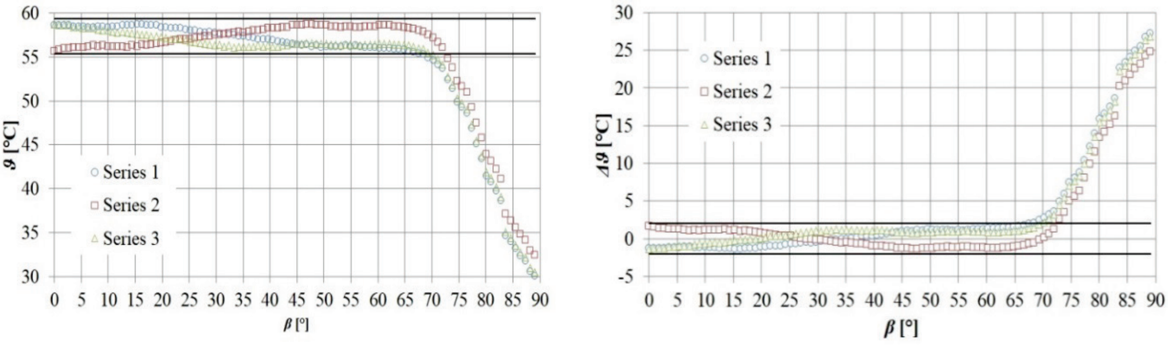


Fig. 2. a) Chart $\vartheta_{cam} = f(\beta)$, b) Chart $\Delta\vartheta_{cam} = f(\beta)$.

## 5. Conclusions

After having analyzed the results presented in Fig. 2, it can be seen that for values of $\beta$ less than 68°, the difference between the temperature of element and the temperature indicated by the thermovision camera is smaller than the error of the camera declared by the manufacturer. This is in line with the theoretical considerations presented in item 2. One can also find that despite applying a thin layer of paint with a known emissivity onto the observed surface, an increase in thermography error of temperature measurement was observed at these values of $\beta$ at which it is observed for metals. It is difficult to control the value of $\beta$ value during actual thermography measurements with an additional lens. Based on the work performed, it can be concluded that when the value of $\beta$ is selected roughly, the value of a measurement error caused by a too high value of this angle shall not exceed 2°C.

## References

[1] Stoynova, A., Bonev, B. Brayanov N. (2018). Thermographic Approach for Reliability Estimation of PCB. In *41st International Spring Seminar on Electronics Technology (ISSE)*, Zlatibor

[2] Dziarski, K. Hulewicz, A. Dombek, G. Frąckowiak, R. Wiczyński, G. (2020) Unsharpness of Thermograms in Thermography Diagnostics of Electronic Elements. *Electronics*. 9(6).897

[3] Zhou, X., Xue, Y., Tian, G., Liu. Z. (2017). Thermal Analysis of Solder Joint Based on Eddy Current Pulsed Thermography. *IEEE Transactions on Components, Packaging and Manufacturing Technology*. *IEEE*, 1111-1118.

[4] Litwa, M. (2010). Influence of Angle of View on Temperature Measurements Using Thermovision Camera. *IEEE Sensors Journal*.10(10).

[5] Więcek, B., De Mey, G. (2011). Termowizja w podczerwieni podstawy i zastosowania. PAK

[6] https://www.flir.com/support/products/e50/#Overview [acess: 4.03.2021 19.02]

# *Measurement in Biomedicine I*

# Comparison of Dipole-Based and Potential-Based Inverse ECG Solutions for the Localization of Ventricular Pacing Sites

**[1]Yesim Serinagaoglu Dogrusoz, [2]Jan Zelinka, [2]Jana Svehlikova**

[1]Middle East Technical University, Ankara, Turkey
[2]Institute of Measurement Science SAS, Bratislava, Slovakia
Email: yserin@metu.edu.tr

***Abstract*** *Two different inverse methods were applied to the two sets of well-defined data from tank experiments to assess the pacing electrode's position by the inverse solution. The use of a simple dipole as the equivalent heart generator provides only the assessment of the pacing site from the very early time interval of activation. The potential-based inverse solution aims to reconstruct the electrograms using the Bayesian estimation so that it needs prior knowledge about the properties of the cardiac sources. The accuracy of the pacing site localization was 8.6 and 18.4 mm for the dipole-based method and varied from 8.6 to 19.4 and from 8.6 to 32.5 mm for the potential-based method depending on the noise model and pacing site estimation method. The advantages of both inverse methods can be combined in the future to improve the inverse localization approaches.*

*Keywords: Electrocardiographic Imaging, Statistical Estimation, Premature Ventricular Contraction, Body Surface Potential Mapping*

## 1. Introduction

Heart rhythm disturbances have been among the reasons for sudden cardiac death. If pharmacological treatment of such diagnosis is not sufficient, the origin of some extrasystoles can be eliminated/deactivated by invasive radiofrequency ablation (RFA). During such a procedure, the origin should be identified via an intracardiac catheter and later exposed to specific radiofrequency energy. Electrocardiographic imaging (ECGI) is a novel approach aiming to identify the origin of the undesired electrical activity of the heart noninvasively, which can lead to the shortening of the invasive RFA procedure. Several methods for ECGI have been developed in the last decades, using multiple-lead EGC measurements, the so-called body surface mapping (BSPM). These methods have been tested mainly on computational models or on physical models combining a human-shaped tank model with animal hearts.

Within the bilateral SAS-TUBITAK project we plan to combine the ECGI approaches of two research groups to localize the origin of a premature ventricular contraction (PVC): the inverse solution using a single dipole [1] and the electrogram (EGM)-based solution using a probabilistic approach, Bayesian Maximum A Posteriori (MAP) estimation [2]. In this work, both methods were applied to the same data, and the results were compared and discussed.

## 2. Subject and Methods

*Data*

Two datasets with ECG measurements with 128 leads were obtained from pig hearts placed in a human-shaped torso tank filled with an electrolytic solution (Fig.1a). The ventricles were stimulated via electrodes from a known position. The experiments were performed in IHU-LIRYC Bordeaux, France, and the data were available within the Signal processing workgroup of the Consortium for ECGI (https://www.ecgimaging.org/workgroups/signal-processing) [3]. The measured signal consisted of 31 and 20 heart cycles for Data-1 and Data-2, respectively.

The inverse solution was computed for one cycle obtained by signal averaging. Among the two datasets, Data-1 was more noisy than Data-2 (Signal to noise ratio of approximately 15dB and 25dB, respectively).

*Inverse Solution Using a Single Dipole (Dipole-Based)*
In the inverse solution using a single dipole as an equivalent cardiac generator (EG), it is assumed that during the starting time interval of PVC the activated area is small enough to be approximated by the activity of a single dipole. Therefore, the relevant result of the inverse solution is searched from the beginning time interval of activation. Assuming a single dipole as EG the BSPM can be computed by the equation:

$$\boldsymbol{m} = \boldsymbol{Td} \tag{1}$$

Where $\boldsymbol{T}$ is a transfer matrix representing geometry and conduction properties of the torso as a volume conductor. It is computed by the boundary element method (BEM) for the defined position of the dipole. Then from the known potentials on the torso ($\boldsymbol{m}$) and the transfer matrix, the parameters of the dipole are obtained as:

$$\boldsymbol{d} = \boldsymbol{T}^*\boldsymbol{m} \tag{2}$$

where $\boldsymbol{T}^*$ is a pseudoinversion of the matrix $\boldsymbol{T}$.

To find the origin of the PVC activation, the possible positions of the representative dipole are evenly distributed over the known heart geometry surface or volume. The dipolar EG is computed for each defined possible dipole position. The quality of a fit of the EG in the selected position is evaluated by the relative residual error (RRE) between the original BSPM and the BSPM computed from a specific EG. Then the position of the EG with the smallest RRE within the first 20 ms of activation is chosen as the representative of the PVC activation origin.

*Bayesian Solutions for Inverse Electrocardiography (EGM-Based)*
In this approach, the cardiac sources are represented in terms of EGMs. Then, the model relating these sources to the BSPM is given as:

$$\boldsymbol{y}_t = \boldsymbol{A}\boldsymbol{x}_t + \boldsymbol{n}_t, \quad t = 1,2,\dots,T, \tag{3}$$

where $\mathbf{y}_t$, $\mathbf{x}_t$ and $\mathbf{n}_t$ are the BSPM, EGM and measurement noise at time instant $t$, respectively, and $\mathbf{A}$ is the forward matrix, which is calculated using BEM in a homogeneous torso model [4]. The inverse problem is often solved at each time instant separately, therefore we drop the time indices in the following descriptions.

In Bayesian MAP estimation, based on the likelihood function, $\boldsymbol{p}(\mathbf{y}\backslash\mathbf{x})$, and the a priori probability density function (pdf) of the EGMs, $\boldsymbol{p}(\boldsymbol{x})$, the posterior pdf is obtained as:

$$\boldsymbol{p}(\boldsymbol{x}\backslash\boldsymbol{y}) = \frac{\boldsymbol{p}(\boldsymbol{y}\backslash\boldsymbol{x})\boldsymbol{p}(\boldsymbol{x})}{\int \boldsymbol{p}(\boldsymbol{y}\backslash\boldsymbol{x})\boldsymbol{p}(\boldsymbol{x})\boldsymbol{dx}} \tag{4}$$

The solution is then chosen to maximize this posterior pdf [2]. If we assume that $\mathbf{n} \sim N(\mathbf{0}, \mathbf{C}_n)$, $\mathbf{x} \sim N(\bar{\mathbf{x}}, \mathbf{C}_x)$, we can write the solution as:

$$\hat{\boldsymbol{x}} = (\boldsymbol{A}^T\boldsymbol{C}_n^{-1}\boldsymbol{A} + \boldsymbol{C}_x^{-1})^{-1}(\boldsymbol{A}^T\boldsymbol{C}_n^{-1}\boldsymbol{y} + \boldsymbol{C}_x^{-1}\bar{\boldsymbol{x}}) \tag{5}$$

Individual beats of the true EGM recordings and the noise in the BSPM were used to obtain the statistical model parameters $\boldsymbol{C}_n$, $\bar{\boldsymbol{x}}$ and $\boldsymbol{C}_x$. The noise was assumed to be independent and identically distributed so that it only sufficed to estimate its variance. We computed two different noise variances: (Model-1) obtained by combining the noise in all beats, (Model-2) obtained from the noise in the averaged BSPM signal. Model-1 yields a larger noise variance compared to Model-2, since signal averaging decreases noise in the measurements.

In the EGM-based solution, the pacing site (the PVC origin) was estimated using two different approaches: (P1) Activation times (AT) were calculated using the spatio-temporal method proposed in [5], and then the pacing site was assigned as the node with the earliest AT. (P2) Integrals of the absolute value of EGMs were computed within the QRS region, then the slope of the integral function was calculated for the first 20 ms of the QRS after fitting a straight line to this integral function. Finally, the lead with the highest slope was assigned as the pacing site.

*Evaluation Metrics*

Both approaches in this study were evaluated based on their performances on PVC localization. Localization error (LE) was computed as the Euclidean distance between the ground truth and estimated pacing locations. Ground truth pacing sites were determined manually from the sock recordings by examining the iso-potential maps and verified by checking the earliest activated node. In addition to LE, the EGM-based solutions and the corresponding ATs were evaluated using Pearson's correlation coefficient (CC). For the EGM evaluation, temporal CC was obtained at each lead by comparing the sock EGMs and the reconstructed EGMs, from which we calculated the first, second (median) and third quartile values.

## 3. Results

Table 1. Summary of LE for the dipole-based solution and all evaluation metrics for the EGM-based solutions. For the temporal CC (EGM-based), first (Q1), second (Q2 - median) and third (Q3) quartile values are given.

| | | Data-1 | Data-2 |
|---|---|---|---|
| Dipole | LE (mm) | 8.58 | 18.39 |
| EGM | Temporal CC [Q1; Q2; Q3] | [0.61; 0.76; 0.87] | [0.27; 0.53; 0.74] |
| Noise Model-1 | AT – CC | 0.93 | 0.92 |
| | P1 – LE (mm) | 19.44 | 14.05 |
| | P2 – LE (mm) | 9.14 | 8.59 |
| EGM | Temporal CC [Q1; Q2; Q3] | [0.27; 0.61; 0.8] | [0.084; 0.49; 0.72] |
| Noise Model-2 | AT – CC | 0.91 | 0.48 |
| | P1 – LE (mm) | 13.81 | 32.55 |
| | P2 – LE (mm) | 8.58 | 8.59 |

Table 1 presents the LE for the dipole-based solution and a summary of all EGM-based evaluations. In terms of EGM reconstruction accuracy, Model-2 resulted in worse EGM-CC values compared to Model-1 for both datasets. EGM accuracy and AT accuracy were related, but the AT-CC value of Model-2 was drastically lower than that of Model-1 for Data-2. The P1-LE accuracy is closely related to the AT accuracy. For example, for Data-2, Model-2, P1-LE was as high as 32.55 mm. P2-based LE values were more robust than P1-based LE values.

For Data-1, LE of the dipole-based method was comparable to P2-LE of the EGM-based method. For Data-2, EGM-based P2-LE was the best; the dipole-based LE was better than P1-LE of Method-2, but worse than P1-LE of Method-1.

## 4. Discussion and Conclusion

The dipole-based inverse method was able to localize the pacing electrode with accuracy from 8 to 18 mm. The EGM-based method provided more complex information about the activation of the heart.

In the EGM-based inverse reconstructions, the P1-LE accuracy is closely related to the AT accuracy, and AT estimation depends on taking the derivative of the EGMs and finding the minimum of this derivative. Noise in the EGMs corrupts the derivative, resulting in incorrect

AT detection. Smoothing applied by the spatio-temporal approach has limited success in correcting these ATs. Thus, LE estimation is also affected. Here we proposed an EGM-based LE estimation method, P2-LE, which had superior performance compared to P1-LE. But it needs to be evaluated using a larger and diverse dataset before its adoption to routine practice.

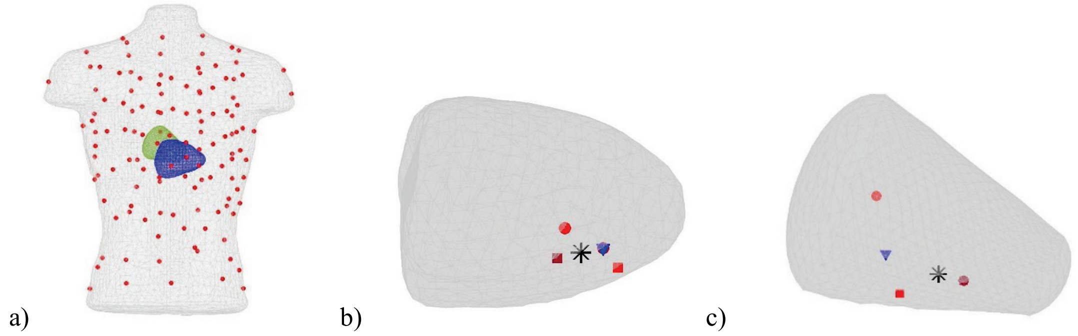


Fig. 1. a) – The human-shaped torso model with inserted hearts (blue: Data-1, green: Data-2) and the electrodes (red dots) for multiple-lead ECG measurements. b), c) the results of the inverse solutions for Data-1 and Data-2, respectively. Black asterisk depicts the true position of the pacing electrode, blue triangle assigns the result by a single dipole, other assign the results obtained by Bayesian estimation.

Noise pdf, as well as the a priori pdf, need to be carefully defined for improving the performance of Bayesian MAP estimation. For both datasets, overestimating the noise variance improved the results. In this study, the a priori pdf is estimated from the recorded EGMs. In a clinical setting, this is not feasible. Thus, alternative approaches such as using simulated datasets are needed. Results provided by the dipole-based approach could be used to either steer these simulations or reconstruct the prior models directly.

## Acknowledgements

The present study was supported by research grants 2/0125/19 from the VEGA Grant Agency in Slovakia, project SAS-TUBITAK/JRP/2020/1144/ClinECGI, TUBITAK-120N200, and COST action CA19137. The Authors thank Laura Bear from the University of Bordeaux, IHU-LIRYC for the data used in this study.

## References

[1] Punshchykova O, Švehlíková J, Tyšler M, Grünes R, Sedova K, Osmančík P, et al. Influence of Torso Model Complexity on the Noninvasive Localization of Ectopic Ventricular Activity. *Meas Sci Rev* 2016:96–102. doi:10.1515/msr-2016-0013.

[2] Serinagaoglu Y, Brooks DH, MacLeod RS. Improved performance of Bayesian solutions for inverse electrocardiography using multiple information sources. *IEEE Trans Biomed Eng* 2006;53:2024–34. doi:10.1109/TBME.2006.881776.

[3] Bear LR, Serinagaoglu Y, Good WW, Svehlikova J, Coll-Font J, van Dam E, et al. The Impact of Torso Signal Processing on Noninvasive Electrocardiographic Imaging Reconstructions. *IEEE Trans Biomed Eng* 2020;00:1–1. doi:10.1109/tbme.2020.3003465.

[4] Stanley PC, Pilkington TC, Morrow MN. ) The effects of thoracic inhomogeneities on the relationship between epicardial and torso potentials. *IEEE Trans Biomed Eng* 1986;33:273–84.

[5] Erem B, Coll-Font J, Orellana RM, St'Ovicek P, Brooks DH. Using transmural regularization and dynamic modeling for noninvasive cardiac potential imaging of endocardial pacing with imprecise thoracic geometry. *IEEE Trans Med Imaging* 2014;33:726–38. doi:10.1109/TMI.2013.2295220.

# Activation Propagation in Cardiac Ventricles Using the Model of the Normal and Disrupted Conduction System

**Elena Cocherová**

Institute of Measurement Science, SAS, Bratislava, Slovakia
Email: elena.cocherova@savba.sk

***Abstract.*** *The goal of the article was to design a model of cardiac ventricles with analytical geometry that enables simulation of normal and disrupted conduction system functions. The conduction system model comprised the His bundle, left and right bundle branches and an endocardial layer with higher conductivity representing the Purkinje fibers. While QRS duration relating to the total activation time of the whole ventricles lies in the physiological range of about 80 to 120 ms for the normal activation, it is more than 120 ms in the case of left or right bundle branch block (LBBB, RBBB). The propagated electrical activation in the model was described by the monodomain reaction-diffusion (RD) equation with the ionic transmembrane current density defined by the modified FitzHugh-Nagumo equations. This RD model of cardiac ventricles was numerically solved in the Comsol Multiphysics environment. Realistic activation time of the whole ventricles of about 98 ms was obtained for the model with a normal conduction system, while 151 ms and 129 ms were obtained for the model with LBBB and RBBB, respectively.*

*Keywords: Reaction-Diffusion Model, Cardiac Ventricles, Conduction System, LBBB, RBBB*

## 1. Introduction

Electrical activation of the heart crosses to the ventricles through the atrioventricular node, propagates to the His bundle that further divides to the left and right bundle branches, then proceeds to the branching fibers of the Purkinje system and finally reaches the myocardium tissue. The role of the conduction system is to lead the activation promptly and synchronously to the working myocardium tissue of the left and right ventricle. The velocity of propagation in the conduction system is several times higher than in the ventricular myocardium. Disruption of the fast-conducting bundle branches leads to the prolongation of the total activation time of the ventricles which is reflected in ECG as QRS duration over 120 ms [1], [2].

The propagation of electrical activation in the heart can be modeled using models based on reaction-diffusion (RD) equations (e.g. the monodomain model) [3], as well as using less time-consuming models (as models based on cellular automaton) [4]. The monodomain model together with the modified FitzHugh-Nagumo (FHN) equations [3], [5] was used to describe the activation propagation in this article. The geometry of the heart ventricles can be derived from CT or MRI scans [3], [6] or a simplified geometry can be defined analytically, e.g. using ellipsoidal and cuboidal segments of the ventricles [4].

In this article, an analytically defined ellipsoidal model of the ventricles was created and used. The His bundle and the left and right bundle branches as structures with higher conductivity were isolated from the myocardium tissue in this model. The Purkinje fibers were modeled as an endocardial layer of higher conductivity only in the free ventricular walls. The left and right bundle branch blocks (LBBB, RBBB) were modeled as non-conducting (isolated) regions of the bundle branch. The total activation times (TAT) when the whole ventricles were activated were computed and compared for all models.

## 2. Subject and Methods

*The Monodomain RD Model*

The electrical activation in the monodomain reaction-diffusion (RD) model of the cardiac tissue [3] was described by the partial differential equation:

$$\frac{\partial V_m}{\partial t} = \nabla \cdot \left( D \nabla V_m \right) - i_{ion} + i_s , \tag{1}$$

where $V_m$ is the membrane potential, $D$ is the tissue diffusivity, $i_{ion}$ is the local ionic transmembrane current density, $i_s$ is the stimulation current density. Current densities were normalized to the membrane capacitance with resulting units A/F. The ionic transmembrane current density $i_{ion}$ was modeled using the modified FitzHugh-Nagumo (FHN) equations [5]. The tissue diffusivity $D$:

$$D = \sigma / \left( \beta C_m \right), \tag{2}$$

is dependent on the tissue conductivity $\sigma$, the membrane surface-to-volume ratio $\beta$, and the membrane capacitance per unit area $C_m$.

*Geometry of the Ventricular Model*

The geometry of ventricles was defined analytically, as is shown in Fig. 1. The outer shape of the model was formed from the lower half of an ellipsoid (with semiaxes of 30, 30 and 70 mm). Left and right free ventricular walls (with the thickness of 10 and 4 mm) were separated by a 10 mm thick septum of cuboidal shape (constructed as a part of rectangular parallelepiped). The His bundle was constructed from the lower half of a cylinder (with a radius of 10 mm and length of 10 mm). The left and right bundle branches (with cross dimensions of 2 and 6 mm) spanned from the His to the heart apex and continued along the endocardial surface of the free ventricular walls up to the level of z = -45 mm (Fig. 1, Fig. 2). The 2 mm thick Purkinje layer spanned from the apex up to the level of z = -30 mm and z = -25 mm in the left and right free ventricular wall, respectively. The His bundle and the bundle branches were isolated from the surrounding tissue by a 0.1 mm thin isolation layer. The only conductive connections between the bundle branches and the Purkinje layer are marked with arrows in Fig. 1. The "Extra Fine" mesh was created in Comsol for the numerical solution.

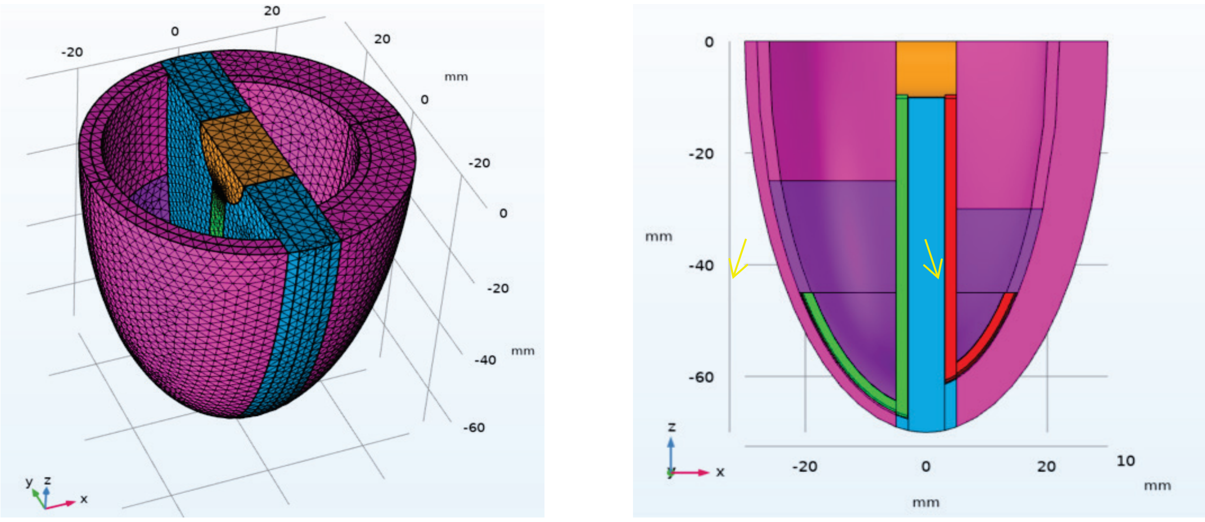


Fig. 1. The geometry of the ventricular model covered with tetrahedral mesh (left). The cross-section of the ventricular model (right): His bundle (orange), left bundle branch (red), right bundle branch (green), Purkinje layer (violet), myocardium tissue in free walls (light violet) and myocardium tissue in the septum (cyan). The arrows point to the connections of bundle branches and the Purkinje layer (sites of initial activation of the Purkinje layer).

*Model Tissue Parameters*

The activation propagation velocity in the bundle branches and Purkinje fibers is several times higher than that in the working myocardium [5].

In the model, the tissue diffusivity of the working myocardium in the free ventricular walls was set to $D = 0.00015\ m^2/s$ (corresponding to tissue conductivity $\sigma = 0.15$ S/m). The diffusivity of the septum (cyan color in Fig. 1) was set anisotropic: $D = 0.00015\ m^2/s$ in the transversal directions and $D = 0.0004\ m^2/s$ in the longitudinal direction (along the heart z-axis).

The tissue diffusivity of the bundle branches and the fast-conducting Purkinje layer was set to $D = 0.003\ m^2/s$ and $D = 0.006\ m^2/s$, respectively. The tissue diffusivity of the His bundle was set to $D = 0.001\ m^2/s$. The activation in the model started from the His bundle, where it was evoked by a stimulation current $i_s$ (amplitude of the normalized stimulation current density 40 A/F, duration 2 ms). Stimulation current was zero in other domains. The initial value of the membrane potential was -0.085 V. Values of other parameters in the modified FHN model were the same as in [5]. The complete LBBB or RBBB was modeled by a thin (0.2 mm) isolating layer of zero conductivity between the His bundle and the particular bundle branch (shown by arrows in Fig. 2).

## 3. Results

The membrane potential $V_m$ in the RD propagation model was numerically solved in Comsol Multiphysics. Spatial distributions of $V_m$ in ventricles with normal conduction system and in the case of LBBB and RBBB are shown in Fig. 2. The time instant, when the activation from the left bundle branch reached the Purkinje layer in the normal heart (site marked by an arrow in Fig. 1), was considered as the time $t = 0$ ms. Since the right bundle branch is longer than the left one, the activation of the Purkinje layer in the right ventricle started with a 9 ms delay (in the time $t = 9$ ms).

In the ventricles with a normal conduction system (Fig. 2 left), activation was propagated in the left and right ventricle quite synchronously. In the case of LBBB and RBBB, activation started in one ventricle, and then propagated with delay to the ventricle with the blocked branch (e.g. about 40 ms delay in RBBB, Fig. 2 right). The total activation time (TAT) when the whole ventricular model was activated was 98 ms in the model with a normal conduction system, and 151 ms and 129 ms in the models with LBBB and RBBB (Table 1).

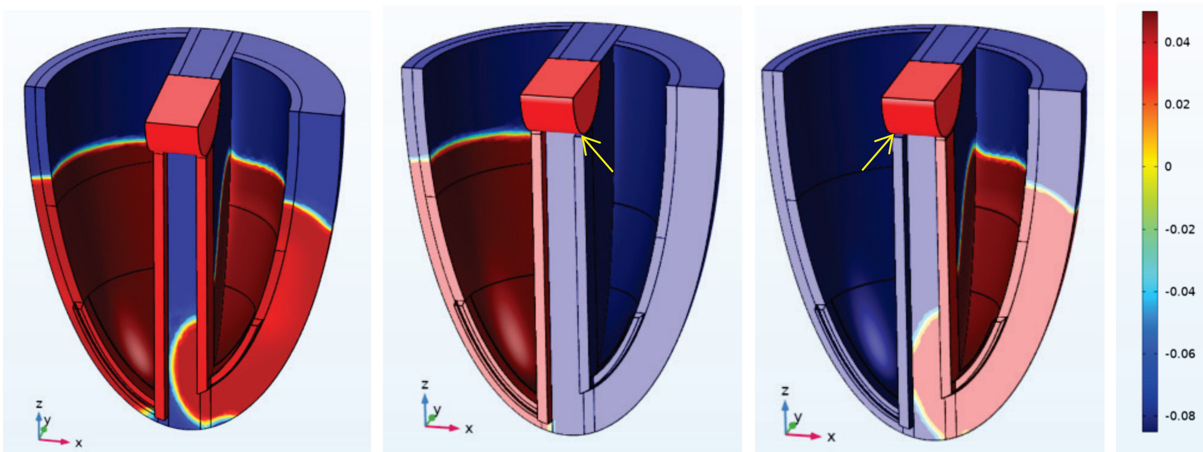


Fig. 2. Spatial distribution of the membrane potential $V_m$ [V] in the ventricular model with normal (left) and disrupted conduction system (LBBB - middle, RBBB - right) in time $t = 40$ ms. Arrows point to the sites of conduction blocks.

Table 1. Total activation times (TAT) in particular ventricular models.

| Model | TAT [ms] |
|---|---|
| Model with normal conduction system | 98 |
| Model with LBBB | 151 |
| Model with RBBB | 129 |

## 4. Discussion

The role of the conduction system is to lead the activation promptly to the working ventricular myocardium tissue, where it is spreading with lower velocity. Any block in the conduction system in the left or right ventricle may cause non-synchronous activation of the ventricles since activation must spread from the healthy ventricle to the ventricle with corrupted bundle brunch through the less conductive muscle tissue in the septum and free ventricular walls.

## 5. Conclusions

Analytically defined ventricular model with a specific conduction system described in this article allows simulation of activation propagation in cardiac ventricles with normal or disrupted conduction system. A simulated total activation time of 98 ms obtained for healthy ventricles agreed well with the expected interval of about 80 ms – 120 ms for a healthy heart. Similarly, total activation times of 151 ms and 129 ms for the LBBB and RBBB were consistent with times over 120 ms observed in patients with complete LBBB or RBBB.

**Acknowledgements**

This work was supported by research grant 2/0125/19 from the VEGA grant agency and by grant APVV-19-0531 from the Slovak Research and Development Agency.

## References

[1] Turagam, M. K., Velagapudi, P., Kocheril, A. G. (2013). Standardization of QRS duration measurement and LBBB criteria in CRT trials and clinical practice. *Curr Cardiol Rev*, 9 (1), 20-23.

[2] Varma, N. (2008). Left ventricular conduction delays induced by right ventricular apical pacing: effect of left ventricular dysfunction and bundle branch block. *J Cardiovasc Electrophysiol*, 19 (2), 114-122.

[3] Potse, M., Dube, B., Richer, J., Vinet, A., Gulrajani, R. M. (2006). A comparison of monodomain and bidomain reaction-diffusion models for action potential propagation in the human heart. *IEEE Transactions on Biomedical Engineering*, 53 (12), 2425-2435.

[4] Bacharova, L., Szathmary, V., Svehlikova, J., Mateasik, A., Gyhagen, J., Tysler, M. (2016). The effect of conduction velocity slowing in left ventricular midwall on the QRS complex morphology: A simulation study. *Journal of Electrocardiology*, 49 (2), 164-170.

[5] Cocherová, E. (2015). Analysis of the activation propagation velocity in the slab model of the cardiac tissue. In *Proceedings of the Measurement 2015: 10th International Conference on Measurement*. Institute of Measurement Science, SAS, 105-108.

[6] Svehlikova, J., Teplan, M., Tysler, M. (2018). Geometrical constraint of sources in noninvasive localization of premature ventricular contractions. *Journal of Electrocardiology*, 51 (3), 370-377.

# Measurements of Arterial Oxygen Saturation in the Presence of the Disturbing Factors

**[1]Arkadiusz Hulewicz**

[1]Institute of Electrical Engineering and Industry Electronics, Poznan University of Technology, Piotrowo 3A, 60-965 Poznan, Poland,
Email: arkadiusz.hulewicz@put.poznan.pl

***Abstract.*** *The subject of the article concerns the interdisciplinary area of research related to the measurements of arterial oxygen saturation. The blood oxygen saturation test determines its oxygenation level and it is carried out by non-invasive or invasive methods. The basics of pulse oximetry which is a non-invasive method of measuring oxygen saturation in arterial blood were presented in the article. It uses the differences in absorption of red and infrared radiation by oxyhemoglobin and deoxyhemoglobin. The devices carrying out this measurement which are characterized by high sensitivity are presented; however, they are sensitive to disturbing factors that increase the value of the measurement error. These factors were presented and tests were carried out with their participation. Based on the carried out series of measurements, the influence of these factors on the measurement result was discussed.*

*Keywords: Oxygen Saturation, Pulse Oximetry, Photoplethysmography (PPG),*

## 1. Introduction

The subject of the article concerns the area of bio-measurements related to the determination of arterial oxygen saturation determining the level of its oxygenation. This topic is particularly important in the times of the COVID-19 pandemic. The article presents non-invasive and invasive methods of measuring this quantity with particular emphasis on the recently popular pulse oximetry. This method uses the differences in absorption of red and infrared radiation by oxyhemoglobin and deoxyhemoglobin, and it is carried out in the transmission or reflection variant.

Pulse oximetry measurements are easy to implement, and the devices of this type are mobile, widely available, characterized by high sensitivity and ever lower price. These properties often reduce the quality of their performance and increase the influence of the disturbing factors on the measurement result. The correct selection of the measuring equipment, the correct location of the sensor and the critical analysis of the obtained results enable a reliable interpretation of the signal parameters and minimize the incorrect diagnostics.

The techniques for measuring PPG signals and the influence of disturbing factors on the measurement results were presented in this article. As part of the work, 10 people were tested, for whom the reference measurement of saturation was performed and when disturbing factors were evoked. All measurements were made with three pulse oximeters with different parameters. The obtained data was analyzed, as a result of which the impact of relevant disturbances on the measurement accuracy of the individual devices was assessed.

## 2. Oxygen Saturation

One of the basic parameters necessary for the proper functioning of the human body is the appropriate level of arterial blood oxygenation. Therefore, its proper transport is very important, guaranteed by the proper cooperation of the respiratory and the cardiovascular systems. The oximetry, which enables the monitoring of the proper functioning of both these systems by measuring the level of arterial blood oxygenation, is determined by arterial blood saturation $SaO_2\%$, which determines the oxygen saturation of hemoglobin and the pressure exerted on the vessels by dissolved oxygen in plasma [1,2]. Blood oxygen saturation is used in monitoring people with suspected hypoxia and determines the percentage of what proportion of the hemoglobin contained in the erythrocytes is oxygenated hemoglobin. The blood oxygen saturation is used in monitoring people with suspected hypoxia and determines the percentage of what proportion of the hemoglobin contained in the erythrocytes is oxygenated hemoglobin. This monitoring has become commonplace in the era of the ongoing COVID-19 pandemic. According to the available definition, blood oxygen saturation is determined by Eq. 1.

$$SaO_{2\%} = \frac{HbO_{2\%}}{HbO_{2\%} + Hb_{\%}}, \tag{1}$$

where

$SaO_2\%$ the oxygen saturation,

$HbO_2\%$ the oxyhemoglobin percentage,

$Hb\%$ the percentage of deoxyhemoglobin.

To determine the oxygen saturation in the blood, it is necessary to determine the content of $HbO_2$ and Hb in the blood. This is most often done by measuring the intensity of optical radiation transmitted through tissues, proportional to its absorption by blood. Currently, two methods are used to determine the value of blood oxygen saturation. The first one includes invasive tests carried out in a clinical setting. The second group consists of non-invasive tests, which, due to their advantages, are becoming more and more popular. In this group, nowadays, the pulse oximetry method is widely used, in which the tissues are affected by the optical radiation of a given wavelength. The result of the interaction is obtained by the appropriate photodetector. Based on the data obtained in this way, it is possible to determine the photoplethysmographic curve (PPG), pulse frequency and saturation. There are two methods of non-invasive acquisition of pulse oximetry signals: transmission and reflection [1].

The transmission method is based on the determination of the optical radiation transmitted through the object. For this reason, it concerns optically thin layers, well supplied with blood, innervated and easily accessible. The sensors are most often placed on the finger. However, the reflection method of acquiring the PPG signal consists of measuring the radiation reflected by the object. Its undoubted advantage is the possibility of placing the sensor on optically thick layers, but it is necessary to choose a place with good blood flow.

## 3. The Pulse Oximetry Measurement

The principle of operation of the pulse oximeter is to measure the absorption factor of radiation of two different wavelengths (infrared and red) absorbed by hemoglobin contained in erythrocytes. The sensor is most often placed on the finger of the examined person. It consists of two alternating LEDs and a photodetector. The photodetector generates a photoelectric current, the value of which is proportional to the intensity of the transmitted radiation. The values of this current change with the rhythm of arterial pulsations [1,3].

In the case of monitoring blood saturation with the use of pulse oximeters, you should see the information on the inaccuracy of the obtained values. The environmental conditions encountered during the use of the oximeter often differ from the conditions in which the device was calibrated (from the nominal conditions). Manufacturers of this type of equipment are obliged to demonstrate to the user how to correctly perform the measurement and confounding factors that should be avoided during the test [3]. Many different factors can limit the reliability of a measurement, and as a result, the obtained results may be misinterpreted. This is particularly important with the widespread availability of portable finger sensors and attempts to use them in self-diagnosis of diseases related to the COVID-19 pandemic. The incorrect measurement of blood saturation may result in improper finger's structure or damage, the improper placement of the sensor, patient's movement, the presence of intravascular pigments, the temperature and light of the environment, changes in the nails (diseases or the use of nail polishes) as well as irregular breathing and arrhythmia [4]. Therefore, it is not recommended to use a pulse oximeter for self-diagnosis, including the diagnosis of COVID-19. This conclusion is confirmed by the research results presented later in the article.

## 4. Methods

To assess the influence of disturbing factors on the pulse oximetry measurements, tests were carried out consisting of measuring blood saturation under the influence of these factors. The tests were carried out with the use of three pulse oximeters such as Contec CMS50E, Contec CMS-VE, Novametrix Oxypleth 520A [5,6,7]. The mentioned devices differ significantly in the metrological parameters and the susceptibility to disturbing factors. To assess the influence of these factors on the change of measured values with the pulse oximeter, the studies were carried out on ten volunteers without diagnosed cardiopulmonary diseases. Three women aged 22 and seven men aged 21-22 participated in the study. All measurements were carried out in the same environmental conditions (temperature, air humidity). In each case, the temperature of the fingers was normal (there was no cold hands phenomenon). During the research, the measurement of reference saturation was carried out during which the tested person was sitting with the still hand placed on the table and with the sensor placed on the index finger of the left hand. In the next steps, the measurement was carried out with raised hand for 60 seconds, the measurement with the sensor placed on the next fingers the measurement in motion, the measurement with the sensor placed backwards, the measurement with the external illumination of the sensor, the measurement with a pinched finger and the measurement a painted nail in red, purple, green blue and black.

## 5. Results

The manufacturers of pulse oximeters recommend taking measurements in a sitting position, with a still hand placed on the table, with the sensor placed on the index finger of the left hand. The measurement carried out in this way was considered correct and treated as a reference measurement. All the saturation values measured in this way were within the range of 97-99%, which will be considered as a reference value. In the case of holding the hand up for 60 seconds, it was noticed that the saturation changed its values relative to the reference measurement. The recorded saturation results were underestimated by 10% -30% compared to the basic measurement. The only exception were the measurements made with the Novametrix Oxypleth 520A pulse oximeter, the differences of which did not exceed 5%. In the case of the saturation measurement with the hand down for any pulse oximeter, no discrepancy with the basic measurement was observed. All the read results of the measurement were within the error limits specified by the manufacturer. Similarly, the change of the finger on which the sensor was placed did not affect the accuracy of the saturation measurement for individual people.

The imitation of hand tremor as well as the bending of the finger during the measurement distorted the PPG waveform presented on the device's display. The measurement of saturation with all devices was affected by a change of measured values in the range of 7-17%. The illumination of the finger sensor with an external light source with a luminous flux of 250 lm and a color temperature of 2700 K, placed at a distance of 20 cm, made it impossible to measure blood saturation for each of the tested pulse oximeters. Similarly, the measurement with a pinched finger near the sensor made it impossible to read the searched value. In the last step, it was examined to what extent the lesions and the nail plate painted with the colored nail varnish increase the change of measured values of blood saturation. For this purpose, the measurements were carried out with a fingernail painted red, purple, green, blue and black. From the conducted research, it was noticed that the measurement results within the error limits were obtained for all devices with the purple nail varnish. The highest error values were obtained for the Contec CMS50E and Contec CMS-VE pulse oximeters when the nails were painted blue, black and green nail varnish. The results displayed on the Novametrix Oxypleth 520A pulse oximeter did not exceed the error limits of the device for all colors of the nail varnish.

## 6. Conclusions

The results of the research showed that the disturbing factors that had the greatest impact on the results of blood saturation measurements were: the external lighting of the sensor, the finger pressure during the measurement and the measurement in motion. Besides these factors for generally available pulse oximeters (Contec CMS50E Contec CMS-VE), the change of measured values was also influenced by: the color of the varnish on the nail and the lifting of the hand while measuring. Comparing all the results (proper and improper conditions of measurement), it was observed that for Novametrix OxypleTH 520A specialist pulse oximeter 124 measurements of the saturation values from the range of 97-99% were recorded out of 150 performed. In comparison, the Contec CMS50E device had 81 reference measurements out of 150 performed, and for Contec CMS-VE it was 78 reference measurements out of 150 taken.

During pulse oximetry measurements, the method and the conditions of the conducted tests are very important. The interference related to changes of blood flow (the arteries' pressure, the hand movement, holding the arm up) and the excessive illumination of the sensor by the external light sources should be avoided as much as possible. These issues become particularly important during the current COVID-19 pandemic and the related diagnostics of blood saturation. The self-diagnosis has caused an increased interest in pulse oximeters; however, the incorrect method of measurement may be a source of error and incorrect diagnosis.

## References

[1] Semmlow J. (2011). *Signals and Systems for Bioengineers*. Elsevier

[2] https://www.howequipmentworks.com/pulse_oximeter, [acess: 09.03.2021 20.00]

[3] Prokop D., Cysewska-Sobusiak A., Hulewicz A. (2010). Application of a multi-sensor set for comparative evaluation of the photoplethysmographic waveforms, *2010 First International Conference on Sensor Device Technologies and Applications.* 242-245.

[4] https://www.webmd.com/lung/news/20210222/fda-warns-of-potential-pulse-oximeter-inaccuracies, [acess: 09.03.2021 20.00]

[5] https://www.medicaltestsupply.com/v/vspfiles/assets/images/manual%20downloads/contec%20manuals/mts%20cms50e.pdf, [acess: 09.03.2021 20.00]

[6] https://www.contecmed.com/index.php?page=shop.product_details&flypage=flypage.tpl&product_id=21&category_id=13&option=com_virtuemart&Itemid=600, [acess: 09.03.2021 20.00]

[7] https://www.medwrench.com/documents/view/13954/philips-oxypleth-pulse-oximeter-novametrix-520-user-manual-pdf dostęp: 10.12.2016r. [acess: 09.03.2021 20.00]

# PPG Signal Measurement in Weak Magnetic Field by a Wearable Sensor

**Jiří Přibil, Anna Přibilová, Ivan Frollo**

Institute of Measurement Science, SAS, Bratislava, Slovak Republic.
Email: Jiri.Pribil@savba.sk

***Abstract.*** *The paper describes a currently developed wearable sensor based on the photoplethysmography (PPG) principle for the non-invasive acquisition of vital information about the cardiovascular system. The proposed sensor enables continual measurement of the PPG signal in the magnetic field environment with the inherent radiofrequency and electromagnetic disturbance. It can monitor the state of a tested person during examination in the scanning area of the open-air magnetic resonance tomograph. The performed experiments verify the practical functionality of the developed sensor including real-time wireless transmission of the measured PPG signal samples to the control device for next processing.*

*Keywords: Photoplethysmographic Wave, Wearable Sensor, Magnetic Resonance Imaging*

## 1. Introduction

During magnetic resonance imaging (MRI), the gradient-coil system vibrates and produces an acoustic noise with possible impact on patients and health personnel [1]. The examined phonating person may be affected by stress that evokes the tension of the vocal cords and the vocal tract with subsequent changes in the produced speech signal. The stress induced in this way can be evaluated also by monitoring the blood pressure (BP) and the heart rate (HR) that is the main aim of our present research.

In our previous study on HR measurement [2], the photoplethysmography (PPG) signal [3] was used for the acquisition of information about the cardiovascular system [4] of a person currently examined inside the MRI scanning device. The practical realization of this measurement shows a disadvantage of the applied interconnection between the measurement sensors, tools, and storage devices. The PPG signal was transmitted via long cables from the shielding cage of the MRI device to the mixer, the analog to digital (A/D) converter, and the data storage. It brings also the next discomfort to a tested person and makes the real-time measurement process rather difficult.

The current work was focused on testing the developed wearable PPG sensor enabling wireless Bluetooth (BT) connection for direct data transfer to the recording device. At first, the proper functions of the sensor were tested by measurement in normal laboratory conditions. The determined HR values were compared with those of the BP monitor (BPM). The main experiment inside the running MRI device shows the necessity of PPG signal filtering and shielding of all PPG sensor parts due to strong radiofrequency (RF) disturbance in the MRI scanning area.

## 2. Subject and Methods

The optical sensors for PPG signal measurement can work in transmission or reflection modes. In the transmission mode, a transmitter (light source – LS) and a receiver (photodetector – PD) are placed on opposite sides of the measured human tissue. For the PPG sensor working in the reflection mode, the PDs measure the intensity of the reflected light and are placed on the same side of the skin surface – see Fig. 1a. The recorded PPG signal contains two maxima representing systolic and diastolic peaks that provide valuable vital information about the pumping action of the heart (see Fig. 1c). A typical HR range for a healthy person is 60 to 100 $\mathrm{min}^{-1}$ (1 to 1.7 Hz) and the useful frequency content of the PPG signal is usually up to 10 Hz [5], so the sampling frequency ($f_s$) of about 150 Hz is sufficient to fulfil the Shannon sampling theorem. The picked-up PPG signal amplitude is usually not constant (with typical signal modulation – $\mathrm{HP_{RIPP}}$) and it can be often partially disturbed or degraded. Therefore, the sensed raw PPG signal must be processed (smoothed, filtered) before the HR determination.

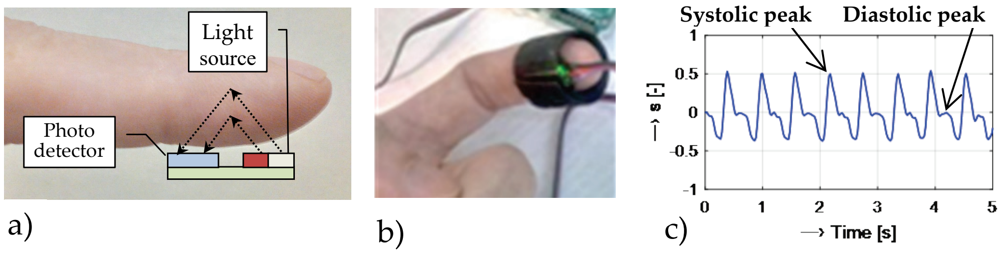


Fig. 1. Examples of reflection PPG sensor: a) principle of reflection sensor type, b) fixed on index finger by the elastic ribbon usable for experimental short-time measurement c) example of the sensed PPG wave.

The wearable PPG sensor enabling the real-time PPG signal measurement consists of three functional parts: (1) basic analog interface integrated on the board together with the LS and PD elements, (2) micro-controller or DSP processor including an A/D converter, (3) BT receiver/transmitter for communication with an external control device. The power supply for the sensor is usually realized by rechargeable batteries to prevent any galvanic connection with other devices powered by a standard AC line. To eliminate any interaction with the magnetic field and prevent possible disturbance inside the running MRI equipment, the PPG sensor must be assembled using a non-ferromagnetic material and all parts must be shielded.

Different approaches to HR determination from the PPG can be used [4, 6]. The real-time processing of the PPG signal requires a fast, simple, but robust and stable algorithm. The proposed method works in four steps – see an example in Fig. 2: (1) setting of the signal level threshold $L_{\mathrm{THRESH}}$, (2) binary clipping of the input pulse wave, (3) determination of pulse periods $T_{\mathrm{HP}}$, (4) calculation of HR values. The clipping produces a sequence $c_{PPG}(i)$ of values 1/0 corresponding to the input signal samples lying above/below the $L_{\mathrm{THRESH}}$. Next, the PPG wave properties are determined: the heart peak ripple as $HP_{RIPP} = (Lp_{\mathrm{MAX}} - Lp_{\mathrm{MIN}}) / Lp_{\mathrm{MAX}} \cdot 100$ [%] from the maximum ($Lp_{\mathrm{MAX}}$) and minimum ($Lp_{\mathrm{MIN}}$) levels of heart peaks, and the relative signal range ($PPG_{SR}$) from the offset level ($L_{\mathrm{OFS}}$), the mean peak level ($\overline{Lp}$), and the numerical range of the used A/D converter ($N_{\mathrm{AD}}$) as $PPG_{SR} = (\overline{Lp} - L_{\mathrm{OFS}}) / N_{\mathrm{AD}} \cdot 100$ [%]. The heart pulse periods $T_{\mathrm{HP}}$ in [samples] are determined from adjacent segments of ones $T_{1\mathrm{P}}$ and zeros $T_{0\mathrm{P}}$ as $T_{\mathrm{HP}} = T_{1\mathrm{P}} + T_{0\mathrm{P}}$. For the used $f_s$, the HR is calculated as $\mathrm{HR} = 60/(T_{\mathrm{HP}} \cdot f_s)$ [$\mathrm{min}^{-1}$]. The HR values obtained from the PPG signal ($HR_{PPG}$) can be compared with those measured by the BPM device ($HR_{BPM}$). For this purpose the differential parameter $HR_{DIFF}$ relative to the mean $HR_{PPG}$ ($\overline{HR_{PPG}}$) in [%] is defined as $HR_{DIFF} = (HR_{PPG} - HR_{BPM}) / \overline{HR_{PPG}} \cdot 100$. These values are next statistically analyzed for comparison purposes.

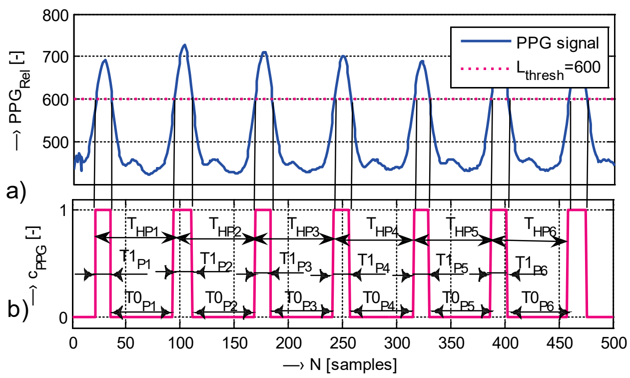


Fig. 2. An example of HR determination: a) 500-sample part of the PPG wave, b) clipped sequence with signed heart pulse periods $T_{\mathrm{HP}}$ from $T_{1\mathrm{P}}$, $T_{0\mathrm{P}}$.

## 3. Experiments and Results

Three types of experiments were performed using the proposed wearable PPG sensor: (1) preliminary identification of conditions for wireless connection through the shielding cage of the MRI device, (2) auxiliary PPG signal measurement in normal laboratory conditions, (3) main PPG signal pick-up in the magnetic field environment of the open-air MRI device E-scan Esaote Opera [7] – see an arrangement photo in Fig. 3. The performed preliminary tests confirm that the BT data transfer is possible because the metal cage of the MRI device consists of 2.5-mm diameter holes practically enabling bidirectional wireless communication at 2.4 GHz.

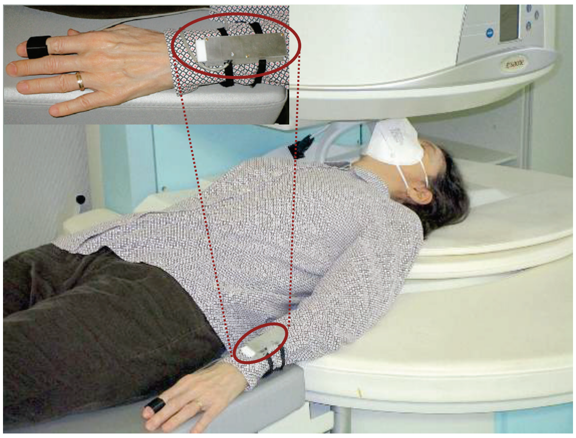

Fig. 3. Arrangement photo of the PPG measurement inside the MRI device with a detail of the wearable PPG sensor.

In auxiliary experiments, the PPG signal was picked up from the little finger to the thumb on both hands (P1L/R, P5L/R) of two male (M1, M2) and two female (F1, F2) persons to obtain a small database consisting of 40 PPG records with a duration of 80 s ($f_s$ = 125 Hz). The optical pulse sensor was fixed on a finger by an elastic ribbon (see Fig. 1b). The tested person always sat without any physical or mental activity. PPG signal sensing was accompanied by parallel HR a BP measurement using the BPM device (Microlife BP A150-30 AFIB). To prevent any influence of an inflated pressure cuff of the BPM on a tested person's blood system, the PPG signal was picked up from the opposite hand. Concerning the used 10-bit A/D converter inside the PPG sensor, the signal maximum value is $2^{10} = 1024 = N_{AD}$. Comparison of $HP_{RIPP}$, $HR_{STD}$, and $HR_{DIFF}$ parameters for five fingers of the left and right hands of all tested persons is shown in Fig. 4.

The main measuring experiment consists of the PPG signal measurement with the tested volunteer healthy person lying in the scanning area of the MRI device. Sensing of PPG signals was realized in three different conditions: (1) with the open door of the shielding cage (*OD*) and no scan sequence (*NS*) of the MRI device, (2) with the closed door of the cage (*CD*) and *NS*, (3) *CD* and the high-resolution scan sequence SE-HF 26 running (*S*1). In this case, the optical pulse sensor was placed on the index finger only. The PPG signals were recorded immediately one after another for three tested conditions. The numerical comparison of $HR_{RIPP}$, $PPG_{RANGE}$, $\overline{HR_{PPG}}$, and $HR_{STD}$ parameters for three measurement arrangements using the left hands of the persons M1, F1 is given in Table 1.

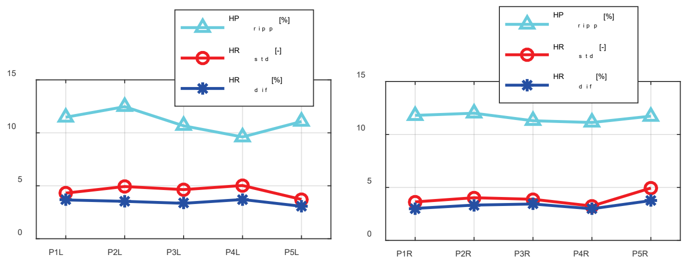


Fig. 4. Mean values of $HP_{RIPP}$, $HR_{STD}$, and $HR_{DIFF}$ parameters for each of five fingers: a) of a left hand, b) a right hand for all tested persons.

## 4. Discusion and Conclusion

The auxiliary measurement experiments in the normal laboratory conditions verify the practical functionality of the developed PPG sensor working on a reflection optical principle. It enables real-time PPG wave sensing and recording for the sampling frequencies from 100 to 500 Hz. Higher $f_s$ (250, 500 Hz) is reasonable only for systolic pulse width determination with higher accuracy. However, a lower number of detected HR periods can bring incorrectness of the statistical analysis results (see Fig. 5). The performed experiments confirm practical usage of the proposed sensor for continual measurement of the PPG signal in the magnetic field environment with additional RF and electromagnetic disturbance.

The analysis of the PPG signals picked up from five fingers has shown the dependence of the signal energy and ripple on the effective finger area and the number of weak capillaries causing worse detection of blood pulses. The PPG signals sensed from the index finger had a relatively small ripple (up to 9 %) and standard deviation of HR values (bellow five – see Fig. 4). The main measurements inside the MRI device showed a few problems to be solved to obtain sufficient PPG signal amplitude, and correct HR and other parameters. It is also important to analyze the influence of the BT transmission in the scanning area on the quality of the scanned MR images.

The PPG signal can be used to determine other parameters further describing changes in the cardiovascular system of a tested person. The applied type of the reflection PPG sensor is also used for continual monitoring of the blood oxygen saturation $SpO_2$ by pulse oximeter devices. Thus, we would like to focus our next research on this perspective application area.

Table 1. PPG signal properties and statistical parameters of HR values for three measurement conditions in MRI device.

| | OD-NS (M1/F1) | CD-NS (M1/F1) | CD-S1 (M1/F1) |
|---|---|---|---|
| $HP_{RIPP}$ [%] | 13/14 | 13/15 | 15/15 |
| $PPG_{RANGE}$ [%] | 41/53 | 31/46 | 38/48 |
| $\overline{HR_{PPG}}$ [min$^{-1}$] | 70/81 | 70/80 | 72/79 |
| $HR_{STD}$ [min$^{-1}$] | 0.4/1.9 | 2.9/4.7 | 3.4/6.2 |

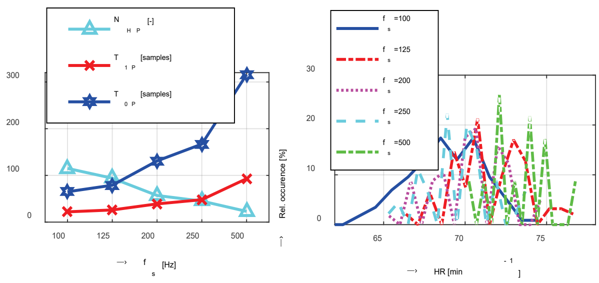

a) b)

Fig. 5. Influence of used $f_s$ on: a) detected number of heart periods $N_{HP}$ and lengths of parts $T_{1P}$, $T_{0P}$ b) histograms of determined HR values; $N_{MEAS}$ =10 k samples, $\overline{HR}$ =70 min$^{-1}$.

## Acknowledgements

This work was funded by the projects VEGA2/0003/20, COST CA16116, and APVV-19-0531.

## References

[1] Steckner, M.C. (2020). A review of MRI acoustic noise and its potential impact on patient and worker health. *eMagRes*, 9 (1), 21-38.

[2] Přibil, J., Přibilová, A., Frollo, I. (2020). First-step PPG signal analysis for evaluation of stress induced during scanning in the open-air MRI device. *Sensors*, 20 (12), 3532.

[3] Allen, J. (2007). Photoplethysmography and its application in clinical physiological measurement. *Physiological Measurement*, 28 (3), R1-R39.

[4] Rundo, F., Conoci, S., Ortis, A., Battiato S. (2018). An advanced bio-inspired PhotoPlethysmoGraphy (PPG) and ECG pattern recognition system for medical assessment. *Sensors*, 18 (2), 405.

[5] Elgendi, M. (2012). On the analysis of fingertip photoplethysmogram signals. *Current Cardiology Reviews*, 8 (1), 14-25.

[6] Blazek, V., Venema, B., Leonhardt, S., Blazek, P. (2018). Customized optoelectronic in-ear sensor approaches for unobtrusive continuous monitoring of cardiorespiratory vital signs. *Int. J. Ind. Eng. Manag.*, 9 (4), 197-203.

[7] Esaote S.p.A. (2008). *E-Scan Opera. User's Manual.* Revision A, Genoa, Italy.

# *Measurement in Biomedicine - Posters IV*

# Steady-State Visual Evoked Potentials SSVEP in Brain-Computer Interfaces

**[1]Arkadiusz Hulewicz, [2]Krzysztof Dziarski**

[1]Institute of Electrical Engineering and Industry Electronics, Poznan University of Technology, Piotrowo 3A, 60-965 Poznan, Poland,
[2]Institute of Electric Power Engineering, Poznan University of Technology, Piotrowo 3A, 60-965 Poznan, Poland
Email: arkadiusz.hulewicz@put.poznan.pl

***Abstract.*** *The subject of the article concerns the interdisciplinary area of research related to the measurement and processing of electrophysiological signals for the needs of the brain-computer interface (BCI). The electrophysiological tests are based on the non-invasive measurement of electrical potentials from the skull surface using the appropriate electrodes. The article presents the issues related to the measurement of these signals, with the particular emphasis on electrophysiological signals from the organ of vision. The signals of the steady-state evoked visual potentials (SSVEP) are shown. The operation of the systems based on brain-computer interfaces was discussed and the methods of extracting from the measured signals of the parameters used in BCI interfaces were described.*

*Keywords: Electrophysiological Studies, Resting Potential, Action Potential, Brain-Computer Interface*

## 1. Introduction

The subject of the article concerns the area of bio-measurements related to the brain-computer interfaces, based on the steady-state visual evoked potentials (SSVEP). The term the brain-computer interface BCI defines the field of science related to biomedical engineering, computer science, signal analysis and medicine. It allows the interaction between a disabled person and a computer (machine), only with the use of the properly registered electrical activity of the brain. Nowadays, it is the only way of communication and the only possibility of regaining (despite the severe disability) partial independence and participation in social life. In the BCI interface presented in the article based on the measurement of the steady-state evoked visual potentials, there is a problem of the complexity of the recorded signal caused by low values of achieved potentials, often reaching the parameters close to the values of the appearing disturbances and noise.

The correct analysis of SSVEP signals obtained for the BCI needs is the most difficult issue of biomedical engineering. The appropriate selection of the measurement procedures enables the reliable acquisition and processing of the basic parameters of the measured signals and minimizes the impact of interference. The methods of analysis and processing of SSVEP signals obtained for the needs of the BCI interface were presented in this article. The potentials related to the influence of a given stimulus were detected and the selected parameters were analyzed and the obtained results were presented.

## 2. The Brain-Computer Interface

In general terms, the brain-computer interface (BCI) is a communication system in which the user's commands are not transmitted by nerves and muscles, but by the signals resulting from the registration of the brain activity. Every muscle movement is performed by humans before it appears in the brain and then through the nervous system goes to the selected parts of the body. Initially, BCI was focused on the application of neuroprosthetics. Nowadays, they are used primarily by paralyzed people, for whom it is the only form of communication with the outside world [1,2].

The first step of the operation of this interface is the recording of signals from brain activity which are input data. This registration is mostly made by using the electrodes placed on the skin of the head. Then, to correctly interpret the recorded signals, it is necessary to extract and select them as well as the appropriate classification. The feature extraction relies on extracting such features from the signal that will clearly describe the expected properties. This is done by filtering, measuring the voltage amplitude and frequency-spectral analysis. The next step is the selection of signal features that are used in the issues related to the processing of large data sets. An example of such sets in BCI interfaces is the so-called vectors feature, the number of which equals to the product of the sampling frequency and the number of measuring electrodes. The selection relies on eliminating of redundant features with the use of appropriate mathematical tools (eg K-Fisher, Genetic Algorithms (GA), Sequence Forward Selection (SFS)). The last of the mentioned steps is data classification, which means comparing the obtained signal with the patterns (eg MLP neural networks, the supporting vector machines (SVM), Linear discriminant analysis (LDA)) [1,3].

To determine the effectiveness of BCI activities, the quality of their operation is assessed [4]. The simplest measure of this assessment is the classification accuracy defined as the quotient of the number of all correctly classified events to the number of all conducted trials. In some cases, the speed of action is determined based on the number of actions performed per unit of time.

## 3. The Electrophysiological Signals

The human brain consists of nerve cells called neurons. In a neuron where ions are electric charge carriers, there is an electric potential difference between both sides of the membrane surrounding the cell. The positive ions are molecules lacking one or more electrons and the negative ions are molecules with an excess of electrons. In the place where the positive and negative ions are separated, a potential difference is created which is called the resting potential (Vsp). When a sufficiently high cell current is applied to the neuron, an action potential (nerve impulse) is created. Among those mentioned, the potentials related to the EEG signals or evoked potentials are the most commonly used in the BCI interface [1,3]. In the article, the authors paid particular attention to BCI interfaces based on steady-state visual evoked potentials SSVEP [5]. BCIs based on visual evoked steady-state potential signals are the fastest and most efficient.

The BCI interfaces working based on signals of steady-state visual evoked potential are the fastest and most efficient. Moreover, they do not require long-term user training and a few measurement channels are used for their implementation. In this method, the optic nerve is stimulated by a stimulus generated by a photostimulator, which may include a lot of stimuli displayed simultaneously and a different blinking frequency is assigned to each of them. The user focuses attention on the stimulus chosen by him, as a result of which a signal appears in the areas of the visual cortex of the brain with a frequency corresponding to the frequency of the administered stimulus. Designing the BCI interface based on SSVEP signals, attention should be paid to the frequency of the generated stimulus [1,6].

## 4. SSVEP Signals in the Brain-Computer Interfaces

As part of the research, a BCI interface based on SSVEP signals was proposed. The stand is made of a computer with dedicated software, an electroencephalograph (Open BCI) and an ATmega 328P microcontroller that acts as a timestamp. The tests were carried out in a room not exposed to electromagnetic disturbances, and to reduce artefacts by 50 Hz, all devices at the test site were disconnected from the power supply. Gilded cup electrodes were used to measure brain activity, which were cleaned and fixed on the head of the tested person with Ten20 conductive paste. During the tests, the Open BCI interface was used which is equipped with eight measurement channels, a 24-bit analog/digital converter and an ADS1299 amplifier. It enables the recording of electroencephalographic signals and the connection with the computer is via Bluetooth technology. Such constructed station cooperated with the ATmega 328P microcontroller, which in the form of a timestamp provides information about the time of the occurrence of the stimulating signal. [3,4,6].

During the tests, signals stimulating neurons of the user's visual cortex were displayed on the computer screen in the form of green squares. When selecting the frequency of the stimulating signal, the influence of frequency on a person and literature data were taken into account. On this basis, the following frequencies were used: 10 Hz, 12 Hz, 14 Hz, 16 Hz. The stimulating signals were assigned the green color, which according to the literature data, is characterized by a high level of detection [2,4] The Open BCI system with the Open BCI Visualizer software was used to record the steady-state visual evoked potentials. The acquired signal was synchronized with a timestamp task of which was to determine the moment of the occurrence of the stimulating signal. The data obtained in this way were analyzed in the MATLAB 2009 software environment.

## 5. Methods

To determine the frequency of the stimulating signal based on the acquired SSVEP signals, mathematical analysis of the recorded signal had to be performed. First, band-stop filtration was performed using a fourth-order Butterworth filter. The signal obtained in this way was subjected to the second filtration to extract the bands related to the frequencies of changes in stimulating signals. A fourth-order Butterworth band-pass filter with the band edge determined by the frequency of the stimulating signal was used. The bandwidth was 0.2 Hz greater than the frequency of the generated stimulus. In the next stage, the obtained signal values were squared. This operation was aimed at improving the graphic representation of the signal as well as at extracting the real-time appearance of the stimulating signal. In the next step, the signal was subjected to a Butterworth low-pass filtration with a cut-off frequency of 1 Hz. In the last step, the standardization process was carried out.

## 6. Results

The study involved 10 volunteers aged 24-25 who had no medical contraindications. The measurement electrodes enabling the acquisition of SSVEP signals were placed on the occipital part of the tested person’s head, according to the 10-20 system, in places corresponding to points O1, Oz and O2, and the reference electrode was attached to the ear [7]. Before the start of the research, a training session was carried out, which allowed the tested person to become familiar with the research methodology. Each study consisted of 5 series for each frequency of the stimulating signal.

For all obtained signals, an analysis was carried out using the previously described methodology. To analyze the effectiveness of the proposed method, an assessment of the time consistency of the increase in the power of the processed signal of a specific frequency with the actual time of the stimulating signal occurrence was carried out. The results obtained from this analysis are presented in Table 1.

Table 1. The number of the correctly identified signals.

| The frequency of the stimulating signal [Hz] | The number of the correctly identified signals | Efficiency of the identification [%] |
|---|---|---|
| 10 | 49 | 98 |
| 12 | 47 | 94 |
| 14 | 46 | 92 |
| 16 | 40 | 80 |

## 7. Conclusions

The brain-computer interfaces are undoubtedly one of the most difficult and constantly evolving interfaces. From among many signals used in BCI interfaces, the use of SSVEP was proposed in the article. The interface built in this way is considered useful when the effectiveness of the stimulus recognition is greater than 90%. Based on the obtained results, it can be concluded that this condition has been met for most of the stimuli. Only in the case of the stimulus with the frequency of 16 Hz the efficiency of recognition was lower than 90% and was 80%. The prepared station and the obtained results allow stating that BCI interfaces based on the SSVEP method are easy to learn before starting the study and very effective in operation. The obtained research results form the basis for further work. According to the authors, the proposed method can be effectively used in the objective assessment of the impact of flickering light on human discomfort.

## References

[1] Woplaw JR., Birbaumer N., Heetderks WJ., McFarland DJ. (2000) Brain-computer interface technology: a review of the first international meeting, *IEEE Trans Rehabil Eng*, 8(2), 161-163.

[2] Vidal J.J. (1973). Toward direct brain-computer communication, *Annu Rev Biophys Bioeng*, 2, 157-180.

[3] Bakardjian H., Tanaka T., Cichocki A. (2010). Optimization of SSVEP brain responses with application to eight-command Brain-Computer Interface, *Neuroscience Letters*, 469, 34-38.

[4] Tello M.R., Muller S.M., Bastos T.F., Ferreira A. (2014). Evaloation of different stimuli color for an SSVEP-Brain BCI, *XXIV Congresso Brasileiro de Engenharia Biomedica*, 25-28

[5] Hulewicz A. (2019). The objective method of the evaluation of the visual acuity, *Int. Journal of Electronics and Telecommunications*, 1(65), 39-44.

[6] Pastor M.A., Artieda J., Valencia M., Masdeu J. (2003). Human Cerebral Activation during Steady-State Visual-Evoked Responses, *The Journal of Neuroscience*, 23(37), 11621-11627.

[7] Oostenveld, R.; Praamstra, P. (2001). The five percent electrode system for high-resolution EEG and ERP measurements, *Clinical Neurophysiology*, 112, 713–719

# Measurement and Evaluation of Electric Pulse Parameters to Improve Efficacy of Electrochemotherapy

**[1]Veronika Malyško, [1]Vitalij Novickij, [2]Augustinas Želvys, [2]Austėja Balevičiūtė, [2]Irutė Girkontaitė[2], [2]Auksė Zinkevičienė**

[1] Faculty of Electronics, Vilnius Gediminas Technical University, Vilnius, Lithuania
[2] State Research Institute Centre for Innovative Medicine, Department of Immunology, Vilnius, Lithuania
Email: veronika.malysko@vilniustech.lt

***Abstract.*** *Electroporation is a highly effective method in various fields of application, including cancer treatment, where when combined with drugs (called electrochemotherapy), it improves treatment via permeabilization of cells. In this work, we analyze current and voltage measurements deviation as an indicator of tumor permeability and conductivity changes in the nano (3.5 kV/cm x 800 ns x 250 x 4) and microsecond (1.4 kV/cm x 100 µs x 8) pulse ranges. The distribution of the electric field inside the tumor was approximated using a finite element method simulation in a COMSOL Multiphysics environment. Our results indicate that both nano and microsecond range pulses are suitable for effective electrochemotherapy, while measurement of the current and voltage deviation can serve as an indicator of successful cell membrane permeabilization.*

*Keywords: Electroporation, Electric Current, in vivo, Tumor.*

## 1. Introduction

Electroporation nowadays is an essential method in cancer treatment and has been investigated for decades; however, the treatment outcomes and effectiveness are still under the scope. It is known that this method is based on permeabilization of the cell membrane triggered by a pulsed electric field (PEF) to deliver poorly permeant chemotherapeutic drugs [1], [2]. Typically, the increase of cell permeability *in vitro* is detected using fluorescent markers [3], although this method cannot be employed for successful *in vivo* analysis, which is usually performed several days after treatment. There are several alternative techniques to interpret the outcome of treatment *in vivo* [4], [5], such as evaluation of the changes in tissue electrical parameters, which might give a possibility to ensure better treatment efficacy and minimize the deviation ensuring effective treatment.

## 2. Subject and Methods

In this work we have used microsecond (1.4 kV/cm x 100 µs x 8) and nanosecond (3.5 kV/cm x 800 ns x 250 x 4) non-thermal PEF (< 10 J) for electrochemotherapy of mice BALB/c Sp2/0 tumors (n = 12) in combination with 12 mg/kg doxorubicin. The tumors were allowed to establish and grow until they reached ~150–500 $mm^3$ for treatment with electrochemotherapy. Doxorubicin was injected 15–20 minutes before the treatment intraperitoneal. Electric pulses were applied using 0–3 kV, 100 ns – 1 ms square wave high voltage and high frequency (up to 1 MHz) pulse generator [6]. For *in vivo* experiment, two-needle electrodes with a gap of 5 mm were used. The observed changes of pulsed current amplitude during the *in vivo* treatment were measured, and the simulations with finite element model to predict electric field distribution were performed.

A finite element method (FEM) model of the tumor with needle electrodes was introduced in the study to assess the spatial distribution of the electric field. A 3D triangular mesh model was developed in the COMSOL Multiphysics environment (COMSOL, Stockholm, Sweden). The tumor was approximated as a conductive sphere of 10 mm diameter with constant 0.2 S/m conductivity (Figure 1). Two 0.8 mm diameter stainless-steel needle electrodes were injected in the middle and the border of the sphere with a 5 mm gap and later repositioned four times by 90 degrees. In each electrode position, electric pulses were applied according to the protocols. Electric field homogeneity and strength was evaluated using COMSOL Multiphysics (COMSOL, Stockholm, Sweden) with Livelink for Matlab (Mathworks, Natick, MA).

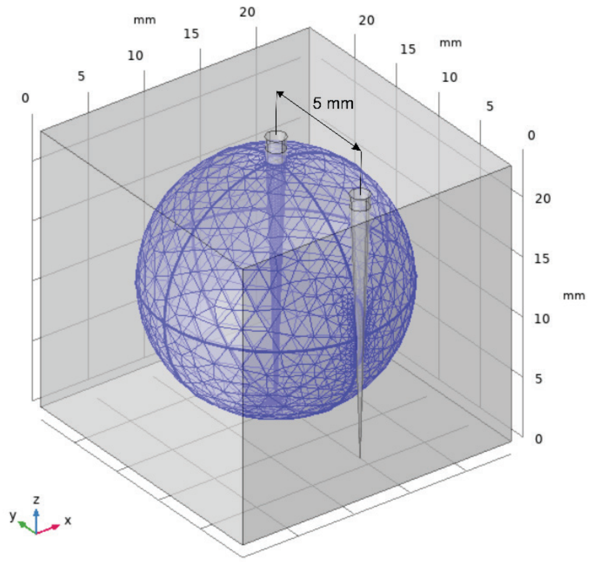


Fig. 1. Finite element model of the tumor.

Voltage drop was measured on the shunting resistor ($R_{SH}$) to determine the current through the tumor according to Ohm's law since the electrodes are connected in series with the shunt.

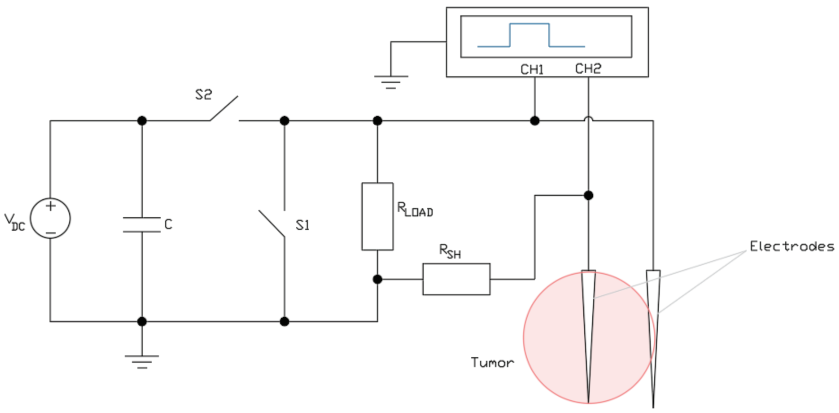


Fig. 2. Experimental circuit for tumor electrochemotherapy.

## 3. Results

During the experiment in the microsecond range, the pulses were delivered with a 30 s delay to minimize the effect of Joule heating. A 9% increase of current was detected between the first and the last pulse; however, the increase of the current was statistically significant only between the first and last pulses ($P < 0.05$, $n = 3$). The current was increasing during the first 3 pulses, followed by saturation. A similar tendency was observed during the nanosecond pulsing procedure. An identifiable increase (up to 10%) of the current between the first two pulsing bursts was detected. The permeabilization rate was saturated after the first 100 pulses. Measurement results have been used as an input for the FEM simulation, which has confirmed that the central part of the tumor was treated with the highest dose of PEF compared to the sides. However, repositioning of the needle electrodes (every 90 degrees) allowed to cover the whole tumor with an above-threshold value of PEF and thus ensure successful delivery of doxorubicin on a cellular level. Independently on the applied protocol, a statistically significant delay in tumor growth was detected.

## 4. Conclusions

Pulse measurement gives additional information about the outcome of treatment and dynamics of tumor conductivity. It allows to development of more accurate FEM models and accounts for possible field inhomogeneity. It was concluded that nanosecond PEF electrochemotherapy in combination with doxorubicin is an effective alternative for already established ESOPE protocols. Lastly, the proposed electrode repositioning strategy can be successfully used to minimize field inhomogeneity and induce a more uniform treatment.

## Acknowledgements

This work was supported by grant Nr. S-MIP-19-22 from Research Council of Lithuania.

## References

[1] Serša, G., Čemažar, M., Miklavčič, D., & Mir, L. M. (1994). Electrochemotherapy: variable anti-tumor effect on different tumor models. *Bioelectrochemistry and Bioenergetics, 35(1-2)*, 23-27.

[2] Marty, M., Sersa, G., Garbay, J.R., Gehl, J., Collins, C.G., Snoj, M., Billard, V., Geertsen, P.F., Larkin, J.O., Miklavcic, D. and Pavlovic, I. (2006). Electrochemotherapy–An easy, highly effective and safe treatment of cutaneous and subcutaneous metastases: Results of ESOPE (European Standard Operating Procedures of Electrochemotherapy) study. *European Journal of Cancer Supplements 4.11*, 3-13.

[3] V. Novickij et al. Measurement of Transient Permeability of Sp2/0 Myeloma Cells: Flow Cytometric Study. *Meas. Sci. Rev*., vol. 16, no. 6, pp. 300–304, 2016.

[4] Langus, J., Kranjc, M., Kos, B., Šuštar, T., & Miklavčič, D. (2016). Dynamic finite-element model for efficient modelling of electric currents in electroporated tissue. *Scientific reports, 6(1),* 1-11.

[5] Pavšelj, N., Miklavčič, D. (2008). Numerical modeling in electroporation-based biomedical applications. *Radiology and Oncology*, 42(3), 159-168.

[6] V. Novickij et al., High-frequency submicrosecond electroporator. *Biotechnol. Biotechnol. Equip*., vol. 30, no. 3, pp. 607–613, May 2016.

# Single-Voxel Proton MR-Spectroscopy Signal Analysis by Fingerprinting

**[1,2]Iurii Venglovskyi**

[1]Institute of Scientific Instruments of the AS CR, Brno, Czech Republic,
[2]Faculty of Electrical Engineering and Communication, BUT, Brno, Czech Republic
Email: iurii@isibrno.cz, xvengl02@stud.feec.vutbr.cz

***Abstract.*** *This paper presents the construction of a prototype fingerprint dictionary for the identification of metabolites using simple linear combinations without a preprocessing and the usage of various algorithms for fitting curves. The identification process is reduced to comparing each point of the unknown spectrum with the value stored in the dictionary. Based on the obtained results, the concept of MR fingerprinting dictionary prototype is considered to be an alternative method for NMR signal analysis, metabolite quantification and preparing data for machine learning approach as a training set with further results comparison with fittings models.*

*Keywords: Nuclear Magnetic Resonance, Single Voxel Spectroscopy, Fingerprinting, Dictionary*

## 1. Introduction

In general, proton magnetic resonance (MR) spectroscopy has two forms: single-voxel MR spectroscopy (SVS) and multi-voxel, better known as MR spectroscopic imaging (MRSI). For SVS, various parameters, including the magnetic field, are optimized to get the best possible spectrum from a relatively small region or volume of interest (VOI) when, in multi-voxel spectroscopy, the selected volume is divided into equal volumetric units. Processing similar parameters, the signal-to-noise ratio of MRI shows significantly lower current values comparing with SVS. However, the use of MRSI allows to acquire a larger quantity of data by collecting each unit of the selected volume. In the estimated sample, one MRSI single-slice typically contains more than 50 voxels. Compared to SWS, this causes a sharp growth of incoming data, which creates difficulties in their clinical assessment. Another feature of SVS is spectral contamination, which is due to the partial volume and chemical shift displacement effect from adjacent tissues. In the case of MRI, the chemical shift aliasing is due to bleeding spectra from the adjacent voxel [1]. Despite the similarity of these two methods, their comparison is considered to be inappropriate because each one can be effective only in solving one specific type of task.

The main focus of this work is based on the analysis of spectra from single-voxel proton MRS using a fingerprinting dictionary to determine the metabolite's relevant concentration. A given method is functionally similar to AI, but relies on the identification of similar patterns (fingerprints) in a massive signal dictionary instead of using any kind of generalized knowledge. In MRI, such an approach has demonstrated respectful results with operations with irregular artefacts received from irregularly undersampled MR scanning, thus enabling acceleration of the quantitative imaging [2].

## 2. Subject and Methods

*The Principle of Using the Dictionary*

The NMR metabolite fingerprint dictionary is based on the concept of creating the spectrum's list from a known concentration of metabolites. Thus, the work of the dictionary lies down in comparison the identification of the unknown spectrum to the spectral data from the data set in the dictionary Fig. 1.

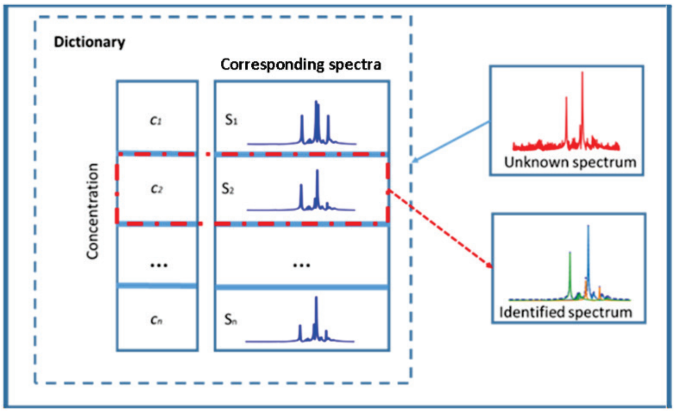


Fig. 1. Schematic representation of the dictionary as a set of concentrations and corresponding spectra for the identification of the unknown spectrum

*Data Simulation*

This section demonstrates a method for obtaining simulation spectra of the basis set of metabolites using the NMRScopeB plugin in the jMRUI software, which is a software package for advanced time-domain analysis of MRSI data [3]. The NMRScopeB plugin provides a simulation of the evolution of coupled spin systems during an NMR experiment. Its main purpose is to calculate the experiment-specific signals expected from each metabolite that can be detected, which then form a basis set used in jMRUI for signal decomposition and metabolite quantitation. However, many functions are designed to support the development of experimental methods.

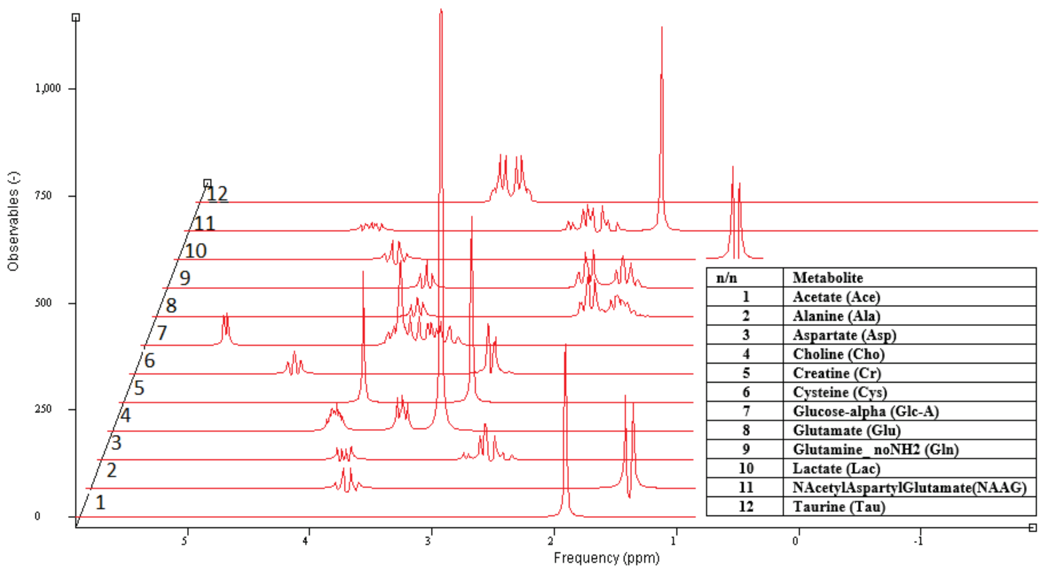


Fig. 2. Simulated selected basis set of metabolites

Fig. 2, shows a list of selected most commonly used metabolites and their corresponding spectral curves in NMR for spectroscopy analysis. All simulations were done on a PC with video adapter NVIDIA GeForce RTX 2060 and CPU Intel Core i3-8100 3.60 GHz using PRESS (Point RESolved Spectroscopy) [4].

*Dictionary Generation*

The idea of creating one detached dictionary, not divided into partitive sub-dictionaries, was rejected due to difficulties to operate large amounts of data which causes run-time errors in the described program. That is why it was decided to construct separate sub-dictionaries and later combine them.

The task was to create sub-dictionaries of spectra's list got by the method of a linear combination of acquired individual metabolites spectra, which were described in the previous chapter. Spectra were achieved with the help of the simulation method.

All of these sub-dictionaries are bound together into one single dictionary with the help of Pandas DataFrame, a data processing toolbox in Python [5].

A DataFrame is a 2-dimensional data structure that can store data of various types (including characters, integers, floating-point values, categorical data, etc) in columns. Pandas provide different facilities for easily combining Series or DataFrame with various kinds of set logic for indexes and relational algebra functionality in the case of join/merge-type and search/compare operations. The extracts are shown on the fig. 3.

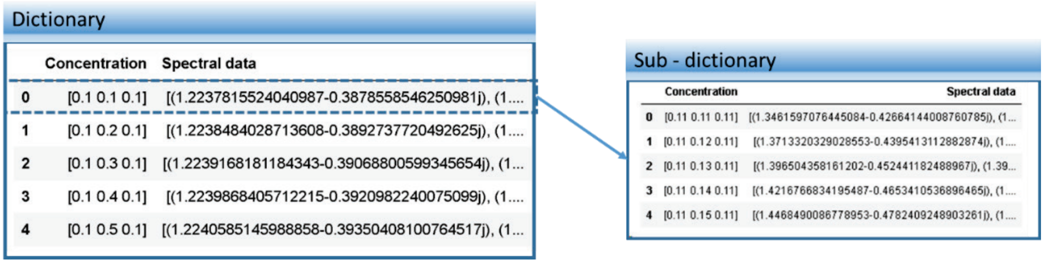

Dictionary

| | Concentration | Spectral data |
|---|---|---|
| 0 | [0.1 0.1 0.1] | [(1.2237815524040987-0.3878558546250981j), (1.... |
| 1 | [0.1 0.2 0.1] | [(1.2238484028713608-0.3892737720492625j), (1.... |
| 2 | [0.1 0.3 0.1] | [(1.2239168181184343-0.3906880059934565 4j), (1... |
| 3 | [0.1 0.4 0.1] | [(1.2239868405712215-0.3920982240075099j), (1.... |
| 4 | [0.1 0.5 0.1] | [(1.2240585145988858-0.3935040810076451 7j), (1... |

Sub - dictionary

| | Concentration | Spectral data |
|---|---|---|
| 0 | [0.11 0.11 0.11] | [(1.3461597076445084-0.4266414400876078 5j), (1... |
| 1 | [0.11 0.12 0.11] | [(1.371332032902855 3-0.4395413112882874j), (1.... |
| 2 | [0.11 0.13 0.11] | [(1.396504358161202-0.452441182488967j), (1.39... |
| 3 | [0.11 0.14 0.11] | [(1.4216766834195487-0.4653410536896465j), (1.... |
| 4 | [0.11 0.15 0.11] | [(1.4468490086778953-0.4782409248903261j), (1.... |

Fig. 3. Fragment example of the dictionary (left) and the corresponding sub – dictionary (right)

## 3. Results and Discussion

The dictionary, based on a linear combination of 3 components was tested to recognize randomly generated spectra with different levels of noise (fig. 4). As can be seen from Fig. 4, all spectra are well identified by a dictionary.

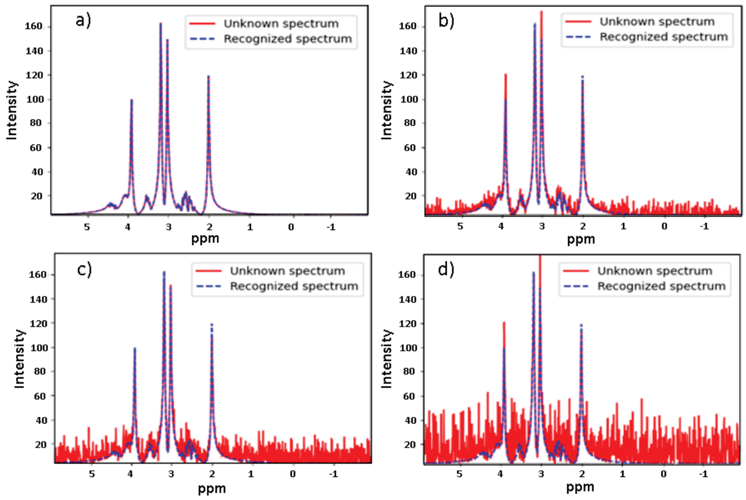


Fig. 4. Recognized spectra: a) no noise b) low noise, c) middle noise: d) high noise

To demonstrate an efficiency, a spectrum of 10 components is shown. As can be seen in Fig.5(a), the spectrum was again well recognized by the dictionary. For checking all ten metabolites presence in the spectrum, each individual component at a known concentration was plotted in Fig. 5(b). As can be seen, all peaks of the individual component correspond to the peaks in the identified spectra.

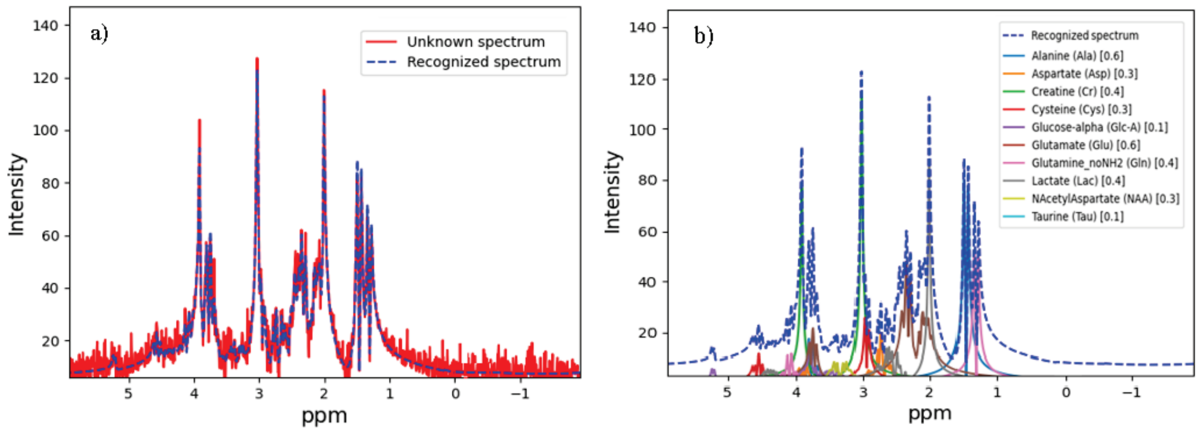


Fig. 5. Recognized spectra with 10 components: a) with unknown spectra; b) with individual components

The obtained result allows us to consider the concept of MR fingerprinting dictionary prototype as an alternative method for NMR signal analysis, metabolite quantification and preparing data. One of the advantages of the method is the possibility of using without in-depth knowledge of NMR spectroscopy, which is very important for clinical research and training new specialists. Since all the data used here were simulated, the method should be verified using measured spectroscopic data.

## 4. Conclusions

This work demonstrates the concept of a fingerprint dictionary model for NMR spectroscopy, which can be applied to single-*voxel spectroscopy for fast signal identification and quantification,* as well as to multi-voxel spectroscopy and NMR imaging. The model presented here allows to identify a metabolite just using a simple linear combination without preprocessing and usage of different curve fitting algorithms.


## Acknowledgements

This research was supported by European Union's Horizon 2020 research and innovation program under the Marie Sklodowska-Curie grant agreement No 813120 (INSPiRE-MED)


## References


[1] Kulpanovich, A., and Tal, A. (2018), “The application of magnetic resonance fingerprinting to single voxel proton spectroscopy,” *NMR in Biomedicine*, Vol. 31, Issue 11, November 2018, pp. 1-14.

[2] Ma, D., Gulani, V., Seiberlich, N., Liu, K., Sunshine, J. L., Duerk, J. L., & Griswold, M. A, “Magnetic resonance fingerprinting,” *Nature*, 495(7440, pp. 187–192, ), 2013 March

[3] Stefan, D., “Quantitation of magnetic resonance spectroscopy signals: the jMRUI software package”, *Measurement Science and Tech*, vol. 20, no. 10, 2009

[4] Starcuk, Göran and Carlsson, A and Ljungberg, Maria and Forssell-Aronsson, Eva, “K-space analysis of point-resolved spectroscopy (PRESS)”*NMR in biomedicine*. 22. 137-147, September 2009

[5] J. Mckinney, Wes. (2011). pandas: a Foundational Python Library for Data Analysis and Statistics. Python High Performance Science Computer.

# Biophysical Characterization of Integral Vectorcardiographic Parameters

**Eduard A. I. Aidu, Vladimir G. Trunov**

Institute for Information Transmission Problems of the Russian Academy of Sciences (Kharkevich Institute), Moscow, Russia
Email: aidu@iitp.ru

***Abstract.*** *The theoretical analysis of three integral vectorcardiographic parameters, namely the integral vectors of the heart ventricle depolarization and repolarization, as well as the spatial vector of the ventricular gradient, was carried out. The systematic description and biophysical interpretation of integral parameters based on the representation of the heart vector through the distribution of characteristics of the cardiomyocyte action potential for the heterogeneous bidomain myocardium model are given. Nowadays, medical research has shown the high efficiency and predictive value of these parameters. The results obtained here are useful in the modeling of vectorcardiograms for various pathological conditions states of the heart ventricles and for various characteristics of the cardiomyocyte action potential, which determine its shape. An explanation with graphic illustration is given for the very informative decartogram of repolarization acceleration.*

*Keywords: Vectorcardiography, Dipole Electrocardiotopography, Ventricular Gradient, Cardiomyocyte Action Potential, Bidomain Model of The Myocardium*

## 1. Introduction

Of great importance to up-to-date diagnostic electrocardiography are the parameters defined as areas under the electrocardiogram (ECG) calculated in different phases of the cardiac cycle. These parameters were introduced back in the early 1930s in the works of the outstanding scientist Frank Norman Wilson (1890–1952), who made a significant contribution to practical and theoretical electrocardiography.

An illustration of the genesis of a vectorcardiogram (VCG) and electrocardiographic designations used below are shown in Fig. 1.

In the work of Wilson et al. [1], the relationship between the spatial gradient of the transmembrane potential and the observed dipole moment of the electric field was explained using a simple example with the activation of a cylindrical fiber. In their subsequent work [2], the next parameters were determined: the *mean electrical axis of QRS*, as the direction in which the excitatory process spreads over the average element of the ventricles; the *mean electrical axis of T*, as the inverse of the direction in which the recovery process spreads over the average element of ventricles; the *area of QT*, a measure of the electrical effects produced by local variations in

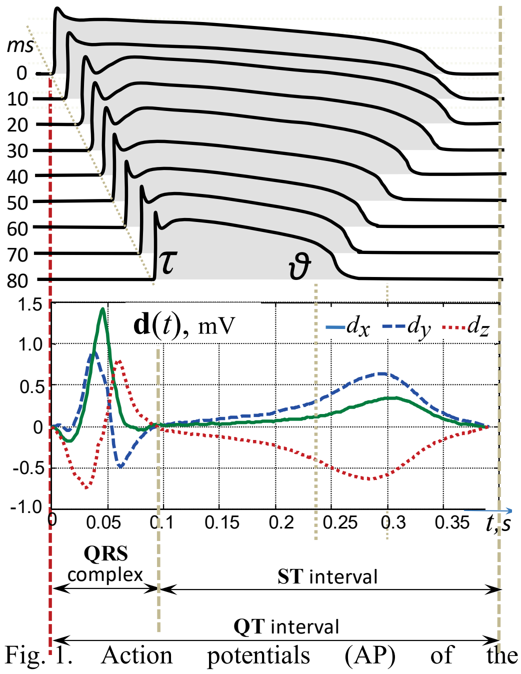


Fig. 1. Action potentials (AP) of the myocardial layers, which turn on during the QRS interval (ventricular depolarization) and turn off during the STT interval (slow and fast repolarization). Three components of the resultant VCG approximating heart vector (dipole moment of the electric heart field) spatial evolution.

the excitatory process; the *mean electrical axis of QT,* the direction of the line along which these local variations are greatest.

The last two of the listed parameters were combined into a vector that was named Ventricular Gradient (VG). This parameter turned out to be very important in terms of theory and practice, especially when moving from the two-dimensional projection in the frontal plane to representation in the three-dimensional space [3].

Some theoretical explanation of the concept VG and more precisely spatial ventricular gradient as a time integral of the heart vector on the QT interval within one cardiac cycle is given by Burger [4]. The modern theoretical description of VG is based on the work by Plonsey and Geselowitz (see, in particular, [5–7]).

## 2. Subject and Methods

*Presentation of ECG and VCG in the Bidomain Myocardial Model*

ECG in lead L at an instant $t$ can be represented by integral of current density $\mathbf{J}(t, r)$ over the excitable media region $\mathcal{M}$ (here it is the myocardium, $r = (r_x\ r_y\ r_z)$ is the point in it, $r \in \mathcal{M}$). For the bidomain model, the current density $\mathbf{J}(t, r)$ is determined by the gradient of the transmembrane potential, and then the result is ( [7]):

$$U_{\mathsf{L}}(t) = \int_{\mathcal{M}} \mathbf{J}(t,r) \cdot \nabla Z_{\mathsf{L}}(r)\ \mathrm{d}v_r = -\int_{\mathcal{M}} \boldsymbol{\sigma}_{\mathrm{i}}(r) \cdot \nabla U(t,r) \cdot \nabla Z_{\mathsf{L}}(r)\ \mathrm{d}v_r\ , \qquad (1)$$

where $\boldsymbol{\sigma}_{\mathrm{i}}$, intracellular conductivity tensor; $\nabla$, the gradient operator; $U(t, r)$ the action potential (AP), i.e., the time course of transmembrane potential at point $r$ of the myocardium; $Z_{\mathsf{L}}(r)$ the lead L field; $\nabla Z_{\mathsf{L}}(r)$ the transfer impedance which relates the current density in the element of the myocardium volume $dv_r$ to the ECG value.

If tensors of intracellular $\boldsymbol{\sigma}_{\mathrm{i}}$ and extracellular $\boldsymbol{\sigma}_{\mathrm{o}}$ conductivities are proportional ($\boldsymbol{\sigma}_{\mathrm{o}} = c \cdot \boldsymbol{\sigma}_{\mathrm{i}}$), the ECG can also be expressed through AP distribution, but over the entire surface of the myocardium $\partial$M [7]:

$$U_{\mathsf{L}}(t) = -\int_{\partial\mathcal{M}} \boldsymbol{\sigma}_{\mathrm{i}}(r) \cdot U(t, r) \cdot \nabla Z_{\mathsf{L}}(r)\ ds_r\ , \qquad (2)$$

The expressions that are analogous to the above would be also true for the heart vector (summary dipole moment of current sources in the myocardium) and thus to VCG $\mathbf{d}(t) = \left(d_x\ d_y\ d_z\right)$, which is the result of measuring the spatial components of the heart vector:

$$\mathbf{d}(t) = \int_{\mathcal{M}} \mathbf{J}(t,r)\ \mathrm{d}v_r = -\int_{\mathcal{M}} \boldsymbol{\sigma}_i(r) \cdot \nabla U(t,r)\ \mathrm{d}v_r;\ \ \text{if}\, \boldsymbol{\sigma}_{\mathrm{o}} = c \cdot \boldsymbol{\sigma}_{\mathrm{i}},\ \ \mathbf{d}(t) = -\int_{\partial\mathcal{M}} \boldsymbol{\sigma}_{\mathrm{i}}(r) \cdot U(t,r)\ \mathrm{d}s_r. \qquad (3)$$

*Representation of VCG Through the Distribution of AP Characteristics of Cardiomyocytes*

The distribution of the transmembrane potential over the myocardium and its change during the systole is determined by the AP $U(t,r)$ of individual cardiomyocytes which turn on during the ventricular depolarization and turn off during the slow and fast repolarization:

$$U(t,r) = a(r) \cdot \Lambda(t,\ \tau(r),\ \theta(r),\ \kappa(r))\ , \qquad (4)$$

where $a(r)$ is the myocyte AP amplitude at point $r$; $\Lambda$ is normalized AP as a function of the AP onset time $\tau(r)$, the AP completion time $\theta(r)$, and other parameters $\kappa(r)$ that determine the shape of the AP at point $r$.

It is convenient to represent the normalized action potential $\Lambda$ as a sum of two functions, that is, an ascending function $\Lambda_\uparrow$ for the depolarization process, increasing from zero to one with the onset at instant $\tau$, and a descending function $\Lambda_\downarrow$ for the repolarization process, decreasing from one to zero, conventionally ending at instant $\theta$:

$$\Lambda(t,\ \tau,\ \theta,\ \kappa) = \Lambda_\uparrow\left(t-\tau,\kappa_\uparrow\right) + \Lambda_\downarrow\left(t-\theta,\kappa_\downarrow\right) - 1; \tag{5}$$

Then the VCG is the sum of three components: $\mathbf{d}(t) = \mathbf{d}_\uparrow(t) + \mathbf{d}_\downarrow(t) + \mathbf{d}_-$, which are, respectively, the result of depolarization and repolarization, as well as a constant component characterizing myocardial inhomogeneity in AP amplitude:

$$\mathbf{d}_\uparrow(t) = -\int_{\mathcal{M}} \boldsymbol{\sigma}_\mathrm{i}(r)\cdot\nabla\Big(a(r)\cdot\Lambda_\uparrow\big(t-\tau(r),\kappa_\uparrow(r)\big)\Big)\mathrm{d}v_r;\ \mathbf{d}_\downarrow(t) = -\int_{\mathcal{M}} \boldsymbol{\sigma}_\mathrm{i}(r)\cdot\nabla\Big(a(r)\cdot\Lambda_\downarrow\big(t-\theta(r),\kappa_\downarrow(r)\big)\Big)\mathrm{d}v_r;$$

$$\mathbf{d}_-(t) = \int_{\mathcal{M}} \boldsymbol{\sigma}_\mathrm{i}(r)\cdot\nabla a(r)\ d\,v_r\ . \tag{6}$$

## 3. Results

*Formulas for Integral VCG Parameters*

Formulas for integral parameters are derived from the above expressions. Assuming that the AP amplitude is constant $a$ and the shape of the ascending and descending parts of AP is invariable all over the myocardium, simple expressions are obtained:

$$\mathbf{D}_\uparrow = \int_{\mathrm{QRS}} \mathbf{d}(t)\,\mathrm{d}t = a\int_{\mathcal{M}} \boldsymbol{\sigma}_\mathrm{i}(r)\,\nabla\tau(r)\,\mathrm{d}v_r;\quad \mathbf{D}_\downarrow = \int_{\mathrm{ST}} \mathbf{d}(t)\,\mathrm{d}t = -a\int_{\mathcal{M}} \boldsymbol{\sigma}_\mathrm{i}(r)\ \nabla\theta(r)\,\mathrm{d}v_r;$$

$$\mathbf{D}_\mathrm{V} = \mathbf{D}_\uparrow + \mathbf{D}_\downarrow = \int_{\mathrm{QT}} \mathbf{d}(t)\,\mathrm{d}t = -a\int_{\mathcal{M}} \boldsymbol{\sigma}_\mathrm{i}(r)\,\nabla\alpha(r)\,\mathrm{d}v_r; \tag{7}$$

where $\mathbf{D}_\uparrow$, $\mathbf{D}_\downarrow$, $\mathbf{D}_\mathrm{V}$ are integrals of the VCG $\mathbf{d}(t)$ on the intervals QRS, ST, and QT, respectively, and they are determined by the gradient distributions of the AP onset time $\tau$, AP completion time $\theta$, and AP duration ($\theta$ (r) – $\tau$ (r) = $\alpha$ (r)) in the heart ventricles.

Under the additional assumption of $\boldsymbol{\sigma}_\mathrm{o} = c\cdot\boldsymbol{\sigma}_\mathrm{i}$ :

$$\mathbf{D}_\uparrow = \int_{\partial M} \sigma_i(r)\cdot\tau(r)\,ds_r;\ \mathbf{D}_\downarrow = -\int_{\partial M} \sigma_i(r)\cdot\theta(r)\,ds_r;\ \mathbf{D}_V = -\int_{\partial M} \sigma_i(r)\cdot\alpha(r)\,ds_r. \tag{8}$$

*Characterization of Integral VCG Parameters*

**D**↑*, integral vector of the heart ventricles depolarization (integral QRS vector)*

Juxtaposing (7, 8) with (3), one can see that the depolarization onset time plays here the role of negative potential. **D**↑ is directed towards increasing the activation time, i.e., it indicates the general direction of the spread of ventricle activation and is, on average, proportional to the difference in the times of the depolarization process onset and end. The related parameters include the mean vector of ventricles depolarization (**D**↑ / *"QRS duration"*); *mean electrical axis of QRS* $\mathbf{D}_\uparrow/\|\mathbf{D}_\uparrow\|$.

**D**↓*, integral vector of the heart ventricles repolarization (integral ST vector)*

Here, the repolarization completion time plays the role of a potential. **D**↓ is directed towards decreasing the repolarization completion time, opposite to the propagation of the heart ventricle repolarization, and is, on average, proportional to the difference in the times of the beginning and end of the repolarization process.

The related parameters include the mean vector of ventricle repolarization ( $\mathbf{D}_{\downarrow}$ / *"ST duration"*); *mean electrical axis of ST* $= \mathbf{D}_{\downarrow} / \left\| \mathbf{D}_{\downarrow} \right\|$.

$\mathbf{D}_{\mathrm{V}}$, *spatial ventricular gradient (integral QRST vector)*

The AP duration plays here the role of a potential. $\mathbf{D}_{\mathrm{V}}$ is directed towards a decrease in the AP duration, and its magnitude is the rate of decrease. The related parameters include repolarization acceleration $\mathbf{D}_{\mathrm{V}} \Big/ \max\limits_{t \in \mathrm{QRS}} \left( \left\| \mathbf{d}(t) \right\| \right)$ [8], Fig. 2; spatial QRST-T angle, the angle between the integral vectors of ventricle depolarization and repolarization, or, which is the same, between the electric axes of the QRS and T.

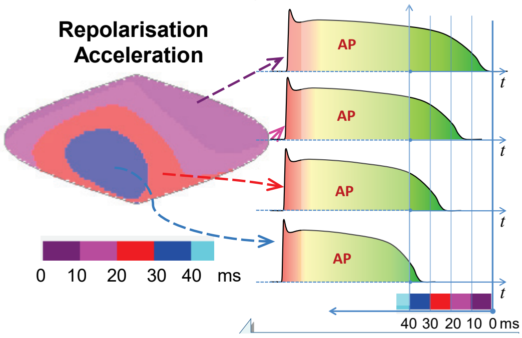


Fig. 2. Decartogram of the repolarization acceleration for a healthy subject (left); on the right, AP in the corresponding areas of the decartogram, with the values of the AP duration decreasing.

## 4. Discussion

A theoretical analysis of integral vector-cardiographic parameters was carried out based on the representation of the heart vector through the distribution of the characteristics of the action potential of cardiomyocytes for the heterogeneous bidomain model of the myocardium. A systematic biophysical description of integral parameters is given. Nowadays medical research has shown the high efficiency and predictive value of these parameters [9]. The results obtained can be useful in modeling vectorcardiograms for different pathological conditions of the myocardium of the heart ventricles with different characteristics of the action potential of cardiomyocytes and its distribution over the myocardium.

## References

[1] Wilson F.N., MacLeod A.G., Barker P.S. (1933) Distribution of the currents of action and injury displayed by heart muscle and other excitable tissues. *University of Michigan Studies, Scientific Series.,* 18: 58.

[2] Wilson F.N., MacLeod A.G., Barker P.S., Johnson F.D. (1934) The determination and the significance of the areas of the ventricular deflections of the electrocardiogram. *American Heart Journal*, 10: 46–61.

[3] Burch G.E., Abildskov A.A., Cronvich J.A. (1954) A study of the spatial vectorcardiogram of the ventricular gradient. *Circulation*, 9: 267–75.

[4] Burger H.C. (1957) A theoretical elucidation of the notion "ventricular gradient". *American Heart Journal*, 53(2): 240–246.

[5] Plonsey R. (1979) A contemporary view of the ventricular gradient of Wilson. *Journal of. Electrocardiology*, 12(4): 337–341.

[6] Geselowitz D.B. (1983) The ventricular gradient revisited: relation to the area under the action potential. *IEEE Transactions on Biomedical Engineering*, 30: 76–77.

[7] Geselowitz D.B. (1992). Description of cardiac sources in anisotropic cardiac muscle. Application of bidomain model. *Journal of electrocardiology*, 25(Suppl): 65–67.

[8] Titomir L.I., Kneppo P., Trunov V.G., Aidu E.A.I. (2009) *Biophysical Basis of Electrocardiotopography Methods*. Fizmatlit, Moscow.

[9] Waks J.W., Tereshchenko L.G. (2016) Global electrical heterogeneity: A review of the spatial ventricular gradient. *Journal of electrocardiology*, 49(6): 824–830.

# A Transthoracic Impedance Measurement System Applied to External Automatic Defibrillators

**Qi Qi[1], Ge Jian Hui[2], Zhang Guang[1], Yu Ming[1, a], Chen Feng[1, b]**

[1]Institute of Medical Support Technology, Academy of Military Medical Science, Tianjin, China

[2]Drug Instrument Supervision and Inspection Station, Wuxi Joint Logistic Support Center, Tianjin, China

Email: 397673089@qq.com

***Abstract.*** *The transthoracic impedance measurement is one of the important functions of an automated external defibrillator (AED). In this paper, the basic knowledge of transthoracic impedance measurement is introduced, and a simple transthoracic impedance measurement system combined with the defibrillation process is proposed. The system is composed of a high voltage detection circuit, defibrillation current detection circuit, AD acquisition and data processing and other parts, without additional hardware excitation measurement structure, which is conducive to the portable design of AED. The measurement results show that the error of transthoracic impedance measured by this system is less than 5%.*

*Keywords: Automated Transthoracic Impedance Measurement, Transthoracic Impedance, AED, Defibrillator*

## 1. Introduction

AED is a first-aid device for electrical defibrillation at the scene of prehospital onset since the late 1980s[1], and the thoracic impedance measurement is an important function of AED. By the size of the thoracic impedance in 25 Ω ~ 200 Ω [2], many factors can affect the thoracic impedance, including the type and area of the electrodes, electric electrodes contact conditions and so on[3]. Measuring transthoracic impedance allows AED to adjust the amount of defibrillation energy in real-time based on the patient's transthoracic impedance, and it can give early warning to dangerous conditions such as lead electrodes fall off, lead electrodes' abnormal contact and so on. For bio-impedance data, a widely utilized equivalent circuit model is known as the Cole-impedance model and was introduced by Kenneth Cole in 1940[4]. Most of the solutions of AED transthoracic impedance measurement are voltage measurement after double electrodes current excitation based on the Cole-impedance model[5], which requires additional hardware circuits and algorithms, and it cannot reflect the change of transthoracic impedance between transthoracic impedance measurement and defibrillation. To detect transthoracic impedance without adding more hardware circuits and improve the instantaneity of transthoracic impedance detection, we proposed a new method of transthoracic impedance detection based on Ohm's law, which combined the process of transthoracic impedance detection with the process of defibrillation. The measured results show that the accuracy of this method can meet the requirements of subsequent transthoracic impedance compensation function, and this method has certain reference significance for the development of AED impedance measurement technology.

## 2. Methods

### A. *High Voltage Detection Circuit*

The high voltage detection circuit detects the voltage across the energy storage capacitor. On the one hand, it feeds back to the charging circuit to ensure that the capacitor is charged to the preset voltage. On the other hand, the highest voltage value transformed by AD is recorded for the calculation of thoracic impedance. The principle of the high-voltage detection circuit is shown in figure 1, and this circuit design shall meet the following requirements: 1. Input range: 0~2200V; 2. Output range: 0~3.3V; 3. Withstand voltage: above 3000V. We use the resistance division and operational amplifier to realize the linear attenuation of the input voltage, and the amplifier model is LM358.

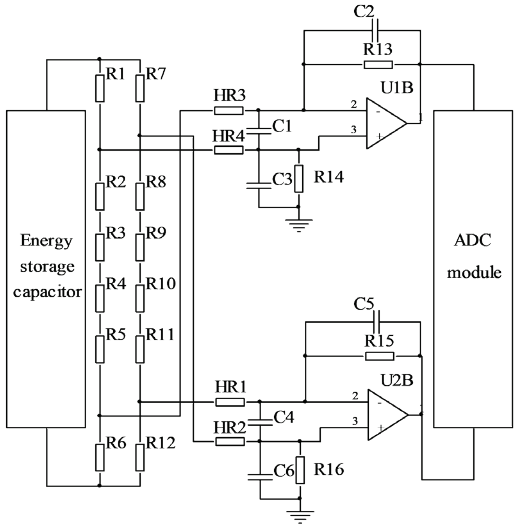


Fig.1. High voltage detection circuit schematic diagram

In addition, this paper uses the "H" bridge structure of the discharge circuit to set up a dual high voltage detection method to ensure the stability and reliability of the high voltage detection.

$R_1$ ~ $R_{12}$ in figure 1 are withstanding voltage resistance of 2.2 MΩ with an accuracy of 1%. $R_{13}$~$R_{16}$ and $HR_1$~$HR_4$ are high-precision resistors with a precision of 0.1% to ensure circuit symmetry and the accuracy of step-down multiple. Assuming that the capacitance-voltage is $V_H$, the output voltage of the resistor divider circuit can be obtained as follows:

$$V_1=\frac{R_2+R_3+R_4+R_5}{R_1+R_2+R_3+R_4+R_5+R_6}V_H=\frac{R_8+R_9+R_{10}+R_{11}}{R_7+R_8+R_9+R_{10}+R_{11}+R_{12}}V_H=\frac{2}{3}V_H \quad (1)$$

In the op-amp circuit, both $U_{1B}$ and $U_{2B}$ are typical voltage amplifier circuits, and the gain coefficient can be obtained as follows:

$$K_{U_{1B}}=K_{U_{2B}}=\frac{R_{13}}{HR_3}=\frac{R_{15}}{HR_1}=\frac{150000}{100000000}=\frac{3}{2000} \quad (2)$$

The final output voltage $V_{OUT1}$ of the high-voltage detection circuit is:

$$V_{OUT1}=\frac{2}{3}\frac{3}{2000}V_H=\frac{V_H}{1000} \quad (3)$$

The high-voltage detection circuit reduces the capacitance-voltage by 1000 times and then outputs it to AD sampling. This multiple can reduce the input voltage of 2200V to 2.2V, which meets the requirements of the system.

### B. *Defibrillation Current Detection Circuit*

Since the peak value of AED defibrillation current may reach more than 40 A[6], the system selects the current transformer to linearly convert the large current of defibrillation into a small voltage for data acquisition. This non-contact measurement method can ensure the accuracy and safety of measurement. In this system, a compensating resistor of 50 Ω is set in the defibrillation circuit to limit the defibrillation current. As shown in figure 2, the RL-3430 current transformer is selected, and the number of sub-turns is 200. High precision load resistance value for $R_t$=10Ω, and the relationship between the output voltage $V_{OUT2}$ and the defibrillation current I is:

$$V_{OUT2}=I\frac{R_t}{200}=\frac{I}{20} \tag{4}$$

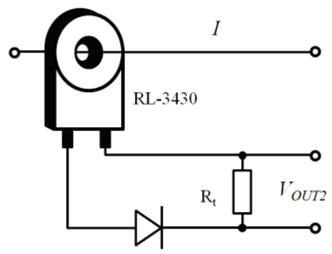


Fig. 1. Defibrillation current detection circuit schematic diagram.

### C. *AD Acquisition and Data Processing*

AD acquisition for high voltage detection and defibrillation current detection is realized by multiplexing of two 12-bit, 1MSPS analog-to-digital converters. In the charging stage of the energy storage capacitor, two AD converters work at the same time to collect dual high voltage values. The AD circuit controls the error and helps the charging circuit charge the capacitor to a preset voltage value, and saves the peak voltage on the energy storage capacitor.

When the AED stops charging, the analog-to-digital converter switches to the acquisition of the defibrillation current. When the operator presses the defibrillation key, the defibrillation current detection circuit detects a very short current signal, and the ADC records the peak value and calculates the transthoracic impedance value, and this process lasts 100 microseconds. Due to the 50 Ω defibrillation circuit impedance in the machine, the thoracic impedance calculation formula is:

$$R_{TTI}=\frac{V_H}{I}\text{-}50=\frac{1000V_{OUT1}}{20V_{OUT2}}\text{-}50=50\frac{V_{OUT1}}{V_{OUT2}}\text{-}50 \tag{5}$$

To improve the measurement accuracy of the system, the correction coefficients K and D are set in the system to correct the measurement error of the system. Based on the ideal linear relationship between the preset impedance value and the calculated voltage value, the measured voltage value is fitted linearly, and K and D are the slope correction coefficient and intercept correction coefficient, respectively. The correction coefficients can significantly reduce the errors caused by the hardware circuit, AD sampling and other links.

## 3. Results and Discussion

The system was tested by simulating transthoracic impedance. Fluke Impulse 6000D defibrillation analyzer and Fluke Impulse 7000DP percutaneous pacemaker analyzer were used to simulate the rhythm of ventricular fibrillation and transthoracic impedance. After thoracic impedance preset 50Ω, 75 Ω, 100 Ω, 125 Ω, 150 Ω, 175Ω, 200 Ω, and capacitance-voltage measurement is 1825 V, and the correction coefficient: K = 0.976, D = 1.294, measurement data are shown in Table 1.

Since most of the impedance compensation strategies of AED divide the transthoracic impedance into several stages, the measurement accuracy of the transthoracic impedance measurement system can meet the subsequent requirements of AED impedance compensation. The measurement results show that the system can control the error of the general thoracic impedance measurement below 5%, and the errors may mainly come from the following aspects:

- AD sampling rate: AD sampling rate still needs to be improved;
- Compensation resistors: The errors are more significant at small transthoracic impedance;
- Gain coefficient: The gain coefficient will vary with temperature as the measurement time progresses.

Table 1. Results of transthoracic impedance measurement.

| Preset value of transthoracic impedance /Ω | $V_{OUT1}$/V | $V_{OUT2}$/V | Measured value of thoracic impedance /Ω | The relative error /% |
|---|---|---|---|---|
| 50 | 1.825 | 0.92 | 49.2 | 1.6% |
| 75 | 1.825 | 0.71 | 78.5 | -4.7% |
| 100 | 1.824 | 0.59 | 104.6 | -4.6% |
| 125 | 1.825 | 0.51 | 128.9 | -3.1% |
| 150 | 1.825 | 0.45 | 152.8 | -1.9% |
| 175 | 1.825 | 0.4 | 178.1 | -1.8% |
| 200 | 1.825 | 0.36 | 203.5 | -1.7% |

## 4. Conclusion

This paper first describes the significance of impedance measurement in AED and proposes a simple transthoracic impedance measurement method that is attached to the defibrillation process. Then the principle and specific implementation of this method was described in detail. Through the thoracic impedance measurement verification, it is shown that this method can measure the transthoracic impedance, and the measurement accuracy meets the functional requirements of AED. The advantages of this measurement method are that it does not need to add additional hardware excitation or measurement circuit, nor does it cause unnecessary current excitation to patients, and it has better measurement timeliness. However, this method still has many shortcomings in the measurement of capacitive impedance and measurement accuracy of transthoracic impedance, and it is proposed to be improved in subsequent studies.

## References

[1] Stokes, N. A., Scapigliati, A., Trammell, A. R., & Parish, D. C. (2012). The effect of the AED and AED programs on survival of individuals, groups and populations. *Prehospital and Disaster Medicine*, 27(5), 419-424.

[2] Kerber, R. E., Grayzel, J., Hoyt, R., Marcus, M., & Kennedy, J. (1981). Transthoracic resistance in human defibrillation. influence of body weight, chest size, serial shocks, paddle size and paddle contact pressure. *Circulation*, 63(3), 676-682.

[3] Deakin, C. D., Ambler, J. J. S., & Shaw, S. (2008). Changes in transthoracic impedance during sequential biphasic defibrillation. *Resuscitation,* 78(2), 141-145.

[4] Maundy, B., Maundy, B., Elwakil, A. S., & Elwakil, A. S. (2012). Extracting single dispersion Cole–Cole impedance model parameters using an integrator setup. Analog Integrated Circuits and Signal Processing, 71(1), 107-110.

[5] Al Hatib, F., Trendafilova, E., & Daskalov, I. (2000). Transthoracic electrical impedance during external defibrillation: Comparison of measured and modelled waveforms. *Physiological Measurement*, 21(1), 145-153.

[6] Kerber, R. E., Martins, J. B., Kienzle, M. G., Constantin, L., Olshansky, B., Hopson, R., & Charbonnier, F. (1988). Energy, current, and success in defibrillation and cardioversion: Clinical studies using an automated impedance-based method of energy adjustment. *Circulation* (New York, N.Y.), 77(5), 1038-1046.

# Prior Model Selection in Bayesian MAP Estimation-Based ECG Reconstruction

**Ege Ozkoc, [1]Elifnur Sunger, Kutay Ugurlu, Yesim Serinagaoglu Dogrusoz**

Electrical and Electronics Engineering Department, Middle East Technical University, Ankara, Turkey

Email: ege.ozkoc@metu.edu.tr, elifnur.sunger@metu.edu.tr, kutay.ugurlu@metu.edu.tr, yserin@metu.edu.tr

***Abstract.*** *The inverse problem of electrocardiography (ECG) aims to reconstruct cardiac electrical activity using body surface potential measurements and a mathematical model of the body. However, this problem is ill-posed; therefore, it is essential to use prior information and regularize the solution to get an accurate solution. A statistical estimation has been applied to the inverse ECG problem with success, but a "good" a priori probability model is required. In this study, the Bayesian Maximum A Posteriori (MAP) estimation method is applied for solving the inverse ECG problem. Several prior models (training sets) are constructed, and the corresponding results are evaluated in terms of electrogram reconstruction, activation time estimation and pacing site localization accuracy. Our results showed that the training data consisting of beats from the 1$^{st}$ or 2$^{nd}$ neighbors of the test beat pacing nodes resulted in more successful results, implying that the prior models, including moderate amount and coverage of training data, might lead to an improved reconstruction of electrograms.*

*Keywords: Electrocardiography, Inverse Problem, Bayesian MAP Estimation*

## 1. Introduction

The objective of electrocardiographic imaging (ECGI) is to reconstruct the electrical activity of the heart using the body surface potentials and a mathematical model of the torso [1]. It provides high-resolution functional images of cardiac electrical activity. However, this is an ill-posed problem and to get a meaningful solution, the solution should be regularized. One of the most widely used regularization methods is Tikhonov regularization, which makes a trade-off between fidelity to the measurements and a good fit to an a priori constraint [2].

Alternatively, statistical estimation methods could also be used where the solution is represented in terms of probability distributions [3],[4]. The most widely used statistical methods are Bayesian Maximum A Posteriori (MAP) estimation and Kalman filtering. Kalman filtering uses an algorithm where the measurements observed over time are used to estimate the solution by representing the solution as state-space formulation [3]. In Bayesian MAP estimation, the solution is chosen to maximize the posterior probability density function (pdf) of the electrograms [4]. However, choosing a "good" prior pdf is still a challenge in the application of the MAP approach to ECGI.

In this study, we compare different prior models based on different training sets in terms of their performance on MAP-based ECGI. Bayesian MAP estimation is applied to 3 different test beats, and solutions are obtained for five different training sets for each test beat. These solutions are examined and compared with each other. Then, how to choose the training set to get the best result is discussed.

## 2. Subject and Methods

*Problem Definition*

The problem can be described by the equation $y_i = Ax_i + n_i$ where $y_i, x_i$ and $n_i$ denote the BSP measurement vector, epicardial surface data to be reconstructed, and noise vector, respectively, at time instance $i$, and $A$ is the forward transfer matrix. The forward matrix $A$ is found using the Boundary Element Method (BEM) in a homogeneous torso [1].

*Bayesian MAP Estimation*

Solving the problem at each time instant separately and dropping the time index, the ECGI solution is chosen to maximize the posterior pdf of the sources, which can be expressed as:

$$\hat{x}_{MAP} = \underset{x}{argmax}\, \boldsymbol{p}(x|y) = \underset{x}{argmax} \frac{\boldsymbol{p}(y|x)p(x)}{\boldsymbol{p}(y)} . \tag{1}$$

In this study, the noise is assumed to be Gaussian zero-mean independent identically distributed ($n \sim N(0,\ C_n)$). The epicardial potentials are also assumed to have Gaussian distribution ($x \sim N(\mu_x,\ C_x)$). Thus, the following expression can be obtained as the MAP solution:

$$\hat{x}_{MAP} = \left(A^T C_n^{-1} A + {C_x}^{-1}\right)^{-1}\left({C_x}^{-1}\mu_x + A^T {C_n}^{-1} y\right), \tag{2}$$

The prior mean ($\mu_x$) and the covariance matrix ($C_x$) are estimated from a training dataset consisting of previously available epicardial potentials [4].

*Experimental Data*

Both the training and test data constitute measurements taken from Utah tank experiments [5]. Sock electrodes with 490 nodes on the epicardial surface were utilized to measure the electrograms (EGM), while BSPs were simulated from these EGMs at 192 electrodes on the torso surface at 30 dB SNR. Three different test beats from two different datasets were used to compare the reconstruction accuracy of the MAP approach. These three test beats, whose pacing nodes have a higher number of neighboring pacing locations, were used. The QRS segment of the test beat was reconstructed using the generated training data.

For each of the three test beats, five different training datasets were generated. Each of the training datasets includes training beats paced from the neighbors of the test beat pacing node up to the respective order given by the training set name. To illustrate, Training Set 3 includes beats initiated from the pacing locations up to the third-order neighborhood of the test beat pacing site. Using the heart surface mesh, first-order neighbors have direct connectivity to the node of interest, second-order neighbors constitute the first order neighbors of the node of interest combined with their first order neighbors, etc. The pacing site of the test beat and those of the training beats are illustrated in Fig. 1. The metrics describing the proximity of the training data pacing nodes to the test data pacing location and the coverage do not remarkably change among the test datasets. The mean distances to the pacing node for Training Set 1 to 5 are about 5 mm, 7.8mm, 10mm, 13mm, and 15.7mm. The numbers of beats in the training sets generated for Test Beat-1 and Test Beat-3 are close to each other, whereas, for Test Beat-2, the number of training beats is significantly larger.

## 3. Results

Reconstructed potentials were evaluated using Pearson's correlation; spatial correlation coefficients (sCC) for each time instant over all leads, and temporal correlation coefficients (tCC) for each lead over all time instants were computed. Activation times (ATs) were estimated using a spatio-temporal approach [6]. The accuracy of AT was evaluated by using

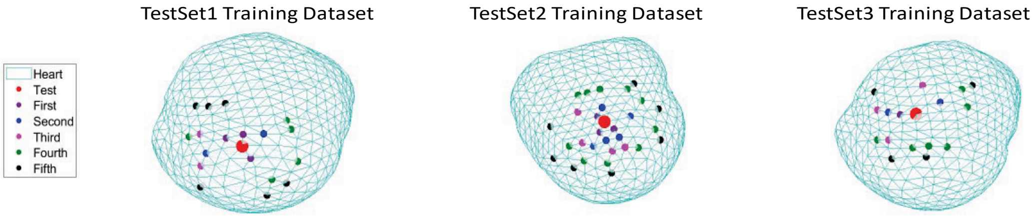


Fig. 1. Neighborhood map of pacing nodes regarding the training and test data.

Pearson's CC. The pacing site was assigned as the earliest activated node. Localization error (LE) was computed as the Euclidean distance between the true and estimated pacing sites.

Fig. 2 presents the box plots for sCC and tCC results for the three test beats and their respective five training data. Test Beat-1 has the lowest median sCC and tCC values for Training Data-1. Other training datasets have similar median values and interquartile ranges (IQRs). All the five training datasets used in the reconstruction of potentials of Test Beat-2 give similar tCC results. However, Training Data-1 and 2 provide slightly smaller IQR for sCC. Therefore, Training Data-1 and 2 outperform other training datasets. For Test Beat-3, median tCC and sCC decrease going from Training Data-1 to Training Data-5. Training Data-1 has a wider IQR than Training Data-2 for sCC results.

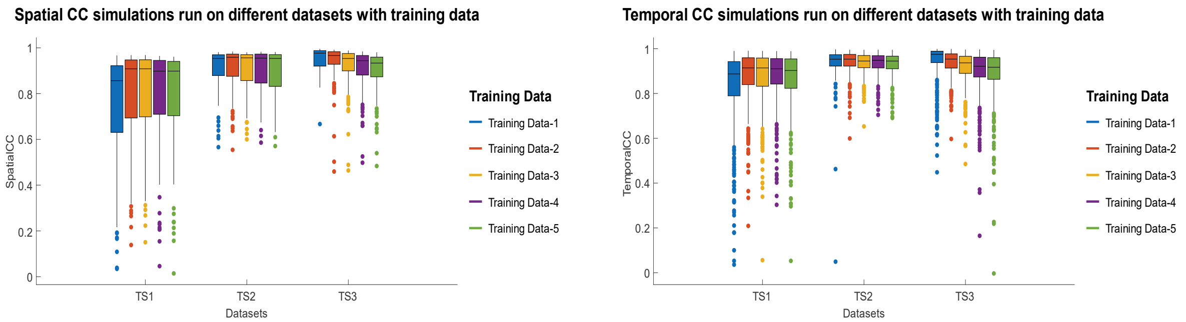


Fig. 2. Box plots for spatial and temporal correlation coefficients between three test beats (TS1, TS2 and TS3) and their Bayesian MAP estimations with five training datasets.

Table 1 and 2 present the CC values for the reconstructed ATs and the LE (mm), respectively. CC results for AT estimation are not significantly affected by choice of training datasets. Unlike the performance in reconstructing the epicardial potential maps, the localization error was not observed to be strictly correlated with the training set choice. To illustrate, the localization error obtained using Training Data-1 is approximately half of that of Training Data-2, although they are equally successful considering sCC and tCC as the evaluation metric.

Table 1. CC values for ATs for three test beats with five training datasets.

| Test Beats | Training Data-1 | Training Data-2 | Training Data-3 | Training Data-4 | Training Data-5 |
|---|---|---|---|---|---|
| Test Beat-1 | 0.95 | 0.96 | 0.95 | 0.95 | 0.95 |
| Test Beat-2 | 0.93 | 0.94 | 0.93 | 0.94 | 0.94 |
| Test Beat-3 | 0.97 | 0.98 | 0.98 | 0.97 | 0.96 |

Table 2. Localization errors (in mm) for three test beats with five training datasets.

| Test Beats | Training Data-1 | Training Data-2 | Training Data-3 | Training Data-4 | Training Data-5 |
|---|---|---|---|---|---|
| Test Beat-1 | 12.98 | 9.50 | 9.50 | 9.41 | 9.50 |
| Test Beat-2 | 4.27 | 9.00 | 8.67 | 8.67 | 8.32 |
| Test Beat-3 | 24.94 | 9.56 | 13.38 | 13.36 | 16.74 |

## 4. Discussion & Conclusion

In this study, we applied the Bayesian MAP estimation to ECGI to evaluate the best-case scenario where we know the pacing node of the test beats from the measured epicardial potentials. We observed that the selection of the training set is essential to get a good result. Including the nodes up to the first or second neighbors of the training set is generally enough to obtain a good estimation. As further nodes are included, the result slightly gets worse but are still adequate in terms of localization. This can be attributed to the fact that the prior pdf may get less successful at representing the local features when the training beats are taken further away from the pacing location. However, the decrease in the performance is very small even with Training Data-5. We did not observe any contradiction in the behavior of spatial and temporal CCs, so considering only one of them to check the results was enough. The seemingly contradictory relation observed in some cases between LE and the other metrics can be attributed to the inaccurate performance of the AT estimation algorithm. The accuracy of the algorithm needs to be improved for a more reliable evaluation of the ECGI methods. Nevertheless, Bayesian MAP estimation has some limitations in clinical tasks since the epicardial covariance matrices cannot be estimated in the absence of epicardial measurements. Tikhonov regularization, which does not require any prior knowledge [2], has an advantage in this sense with a trade-off of reconstruction success. The success of the prior model constructed with simulated training data will be investigated to overcome this problem.

## Acknowledgements

This work was supported by the grant: TUBITAK-118E244. The authors thank Dr. Robert S. MacLeod and his colleagues from the University of Utah for the data used in this study. All authors have contributed equally to this study.

## References

[1] Gulrajani, R.M. (1998). The forward and inverse problems of electrocardiography. *IEEE Engineering in Medicine and Biology Magazine*, 17(5), 84–101.

[2] Cluitmans, M.J.M., *et al.* (2017). In vivo validation of electrocardiographic imaging, *JACC: Clinical Electrophysiology*, 3(3), 232–242.

[3] Erenler, T., Serinagaoglu Dogrusoz, Y. (2019). ML and MAP estimation of parameters for the Kalman filter and smoother applied to electrocardiographic imaging. *Medical & Biological Engineering & Computing*, 57(10), 2093–2113.

[4] Serinagaoglu Y., *et al.* (2005). Bayesian solutions and performance analysis in bioelectric inverse problems, *IEEE Transactions on Biomedical Engineering*, 52(6), 1009–1020.

[5] MacLeod R. S., *et al.* (1995). Electrocardiographic mapping in a realistic torso tank preparation. In *Proceedings of 17th International Conference of the EMBS*, 45–246.

[6] Erem B., *et al.* (2014). Using transmural regularization and dynamic modeling for noninvasive cardiac potential imaging of endocardial pacing with imprecise thoracic geometry, *IEEE Transactions on Medical Imaging*, 33(3), 726-738.

# SmartPatch for Victims Management in Emergency Telemedicine

**[1,3]Fedor Lehocki, [2]Ana Madevska Bogdanova, [3]Milan Tysler, [3,4]Beata Ondrusova, [2]Monika Simjanoska, [2]Bojana Koteska, [2]Magdalena Kostoska, [1]Martin Majak, [1]Miroslav Macura**

[1]Faculty of Informatics and Information Technologies, STU in Bratislava, Bratislava, Slovakia
[2]FCSE, Ss. Cyril and Methodius University, Skopje, North Macedonia
[3]Institute of Measurement Science, Slovak Academy of Sciences, Bratislava, Slovakia
[4]Faculty of Electrical Engineering and Information Technology, STU in Bratislava, Slovakia
Email: fedor.lehocki@stuba.sk

***Abstract.*** *Wearable real-time systems collecting and smartly analyzing information about patient health status could help medical personnel adopting the most suitable countermeasures in case of highly stressful situations in military and civil scenarios. Such situations include terrorist attacks or rescue operations. We propose the design and development of a patch-like device prototype (SmartPatch) and a methodology enabling continuous evaluation of victims' vital parameters. Using this innovative platform after the first triage, the onsite emergency teams will have continuous information about the health status of each person wearing the SmartPatch. If the health status of a victim is changed, SmartPatch is able to generate an alert and prevent overlook of critical health changes causing potential severe life-threatening consequences or death.*

*Keywords: Wearable Body Sensors, Cuffless Blood Pressure Measurement, Triage, Emergency, Telemedicine*

## 1. Introduction

Over the last few years, various wearable real-time systems have been developed to monitor the health status of patients and thus to improve the provided health care. The use of wearable devices to monitor patients in the hospital ward or at home reduces the frequency of regular check-ups by the medical staff and increases the likelihood of early detection of the patient's health deterioration [1]. Chest-based patch devices like Sensium®Patch are used in the ward for early detection of health worsening signs. This device monitors the patient's heart rate from a single lead ECG, respiratory rate and auxiliary temperature. Three hours of recorded data can be stored, and the device battery lasts for 5 days [2]. VitalPatch® can be connected to a mobile phone and used for remote monitoring at the patient's home. It measures single-lead ECG, heart rate and its variability, respiratory rate, body and skin temperature for up to 7 days. In 2019, a prototype of a health patch was introduced by the Interuniversity Microelectronics Centre (IMEC) that measures heart and respiratory rate but also $SpO_2$ by using photo-plethysmography (PPG). Advantageous properties of the above-mentioned types of wearable health monitoring devices suggest that similar devices could also be used in emergency telemedicine to improve the management of victims during mass injury events such as terrorist attacks or natural disasters. Such management requires improvement of the rescue procedures as well as the development of adequate supporting systems [3].

In this paper, we present the design of a wearable monitoring system that uses integrated wireless sensor SmartPatch (SP) for continuous recording and measurement of selected vital parameters of the victim and modular software capable of basic onsite real-time diagnostics based on advanced signal processing methods and artificial intelligence.

## 2. Subject and Methods

Simple triage and rapid treatment (START) is a triage method used by first responders to quickly classify victims of mass casualty incidents based on the severity of inflicted injuries. Victims are evaluated into four categories: walking wounded (Green), delayed (Yellow), immediate need for treatment (Red), and deceased (Black). Based on this evaluation, decisions are made about priorities for treatment and evacuation to the hospital. The wearable technologies can substantially improve the decisions and the medical response to the mass victim events by continuously measuring vital parameters and generating timely warnings if the victim's health status has changed.

When implementing the wearable technology, we have considered three aspects of the solution: the design and development of the patch-like biosensor SP, the methodology for analysis of acquired physiological data and their interdependencies reflecting changes of the health status, and finally, some modifications of victims' management processes brought on by the introduction of the new technology.

The proposed SP sensor provides continuous recording of the electrical activity of the heart - the ECG signal, body temperature, blood oxygen saturation sensed by changes of the light absorption - the PPG signal, and chest movements - the respiratory signal. Given the signals, the device has the processing power to provide real-time calculation of the pulse, systolic and diastolic blood pressure, respiratory rate, and the chest-based $SpO_2$.

The SP device is accompanied by relevant methodology implemented in software modules enabling signal processing and data analysis for detection of health status changes corresponding to transitions to Yellow or Red status. If some data are transferred from the SP to the first responders or to the central server, security aspects of the data transfer are considered.

During the modified triage process, victims labeled as Green or Yellow get the SP placed on their chests. The SP is designed to alert the first responders by visual (flashing diodes) and audio (sound alarm) signals if the health status transition from Green to Yellow or Yellow to Red is identified. This improves the dynamics and quality of the triage process.

## 3. Proposed Solution

*Design and development of the integrated SP*

Besides implementation of existing (or being developed in parallel) sensors, electronics and data processing methods, design of the integrated SP poses several research questions. These include the cuffless blood pressure measurement and the chest-based $SpO_2$ measurement.

In 2014, the IEEE standard for wearable cuffless blood pressure (BP) measuring devices was introduced. Algorithm for BP estimation based on both pulse transit time (PTT) and PPG intensity ratio (PIR) achieved an accuracy of $-0.37 \pm 5.21$ mmHg for systolic and $-0.18 \pm 4.13$ mmHg for diastolic blood pressure. We use machine learning techniques for BP estimation from ECG signal [4] to minimize the need of calibration and recalibration of the cuffless system and to ensure the accuracy of the estimation. Recent development includes using deep learning in the estimation of BP [5].

During some life-threatening situations, blood circulation is limited to the torso and head. Thus, monitoring blood oxygenation from the finger can result in corrupted blood saturation reading due to poor blood circulation [6]. Integration of $SpO_2$ sensor into the chest-based patch device (e.g. central area of the manubrium bone) enables a reduction in measurement delays of blood saturation by several seconds comparing to the finger-based sensor. This is especially important in emergency situations and enables rescue teams to introduce treatment more rapidly. However, as the reflective chest-based sensors use a PPG waveform that is several times weaker than that obtained from the finger-based transmission sensor, the signal is more prone to noise and distortions due to motion artefacts of the skin. Successful measurement requires proper illumination of the chest tissue, large gain, adjustment of the power supply voltage, proper angular rotation of the photodiode and LEDs regarding the sensor surface, and high filtering.

The ECG signal is recorded by two patch electrodes, processed by instrumental and rail to rail operational amplifiers and sampled at 1 kHz by a 10-bit A/D converter. The temperature is sensed by an infrared or contact sensor, respiratory is estimated by a chest tensometer. The patch device is powered by Li-on, Li-Fe or Li-poly battery that provides the best energy to size ratio. The SP hardware is a proof of concept prototype, where the main goal was to determine whether it is possible to build a reliable and functional device.

The SP device enables data transmission to the nearest rescue team member mobile phone via Bluetooth and then by WiFi or a mobile network to the central data repository with all relevant security and privacy consideration. Data encryption and access permission for data packing and transfer use existing NATO standards (e.g. APP-11, APP-11 NATO Message Catalogue, ADatP-3, AMedP-5.1). The service for reading data from the SP and transferring them to the central data repository is installed on mobile phones carried by the rescue team members. The data transferring process from the disaster site to the relevant stakeholder for further victim's vital signs analysis is shown in Fig.1.

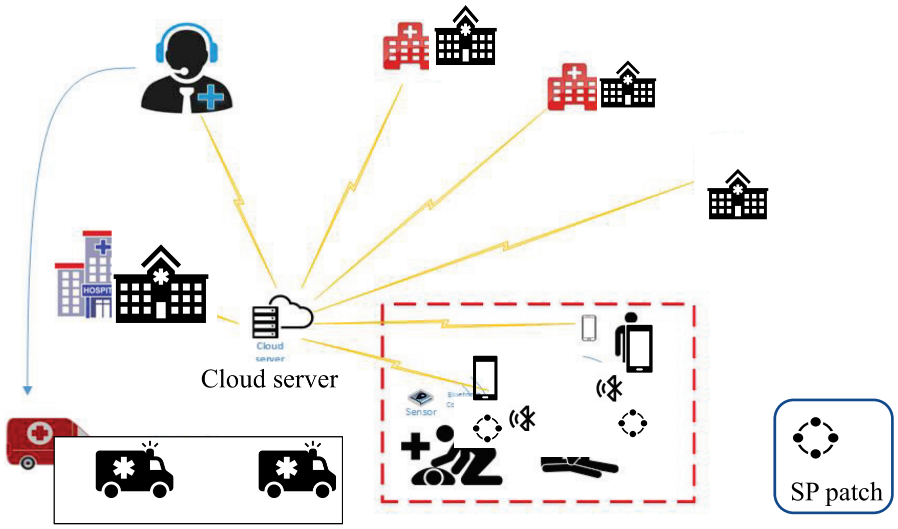


Fig. 1. Data transfer process using the SP patch.

*Processing and analysis of physiological data and the alert system*

The methodology for the Green to Yellow (GtoY) and Yellow to Red (YtoR) alert consists of two parts: 1. decision-making process according to the START method, and 2. machine learning (ML) model, as validation support. According to the START triage procedure, heart rate and respiratory rate give enough information to detect possible deterioration of the victim's health status. For the ML part, the existing databases [4] of vital parameters and the publicly available ones (such as https://www.physionet.org) stand as a valuable asset for the development of the most appropriate ML model, chosen among support-vector machines, deep neural networks or ensemble methods. These models, considering the whole pipelining process, are developed off-line, and the label classification part is done on the Smart Patch in real time. The processing power of the SP allows deploying of this twofold decision-making process.

*Victims management*

The standard START triage procedure has limitations in that it does not provide resource allocation. The classification procedure does not depend on the number of victims or resources available (medical emergency crew members). Also, it does not prioritize patients within each of the three triage groups and does not follow the changes in their health status. The introduction of the SP technology addresses the limitations mentioned above of the triage system and allows to consider how to redesign existing processes of the victims' management on the site of the accident and how to support the coordination of medical teams in the field.

## 4. Discussion and Conclusions

We proposed a new type of chest patch – the SmartPatch prototype, a wearable technology that can help to improve the process of victims' management after mass victims events. The SP devices can be a part of the emergency unit equipment or publicly available as medical kits at potential targets of terrorist attacks (shopping malls, sports arenas, public squares and similar surroundings). Integrating the technology into the existing emergency strategies will require mechanisms for building trust and achieve error-free communication among the emergency professionals in order to avoid misunderstanding and ignorance. Medical experts should be directly included in the real-life simulation exercises and in the patch-like device prototypes testing. This is a part of the strategy for ensuring SP's acceptance by the medical responders within their existing protocols.

However, due to constraints of the Bluetooth technology with limited connections to its peers and possible unavailability of the mobile network at the site of accident (rural area, overloaded network), the data transmission, sharing, and remote evaluation might be feasible only in the emergency vehicle during patient transportation to the hospital. Even this will enable timely setup of the needed care in the hospital.

## Acknowledgements

This work was supported by the NATO SPS project G5825 "Smart Patch for Life Support Systems (SP4LIFE)" and the project ITMS 313021X329 "Advancing University Capacity and Competence in Research, Development and Innovation (ACCORD)" within the Operational Program Integrated Infrastructure, co-funded by the European Regional Development Fund (ERDF).

## References

[1] Posthuma, L.M., Downey, C., Visscher, M.J., Ghazali, D.A., Joshi, M., Ashrafian, H., Khan, S., Darzi, A., Goldstone, J., Preckel, P. (2020). Remote wireless vital signs monitoring on the ward for early detection of deteriorating patients: A case series. *International Journal of Nursing Studies*, 104, 1-9.

[2] "Early Detection of Patient Deterioration." The Surgical Company, www.sensium.co.uk/ (March, 2021).

[3] Lehocki, F., Bacigal, T.: "Telemedicine and mHealth system for complex management in T1DM and T2DM patients: Results of 6 months study", (2016) *IFMBE Proceedings*, 57, pp. 1125-1130.

[4] Simjanoska, M., Gjoreski, M., Gams, M., & Madevska Bogdanova, A. (2018). Non-Invasive Blood Pressure Estimation from ECG Using Machine Learning Techniques. *Sensors*, 18(4), 1160.

[5] Eom H, Lee D, Han S, et al. End-to-End Deep Learning Architecture for Continuous Blood Pressure Estimation Using Attention Mechanism. *Sensors* (Basel). 2020;20(8):2338.

[6] C. Schreiner, P. Catherwood, J. Anderson and J. McLaughlin, "Blood oxygen level measurement with a chest-based Pulse Oximetry prototype system," *2010 Computing in Cardiology*, 2010, pp. 537-540.

# *Young Investigator Award Session II*

# Identification of Non-Polynomial Calibration Dependence Accounting for Instrumental Uncertainties of Measuring Instruments

**[1,2]Igor Zakharov, [1]Pavel Neyezhmakov, [1]Valery Semenikhin**

[1]National, scientific centre "Institute of metrology" Kharkiv, Ukraine,
[2]Kharkov national university of radio electronics, Kharkiv, Ukraine
Email: newzip@ukr.net

***Abstract.*** *An algorithm for the identification of non-polynomial calibration dependences, which can be reduced to linear dependences by change of variables, has been developed. The parameters of linear dependences are found by the least-squares method. An algorithm for measurement uncertainty evaluation using the identified dependence is given, accounting for the instrumental measurement uncertainties of the responses of the calibrated measuring instrument and the values of the calibration points.*

*Keywords: Non-Polynomial Calibration Dependence, Change of Variables, Least Squares Method, Instrumental Uncertainties.*

## 1. Introduction

The problem of plotting calibration dependences of measuring instruments is solved using a measurement experiment, during which values are measured with some uncertainties. The identification of a given type of dependence is carried out using the obtained values of the measured quantities for the dependence. The most common method for solving the identification problem is the least-squares method, which is well implemented for polynomial dependencies. In metrological practice, one often has to deal with the case when an increase in the degree of the polynomial within reasonable limits does not lead to a significant decrease in the approximation error when identifying a nonlinear calibration dependence. In this case, the transformation of the original dependence into a linear dependence is applied by the change of variables. The parameters of the linearized dependence are subsequently found using the least-squares method.

The paper discusses the solution to the problem of uncertainty evaluation of the non-polynomial dependence identification accounting for the instrumental uncertainties of the measured values.

## 2. Transformation of Non-Polynomial Calibration Dependence: Basic Relations

The measuring instrument (MI) response is measured at *N* calibration points of the considered range $X_1, X_2, ..., X_N$ to plot the calibration dependence of the MI. At each $X_j$ calibration point, measurements of the MI readings $Y_{ji}$ ($i$ = 1, 2, ..., $n$) are carried out and repeated *n* times. Based on the measurements, a calibration dependence is plotted and its approximation is carried out by a mathematical dependence. Finding the parameters (identification) of the dependence is most often performed by the least-squares method (LSM) [1], which provides the best results when the approximation dependence is a polynomial.

In metrological practice, one often has to deal with the case when an increase in the degree of the polynomial within reasonable limits does not lead to a significant decrease in the approximation error when identifying a nonlinear calibration dependence. In this case, the transformation of the original dependency

$$Y = f(X, A, B) \tag{1}$$

within linear dependence

$$y = a + bx \tag{2}$$

by the change of variables [1]:

$$x = \Phi(X); \tag{3}$$

$$y = \Psi(Y). \tag{4}$$

is applied.

Expressions (1) for nonlinear functions (1) reduced to linear ones are given in the first column of Table 1, the second column of which contains expressions (3), (4) for the functions.

Table 1. Basic expressions for implementing the variable replacement method

| $Y = f(X, A, B)$ | $x = \Phi(X)$<br>$y = \Psi(Y)$ | $\hat{A}$, $\hat{B}$ | $X = f^{-1}(Y, \hat{A}, \hat{B})$ | $c_X$; $c_Y$ | $c_x$ |
|---|---|---|---|---|---|
| $Y = Ae^{BX}$ | $x = X$<br>$y = \ln Y$ | $\hat{A} = e^{\hat{a}}$<br>$\hat{B} = \hat{b}$ | $X = \dfrac{\ln Y - \ln \hat{A}}{\hat{B}}$ | $c_X = 1$<br>$c_Y = 1/Y$ | $c_x = 1$ |
| $Y = AX^B$ | $x = \ln(X)$<br>$y = \ln(Y)$ | $\hat{A} = e^{\hat{a}}$<br>$\hat{B} = \hat{b}$ | $X = \exp\left(\dfrac{\ln Y - \ln \hat{A}}{\hat{B}}\right)$ | $c_X = 1/X$<br>$c_Y = 1/Y$ | $c_x = e^x$ |
| $Y = A + B\ln(X)$ | $x = \ln(X)$<br>$y = Y$ | $\hat{A} = \hat{a}$<br>$\hat{B} = \hat{b}$ | $X = \exp\left(\dfrac{Y - \hat{A}}{\hat{B}}\right)$ | $c_X = 1/X$<br>$c_Y = 1$ | $c_x = e^x$ |
| $Y = A + \dfrac{B}{X}$ | $x = 1/X$<br>$y = Y$ | $\hat{A} = \hat{a}$<br>$\hat{B} = \hat{b}$ | $X = \dfrac{\hat{B}}{Y - \hat{A}}$ | $c_X = -1/X^2$<br>$c_Y = 1$ | $c_x = -1/x^2$ |
| $Y = \dfrac{1}{A + BX}$ | $x = X$<br>$y = 1/Y$ | $\hat{A} = \hat{a}$<br>$\hat{B} = \hat{b}$ | $X = \dfrac{1/Y - \hat{A}}{\hat{B}}$ | $c_X = 1$<br>$c_Y = -1/Y^2$ | $c_x = 1$ |
| $Y = \dfrac{X}{A + BX}$ | $x = 1/X$<br>$y = 1/Y$ | $\hat{A} = \hat{b}$<br>$\hat{B} = \hat{a}$ | $X = \dfrac{\hat{A}Y}{1 - \hat{B}Y}$ | $c_X = -1/X^2$<br>$c_Y = -1/Y^2$ | $c_x = -1/x^2$ |

The estimates $\hat{a}$, $\hat{b}$ of the parameters of the linearized dependence are subsequently found using the LSM [2]. When evaluating the uncertainty of the calibration dependence (1), one should take into account the uncertainty of the values of the output signal $u_Y$ of the MT. The values are evaluated both by type A (due to random errors of the MT) and by type B (due to instrumental measurement errors during calibration, as well as the uncertainty in determining the values (evaluated by type B) of $u_X$ calibration points). It should be considered that since the values of $Y$ and $X$ are directly measured with the help of the MI, the instrumental uncertainties $u_Y$ and $u_X$ must be recalculated into instrumental uncertainties $u_y$ and $u_y$ when identifying the linearized dependence (2) just as:

$$u_x = \frac{\partial \Phi(X)}{\partial X} u_X = c_X u_X; \tag{5}$$

$$u_y = \frac{\partial \Psi(Y)}{\partial Y} u_Y = c_Y u_Y. \tag{6}$$

The expressions for the sensitivity coefficients $c_X$, and $c_Y$ for different initial dependencies (1) are given in the fifth column of Table 1.

After identifying the linear dependence, it is necessary to perform its inverse transformation into the original one, according to which it will be necessary to calculate the uncertainty of finding the value $X$ for any value $Y$. The values of the coefficients $\hat{A}$ and $\hat{B}$ recalculated from the obtained coefficients are given in Table 1. Expressions for sensitivity coefficients $c_x = \frac{\partial X}{\partial x}$, linking uncertainties $u_X$ and $u_x$ for different initial dependencies (1), are given in the fifth column of Table 1. The expressions for sensitivity coefficients, linking uncertainties,

$$u_X = c_x u_x \tag{7}$$

are given in the last column of Table 1.

## 3. Algorithm for Identifying the Required Dependence Using a Linear Dependence of a General Form

The general linear dependence has the form [2]:

$$y = a_0 + b(x - \overline{x}). \tag{8}$$

Using dependence (8) instead of (2) eliminates the correlation between estimates $\hat{a}_0$ and $\hat{b}$ [2]. The algorithm for estimating the measurement uncertainty for the dependence will consist of the following points.

1. According to the experimental points $\overline{Y}_j = \frac{1}{n}\sum_{i=1}^{n} Y_{ji}$, the dependence

$$\overline{Y}_j = f(X_j), \tag{9}$$

is plotted, which is approximated by one of the functions $Y = f(X, A, B)$ of the first column of Table 1.

2. The initial dependence (9) is linearized using the expressions $x = \Phi(X)$ and $y = \Psi(Y)$ from the second column of Table 1.

3. The estimates of the linearized dependence (2) coefficients $a$ and $b$ are calculated using the expressions [2]:

$$\hat{b} = \sum_{j=1}^{N} \overline{y}_j (x_j - \overline{x}) \Big/ \sum_{j=1}^{N} (x_j - \overline{x}). \tag{10}$$

$$\hat{a} = \frac{1}{N}\sum_{j=1}^{N} \overline{y}_j - \hat{b}\sum_{j=1}^{N} x_j = \frac{1}{Nn}\sum_{j=1}^{N}\sum_{i=1}^{n} y_{ji} - \hat{b}\sum_{j=1}^{N} x_j ; \tag{11}$$

where

$$\overline{x} = \frac{1}{N}\sum_{j=1}^{N} x_j ; \tag{12}$$

$$\overline{y}_j = \frac{1}{n}\sum_{i=1}^{n} y_{ij} . \tag{13}$$

4. According to the obtained values $\hat{a}$ and $\hat{b}$, the values of the coefficients $\hat{A}$ and $\hat{B}$ are calculated, using the formulas from the third column of Table 1, obtaining a model of the original dependence $Y = f(X, \hat{A}, \hat{B})$.

## 4. Measurement Uncertainty Evaluation Using the Identified Dependence

1. For a given value $Y$, the value $X$ is calculated according to the corresponding formula $X = f^{-1}(Y, \hat{A}, \hat{B})$ from the fourth column of Table 1.

2. The uncertainty of finding the value $x$ is calculated by formulas [2]:

$$u_{LSM}(x) = \sqrt{\left[\frac{1}{N} + (x - \overline{x})^2 \Big/ \sum_{j=1}^{N} (x_j - \overline{x})^2\right] \cdot \left[u^2(\overline{y}) + b^2 u_B^2(x)\right]}, \tag{14}$$

if $x_j$, $j = 1,...,N$ are not correlated ($\mathrm{cov}(x_j, x_k) = 0$ for any $j,k = 1,...,N$ if $j \neq k$).

If the values $x_j$, $j = 1,...,N$ are correlated (aggravated by the same constant error), the standard uncertainty $u_{LSM}(x)$ is calculated just as:

$$u_{LSM}(x) = \sqrt{\left[\frac{1}{N} + (x - \overline{x})^2 \Big/ \sum_{j=1}^{N} (x_j - \overline{x})^2\right] \cdot u^2(\overline{y}) + b^2 u_B^2(x)}\ . \tag{15}$$

In this case, the values $u(\overline{y})$ are found by the formula:

$$u(\overline{y}) = \sqrt{u_A^2(\overline{y}) + u_B^2(\overline{y})}, \tag{16}$$

where

$$u_B(\overline{y}) = c_Y u_B(Y); \tag{17}$$

$$u_B(x) = c_X u_B(X); \tag{18}$$

$$u_A(\overline{y}) = \sqrt{\frac{1}{(Nn-2)n} \sum_{j=1}^{N} \sum_{i=1}^{n} (y_{ji} - \hat{a} - \hat{b} x_j)^2}, \tag{19}$$

Moreover, the sensitivity coefficients $c_X$ and $c_Y$ are calculated by the formulas from the fifth column of Table 1.

3. Uncertainty $u_{LSM}(x)$ is recalculated into uncertainty $u_{LSM}(X)$ according to formula (7), using the values of the sensitivity coefficients $c_x$ from the last column of the Table 1.

## References

[1] Granovsky V.A., Siraya T.N. Methods for experimental data processing at measurements, L. “Energoatomizdat”. 1990, 288 p.

[2] RMG 115-2019 State system for ensuring the uniformity of measurements. Calibration of measuring instruments. Algorithms for processing measurement results and evaluating uncertainty.

# Components of the Uncertainty of Thermography Temperature Measurements with the Use of a Macro Lens

[1]Krzysztof Dziarski, [2]Arkadiusz Hulewicz

[1] Institute of Electric Power Engineering, Poznan University of Technology, Piotrowo 3A, 60-965 Poznan, Poland,

[2] Institute of Electrical Engineering and Industry Electronics, Poznan University of Technology, Piotrowo 3A, 60-965 Poznan, Poland

Email: Krzysztof.Dziarski@put.poznan.pl

***Abstract.*** *This article presents an uncertainty budget for a thermography temperature measurement with the use of a macro lens. It explains the influence of different factors on the uncertainty value of a thermography temperature measurement with the use of a macro lens. It shows the way of determining the uncertainty contributions of a thermography temperature measurement with the use of a macro. It presents the designed uncertainty budget and discusses factors related to the largest contributions in the designed budget.*

*Keywords: Uncertainty Budget, Thermography, Metrology*

## 1. Introduction

To perform a thermography temperature measurement that will be encumbered with the smallest possible error, one should take into account the conditions prevailing during the measurement. The intensity of phenomena that influences the indication of a thermal camera depends on conditions prevailing during the measurement. The intensity of these phenomena is reflected by values of the following factors: relative humidity $\omega_{\%}$, ambient temperature $\vartheta_a$, atmospheric transmittance $\tau_a$, the distance between the lens and the observed object $d$, emissivity factor $\varepsilon$ of the observed surface and the reflected temperature $\vartheta_{refl}$. All these factors are the components of the uncertainty of a thermography temperature measurement. The contribution of individual factors varies depending on the intensity of the phenomena that influence the indication of a thermal camera. When it is necessary to observe small areas (in the order of square millimetres), there's a need to use an additional macro lens. Using such a lens makes it important to precisely select $d$ = 33 mm [1]. When determining the uncertainty of a thermography temperature measurement performed with an additional lens, in addition to the aforementioned factors, one should take into account two other factors: the temperature of additional lens $\vartheta_l$ and the transmittance of additional lens $\tau_l$. Knowledge of the value of the contribution of components in the uncertainty of a thermography temperature measurement provides knowledge about the effect of individual factors on the result of a thermography temperature measurement $\vartheta_{cam}$ and to which factor's compensation one should pay special attention. For this reason, tests were conducted to determine the contribution rates related to the occurrence of individual factors in the uncertainty budget of the uncertainty of a thermography temperature measurement performed with an additional lens.

## 2. Determination Method of Uncertainty

The measurement uncertainty of a thermography temperature measurement is a non-negative parameter related to the value of temperature being measured. It characterizes the scattering of values that can reasonably be assigned to the temperature measurand. The measurement uncertainty may be determined using the B-type method. This method consists of scientific analysis of the effect of individual factors on the measurement result. The work began with distinguishing factors that influence the indication of a thermal camera. For this purpose, the equation describing the total $W_{tot}$ radiation received by the thermal camera was used [2]. When taking into account the Stefan-Boltzmann law and using an additional lens and making transformations, this equation takes the form (1), which allows for the calculation of the temperature of the observed surface.

$$\vartheta_{obj} = \sqrt[4]{\frac{W_{tot} - (1-\varepsilon)\cdot\tau_a\cdot\sigma\cdot\vartheta_{refl}^4\cdot\tau_l - (1-\tau_a)\cdot\sigma\cdot\vartheta_a^4\cdot\tau_l - (1-\tau_l)\cdot\sigma\cdot\vartheta_l^4}{\varepsilon\cdot\tau_a\cdot\sigma\cdot\tau_l}} \tag{1a}$$

$$\tau_a(d,\omega) = K_a\cdot\exp[-\sqrt{d}\cdot(\alpha_1+\beta_1\sqrt{\omega})] + (1-K_a)\cdot\exp[-\sqrt{d}\cdot(\alpha_2+\beta_2\sqrt{\omega})] \tag{1b}$$

$$\omega(\omega_{\%},\vartheta_a) = \omega_{\%}\cdot\exp(h_1 + h_2\cdot\vartheta_a + h_3\cdot\vartheta_a^2 + h_4\cdot\vartheta_a^3) \tag{1c}$$

where: σ - Boltzmann constant (= 5.67 cm · $10^{-8}$ W/m$^2$·K$^4$), $W_{tot}$ [W/m$^2$] - total radiation received by a thermal camera, $\vartheta_{obj}$ [K] - temperature of the observed surface, $\omega$ [-] - factor indicating the amount of water vapour in the atmosphere, $\omega_{\%}$ [%]- relative humidity, $K_{atm}$ = 1.9 [-] - atmosphere damping factor, $\alpha_1$ (=0,0066) and $\alpha_2$ (= -0,0126) - damping factors for an atmosphere without water vapour, $\beta_1$ (= - 0,0023) and $\beta_2$ (= - 0,0067) - damping factors for water vapour, $h_1$=1.5587, $h_2$ = 6.939· $10^{-2}$, $h_3$=-2.7816· $10^{-4}$, $h_4$ = 6.8455· $10^{-7}$ [2,3].

To determine the contributions of individual factors in the standard uncertainty of a thermography temperature measurement with additional lens u($\vartheta_{obj}$), the scope of values of components listed on the right of equations 1a-1c was determined. The limits of scopes of $\tau_a$ ( - ) and $W_{tot}$ (in W/m$^2$) were determined based on simulation works, during which the equations 1a - 1c were used. The scope of $\omega_{\%}$ values was assumed at 40% - 60%, while for $\vartheta_a$ the scope was assumed at 18 °C - 35 °C. These scopes included the values of $\omega_{\%}$ and $\vartheta_a$ during laboratory measurements. The $\vartheta_{refl}$ values were by observing the reflecting surface with a thermal camera with disabled $\varepsilon$ ( - ) and $d$ (in mm) compensation. As the $\tau_l$ ( - ) scope, the selected was the widest material transmittance scope, which is used for manufacturing thermal camera lenses within the LWIR (Long Wave Infrared) scope. The scopes of other factors included in equations 1a-1c were determined on the basis of experimental work during which a resistance temperature sensor with a known temperature value was being observed. The equal probability of occurrence of values in the determined scopes made it possible to assign a rectangular probability distribution to all quantities. Standard uncertainties of quantities on the left of equations 1a-1c were determined by using the B-type uncertainty evaluation method. In this way, a three-tier uncertainty budget was done. Assigning the values on the right of equations 1a-1c a rectangular probability distribution made it possible to set an estimate of value related to a given factor using equation 2 [4]

$$x_i = \frac{1}{2}(a_+ + a_-) \tag{2}$$

Where $a_+$ - upper scope limit, $a_-$ - lower scope limit, $x_i$ - obtained estimate. The standard uncertainty u($x_i$) was determined as the root of the variance. The uncertainty was obtained using equation 3 [4]

$$u(x_i) = \sqrt{\frac{1}{12}(a_+ - a_-)^2} \tag{3}$$

To determine the contribution in uncertainty u$_i$($y$), value u($x_i$) was multiplied by the sensitivity factor $c$. The value of $c$ represents the value of the first derivative of equations 1a-1c in relation to the variable representing the factor in question. The standard uncertainty of the factor on the left of equation u($y$) was determined as the root of the sum of squares of values of individual contributions.

## 3. Uncertainty Budget

As a result of the conducted laboratory and experimental work, the scopes of the variability of factors influencing the indication of a thermal camera in the case of measurement with the use of a macro lens were determined. Based on the performed simulation work, it was found that the limits of the $W_{tot}$ scope are 0.1669 W/m - 0.1439 W/m. Based on the experimental work, it was found that the limits of $\vartheta_{refl}$ scopes are: 25 °C - 35 °C, $\tau_l$: 0,9-1, $\varepsilon$: 0.95 – 0.98 and the scope $d$ varying from 20 mm - 50 mm. In addition, it was assumed that $\vartheta_a = \vartheta_l$. In the beginning, based on equation 1c, the uncertainty budget for $\omega$ was determined. The budget is presented in Table 1.

Table 1 Uncertainty budget ω.

| Symbol $X_i$ | Estimate of quantity $x_i$ | Standard uncertainty $u(x_i)$ | Probability distribution | Sensitivity factor $c_i$ | Uncertainty contribution $u_i(y)$ |
|---|---|---|---|---|---|
| $\vartheta_a$ | 26.5 | 4.90 | rectangular | 0.62 | 3.04 |
| $\omega_{\%}$ | 44.5 | 17.32 | rectangular | 0.25 | 4.33 |
| $\omega$ | 13.93 | | | | 5.29 |

Similarly, based on equation 1b, the uncertainty budget for $\tau_a$ was determined. The budget is presented in Table 2. Estimates of $\omega$ and $\tau_a$ were determined using equation 2. As the $\omega$ and $\tau_a$ variability scope, the highest and lowest possible values were assumed, depending on quantities of variables on the right of equations 1b and 1c. By virtue of the Central Limit Theorem, both quantities are assigned a normal probability distribution.

Table 2 Uncertainty budget $\tau_a$, superior to the budget for ω.

| Symbol $X_i$ | Estimate of quantity $x_i$ | Standard uncertainty $u(x_i)$ | Probability distribution | Sensitivity factor $c_i$ | Uncertainty contribution $u_i(y)$ |
|---|---|---|---|---|---|
| ω | 13.93 | 5.29 | normal | $-3.78 \cdot 10^{-5}$ | -0.003 |
| d | 0.033 | 0.0057 | rectangular | -0.0204 | -0.0007 |
| $\tau_a$ | 0.9987 | | | | 0.0010 |

The final uncertainty budget done for the quantity $\vartheta_{obj}$ is presented in Table 3.

Table 3 Primary uncertainty budget for the quantity $\vartheta_{obj}$.

| Symbol $X_i$ | Estimate of quantity $x_i$ | Standard uncertainty $u(x_i)$ | Probability distribution | Sensitivity factor $c_i$ | Uncertainty contribution $u_i(y)$ |
|---|---|---|---|---|---|
| $\tau_a$ | 0.9987 | 0.0010 | normal | 0.4488 | 0.0004 |
| $W_{tot}$ | 0.1554 | 0.0066 | rectangular | 67.7701 | 0.4472 |
| ε | 0.9700 | 0.0086 | rectangular | -7.6450 | -0.0657 |

| | | | | | |
|---|---|---|---|---|---|
| $\vartheta_{refl}$ | 30 | 2.8868 | rectangular | 0.0119 | 0.0344 |
| $\tau_l$ | 0.9500 | 0.0289 | rectangular | -10.3189 | 0.2982 |
| $\vartheta_a$ | 26.500 | 4.9000 | rectangular | -0.0151 | -0.0740 |
| $\vartheta_l$ | 26.500 | 4.9000 | rectangular | -0.0151 | -0.0740 |
| $\vartheta_{obj}$ | 41.357 | 0.0010 | | | 0.5525 |

The expanded uncertainty value U($y$) was obtained by multiplying the value of u($y$) =0.55 °C by the coverage factor $k$ = 2. The value of expanded uncertainty U($\vartheta_{obj}$) was 1.11 °C for $\vartheta_{obj}$ = 41.36 °C.

## 4. Conclusions

When analysing the contribution of uncertainty components of a thermography temperature measurement with the use of an additional macro lens (tables 1-3), it can be noticed that the humidity has little effect on the temperature measurement error. The temperature and transmittance of additional lens largely influence the uncertainty of temperature measurement. It is worth noting that it is often impossible to freely influence the value of these quantities. Other factors that largely influence the value of thermography measurement error with the use of a macro lens include the correct selection of the emissivity factor and the reflected temperature. For this reason, before performing the thermography temperature measurement with the use of a macro lens, special attention should be paid to the correct selection of the emissivity factor and the compensation of the reflected radiation. It is worth noting that the skill of analyzing the uncertainty components may also be helpful in planning measurements of other quantities [5].

## References


[1] Dziarski, K., Hulewicz, A., Dombek, G,. Frąckowiak, R., Wiczyński, G. (2020) Unsharpness of Thermograms in Thermography Diagnostics of Electronic Elements. *Electronics*. 9(6).897

[2] Tran, Q.H., Han, D., Kang, C., Haldar, A., Huh, J. (2017). Effects of Ambient Temperature and Relative Humidity on Subsurface Defect Detection in Concrete Structures by Active Thermal Imaging. *Sensors*, 17 (8), 1718-1736.

[3] Waldemar, M., Klecha, D. (2015). Modeling of Atmospheric Transmission Coefficient in Infrared for Thermography Measurements. In *Proceedings of the Sensor 2015 and IRS2 2015 AMA Conferences,* Nürnberg, Germany.

[4] https://www.pca.gov.pl/publikacje/dokumenty/ea-/ [acess: 28.02.2021, 15:07]

[5] Kuwałek, P., Otomański, P., Wandachowicz, K. (2020). Influence of the Phenomenon of Spectrum Leakage on the Evaluation Process of Metrological Properties of Power Quality Analyser. *Energies*, 13 (20), 5338-5335.

# Influence of Voltage Variation on the Measurement of Total Harmonic Distortion (THD) by AMI Smart Electricity Meters

**Piotr Kuwałek**

Institute of Electrical Engineering and Electronics, Poznan University of Technology, Poznan, Poland
Email: piotr.l.kuwalek@doctorate.put.poznan.pl

***Abstract.*** *Power quality parameters specified in standards IEC 61000–4–30 and EN 50160 are used to power quality evaluation in the power grid. These parameters are, among others higher harmonics and the Total Harmonic Distortion (THD). Measurement and recording of power quality parameters is carried out mainly by power quality analyzers. However, nowadays these measurements are also carried out by AMI smart electricity meters with the functionality of measuring power quality parameters. The paper presents exemplary results of THD measurement by AMI smart electricity meters and a selected class A power quality analyzer in the case of voltage variation occurrence. Metrological interpretation of the obtained results and formulations of conclusions have been presented in the paper.*

*Keywords: Harmonics, Total Harmonic Distortion (THD), Power Quality, Voltage Variation, AMI Smart Electricity Meters*

## 1. Introduction

The development of electronics causes that there are more power loads that force to flow distorted (non–sinusoidal) current in the power grid. Supplying this type of load from the power grid causes power quality parameters reduction caused by voltage distortion (e.g. related to the higher harmonics occurrence).

Measurement of power quality parameters is carried out with the use of power quality analyzers. Three measurement classes (A, B and S) of these measuring and recording devices are defined in the standard IEC 61000–4–30. In the case of complaints related to the power quality, in accordance with the recommendations of the standard IEC 61000–4–30, it is necessary to use class A power quality analyzers. According to the recommendations of the same standard, class A analyzers should allow measurement of all power quality parameters with the specified accuracy to provide the obtained measurement results repeatability. There are also AMI smart electricity meters, which are equipped with functionalities for measuring power quality parameters (including rms value of voltage, coefficient of zero and negative sequence content, higher harmonics, Total Harmonic Distortion (THD) of voltage, short-term and long-term flicker indicator). There are only a few models of available AMI meters, which have the presented functionalities for measuring power quality parameters. Manufacturers of such meters include: EMH Metering, ADD Grup, EDMI, Iskraemeco, Itron Polska, Elgama–Elektronika, Landis+Gyr. Currently, such meters are installed mainly in electrical substation, but in some countries (e.g., Poland) legal documents are being prepared that will oblige power distributors to the installation of meters equipped with the functionality of measuring power quality parameters at every households. Hence, it is important to assess the errors in measuring power quality parameters by these meters. The paper focuses on the measurement of THD by AMI meters in the case of voltage variation occurrence, which is typical disturbances in the real power grid [1, 2]. The research was carried out for six AMI meters from two from the above-mentioned producers.

## 2. Basics of THD Measurement

The standard EN 50160 specifies the acceptable, determined relatively, limit values of individual harmonics of the supply voltage $u_h$ and THD, defined by the eq. [3]:

$$\mathrm{THD} = \sqrt{\sum_{h=2}^{40} (u_h)^2}, \tag{1}$$

where $u_h$ is the relative value of the voltage in percentage of the fundamental harmonic, and $h$ is the order of the higher harmonic.

On the other hand, power quality analyzers measure THD in accordance with the standard IEC 61000–4–30, which refers to the standard IEC 61000–4–7 for $u_h$ and THD measurements. The standard IEC 61000–4–7 specifies the method of measuring $u_h$ by using Discrete Fourier Transform (DFT) for a signal with a duration of $N \cdot T_c$, where $T_c$ is the fundamental period of the measured signal and $N$ is the number of fundamental periods in the measurement window ($N$=10 for $T_c$=1/50 s and $N$=12 for $T_c$=1/60 s). The resulting DFT components have a resolution $\Delta f = 1/(N \cdot T_w)$. The standard IEC 61000–4–7 defines the subgrouping method to reduce the effects of "spectrum leakage", when a loss of synchronization occurs [4, 5], to determine the values of $u_h$ and THD. THD determined using the subgrouping method is described by the eq. [3]:

$$\mathrm{THD} = \sqrt{\sum_{h=2}^{40} \left( \frac{\sum_{i=-1}^{1} \left(U_{C,N \cdot h+i}\right)^2}{\sum_{i=-1}^{1} \left(U_{C,N \cdot 1+i}\right)^2} \right)^2}, \tag{2}$$

where $U_{C,k}$ is the rms value of the $k$–th DFT components with frequency $f_k$ that is total multiple of the frequency resolution $f_k = k \cdot \Delta f$.

Considering the limited computing performance of AMI meters, manufacturers declare that THD is determined in accordance with the eq.:

$$\mathrm{THD} = \sqrt{\frac{U^2 - {U_1}^2}{{U_1}^2}}, \tag{3}$$

where $U$ is the rms value of the measured signal and $U_1$ is the rms value of the fundamental harmonic. The result of eq. (3) is the same as the result of eq. (1) and eq. (2) if only harmonic signal distortion occurs. In case of compliance with eq. (2), the condition of maintaining synchronization by the measuring and recording device should be additionally considered.

## 3. Research Results

In experimental studies, the voltage variation was modeled as amplitude modulation (AM) without suppressed carrier [6]. The adopted model is correct for the real stiff power grid, because in this case the frequency deviation is negligible. The test signal in experimental studies is described by the eq.:

$$u(t) = \overbrace{\sqrt{2}U \sin\left(2\pi f_c t\right)}^{\text{carrier signal}} \cdot \left[ 1 + \overbrace{\frac{1}{2}\frac{\Delta U}{U}\frac{1}{100} \mathrm{sign}\left[\sin\left(2\pi f_m t\right)\right]}^{\text{modulating signal}} \right], \tag{4}$$

where: $U$=230 V, $f_c$=50 Hz, $f_m$ is modulation frequency, $(\Delta U/U)$ is modulation depth. In eq. (4), a rectangular signal was adopted as the modulating signal, because nowadays voltage variation in the power grid have this shape resulting from cyclic switching on and off of loads [7, 8]. The studies were carried out in the stand with the block diagram shown in Figure 1.

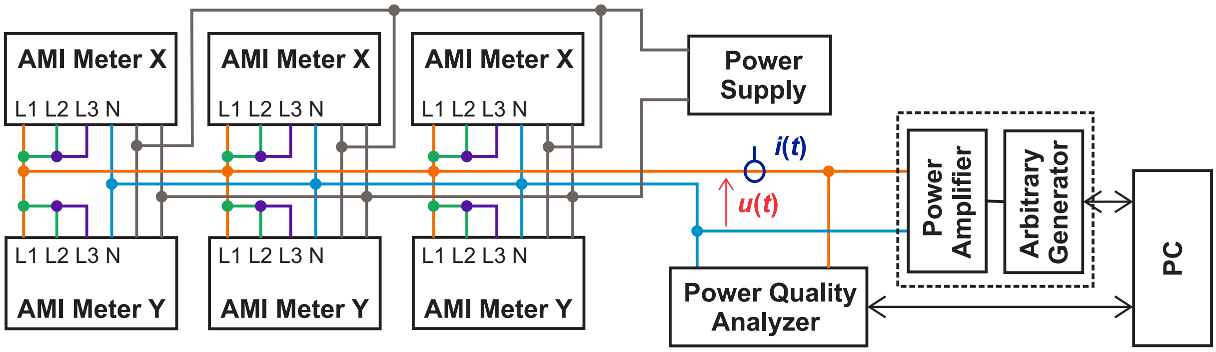


Fig. 1: The block diagram of the laboratory stand

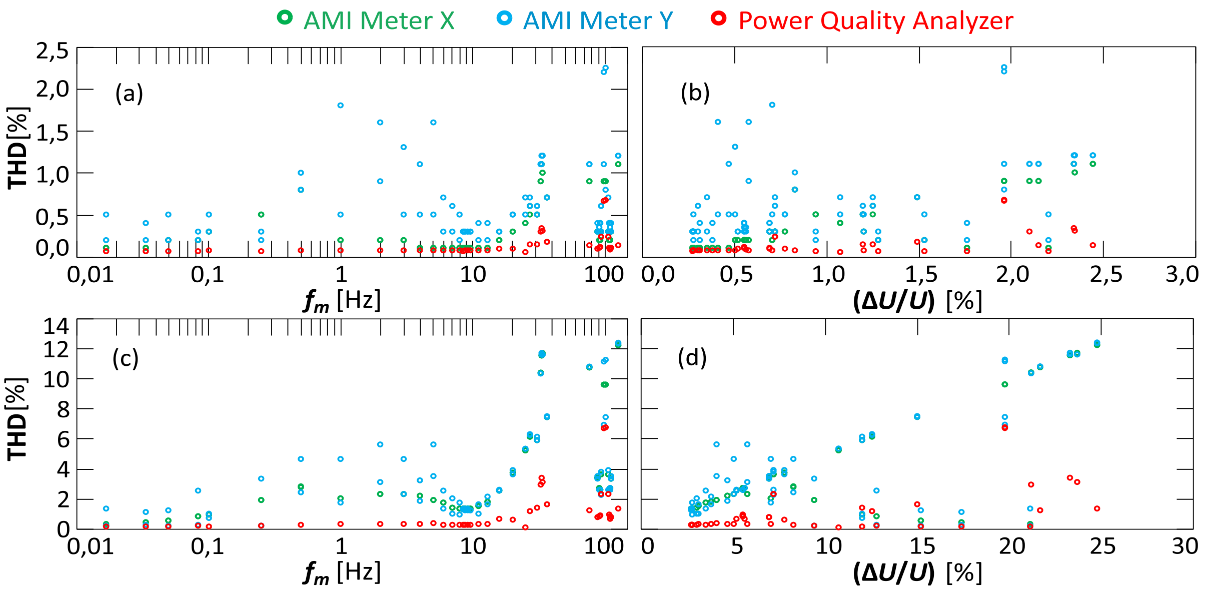


Fig. 2: The characteristic: (a) THD=**f**$(f_m, P_{st} = 1 = \text{const})$, (b) THD=**f**$((\Delta U/U), P_{st} = 1 = \text{const})$, (c) THD=**f**$(f_m, P_{st} = 10 = \text{const})$, (d) THD=**f**$((\Delta U/U), P_{st} = 10 = \text{const})$

The paper presents the results of THD measurement by six AMI meters from two different manufacturers and by a class A power quality analyzer PQ BOX 100 (reference measurement) for different modulating frequency in two cases. The modulation depth was selected in such a way as to keep a constant value of the short–term flicker $P_{st} = 1$ (the limit value of obnoxious voltage variation in the low voltage network) in the first case and $P_{st} = 10$ in the second case (significant voltage variation). The measurement process was consisted of a set of 20 min intervals. During this time, the THD and $P_{st}$ values were registered, considering the aggregation for an interval of 10 min (necessary requirement for power quality evaluation process), in accordance with the recommendations of the standard IEC 61000–4–30. Hence, the set of 20 min intervals allowed the recording of two THD and $P_{st}$ values per phase by AMI meters and the power quality analyzer. The THD and $P_{st}$ values for the first 10 min intervals in the set of 20 min intervals were rejected from the analysis. In this way, the time necessary for the disappearance of the transient component in the flickermeter signal chain after setting a new voltage (signal test) was obtained and the synchronization of the laboratory stand with the used meters was ensured [9]. Figure 2 shows the obtained research results. Only the minimum and maximum THD values for individual tested AMI meters were marked on the characteristics for particular modulating frequencies and modulation depth.

## 4. Discussion and Conclusion

The research results shows that THD values measured by AMI smart electricity meters is always greater than THD values measured by a class A power quality analyzer in the case of voltage variation occurrence. If the severity of voltage variation increases, then the differences in THD measurements by tested AMI meters increase. This situation results from the fact that in the case of voltage variation occurrence, subharmonics and interharmonics are almost always occurred [10], the value of which increases with the increasing severity of voltage variation. These components are not included in the measurement of THD by power quality analyzers (see eq. (1) and eq. (2)), unless they are components with the frequency $h \cdot f_c$ (see eq. (1) and eq. (2)) or the frequency $h \cdot f_c \pm \Delta f$ (see eq. (2)). Apart from the presented exceptions, the measurement of THD by AMI meters suggests the occurrence of harmonic voltage distortion, although in reality only voltage variation occurs. Currently, research on the accuracy of THD measurement by AMI meters is continued, in which it is planned to consider the impact of ambient temperature on the THD measurement, by placing the tested meters in a thermal chamber and monitoring the real temperature of the AMI meters with a thermal imaging camera [11].

## References

[1] Wiczynski G. (2020). Determining location of voltage fluctuation source in radial power grid. *Electric Power Systems Research*, 180, art. no. 106069.

[2] Otomanski P., Wiczynski G. (2011). The usage of voltage and current fluctuation for localization ofdisturbing loads supplied from power grid. *Przeglad Elektrotechniczny*, 87(1), 107–111.

[3] Otomanski P., Wiczynski G. (2015). The application of programmable AC source to generation of higher harmonics in examination of power quality. *Przeglad Elektrotechniczny*, 91(8), 38–41.

[4] Kuwalek P., Otomanski P., Wandachowicz K. (2020). Influence of the Phenomenon of Spectrum Leakage on the Evaluation Process of Metrological Properties of Power Quality Analyser. *Energies*, 13(20), art. no. 5338.

[5] Kuwalek P., Otomanski P. (2019). The Effect of the Phenomenon of "Spectrum Leakage" on the Measurement of Power Quality Parameters. In *12th International Conference on Measurement*. IEEE, 70–73.

[6] Wiczynski G. (2017). Estimation of $P_{st}$ indicator values on the basis of voltage fluctuation indices. *IEEE Transactions on Instrumentation and Measurement*, 66(8), 2046–2055.

[7] Kuwalek P. (2021). Estimation of Parameters Associated With Individual Sources of Voltage Fluctuations. *IEEE Transactions on Power Delivery*, 36(1), 351–361.

[8] Kuwalek P., Jesko W. (2020). Recreation of Voltage Fluctuation Using Basic Parameters Measured in the Power Grid. *Journal of Electrical Engineering & Technology*, 15(2), 601–609.

[9] Majchrzak J., Wiczynski G. (2012). Basic Characteristics of IEC Flickermeter Processing. *Modelling and Simulation in Engineering*, 2012, art. no. 362849.

[10] Wiczynski G. (2010). Analysis of flickermeter's signal chain for input signal with two sub/interharmonics. *Przeglad Elektrotechniczny*, 86(4), 328–335.

[11] Dziarski K., et al. (2020). Unsharpness of Thermograms in Thermography Diagnostics of Electronic Elements. *Electronics*, 9(6), art. no. 897.

# Impact of Washing on Shielding Effectiveness of Stainless-Steel Textile Fabric

**[1]Marta Jarak, [2]Krešimir Malarić, [1]Bosiljka Šaravanja, [3]Tanja Pušić**

[1]Department of Clothing Technology, University of Zagreb
Faculty of Textile Technology, Zagreb 10000, Croatia
[2]Department of Communications and Space Technologies, University of Zagreb
Faculty of Electrical Engineering and Computing, Zagreb 10000, Croatia
[3]Department of Textile Chemistry and Ecology, University of Zagreb
Faculty of Textile Technology, Zagreb 10000, Croatia
Email: kresimir.malaric@fer.hr

***Abstract.*** *This paper describes the measurements and stability of the shielding protective properties of stainless-steel textile fabric which can be used for making working clothing. Measurements were done using sources of electromagnetic radiation on frequencies that are being widely used in everyday life. The textile material containing stainless steel was washed, and the changes in shielding effectiveness were measured. The results show the influence of the washing on the protective properties of the fabric in relation to unprocessed fabric.*

*Keywords: Shielding Effectiveness, Measurements, Washing, Stainless-Steel Textile*

## 1. Introduction

The electromagnetic field cannot be smelled or felt by human senses. There is electromagnetic smog around people, i.e., fields of different frequencies whose radiation builds up. Every electric device radiates electromagnetic energy. If this radiated energy exceeds the safety level, it can affect the operation of other electrical devices by degrading or disabling the operation of other devices. Also, the radiated energy can be harmful to the heath of living organisms located in the vicinity of such devices. Today, mobile phones are the biggest potential source of radiation for most people. A small proportion of people are exposed to stronger radiation that can be harmful to human health. The electromagnetic field can be measured with electric or magnetic sensors. These are professional devices designed to protect people. The electromagnetic shield works by two main electromagnetic mechanisms, and these are a reflection from the leading surface and absorption in the volume of the fabric. Part of the electromagnetic radiation is reflected, while the rest is transmitted and attenuated as it passes through the material (Fig 1) [1,2].

The ratio of the level of the electric field at a certain distance from the source without protection and the level of the electric field with protection is defined as shielding effectiveness (SE) and is expressed in dB. The shielding effectiveness of SE is described as the sum of reflection losses, absorption loss and secondary reflection loss and is calculated according to equation [3]:

$$\mathrm{SE} = R + A + R_r , \tag{1}$$

where

$R$ reflection losses,

$A$ absorption loss,

$R_r$ secondary reflection loss.

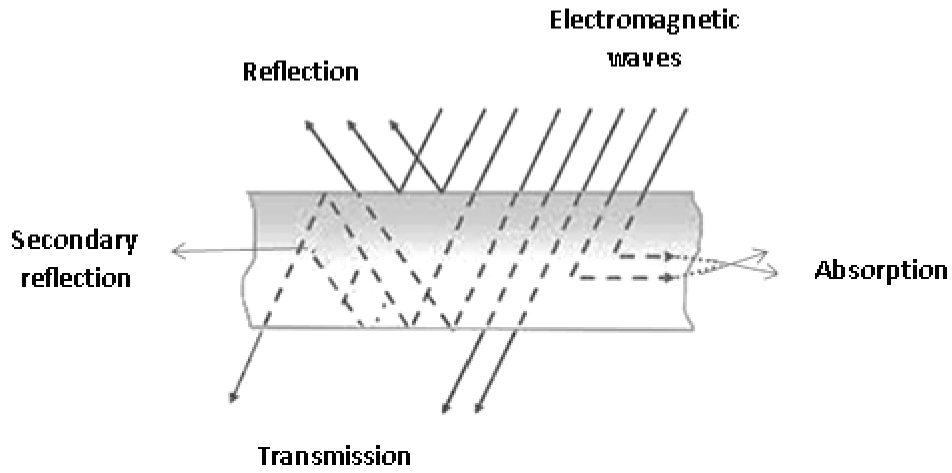


Fig. 1. Schematic presentation of the signal propagation through a material with protective properties.

Sometimes protection against electromagnetic radiation is needed at high as well as low frequencies. Conductive materials, fabric, and knits with metal fibers and metal wire are used to protect against electromagnetic radiation to reduce EM radiation transmission that affects people and devices. Today there are many electrically conductive materials for protection against low-frequency and high-frequency electric fields, fabric can contain copper, nickel, silver, or stainless-steel threads [2].

It is important to emphasize that protective and work clothing with its certain properties protects the body from possible injuries, combining active and passive safety attitudes. Any working clothing used must prove that it has been properly tested and meets the relevant regulations and standards. All protective clothing for permanent use should be cleaned regularly in accordance with the instructions and recommendations of the manufacturer [4].

## 2. Subject and Methods

The goal of this measurement was to make a comparison of the untreated sample of the fabric and the sample that was treated with a special powder detergent Texcare after 1st, 3td, 5th and 7th wash. The material that is tested and used as protection against EM radiation by raw material composition is a mixture of cotton and stainless-steel threads that are entangled in the warp and weft. The protective properties of EM radiation were monitored by examining the properties of the shield at frequencies of 0.9 GHz, 1.8 GHz, 2.1 GHz and 2.4 GHz. The shield efficiency of the tested samples was measured under the following operating conditions:

temperature 23 ± 1◦C,

relative humidity 50 ± 10%.

The measuring setup (Fig. 2) was done according to the recommendations of IEE-STD 299 97, MIL STD 285 and ASTM D-4935-89, and consist of [3]:

a measuring instrument: NARDA SRM 3000,

an HP 8350 B signal generator,

an IEV horn antenna (Telecommunication Industry), Ljubljana, Type A12,

a wooden frame, in which a sample of PA/Ag material of 1 m × 1 m was placed.

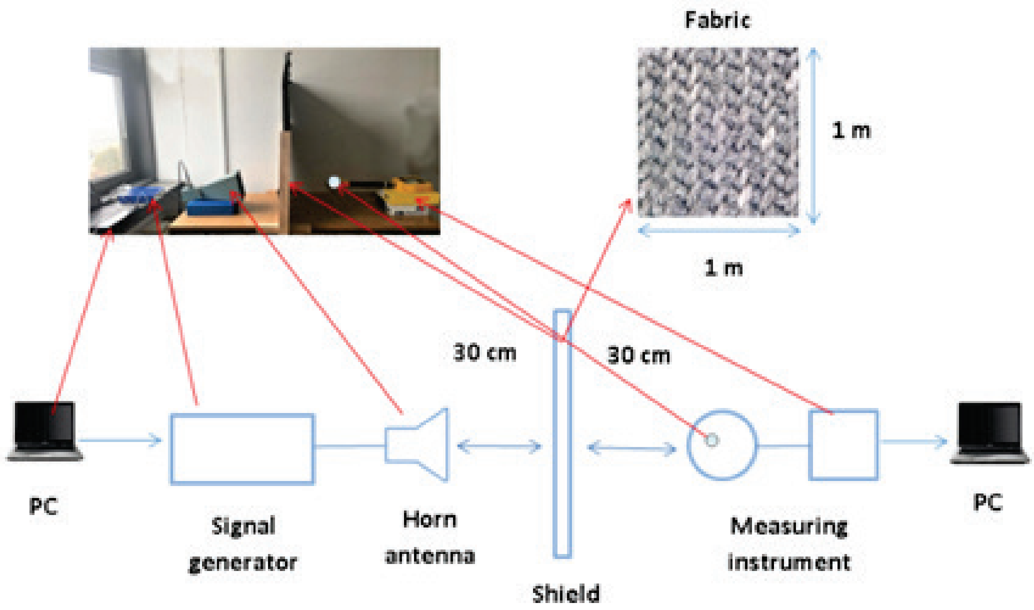


Fig. 2. Shield effectiveness measurement setup.

For washing, we used functional detergent Texcare (Fig. 3) used for washing materials with electromagnetic radiation shielding properties, Y-shield GmbH.


Fig. 3. Texcare powdered detergent Y-shield.

Washing is done in a PolyColor Mathis. We poured the required amount of soft water into the drum in which we wash the material at the same time as the required amount of detergent and finally added the fabric. The processing conditions are as follows [5]: temperature 30° C, time of washing 20 minutes, 10 rpm, 2 minutes turn in one, then in the other direction.

After each wash, the material is rinsed three times with soft water, then centrifuged, and finally air-dried. The measurement results were recorded in tabular form; after each measurement, the protective efficiency calculated according to the above formula.

## 3. Results

In order to obtain a complete overview of the influence of different electromagnetic radiation intensities, measurements were performed at frequencies of 0.9 GHz, 1.8 GHz, 2.1 GHz and 2.4 GHz towards face and reverse of protective material. Before starting each measurement, we measured the strength of electromagnetic radiation without a protective material (shield) later to obtain the exact protective effectiveness of the test material. Table 1 shows the results of the protective performance of the face and reverse of the untreated sample and washed samples.

Table 1. The difference between the protective effectiveness of the untreated sample and the washed sample.

| Frequency (GHz) | | 0.9 | 1.8 | 2.1 | 2.4 |
|---|---|---|---|---|---|
| Untreated Fabric | SE (db) Face | 7.20 | 14.33 | 15.58 | 17.60 |
| | SE (dB) Reverse | 7.05 | 13.95 | 15.14 | 17.36 |
| After 1st wash | SE (dB) Face | 5.52 | 12.47 | 10.04 | 12.15 |
| | SE (dB) Reverse | 5.27 | 12.27 | 9.80 | 11.92 |
| After 3rd wash | SE (dB) Face | 3.52 | 12.06 | 7.58 | 10.92 |
| | SE (dB) Reverse | 3.08 | 11.69 | 7.42 | 9.74 |
| After 5th wash | SE (dB) Face | 2.77 | 11.54 | 7,10 | 9,74 |
| | SE (dB) Reverse | 2.57 | 11.06 | 6,88 | 9,46 |
| After 7th wash | SE (dB) Face | 1.91 | 10.47 | 6,07 | 7,85 |
| | SE (dB) Reverse | 1.58 | 10.26 | 5,82 | 7,58 |

The protective properties of the face and reverse of all samples at all frequencies are almost identical, and there is no significant difference. The table shows a decrease in protection efficiency after certain wash cycles. The highest degree of protection was obtained at 2.4 GHz (SE = 17.60) in the untreated sample. In comparison, the lowest degree of protection was obtained at 0.9 GHz (SE = 1.58) in the sample after the 7th cycle of washing with the powder detergent. If we consider the ratio of untreated and repeatedly washed sample, it can be concluded that the results are expected and that the decrease in protective efficiency is acceptable. It is important to mention that any subsequent processing of the sample can significantly affect the change in the structure of fabric as well as its basic properties, so it is important to treat the material according to correct instructions to avoid an unwanted premature decline in the shielding effectiveness.

## 4. Conclusions

Cotton fabric with stainless steel threads woven in the warp and weft direction has an optimally good electromagnetic protection efficiency in the frequency range from 0.9 GHz to 2.4 GHz. The initial efficiency properties of the electromagnetic shield were declining along with the increased number of washing cycles with Texcare powder detergent. Since the material tested on both sides, the results are almost identical and show almost equal EM protection of the face and reverse.

## Acknowledgements

This work has been fully supported by Croatian Science Foundation under the project (IP-2018-01-7028).

## References

[1] Malarić, K. Šimunić, Zentner, R. (2016). Ekonomija i ekologija radiokomunikacijskih sustava, Merkur A.B.D., Zagreb.

[2] Dharmendra, N. P., Arindam B., Pramod K. (2018) Study of Electro Conductive Textiles: A Review, *International Journal of Scientific Research Engineering & Technology* (*IJSRET*), 7 (10), 744-749.

[3] Pušić, T. Šaravanja, B., Malarić, K. (2021) Electromagnetic Shielding Properties of Knitted Fabric Made from Polyamide Threads Coated with Silver, *Materials* , Mar;14 (5), 1281.

[4] Pejnović, N. (2015). Osobna zaštitna oprema za zaštitu tijela, Sigurnost 57 (3) 229-242.

[5] Kayacan, O. (2014). The effect of washing processes on the electromagnetic shielding of knitted fabrics. *Tekst. Ve Konfeksiyon*, 24, 356–362.

# Destructive Activity Analysis of Ferritin Derivatives on Lysozyme Amyloid Fibrils

**[1]Jan Gombos, [2]Lucia Balejcikova, [3]Marianna Batkova, [3]Peter Kopcansky, [4]Oliver Strbak**

[1]Department of Medical Biochemistry, Jessenius Faculty of Medicine, Comenius University, Martin, Slovakia
[2]Institute of Hydrology, Slovak Academy of Sciences, Bratislava, Slovakia
[3]Institute of Experimental Physics, Slovak Academy of Sciences, Kosice, Slovakia
[4]Biomedical Center Martin, Jessenius Faculty of Medicine, Comenius University, Martin, Slovakia
Email: gombos8@uniba.sk

***Abstract.*** *Neurodegenerative diseases, such as Alzheimer's, Parkinson's, or systemic amyloidosis, are still considered as incurable diseases of the human brain. Their formation is associated with the transformation of specific proteins from their native state to a stable, insoluble form, for example, in the form of amyloid plaques. The specific interest for biomedical applications is the search for biocompatible magnetic nanoparticles that would serve as a potential therapeutic agent to eliminate these plaques. Such materials include ferritin derivatives such as magnetoferritin and reconstructed ferritin. By interacting with lysozyme amyloid fibrils, these complex biomacromolecules can form a suitable therapeutic approach to address their reduction and explain the accumulation of iron during the development of neurodegenerative diseases.*

*Keywords: Ferritin, Magnetoferritin, Reconstructed Ferritin, Lysozyme Amyloid Fibrils*

## 1. Introduction

A lot of human diseases, which are characterized by the formation of insoluble extracellular deposits of proteins, have been recognized for almost two hundred years [1]. Diseases in which normally soluble proteins accumulate in the extracellular space of various tissues as insoluble aggregates have been defined as amyloidoses. These deposits are defined as fibrils, with approximately 10 nm in diameter [2]. Neurodegenerative disorders such as Alzheimer's disease are characterized by the formation of amyloid aggregates in tissues. It is known that secreted circulating proteins can, under abnormal circumstances, be converted in part to highly stable extracellular fibrils. These include, for example, amylin in the diabetic pancreas, immunoglobulins in primary systemic amyloidosis, or small soluble proteins of unknown function such as amyloid β-peptide (Aβ) in Alzheimer's disease [1]. The mechanism of normal and soluble proteins turning into fibrillar and insoluble aggregates still remains a mystery [3]. Regardless of the sequence or native fold, the commonly formed amyloid fibrils are defined as self-assembled, elongated, and unbranched (fibrillar) polypeptide aggregates with a cross-β conformation [4]. Of particular interest to biomedical applications is the search for biocompatible magnetic nanoparticles that would serve as potential therapeutic agents for the elimination of amyloid plaques [5]. Such a material could be magnetoferritin (MF), a derivative of the iron-ferritin storage protein, with an outer diameter of about 12 nm, which surrounds the synthetically prepared magnetic nanoparticles [5]. Magnetoferritin was used in our work as a model system to study its interaction with lysozyme amyloid fibrils (LAF). Modification of physicochemical conditions allows the formation of reconstructed ferritin (RF), prepared for the simulation of the pathological accumulation of iron in ferritin structures [5].

The present paper describes the interaction between ferritin derivatives: magnetoferritin and reconstructed ferritin and lysozyme amyloid fibrils. The destructive activity was confirmed using atomic force microscopy, and the fluorescence intensity decrease. Using zeta potential and UV-VIS measurements, we observed $Fe^{3+}$-core reduction during MF/RF interaction with LAF.

## 2. Subject and Methods

*Samples Preparation*
LAF were prepared by the standard process reported in [5]. MF and RF were prepared and characterized by procedures described previously [5].

*Atomic Force Microscopy*
Atomic force microscopy (AFM) was realized by the method noticed in [5].

*Transmission Electron Microscopy*
A low-voltage LVEM 5 transmission electron microscope (TEM) was used to study the size and morphology of the studied samples. Its energy was only 5 keV, which increased the scattering of electrons and thus increased the contrast of the tested sample. The method uses an electron beam to create the image. A small amount of sample (5 µl) was carefully applied to a 2 nm thick carbon nanolayer and the sample was allowed to dry for about 1 hour. The grid had a diameter of 3,05 mm and the resolution ability was 2,5 nm. The magnification of the image was from 1,500 to 150,000 times.

*Determination of the amount of Lysozyme Amyloid Fibrils*
The amount of lysozyme amyloid fibrils before and after the interaction with magnetoferritin and reconstructed ferritin was examined by a fluorescence assay using the fluorescent dye thioflavin T (10 $\mu mol.dm^{-3}$). A sample of magnetoferritin and reconstructed ferritin was added to the prepared lysozyme amyloid fibrils in a weight ratio of 2:1, 1:1, 1:2, 1:5 and 1:10, and after incubating these mixtures at 37 °C for 24 hours, fluorescence measurements were performed by adding fluorescent dye. The presence of lysozyme amyloid fibrils was determined as the change in fluorescence intensity measured by a spectrofluorimeter (Shimadzu, RF-5000). Measurements were performed using 1 cm thick semi-micro-cuvettes. The excitation was set at 440 nm and the emission captured at 485 nm. For excitation and emission, the slits were adjusted to 1,5 and 3,0 nm.

## 3. Results

*Preparation of Reaction Mixtures*
The clear colorless lysozyme solution was turned into a white milk mixture after two hours of synthesis during the *in vitro* conditions for the preparation of lysozyme amyloid fibrils. The samples were used for the study of their interaction with the prepared ferritin derivatives, MF with LF 160 and RF with LF 144 (LF – loading factor, the average number of iron atoms per one protein biomacromolecule).

*Atomic Force Microscopy*
We used AFM as the first method to study the effect of ferritin derivatives on lysozyme amyloid fibrils. Figure 1 A) shows the prepared LAF in the range of up to 1 µm in length. These LAFs were used to interact with ferritin derivatives and were imaged by AFM after incubation of these mixtures. In Figure 1 B), which represents specific mixtures of LAF and magnetoferritin, we did not observe any fibrillar formation. Therefore, we assume that magnetoferritin had a destructive effect on the fibrils in the solution.

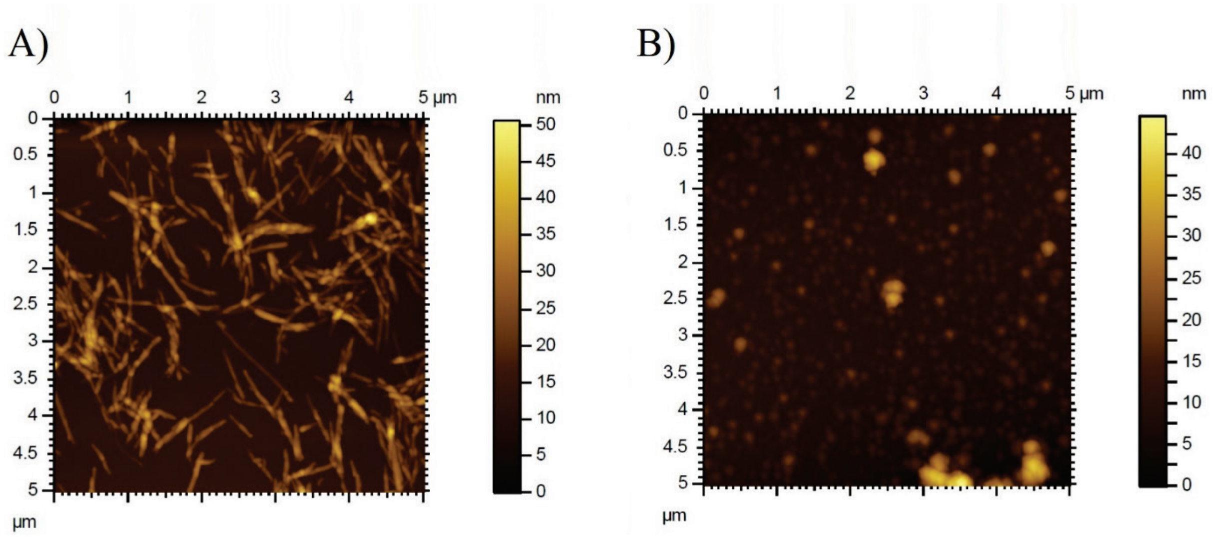


Fig. 1. AFM imaging of the morphology of A) LAF itself and B) mixture of magnetoferritin with LAF.

*Transmission Electron Microscopy*

To confirm the destructive activity of ferritin derivatives on LAF, we used TEM as a support method. Figure 2 A) shows a mixture of lysozyme amyloid fibrils with reconstructed ferritin and figure 2 B) with magnetoferritin. In both cases, we demonstrated the destructive activity of ferritin derivatives on fibrillar structures. Dark spherical shapes probably belong to the inorganic cores of ferritin derivatives and the lighter structures are probably remnants of fibrillar structures.

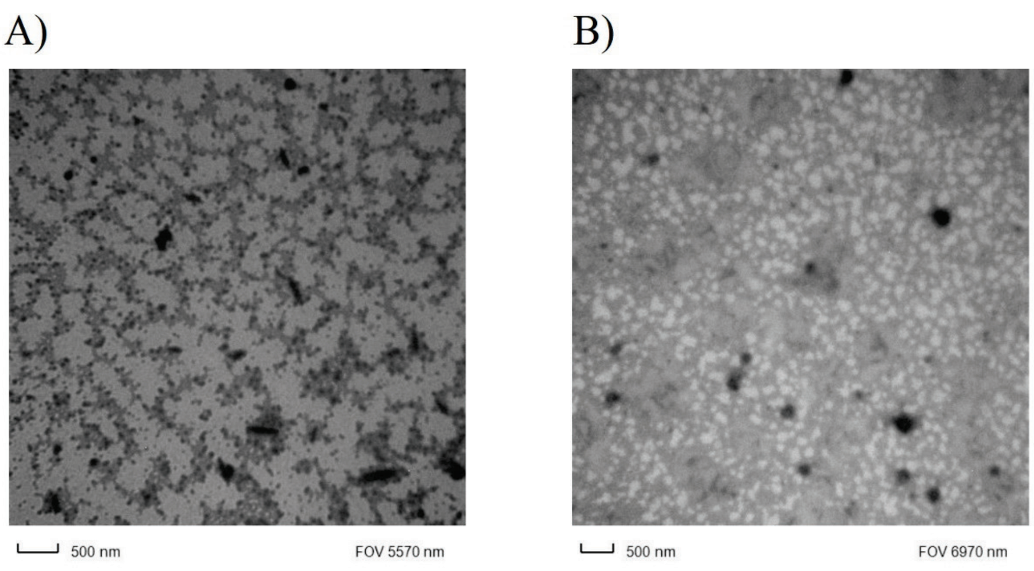


Fig. 2. TEM imaging of samples of LAF in the presence of A) reconstructed ferritin and B) magnetoferritin.

*Determination of the Amount of Lysozyme Amyloid Fibrils*

The effect of ferritin derivatives, magnetoferritin (MF) and reconstructed ferritin (RF) on LAF was also investigated using the thioflavin fluorescence test (ThT test). The measured fluorescence intensity in direct proportion depends on the number of detected fibrils into the structure of which the fluorescent dye, thioflavin T, binds. Table 1 shows the measurement results for different weight ratios LAF: MF (RF).

Table 1 Fluorescence intensities expressed in % for LAF + MF / RF solutions and mixtures

| n. | Solution / Mixture / Loading factor / Weight ratio | Fluorescence (%) | Stand. dev. ± (%) |
|---|---|---|---|
| 1. | LAF in AMPSO with pH = 8,6 | 100 | 7,8 |
| 2. | LAF/MF LF 160 2:1 | 106 | 7,3 |
| 3. | LAF/MF LF 160 1:1 | 79,4 | 5,1 |
| 4. | LAF/MF LF 160 1:2 | 66,0 | 9,9 |
| 5. | LAF/MF LF 160 1:5 | 31,3 | 6,0 |
| 6. | LAF/MF LF 160 1:10 | 88 | 12,1 |
| 7. | LAF in HEPES with pH = 7,4 | 100 | 3,4 |
| 8. | LAF/RF LF 144 2:1 | 104,8 | 6,5 |
| 9. | LAF/RF LF 144 1:1 | 93,3 | 8,6 |
| 10. | LAF/RF LF 144 1:2 | 92,4 | 9,7 |
| 11. | LAF/RF LF 144 1:5 | 60,6 | 2,1 |
| 12. | LAF/RF LF 144 1:10 | 53,0 | 3,2 |

Fluorescence intensities for pure buffers, MF and RF were negligible and the fluorescence for pure LAF always represented 100% signal intensity. In the presence of RF and MF, a significant decrease in fluorescence intensity was observed with increasing volume. Only in the case of LAF / MF LF 160 1:10 was an unexpectedly high (88%) signal measured, which may be related to the higher density of MF and thus the possible formation of MF aggregates, which could affect the fluorescence.

## 4. Discussion and Conclusions

Our results, based on changes in morphology and fluorescence intensity, confirmed the destructive activity of ferritin derivatives (MF and RF) on LAF. Due to the very good biocompatibility of ferritin derivatives, they can be used in various biomedical applications, including a model system for pathological ferritin, for possible targeted therapy, or MRI diagnostics. Moreover, based on our results, the derivates could potentially slow down the course of Alzheimer's disease, which is manifested by the formation of amyloid plaques in the brain. However, this requires further and more detailed in-vitro and in-vivo studies.

## References

[1] Selkoe, D. (2003). Folding proteins in fatal ways. *Nature* 426, 900-904.

[2] Sunde, M., & Blake, C. (1998). From the globular to the fibrous state: Protein structure and structural conversion in amyloid formation. *Quarterly Reviews of Biophysics* 31(1), 1-39.

[3] Skaat H, Belfort G, Margel S. (2009). Synthesis and characterization of fluorinated magnetic core-shell nanoparticles for inhibition of insulin amyloid fibril formation. *Nanotechnology* 20(22): 225106.

[4] Nelson, R. & Eisenberg, D. (2006). Recent atomic models of amyloid fibril structure. *Curr. Opin. Struct. Biol.* 16, 260-265.

[5] Balejčíková L., Petrenko V. I., Baťková M., Šipošová K., Garamus V. M., Bulavin L. A., Avdeev M. V., Almasy L., Kopčanský P. (2019). Disruption of amyloid aggregates by artificial ferritins. *Journal of Magnetism and Magnetic Materials*, 473, 215-220.

# *Measurement in Biomedicine II*

# Design of Instrumented Glove for Hand Motion Evaluation

**Maros Smondrk, Andrea Jandurova, Branko Babusiak, and Stefan Borik**

Department of Electromagnetic and Biomedical Engineering
Faculty of Electrical Engineering and Information Technology, University of Zilina
Zilina, Slovakia
Email: maros.smondrk@feit.uniza.sk

***Abstract.*** *Measurement of fingers and hand kinematics during the grasping activities and manipulation with various objects play an essential role in ergonomics, sport science, occupational medicine, and rehabilitation, as it is an indicator of hand function. That is why the design and realization of a device for finger flexion and extension and forearm motion became the main objective of this article. The work deals with designing and implementing the system prototype, its calibration, and testing under laboratory conditions. The designed device is promising to be used in occupational medicine and rehabilitation applications such as the device to assess the hand function impairment and track patient hand function disability recovery progress.*

*Keywords: Instrumented Glove Body, Force Sensitive Resistor, Inertial Measurement Unit*

## 1. Introduction

Human motion tracking technologies are of great interest to a wide range of research fields, such as medicine, sports science, the automotive industry, virtual reality, and video games. Several studies have been carried out in these fields, and various methods have been implemented, such as video-based motion capture systems, joint angular measurements, and inertial measurement systems, to obtain a three-dimensional positioning and motion tracking of the entire human body or its particular segments [1, 2]. Especially, the motion tracking of human hands and fingers is nowadays a key feature of several industrial and biomedical applications. In industrial applications, the finger position sensing systems could act as human–machine interfaces controlled by both the precise real-time hand and finger motion tracking or less accurate hand gestures recognition [3]. Additionally, hand and finger movement data is valuable for workplace health protection or work comfort improvement and could help optimize industrial production where repetitive hand operations are required for manufacturing. Another application of the measurement of hand kinematics represents hand rehabilitation to assess and restore the hand function impairment. By assessing the two main characteristics, the kinematics of the hand and fingers and the fingertips' force, physicians can keep track of patient hand function disability recovery progress [4]. Patients who suffer the hand function impairment usually undergo a long-term regular hand rehabilitation program. It consists of hand and/or fingers motion capabilities evaluation (range of motion, ability to perform functional tasks) and several functional tasks such as grasping daily life objects, etc. Range of motion has historically been a manual examination in which a traditional goniometer is used to assess a particular joint's flexion and extension. However, using the goniometer during the performance of functional tasks, it is not possible to evaluate the hand's functional capacity.

Several studies have proposed various technical solutions for the capture of hand kinematics over the last decade. Video-based systems use optical markers to track a user's hand, while the user does not have to wear any devices [5]. However, video-based systems suffer from time-consuming calibration, line-of-sight shielding, high costs, and low portability [6]. Nowadays, sensor-based systems are primarily used for tracking a patient's hand motion. The sensors usually embedded in the instrumented gloves include bend sensors [7, 8], optical encoders [9], optical fiber sensors [10, 11], and inertial measurement units [1, 2]. The sensors are usually applied near the interphalangeal joints while the data acquisition unit is placed on the subject's wrist. The instrumented gloves, therefore, feature greater portability and lower costs compared to the video-based systems. Because of the low price and ease of use, the bending sensors are widely used even though the bending sensor's transfer function is not linear and they lack high sensitivity at a slight angle change [12]. A common inertial measurement unit comprises an accelerometer and gyroscope, providing linear acceleration and angular velocity data. However, estimating hand kinematics using inertial sensors is challenging due primarily to the noisy accelerometer readings and integrating gyroscopes readings' errors [13].

This paper proposes a simple, low-cost, wireless, and portable instrumented glove prototype that allows us to measure flexion and extension of 5 proximal interphalangeal finger joints and forearm motion. The prototype's design utilizes flexible bend sensors embedded into a glove and inertial measurement unit situated at the forearm within the data acquisition unit. The data acquisition unit features a wireless module that ensures that the data are transmitted to a remote unit (a PC), where it is possible to record and display data in real-time. The key design specifications of the instrumented glove prototype are low-cost and portability. Subsequently, a series of experiments to evaluate data acquisition reliability were conducted in a laboratory environment.

## 2. System Design

A block diagram of the developed system prototype is depicted in Fig. 1. The system is composed of an instrumented glove and a data acquisition unit. The instrumented glove encompasses five flexible bend sensors in total. Bend sensors are placed at the region of proximal interphalangeal finger joints, the activation of which is dominant for both pinching and gripping activities. Bend sensors outputs are connected to a data acquisition unit through front-end electronics. The data acquisition unit's principal part represents the microcontroller, which performs management of the sensor measurement, interfacing, conditioning, and digitization of the analogue signal and its wireless transmission to a remote device. Additionally, the data acquisition unit consists of a 9-axis inertial measurement unit. The remote device in the form of a PC equipped with a wireless receiver ensures the recording and displaying of measured data in real-time. The design and implementation of each prototype's component, such as the bend sensors, inertial measurement unit, and data acquisition unit, are discussed separately in the following subsections.

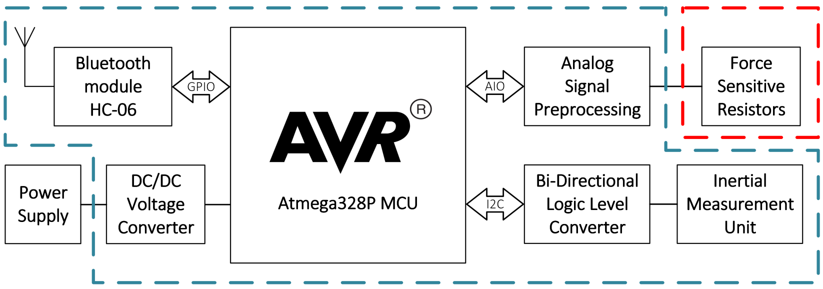


Fig. 1: Block diagram of the proposed system. The red dashed-line box represents the instrumented glove, and the blue dashed-line box represents the data acquisition unit.

### *Bend Sensors and Analog Signal Preprocessing*

The proposed instrumented glove contains five unidirectional flexible bend sensors (Flexpoint Sensor Systems, USA). The bend sensor consists of a single thin layer flexible piece of material coated with a proprietary carbon/polymer base. Due to the resistive carbon material, which changes electrical conductivity as it is bent, the bend sensor acts as a potentiometer. The rate of electrical conductivity change is dependent on two factors, the bend radius, and angular deflection. In general, a smaller bend radius leads to a more remarkable electrical conductivity change. Additionally, the more the sensor is bent around for a given radius, the more significant the electrical conductivity change [14]. Due to the lack of precise resistance vs. sensor angular deflection characteristic, sensor calibration is needed. To measure finger motion, we placed sensors at a region of proximal interphalangeal finger joints. So we consider a maximum angular deflection of 110° in the calibration measurement. To ensure accuracy and repeatability as much as possible, we constructed the sensor calibration equipment using the 3D printer (Fig. 2A). Calibration equipment embeds the conventional goniometer, considered a gold standard for angular deflection measurement. The sensor resistance was measured by Agilent 34401A digital multimeter (Agilent Technologies, USA) while all five sensors were sequentially bent from 0 to 110°.

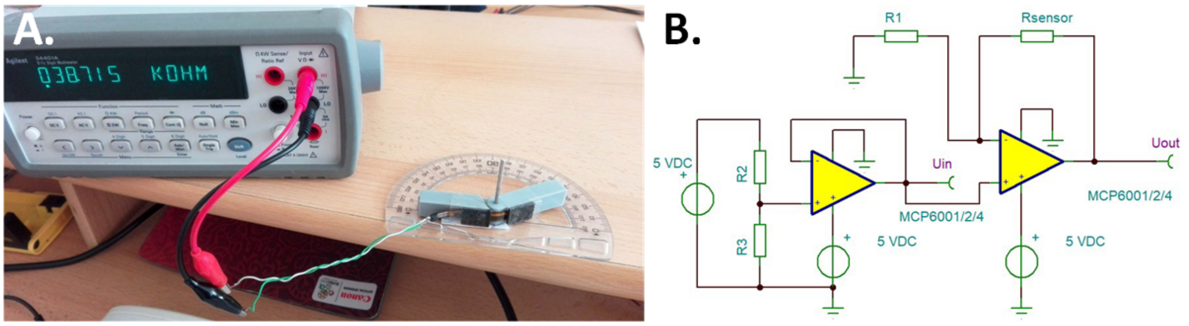


Fig. 2: A - The developed sensor calibration equipment utilizing the goniometer considered as a gold standard. B - The circuit diagram of the resistance to voltage converter.

In order to convert the sensor's electrical conductivity change to electrical voltage, we designed an electrical circuit whose key element represents a non-inverting operational amplifier MCP6002 (Microchip Technology, USA). The circuit diagram is depicted in Fig. 2B. At the first stage, the electrical circuit created by the resistor voltage divider ($R_2$, $R_3$) and voltage follower (first operational amplifier) convert the input voltage (5 VDC from the power supply) to the desired reference voltage. The output of the voltage follower is connected to a non-inverting input of the second operational amplifier. This amplifier senses the bend sensor ($R_{sensor}$) connected in the amplifier feedback loop, whose resistivity changes as it is bent. Modifying the input resistor's value ($R_1$) makes it possible to adjust circuit sensitivity regarding the sensor's resistivity changes. The following equation describes the output of Fig. 2B:

$$U_{out} = U_{in} \cdot \left(1 + \frac{R_{sensor}}{R_1}\right) \tag{1}$$

This processing principle is applied to each sensor separately.

*Inertial Measurement Unit*

The proposed system contains a 9-axis inertial measurement unit LSM9DSO (ST Microelectronics, Switzerland). The sensor features a 3-axis accelerometer, 3-axis gyroscope, and 3-axis magnetometer embedded in one package. It allows measuring linear acceleration, angular velocity, and magnetic field. The inertial measurement unit is placed on the data acquisition unit attached to the subject's forearm, thus accurately measuring a relative position and rotation of the subject's forearm.

*Data Acquisition Unit and Software Design*

The data acquisition unit represents the key element of the entire developed system prototype and is mounted on the subject's forearm. A 5 VDC battery power bank with 2600 mAh capacity provides power to the system. A popular and easy-to-use microcontroller with an inexpensive price, a microcontroller unit (MCU) ATmega328P (Microchip Technology, USA) was used. MCU controls the peripheral and sensory components and collects the raw data from utilizing digital communication interfaces such as the two-wire interface (I2C), universal asynchronous receiver-transmitter interface (UART), and analogue inputs of a built-in 10-bit analogue-to-digital converter (ADC). The bend sensors embedded inside the instrumented glove are connected to the MCU's ADC through the previously mentioned analogue signal preprocessing block. MCU encapsulates the bend sensor data and the IMU readings into the data packets. The packets are sent to the Bluetooth module via UART at a frequency of 50 Hz. The data packet stream is conditioned by the successful receiving of char 'S' from the remote unit (a PC with a Bluetooth module). The flowchart of developed MCU firmware is depicted in Fig. 3A. The firmware starts right after the battery is inserted. The designed prototype of the instrumented glove and data acquisition unit is depicted in Fig. 3B.

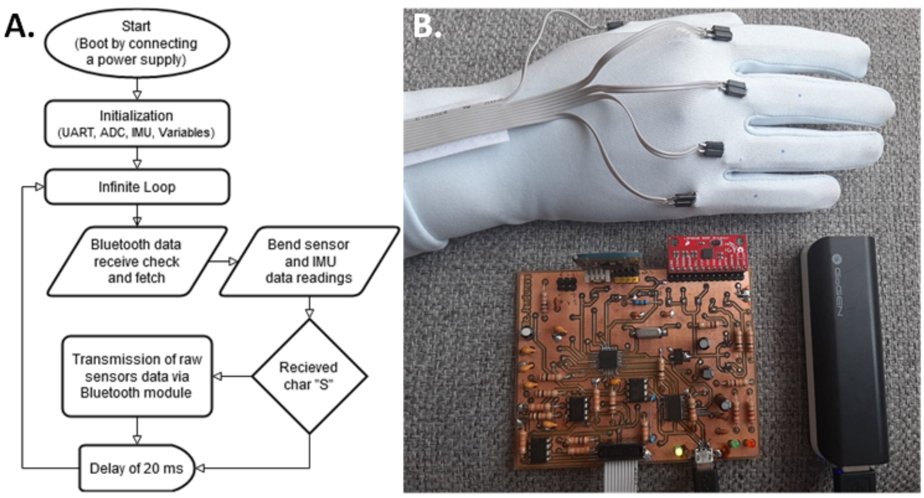


Fig. 3: A - The flowchart of the developed MCU firmware. B - The printed circuit board of the system prototype and instrumented glove with embedded sensors.

## 3. Results and Discussion

A measurement of the bend sensors' electric resistance was performed using the developed calibration equipment utilizing the goniometer. The resistance readings were recorded as the sensor was bent in the range from 0 to 110° with a step of 5°. The results for five tested bend sensors can be seen in Fig. 4. The results reveal the non-linear functional dependence of the sensor resistance while bent. The estimated regression equation allows us to convert a particular sensor's resistance into angular deflection. Subsequently, the designed analogue circuit of the resistance to voltage converter utilizing the non-inverting operational amplifier could be used to convert measured and digitized output voltage by ADC into the angular deflection. In our design, we used a 1 VDC reference voltage created by the voltage divider formed by resistors $R_2$ (400 kΩ) and $R_3$ (100 kΩ). The input resistor's value ($R_1$) was chosen according to the calibration measurement, which has revealed that the sensor resistance, while not bent, is equal to approximately 30 kΩ. In that case, the output voltage of the resistance to voltage converter would be 2 VDC. Considering the sensor resistance while bent at 110°, the output voltage would be 5 VDC.

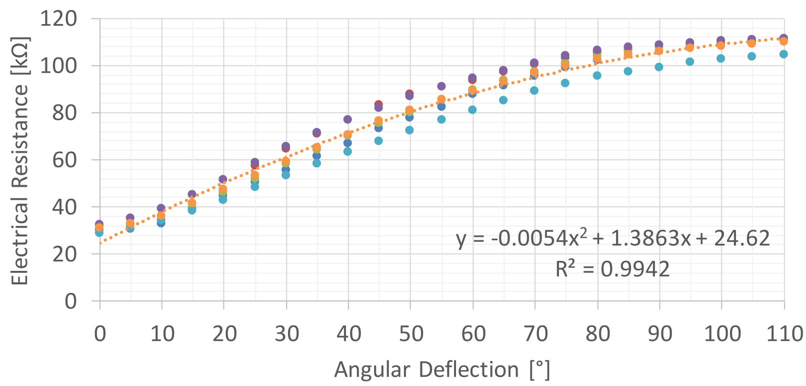


Fig. 4: The characteristic of the five tested bend sensor's resistance as a function of its angular deflection. The polynomial regression trend-line of the 2nd order is depicted as well.

To evaluate data acquisition reliability and wireless transmission, a series of tests were conducted in a laboratory environment. A healthy subject was instrumented in bending each finger at full range three times separately. Besides, a subject was instrumented in making a fist five times separately by flexing the fingers. The results are shown in Fig. 5A and Fig. 5B, respectively. It is evident that the reliability of data acquisition is satisfactory. However, during the ring

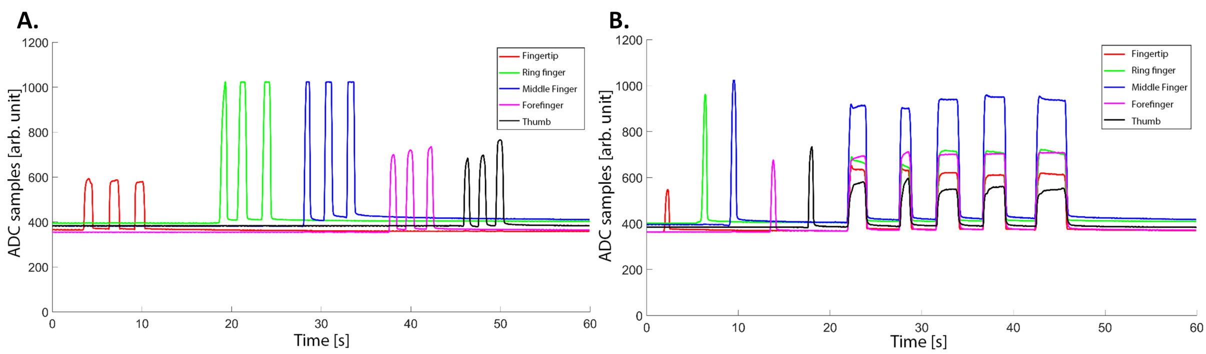


Fig. 5: The measured angular deflection of proximal interphalangeal finger joints; A - while bending each finger three times separately, B - while flexing the fingers in making a fist five times separately.

and middle finger bent is the amplifier's output voltage saturated. This could be overcome with the change in the input resistor's value at the cost of lower sensitivity to the output. The overall cost of the system developed at this stage is approximately 80 USD. In the future design, we would endeavour to minimize the data acquisition unit's geometric constraints, thus increasing system portability and patient comfort during grasping tasks. During the measurements performed on the healthy and injured subjects, it would be possible to study and investigate the particular hand function impairment grasp pattern. Finally, using the specific analysis, we could detect possible variations and give the rehabilitation progress objective measures.

## 4. Conclusion

This work describes the system prototype's design and implementation, capable of measuring the flexion and extension of 5 finger joints and forearm motion. The key element represents the resistive bend sensors embedded into a glove and inertial measurement unit. The system prototype could serve as a sensor device to measure and record the hand and fingers' kinematics in laboratory conditions. It aims to keep track of patient hand function disability recovery progress.

**Acknowledgements**

This work was supported by the Slovak Research and Development Agency under the contracts no. APVV-18-0167 and no. APVV-16-0190.

**References**

[1] Zaldivar-Colado, U., Campos-Leal, J.A., Garbaya, S., Zaldivar-Colado, X.P., Blazevic, P. (2018). Design of a high precision data glove based on inertial sensors. In: *2018 XX Congreso Mexicano de Robótica (COMRob)*.

[2] Chang, H.-T., Chang, J.-Y. (2020). Sensor glove based on novel inertial sensor fusion control algorithm for 3-d real-time hand gestures measurements. *IEEE Transactions on Industrial Electronics*, 67(1), 658–666.

[3] Bellitti, P., Angelis, A.D., Dionigi, M., Sardini, E., Serpelloni, M., Moschitta, A., Carbone, P. (2020). A wearable and wirelessly powered system for multiple finger tracking. *IEEE Transactions on Instrumentation and Measurement*, 69(5), 2542–2551.

[4] Simone, L.K., Sundarrajan, N., Luo, X., Jia, Y., Kamper, D.G. (2007). A low cost instrumented glove for extended monitoring and functional hand assessment. *Journal of Neuroscience Methods*, 160(2), 335–348.

[5] Erol, A., Bebis, G., Nicolescu, M., Boyle, R.D., Twombly, X. (2007). Vision-based hand pose estimation: A review. *Computer Vision and Image Understanding*, 108(1-2), 52–73.

[6] Yun, Y., Agarwal, P., Deshpande, A. D. (2013). Accurate, robust, and real-time estimation of finger pose with a motion capture system. In: *2013 IEEE/RSJ International Conference on Intelligent Robots and Systems*.

[7] Borghetti, M., Sardini, E., Serpelloni, M. (2013). Sensorized glove for measuring hand finger flexion for rehabilitation purposes. *IEEE Transactions on Instrumentation and Measurement* 62(12), 3308–3314.

[8] Ganeson, S., Ambar, R., Jamil, M.M.A. (2016). Design of a low-cost instrumented glove for hand rehabilitation monitoring system. In: *2016 6th IEEE International Conference on Control System, Computing and Engineering (ICCSCE)*.

[9] Jones, C. L., Wang, F., Morrison, R., Sarkar, N., Kamper, D.G. (2014). Design and development of the cable actuated finger exoskeleton for hand rehabilitation following stroke. *IEEE/ASME Transactions on Mechatronics*, 19(1), 131–140.

[10] Nishiyama, M., Watanabe, K. (2009). Wearable sensing glove with embedded hetero-core fiber-optic nerves for unconstrained hand motion capture. *IEEE Transactions on Instrumentation and Measurement*, 58(12), 3995–4000.

[11] Fujiwara, E., Wu, Y.T., Miyatake, D.Y., Santos, M.F.M., Suzuki, C.K. (2013). Evaluation of thumb-operated directional pad functionalities on a glove-based optical fiber sensor. *IEEE Transactions on Instrumentation and Measurement*, 62(8), 2330–2337.

[12] Saggio, G., Riillo, F., Sbernini, L., Quitadamo, L. R. (2015). Resistive flex sensors: A survey. *Smart Materials and Structures*, 25(1), 013001.

[13] Janota, A., Šimák, V., Nemec, D., Hrbček, J. (2015). Improving the precision and speed of euler angles computation from low-cost rotation sensor data. *Sensors*, 15(3), 7016–7039.

[14] Flexpoint Sensor Systems (2015). Bend Sensor Technology: Mechanical Application Design Guide. Technical report.

# Thermoelectric Medical Device for Measuring Heat Flux from Ocular Surface

[1,2] Lukian Anatychuk,[1,3,4]Orest Kochan, [5]NNatalia Pasechnikova, [5]Volodymyr Naumenko, [5]Oleg Zadorozhnyi, [1]Lyudmyla Vikhor, [1,2]Mykola Havryliuk, [1,2]Roman Kobylianskyi, [3,6]Mariana Levkiv

[1]Institute of Thermoelectricity of the NAS and MES of Ukraine, Chernivtsi, Ukraine
[2]Yu. Fedkovych Chernivtsi National University, Chernivtsi, Ukraine
[3]School of Computer Science, Hubei University of Technology, Wuhan, China
[4]Lviv Polytechnic National University, Lviv, Ukraine
[5]State Institution The Filatov Institute of Eye Diseases and Tissue Therapy of the National Academy of Medical Sciences of Ukraine, Odesa, Ukraine
[6]I. Horbachevsky Ternopil National Medical University, Ternopil, Ukraine
Email: romakobylianskyi@ukr.net

***Abstract.*** *The paper presents the design and technical characteristics of the newly developed and patented thermoelectric device for measuring heat flux from the ocular surface. The device is promising for the diagnosis and monitoring of ophthalmic diseases, which allows increasing the effectiveness of early diagnosis of pathology of the eye, to observe the dynamics of the pathological process in the eye structures, as well as to increase the effectiveness of treatment of acute and chronic eye diseases. The developed thermoelectric device allows real-time monitoring of both the temperature and thermal state of the ocular surface.*

*Keywords: Thermoelectric Medical Device, Heat Flux, Ophthalmology*

## 1. Introduction

Estimation of heat exchange processes in the human body is based on the measurement of temperature and heat flux. Both temperature and heat flux are characteristics of the thermal phenomenon [1]. Traditionally temperature measurements, including that in ophthalmology, have well-developed instrumentation and metrology [2]. The temperature in different parts of the eye can be determined by either noninvasive or invasive methods. These methods of thermometry have both pros and cons [3]. Concerning the local measurements of the heat flux from the surface of the human body, appreciable success has been recently achieved in the development of modern means of its measurement [4]. Thermoelectric heat flux sensors (THFS) are promising for the study of local heat dissipation of the human body. They combine high sensitivity, accuracy, speed, stability of parameters in a wide range of operating temperatures and are compatible with modern data acquisition equipment [5-7]. The use of such sensors allows achieving high accuracy of thermometric measurements. However, it should be noted that there is still no thermoelectric device in the world to measure heat flux from the ocular surface.

It is known that a number of ophthalmic acute and chronic diseases are accompanied by changes in intraocular thermal processes. Thus, some studies showed the relationship between the temperature of the outer surface of the eye with the state of blood circulation in the eyes, intraocular pressure, and the presence of inflammation [8]. A change in the thermal characteristics of the eye tissues can occur in the early phase of the disease before the onset of pronounced clinical symptoms. Registration of these changes is a promising area of early diagnosis of various eye pathologies. Diagnosis of the pathological process at an early stage will increase the effectiveness of treatment and reduce the risk of complications.

Therefore, the purpose of this work is to develop a thermoelectric medical device for measuring heat flux from the ocular surface, which allows increasing the effectiveness of early diagnosis of ophthalmic diseases.

## 2. Design and Technical Parameters of Developed Device

The thermoelectric device for measuring heat flux from the ocular surface was developed at the Institute of Thermoelectricity of the NAS and MES of Ukraine within the framework of the agreement on cooperation with State Institution The Filatov Institute of Eye Diseases and Tissue Therapy of the National Academy of Medical Sciences of Ukraine. The device is designed for the diagnosis and monitoring of ophthalmic diseases, which allows increasing the effectiveness of early diagnosis of pathology of the eye, to observe the development of the pathological process in the eye, as well as to increase the effectiveness of treatment of acute and chronic eye diseases. The developed thermoelectric device is patented [9]. The external view of the device and its technical parameters are shown in Fig.1 and Table 1.

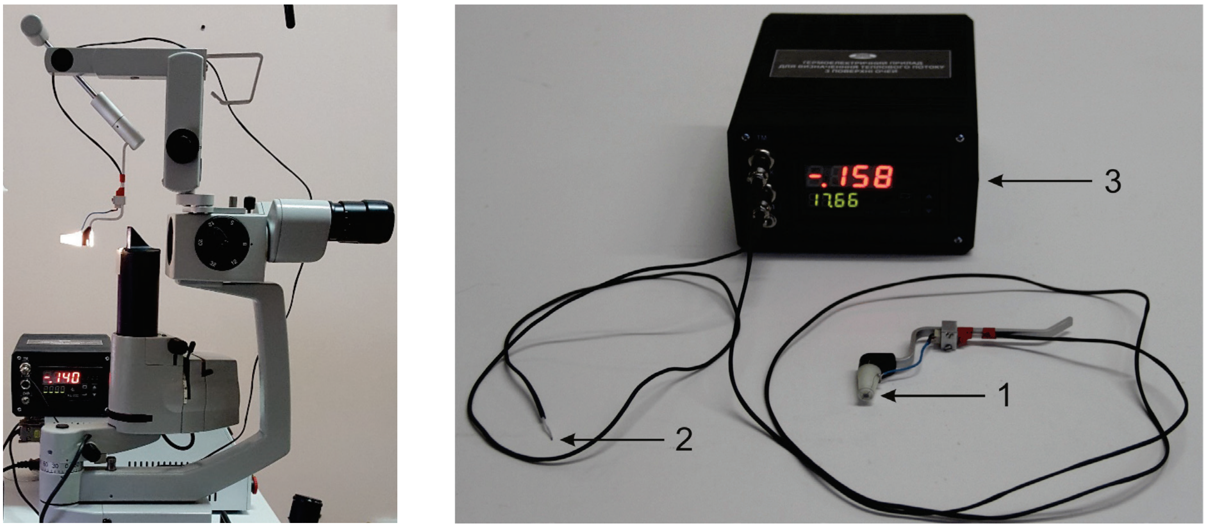


Fig. 1. Left: Thermoelectric medical device for measuring heat flux from the ocular surface. Right: 1 – thermoelectric heat flux sensor, 2 – thermoelectric sensor of temperature (thermocouple), 3 – data acquisition unit.

Table 1. Technical parameters of the device.

| Parameter | |
|---|---|
| Number of measurement channels | 4 |
| Number of thermoelectric heat flux sensors | 1 |
| Number of thermoelectric temperature sensors | 1 |
| Heat flux density measurement range | 0.01÷50 mW/cm$^2$ |
| Heat flux density measurement accuracy | ± 5 % |
| Temperature measurement range | 0÷50 °C |
| Resolution of temperature measurement | ± 0.01 °C |
| Room temperature measurement range | 0÷50 °C |
| Resolution of room temperature measurement | ± 0.01 °C |
| Battery supply voltage | 3.7÷4.5 V |
| Time of device continuous operation from a charged battery | 12 h |
| Overall dimensions of thermoelectric heat flux sensor | Ø3×0.7 mm |
| Overall dimensions of the electronic control unit | 180×140×90 mm |
| Weight | 0.6 kg |

## 3. Manufacture and Calibration of the THFS

For this thermoelectric device, a miniature THFS was developed and manufactured using a special patented technology [9, 10]. The thermoelectric micromodule with the dimensions of (2×2×0.5) mm comprises 100 pcs. of n- and p-type crystals with dimensions (0.17×0.17×0.4) mm of high-performance thermoelectric material based on $Bi_2Te_3$. Such a thermoelectric micromodule is placed between two ceramic plates based on $Al_2O_3$ with a diameter of 3 mm and a thickness of 0.1 mm each, and the side surface is sealed with a special sealant. Thus, the diameter and height of the manufactured THFS are 3 mm and 0.7 mm, respectively. The required diameter of the developed heat flux sensor was determined according to medical requirements. The electrical resistance of such a thermoelectric sensor is $R$ = 14 Ω.

To measure the volt-watt sensitivity of the heat flux sensor of the above-mentioned device, a blackbody-type thermal energy emitter was used as a heat flux source. The schematic of the test bench for measuring the volt-watt sensitivity of the THFS is shown in Fig.2.

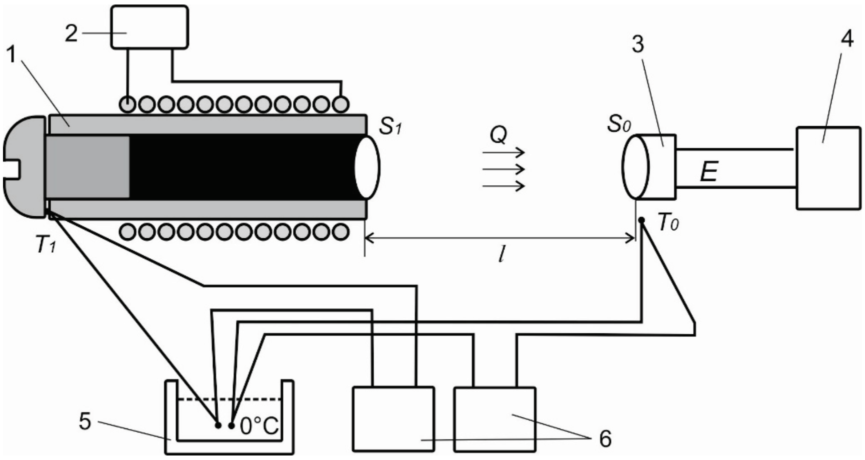


Fig. 2. Schematic of the test bench for measuring volt-watt sensitivity of the thermoelectric heat flux sensor: 1 – blackbody, 2 – power supply unit of blackbody heater, 3 – thermoelectric heat flux sensor, 4 – millivoltmeter, 5 – zero-thermostat of thermocouples, 6 – temperature meters.

The volt-watt sensitivity of the THFS is determined by the following expression:

$$\nu = \frac{E}{Q}, \tag{1}$$

where ν is the volt-watt sensitivity of THFS(V/W), $E$ is the thermoEMF of the THFS (V), $Q$ is the heat flux (W).

The heat flux emitted by the blackbody and absorbed by the receiving pad of the thermoelectric sensor is determined as follows:

$$Q = \frac{\varepsilon_1 \varepsilon_2 \sigma (T_1^4 - T_0^4) s_1 s_2}{\pi l^2}, \tag{2}$$

where $\sigma = 5.67 \cdot 10^{-12}$W/(cm$^2 \cdot$K$^4$) is the Boltzmann constant, $\varepsilon_1$=1 for black body emitter, $\varepsilon_2$=0.82 for receiving pad, i.e. polished ceramics based on $Al_2O_3$, $T_1$ is the temperature of the black body housing, $T_0$ is the temperature of the receiving pad which is close to ambient temperature, $s_1$ is the area of blackbody slot, $s_2$ is the area of receiving pad, $l$ is the distance between the output aperture of the emitting blackbody and receiving pad, which are parallel to each other and their centers are on the same axis.

For this test bench (Fig.2) we have the following values: $s_1$=0.059 cm$^2$, $s_2$=0.07065 cm$^2$, $l$=0.9 cm. The results of measurements are given in Table 2.

Table 2. Results of measuring volt-watt sensitivity of the THFS.

| $T_0$, °C | $T_1$, °C | $E$, mV | $Q$, μW | ν, V/W |
|---|---|---|---|---|
| 18.5 | 50 | 0.096 | 27.9 | 3.43 |
| 18.5 | 58 | 0.124 | 36.44 | 3.40 |

Thus, the THFS was calibrated and the conversion factor $k$ = 4.163 mW/(mV·cm$^2$) of the thermoEMF of the thermoelectric sensor into a physical quantity in units of heat flux density (mW/cm$^2$) was determined.

## 4. Conclusions

For the first time, a thermoelectric medical device was developed and manufactured to measure heat flux from the ocular surface. The developed thermoelectric device allows real-time monitoring of the thermal and temperature state of the surface of the human eye, which is extremely important for the diagnosis of ophthalmic diseases in the early stages.

## References


[1] Grishchenko, T. (2017). Heat flux measurement: theory, metrology, practice. Methods and tools for heat flux measurement. Kyiv [in Russian].

[2] Kochan, R., Kochan, O., Chyrka, M., Jun, S., Bykovyy, P. (2013). Approaches of voltage divider development for metrology verification of ADC. In International Conference on Intelligent Data Acquisition and Advanced Computing Systems. IEEE, Vol. l, 70-75.

[3] Anatychuk, L., Pasechnikova, N., Zadorozhnyi, O., Nazaretyan, R., Mirnenko, V., Kobylianskyi, V., Kobylianskyi, R., Havrylyuk, N. (2015). Original device and approaches to studying temperature distribution in different eye compartments. Journal of Ophthalmology (Ukraine), 6, 50-53 [in Russian].

[4] Anatychuk, L., Ivaschuk O., Kobylianskyi, R., Postevka, I., Bodiaka, V., Gushul, I. (2016). Thermoelectric device for temperature and heat flux density measurement "ALTEC-10008". Thermoelectricity, 1, 76-84.

[5] Thermoelectrics Handbook. Macro to Nano. (2006) D.M. Rowe (Ed.). N.Y.: CRC Press.

[6] Wang, J., Kochan, O., Przystupa, K., Su, J. (2019). Information-measuring system to study the thermocouple with controlled temperature field. Measurement Science Review, 19(4), 161-169.

[7] Jun, S., Kochan, O., Chunzhi, W., Kochan, R. (2015). Theoretical and experimental research of error of method of thermocouple with controlled profile of temperature field. Measurement Science Review, 15(6), 304-312.

[8] Galassi, F., Giambene, B., Corvi, A. (2007). Evaluation of ocular surface temperature and retrobulbar haemodynamics by infrared thermography and colour Doppler imaging in patients with glaucoma. British Journal of Ophthalmology, 91, 878–881.

[9] Patent of Ukraine №136185 (2019). Anatychuk, L., Kobylianskyi, R., Bukharayeva, N., Havrylyuk, M., Tiumentsev, V. Thermoelectric device for the measurement of temperature and heat flux from ocular surface [in Ukrainian].

[10] Anatychuk, L., Pasyechnikova, N., Naumenko, V., Zadorozhnyy, O., Gavrilyuk, M., Kobylianskyi, R. (2019). A thermoelectric device for ophthalmic heat flux density measurements: results of piloting in healthy individuals. J. ophthalmol (Ukraine), 3, 45-51.

# The Acoustic Spectroscopy of Biocompatible Fluid in a Magnetic Field

**Štefan Hardoň, Jozef Kúdelčík, Miroslav Gutten**

Faculty of Electrical Engineering and Information Technology,
University of Žilina, Univerzitná 1, 010 26 Žilina, Slovakia
Email: stefan.hardon@feit.uniza.sk

***Abstract.*** *The utilization of magnetic nanoparticles in the area of medicine is able because of their biocompatibility, non-toxicity, and common use in several medical applications. Biocompatible magnetic fluids are used for diagnostics and therapy in medical applications, in pharmacy, and in biosensors. These fluids are used as a delivery system for anticancer agents in a locoregional tumor therapy-magnetic drug targeting and hyperthermia. The water-based magnetic fluid is constituted by coating the small magnetic nanoparticles with oleic acid and further dispersion in water. For the study of the influence of an external magnetic field on the aggregation processes of magnetic nanoparticles in biocompatible magnetic fluids, acoustic spectroscopy as a useful tool was used. The goal of the article is to bring new information about the creation of structures in the presence of different application processes of magnetic fields and the temperature of the investigated biocompatible fluid.*

*Keywords: Ultrasound Spectrometer, Biocompatible Magnetic Fluid, Structures*

## 1. Introduction

All types of magnetic fluids (ferrofluids, magnetorheological, or biocompatible magnetic fluids) are materials whose properties could be changed when external magnetic / electro fields are applied. The academics and researchers considered them as ‘‘smart materials’’ because their physical characteristics can be adapted to different conditions or functionalities with very interesting applications from industry to medicine. The preparation processes of magnetic nanoparticles are controllable from sizes ranging from a few nanometers up to tens of nanometers. In biomedicine, magnetic nanoparticles are mixed into a suitable biological solution to form the biocompatible magnetic fluids (BMF) with a wide range of uses in living organisms [1, 2].

The great subject of applied research in the area of magnetic fluids (MF) is the method of cancer treatment by magnetic hyperthermia of tissues. Hyperthermia offers an alternate treatment option for fighting against cancer due to its potential biocompatibility, minimal side effects, and efficient treatment modalities. Most of the magnetic hyperthermia experiments are performed on colloidal suspensions in BMF [3, 4].

The studied substance was the BMF based on the water. The basic properties of $Fe_3O_4$ nanoparticles (NPs) are as follows: purity 97%, form nanopowder, spherical shape, diameters 50–100 nm (SEM) [5], surface area 60 $m^2/g$, and bulk density 0.84 g/mL. A surfactant, oleic acid, was used to stabilize the nanoparticles (NPs) and prevent them from coalescing. The magnetic volume fraction was 4%. The properties of the BMF in the magnetic field have been studied by several authors [6, 7, 8]. The acoustic spectroscopy can be used to investigate MF under the application of the magnetic field, because the structural changes in the reorientation of NPs influence the acoustic parameters, such as the ultrasound wave velocity (c) and the absorption coefficient (α) of ultrasonic wave [9].

## 2. Characterization of a Sample Using the Acoustic Spectrometer

For determination of a mean diameter of NPs in the biocompatible fluid was the ultrasound spectrometer DT-100. The attenuation spectrums at a temperature of 25 °C using this spectrometer were determined. From Fig. 1a) it is evident that the attenuation in the studied fluids increases with frequency, and for water was smaller as in the BMF. Minimal attenuation was measured in water. With the addition of magnetic NPs, the scattering of the acoustic wave increased, which also caused an increase in attenuation. The attenuation for the magnetic fluid also increased due to the NPs cause additional dissipative attenuation. On the base of this measurement was calculated particle size distribution (Fig. 1b) with a mean hydrodynamic diameter of 64 nm. This value agrees with the value determined from a magnetization measurement.

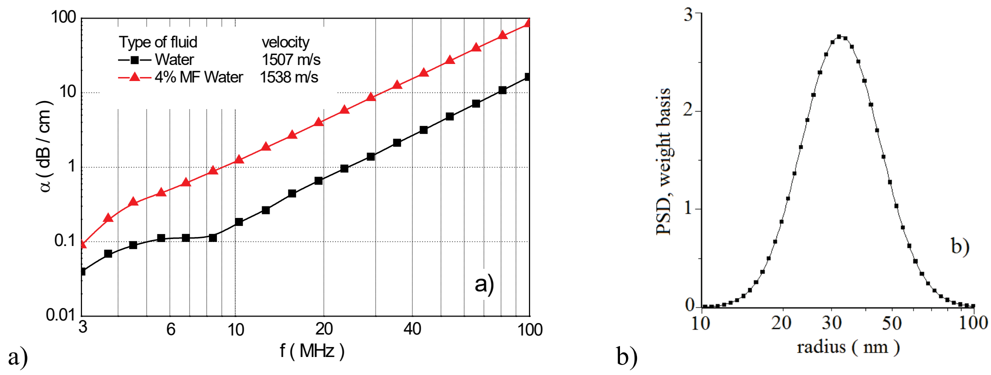


Fig. 1. a) Dependence of the acoustic attenuation on frequency for water and BMF and b) a particle size distribution for the radius of $Fe_3O_4$ NPs measured by the ultrasound spectrometer DT-100 at temperature 25 °C.

## 3. The Influence of Temperature and a Magnetic Field on the Acoustic Attenuation

The study of an influence of external parameters on the acoustic attenuation was done at the frequency of the acoustic wave 11.7 MHz with a pulse length of 0.24 μs. The experimental arrangement of the acoustic spectroscopy and its more detailed description can be found in the work [8, 9]. As with all materials, the parameters of the biocompatible fluid depend also on the temperature. This dependence is evident from a decrease of acoustic attenuation and an increase of velocity of the acoustic wave with temperature (Fig. 2).

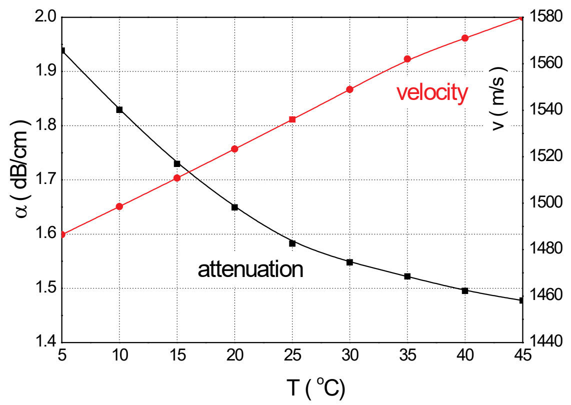


Fig. 2. The temperature dependence of the acoustic attenuation and the acoustic velocity in the BMF.

Fig. 3 depicts the changes in acoustic attenuation during jump changes of the magnetic field from 0 mT to 200 mT at different temperatures (25 °C, 35 °C, and 45 °C). The application of the magnetic field was a parallel orientation to the vector of the acoustic wave. Immediately after the change of amplitude of the magnetic field, the various changes of the acoustic attenuation (Δα) were observed, and their developments depended on the temperature. The smallest Δα was at the temperature of the investigated fluid at 25 °C, where α was stable after 15 minutes from application of the magnetic field. The increase of Δα was due to the rotation of magnetic NPs in the direction of the magnetic field and their sequential connection to new structures [7, 8]. The stable value of acoustic attenuation was after 25 minutes when the investigated fluid has 35 °C. At 45 °C the acoustic attenuation increased faster than at 35 °C and the stable value was achieved after 20 minutes. After switch off the magnetic field, the acoustic attenuation decreased around 3 minutes to almost half the value of the stable α for each temperature. This value was constant for more than tens of minutes. For this reason, we can conclude that a lifetime of a part of NPs structures was relatively long.

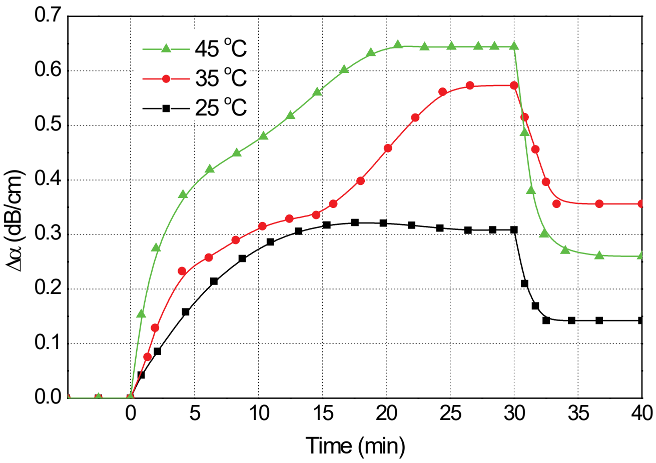


Fig. 3. Experimental data of the changes of the acoustic attenuation for three temperatures (■ 25 °C, ● 35 °C, ▲ 45 °C) at the value of magnetic flux density 200 mT.

## 4. Discussion

An external magnetic field causes a rotation of the magnetic moments of the NPs in the water-based BMF to its direction. This phenomenon causes, that NPs to merge as they approach and, with increasing time, they form new structures like dimers, trimers, thin and thick chains, or clusters [7, 8, 9]. These rearrangements of NPs in the fluid cause the changes of α because the interaction between created structures and the propagated acoustic wave leads to the additional attenuation of the acoustic wave. The application of the jumped magnetic flux density of constant value clearly showed that processes leading to the creation of structures were time-dependent and step-by-step (Fig. 3). The acoustic spectroscopy at various temperatures also confirmed that the rearrangement of NPs is temperature-dependent. At the temperature of 25 °C and 200 mT, the processes of rearrangement of NPs took the shortest time (Fig. 3). Since the Δα was smaller as at higher temperatures, we suppose that the final structures were dimers, trimers, or thin chains. At this temperature, longer chains cannot be created because Brown motion is small, and NPs hardly overcome double layer of surfactant on their surface.

For higher temperatures, Δα was higher (the structures could be bigger, thick chains or clusters), and the process of NPs restructuring took a longer time. At higher Brownian thermal motion, the NPs get closer more easily because their kinetic energy is insufficient to overcome the barrier's double layer of surfactant around them [6, 7, 8]. When they are close enough bond together due to a strong magnetic force and with time could be created bigger structures. This is the reason why we observed higher values of Δα (thick chains or clusters) at higher temperatures than at lower temperature (Fig. 3). On the other hand, when smaller NPs were used, they move too fast with increasing temperatures, and their weaker magnetic forces cannot connect them, which caused a decrease of $\Delta\alpha$ with temperature [9].

## 5. Conclusions

The presented results for the biocompatible magnetic fluid based on the water showed the creation of structures in the present magnetic field, which was confirmed by the change of the acoustic attenuation. Due to the larger diameter of the nanoparticles with increasing temperature, bigger nanoparticle structures could be formed. From this could be concluded that for practical application in biomedicine is better smaller NPs. Investigated biocompatible magnetic fluid appears as a perspective tool for application in clinical trials and can also be used for magnetic hyperthermia.

## Acknowledgments

This work was supported by VEGA 1/0471/20, and the modernization of the University of Zilina infrastructure with attention to the IKT ITMS 26250120021.

## References

[1] Rodrıguez-Lopez, J., Segura, L.E., Freijo, F.M. (2012). Ultrasonic velocity and amplitude characterization of magnetorheological fluids under magnetic fields, *Journal of Magnetism and Magnetic Materials,* 324, 222–230.

[2] Korobko, E.V., et all. (2015). Time stability studies of electrorheological response of dispersions with different types of charge carriers. *Journal of Intelligent Material Systems and Structures,* 26(14), 1782–1788.

[3] Molcan, M., et all. (2020). Magnetic hyperthermia study of magnetosome chain systems in tissue-mimicking phantom, *Journal of Molecular Liquids,* 320, 114470.

[4] Parekh, K., Bhardwaj, A., Jain, N. (2019). Preliminary In-Vitro Investigation of Magnetic Fluid Hyperthermia In Cervical Cancer Cells, *Journal of Magnetism and Magnetic Materials*, 497, 166057.

[5] Kaczmarek, K.. et all. (2018). Dependence of Ultrasonic and Magnetic Hyperthermia on the Concentration of Magnetic Nanoparticles, *Acta Physica Polonica,* 133(3), 716-718.

[6] Hornowski, T., Józefczak, A., Skumiel, A., Łabowski, M. (2010). Effect of Poly(Ethylene Glycol) Coating on the Acoustic Properties of Biocompatible Magnetic Fluid. *International Journal of Thermophysics*, 31, 70-76.

[7] Józefczak, A. (2005). Acoustic properties of PEG biocompatible magnetic fluid under perpendicular magnetic field. *Journal of Magnetism and Magnetic Materials*, 293, 240-244.

[8] Bury, P. et all. (2015). Acoustic investigation of biocompatible fluid under magnetic field. *Physics Procedia*, 75, 1029-1034 (2015).

[9] Kúdelčík, J., Bury, P., Kopčanský, P., Timko, M. (2015). Structure of nanoparticles in transformer oil-based magnetic fluids, anisotropy of acoustic attenuation, *Journal of Magnetism and Magnetic Materials,* 388, 28–34.

# Investigation of Magnetic Flux Density Variation Influence on the Biological Response of Cell Cultures

[1]Roman Radil, [1]Jan Barabas, [1]Ladislav Janoušek, [2]Patrik Kamencay

[1]Department of Electromagnetic and Biomedical Engineering, Faculty of Electrical Engineering and Information Technology, University of Zilina, Zilina, Slovak Republic,

[2]Department of Multimedia and Information and Communication Technology, Faculty of Electrical Engineering and Information Technology, University of Zilina, Zilina, Slovak Republic,

Email: roman.radil@feit.uniza.sk

***Abstract.*** *The presented paper focuses on the investigation of selective biological response induced by the application of the exogenous, time-varying low-frequency magnetic field. The research is inspired by the lack of sufficient scientific evidence regarding the generally accepted nonthermal physical mechanism of action at the cellular or subcellular level. Results observed and discussed within the scope of this article complement existing experimental evidence supporting the capability of biological system response alteration via application of exogenous low-frequency magnetic field at a cellular level. Experiments conducted on Saccharomyces cerevisiae cultures have shown that magnetic flux density variations are capable of provoking antagonistic proliferation response.*

*Keywords: Time-Varying Low-Frequency Magnetic Field, Saccharomyces Cerevisiae, Magnetic Flux Density, Inhibition Effect, Biological Effects*

## 1. Introduction

Research of possible biological effects of nonionizing electromagnetic fields (EMF) is becoming more and more popular during the past few years. Public awareness and scientific interest increased especially after the advent of 5G technologies, and without doubt, will continue to do so since scientific evidence of possible impact on health or environment caused by artificial sources of EMF is full of discrepancies and contradictions. The lack of scientifically undisputable results is a strong motivation to perform further investigation within the scope of the mentioned field of research.

Research of various scientific groups and published works thereof present valuable evidence regarding possible risks associated with the continuous irradiation of EMF. The available body of evidence served as a basis for the decision of the International Agency for Research on Cancer (IARC) to classify electromagnetic fields as group 2B carcinogen in 2013. Works of similar quality can be found within the whole frequency spectrum - from extremely low frequency (ELF) EMF up to radio frequency (RF) EMF and beyond. Current research in Slovakia in the RF-EMF range includes investigation of impact thereof on heart rate variability in [1], with experimental methodology rigorously described in [2], or the biological effects and physical parameters of mobile communication presented within works [3,4]. Research within the ELF-EMF spectrum focuses predominantly on cellular and subcellular levels - for example, in the case of [5], ELF magnetic field effects on blood lymphocytes are explored. Additional scientific evidence of cellular-level biological effects induced by low-frequency EMF are documented in our previously published papers (e.g. [6, 7]), where biologically active frequencies of applied exogeneous EMF have been identified. These experiments conducted on

Saccharomyces cerevisiae yeast cells were inspired by works [8 - 10], but also support findings regarding ion transport changes presented in [11,12].

Within the scope of this paper, we will continue research presented in [6], focusing on the investigation of possible effects of magnetic flux density changes of externally applied time-varying, low-frequency magnetic field (LF MF) on the proliferation response of cultivated cells.

This research intends to elucidate another variable – magnetic flux density magnitude, which can be considered a biologically active parameter of the applied electromagnetic signal. We would like to show that the definition of the exact value of this attribute could lead to interesting changes within the proliferation response of cultivated cells in comparison to already published frequency-related changes.

## 2. Materials and Methods

*Cell Cultivation*

Yeast cell samples were continuously irradiated by electromagnetic signal with specific parameters during 8 hours, representing the log phase (exponential growth) within the *S. Cerevisiae* Growth Curve.

Biological samples were precultivated in YPD (yeast-peptone-dextrose) medium for 24 hours at ambient temperature before each experiment. The cultivated medium was then diluted to obtain equal amounts of experimental solution within two Erlenmeyer flasks, used in subsequent LF EMF experiments. The diluted samples in Erlenmeyer flasks were cultivated in a commercial incubator during the whole experiment - exposed samples were placed within the cavity of the exposure coil, while the control samples were shielded from the generated EMF. The ambient temperature was maintained at a constant 30$^{o}$ C.

*Physical Parameters and Exposure Setup*

In our previously published works [6, 7], we succeeded in predicting the bioactive frequency targeting $Ca^{2+}$ and $K^{+}$ ions. The said frequency was calculated based on equation 1:

$$f = \frac{1}{n}\frac{q}{2\pi m}B_{gen}, \tag{1}$$

where $f$ represents the frequency of the time-varying LF MF, $q$ is the elementary electric charge of target ion, $m$ is the molecular mass of the target ion and $B_{gen}$ is the value of generated magnetic flux density.

For experiments presented herein, we decided to investigate the possibility of targeting the same ions but via magnetic flux density change, using an appropriate modification of equation 1:

$$B_{gen} = \frac{nf2\pi m}{q}, \tag{2}$$

where all parameters remain the same as in the previous case, enabling calculation of $B_{gen}$ at a known frequency. Using the target frequency f = 915.66 Hz results in magnetic flux density $B_{gen}$ = 1.195 mT for $Ca^{2+}$ ions and $B_{gen}$ =2.332 mT when targeting $K^{+}$ ions in this set of experiments. The mentioned physical parameters were achieved using our modernized exposure system, presented in Figure 2, incorporating harmonic signal generator (driving current), amplifier, incubator and shielding plate, as well current and voltage measurement devices.

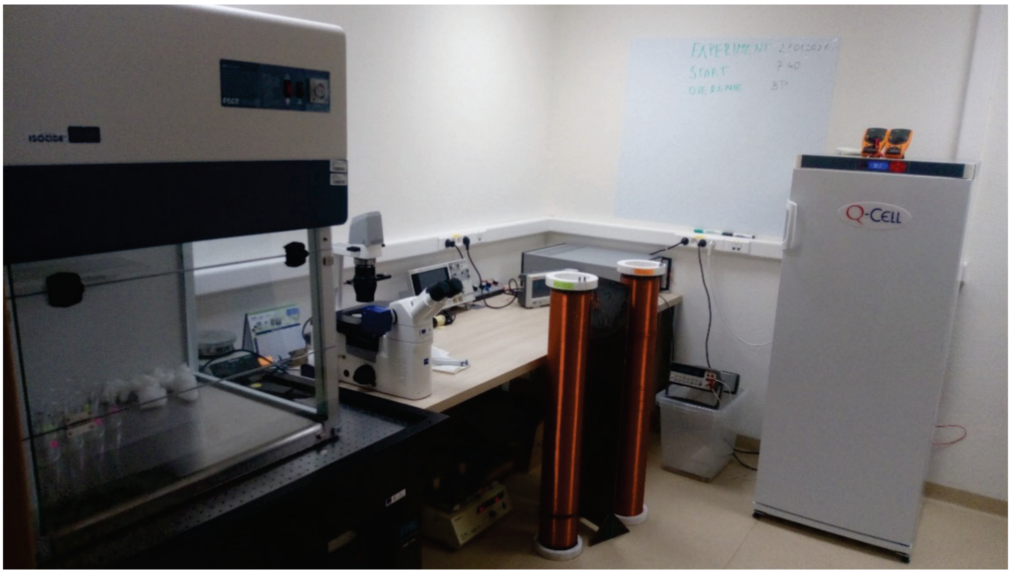


Fig. 1. Laboratory with exposure setup for experiments of nonthermal EMF effects on biological samples.

## 3. Results

Using the aforementioned methodology, we performed 5 experiments for each value of applied magnetic flux density. Evaluation and results quantification was performed via the growth dynamics coefficient (GDC) described in [6]. Observed results are presented graphically in Figure 3.

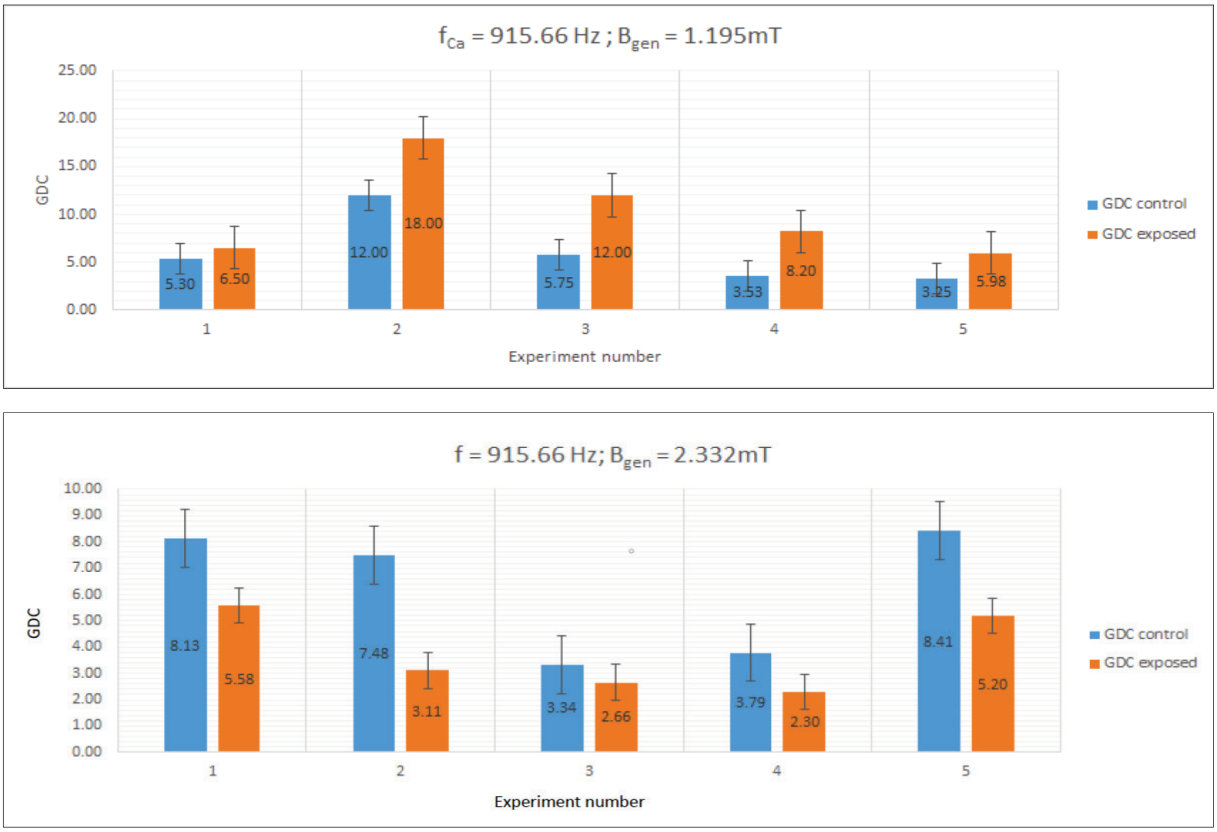


Fig. 2. Comparison of results achieved by magnetic flux density changes at a constant frequency (915.66 Hz).

## 4. Discussion and Conclusions

Our experimental results show the interesting behavior of *Saccharomyces cerevisiae* cultures when exposed to varying magnetic flux density at a constant frequency of the applied EMF. Opposite proliferative effects were observed – either stimulating growth of the exposed cell cultures (targeting $Ca^{2+}$) or inhibiting growth thereof (targeting $K^{+}$) using the same frequency but different magnetic flux densities. Observed results present a strong motivation for further research in this area, results of which could potentially be useful in the medicine or food industry.

Moreover, European Union policies call on national governments to ensure simple and feasible public access to information regarding the potential risks of electromagnetic fields and the environmental impact thereof and to apply the principle of "reasonable prevention" following the international standard ALARA - "as low as reasonably achievable".

We believe that research presented within this paper could be a part of scientific evidence of the possible effects of LF MF on biological samples at cellular levels.

## Acknowledgements

This work was supported by the Slovak Research and Development Agency under contract No. APVV-19-0214.

## References

[1] Misek, J., Veternik, M., Tonhajzerova, I., Jakusova, V., Janousek, L., Jakus, J. (2020) Radiofrequency electromagnetic field affects heart rate variability in rabbits. *Physiological Research*, 2020, 69(4), p. 633-643.

[2] Misek, J., Vojtek, J., Veternik, M., Kohan, M., Jakušová, V., Spanikova, G., Belyaev, I., Jakus, J. (2018) New radiofrequency exposure system with real telecommunication signals. *Advances in Electrical and Electronic Engineering*. vol. 16, 2018, p. 101-107.

[3] Jakusova, V. Ultrafialove ziarenie a mobilna komunikacia: fyzikalne vlastnosti, biologicke ucinky a ochrana zdravia.(2009) *1. vyd. Bratislava: Samosato*, 2009. 97 s. ISBN 978-80-89464-00-5

[4] Psenakova, Z., Benova, M. (2008) Measurement evaluation of EMF effect by mobile phone on human head. *Advances in Electrical and Electronic Engineering*. No. 1-2, Vol. 7/2008, ISSN. 1336-1376, p. 350-353.

[5] Zastko, L., Makinistian, L., Moravcikova, A., Jakus, J., Belyaev, I. (2020) Effect of intermittent ELF MF on umbilical cord blood lymphocytes. *Bioelectromagnetics*, 2020, vol. 41, no. 8, p. 649-655.

[6] Radil, R., Barabas, J., Kamencay, P., Bajtos, M., Hargasova, K. (2019) Targeting $Ca^{2+}$ and $K^{+}$ Ions Using LF EMF to Induce Proliferation Response of S. Cerevisiae. *MEASUREMENT 2019*. 12$^{th}$ International Conference on Measurement, Smolenice, Slovak Republic, Institute of Measurement Science, SAS, 2019, p. 119-123.

[7] Radil, R., Barabas, J., Janousek L., Bereta, M. (2020) Frequency dependent alterations of S. Cerevisiae proliferation due to LF EMF exposure. *Advances in Electrical and Electronic Engineering*, 2020, 18(2), p. 99-103.

[8] Liboff, A. R. Geomagnetic cyclotron resonance in living cells. (1985) *Journal of Biological physics*. 1985, vol. 13, iss. 4, p. 99-102. ISSN 0092-0606.

[9] Lednev, V.V. Possible mechanism for the influence of weak magnetic fields on biological systems. (1991) *Bioelectromagnetics*. 1991, vol. 12, iss. 2, p. 71-75. ISSN 0197-8462.

[10] Jelinek, F. (2009). Measurement of electrical oscillations and mechanical vibrations of yeast cells membrane around 1 kHz, *Electromag. Biol. Med.,* 2009; vol. 28, p. 223-232.

[11] Choe, M., Choe, W., Cha S. Lee, I. (2018) Changes of cationic transport in AtCAX5 transformant yeast by electromagnetic field environments. *Journal of Biological Physics.* 2018, vol. 44, iss. 3, p. 433-448.

[12] Lin, K.-W., Yang, Ch.-J. , Lian, H.-Y.,Cai, P. (2016) Exposure of ELF-EMF and RF-EMF Increase the Rate of Glucose Transport and TCA Cycle in Budding Yeast. In: *Frontiers in Microbiology*. 2016, vol. 7. ISSN 1664-302X.

# Measurement System for Monitoring of Magnetic Field Effects on Yeast Cells by Impedance Spectroscopy

[1]Michal Teplan, [1]Hoang VuViet, [2]Martin Bereta, [1]Ivan Bajla

[1]Institute of Measurement Science, SAS, Bratislava, Slovakia
[2]Faculty of Health, Catholic University in Ružomberok, Slovakia
Email: michal.teplan@savba.sk

***Abstract.*** *The development of innovative measurement approaches to investigate magnetic field (MF) biological effects is of great importance since we currently do not have any satisfying explanation of the MF biological interactions. The impedance spectroscopy is a well-known technique in the field of biological sample growth characterization. Here we present a proof of concept for cell culture impedance monitoring during the experiment with magnetic field exposure. We also emphasize the precise temperature monitoring has a key role in the exact interpretation of results since the minor temperature differences could lead to a substantial change in cell growth parameters.*

*Keywords: Magnetic Field, Biological Response, Impedance Spectroscopy*

## 1. Introduction

The biological effects of magnetic fields (MF) have become a widely discussed issue both among scientists and the general public in recent years, mainly due to extending daily use of various artificial MF sources. Although extensive research during the last few decades has been performed [1], we still lack an unambiguous explanation of the mechanisms of biological MF interactions. There are many irreproducible and contradictory results in this research field [2], which do not allow us to state a comprehensive interpretation of results obtained by different research groups. Moreover, there is data indicating peculiar behavior in terms of proliferation inhibition or stimulation depending sensitively on frequency and amplitude parameters [3].

There are several limitations of the current measurement methods, which are used for biological MF effects monitoring and evaluation. One of these limitations is the real-time monitoring of MF effects on living biological structures. Typically, the biological material, e.g. cell culture is exposed to a magnetic field for a particular time (minutes to hours), and the state of culture is monitored after the experiment, which does not allow to monitor immediate effects of MF exposure.

To eliminate this limitation, we suggest real-time monitoring of cell culture during its cultivation utilizing impedance spectroscopy. This method is well-known in the field of cell culture growth monitoring [4] and could serve as an innovative tool in the field of MF biological effects research.

## 2. Subject and Methods

The experimental platform consists of five parts: pair of cultivation chambers, optical microscope, system for magnetic field generation, impedance spectroscopy analyzer, and central control and data acquisition unit (Fig.1). Yeast *Saccharomyces cerevisiae* was used as a biological model. Cells are cultivated with yeast extract peptone dextrose (YPD). To prepare conditions for the most sensitive growth curve changes, we searched for an appropriate starting concentration that would yield maximal proliferation during the cultivation running for 16 hours. It was found empirically that for the original concentration of $2.5x10^5$ cells/ml it was possible to increase concentration 250-fold. Furthermore, the time efficiency of the experimental procedure was optimized: due to the 8-hour pre-cultivation period, time for the single run was compressed into 24 hours.

For optical inspection of samples, an inverted light microscope (Kern OCL-2) suitable for the observation of live biological samples is used. Digital camera (FLC 1600H, CMOS pixel size 1.34 µm) with a resolution of 16 MP and 60x objective offers an effective magnification (without digital zoom) at the level of 5800.

A cultivation chamber with 30 °C provides a stable and optimized environment for yeast cells' growth. The cell culture is cultivated in quasi-homogeneous MF in a media solution placed in Helmholtz coils. The optimal coil design modeled in Matlab resulted in N = 2 x 50 turns of copper wire of 2.2 mm diameter. The frequency and amplitude are adjustable by an arbitrary waveform generator and a power amplifier (Behringer NX3000D), providing AC currents up to 6.6 $A_{rms}$ for the coils generating MF in 0-2 kHz frequency range with intensity up to 4.3 mT.

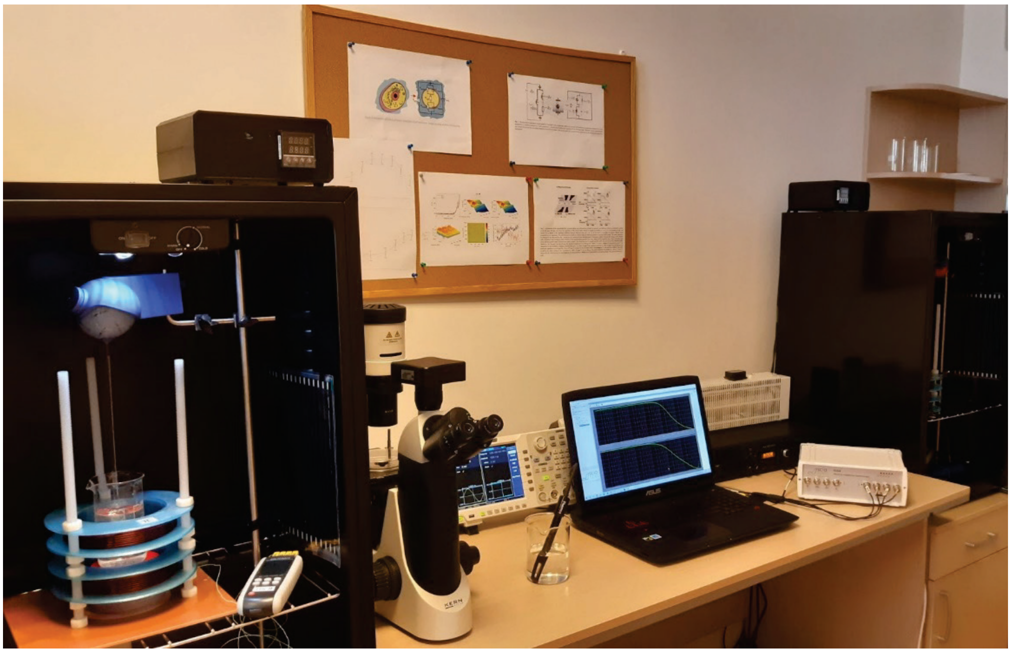

Fig 1. Composition of the experimental platform: Pair of cultivation chambers with PID temperature regulators (above) and 4-channel temperature data logger, Helmholtz coils, inverted light microscope, signal generator, power amplifier, impedance spectroscopy analyzer, and impedance probe.

ISX-3 (Sciospec) was used for impedance spectroscopy measurements, with a frequency range up to 10 MHz. 4-wire configuration was utilized with Orion (ThermoFisher Scientific) probe. The geometry of the electrodes was circular, with outer rings for injection of probing current.

As yeast cells in the medium can be modeled as a circuit consisting of capacitors and resistors, their growth can be expressed by the changes of vector electrical impedance. The conductivity alone cannot be used for concentration estimation, as the extracellular environment varies as consumption of the nutrient medium and other cell metabolism processes take place. However, the relative proportion between the low frequency and high-frequency values of impedance magnitude can reflect changes in cell concentration. In this way, one can monitor cell population by the following biomass estimator [4]

$$E_2 = 100 * \left(1 - \frac{|Z(HF)|}{|Z(LF)|}\right) \tag{1}$$

where $|Z(LF)|$ is the impedance magnitude at low-frequency $f \ll f_c$ and $|Z(HF)|$ is the impedance magnitude at high-frequency $f \gg f_c$, where $f_c$ is cutoff frequency. Relative values of $E_2$ are transformed into cell concentration values by the calibration with real cell numbers counted in the Bürker counting chamber.

## 3. Results

For automatic temperature regulation in the cultivation chambers, different control systems were deployed. The replacement of the On-Off controller with the proportional-integral-derivative (PID) controller improved heat control and hence temperature stability inside the chamber from 2.5 °C (max-min temperature in medium) to below 1 °C. Moreover, after the investigation of the temperature distribution inside the cultivation chamber, we obtained a discrepancy over 10°C between two extreme sensor positions (Fig.2). As expected, the main factor was the height of the sensor location. However, as air circulation and obstacles like coils with their geometry and thermal properties are involved, 3D temperature field distribution was rather complex.

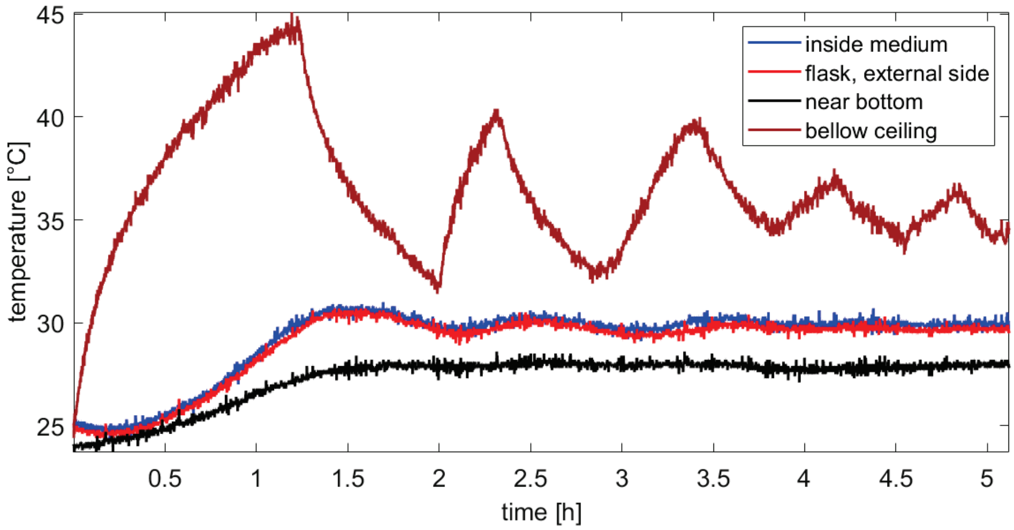


Fig. 2: Temperature monitored in different positions of the cultivation chamber: two in direct proximity of cells and two in distant locations within the chamber.

As it is disadvantageous to keep the regulation temperature sensor directly immersed in the medium, the only place where the temperature curve correlated well with the one from the medium directly was on the external side of the flask with the medium.

The proof of the concept of impedance monitoring has been utilized in the form of a cell sedimentation experiment. The samples of impedance spectra together with a sample of evolving cell concentration estimator calculated according to (1) are presented in Fig. 3.

The continual mode of the impedance measurement consisted of measurement of the whole spectrum (10 Hz -10 MHz) with logarithmically distributed 370 frequency points and 90 s duration. The optimization of $E_2$ parameters resulted in the choice of 10 kHz and 1 MHz for low-frequency and high-frequency, respectively.

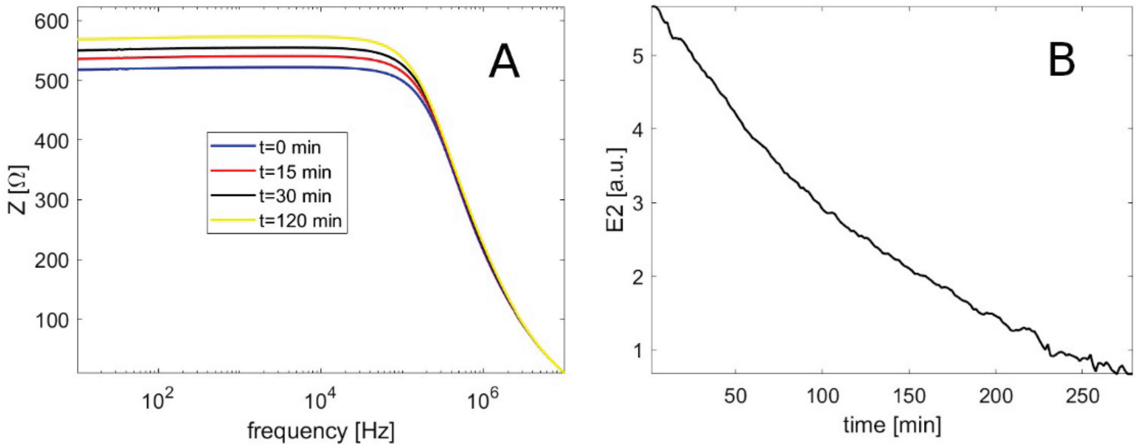


Fig. 3: Performance of $E_2$ estimator during sedimentation of the cells. A: sample of the impedance spectra. B: sample of the concentration estimator with LF = 10 kHz, HF = 1 MHz, a.u. - arbitrary units.

## 4. Discussion and Conclusions

Slight differences in experimental conditions between the test and control chamber could eventually have a substantial influence on the final results. The precise temperature monitoring even in standard experimental conditions could reveal a crucial impact of slight temperature changes, especially in long-term experiments. Therefore, we aim to accurately monitor temperature during each experiment, which could be one of the secondary, but still very important contributions of our work in the field of MF biological effects monitoring.

We also found out a dependence of the cell concentration estimator on impedance calibration. This issue is related to the calibration procedure in the radio-frequency range. After the completion of the experimental platform, we aim to focus on an exploration of the frequency and amplitude-dependent biological response of cell proliferation in the frequency range of 0-2 kHz, and magnetic flux density at mT level.

## Acknowledgements

The study was supported by the research grant 2/0157/19 from the VEGA Grant Agency. Authors also participate in COST Action CA17115.

## References

[1] Cifra M, Fields JZ, Farhadi A. (2011). Electromagnetic cellular interactions. *Prog Biophys Mol Biol.*, 105(3): 223-46.
[2] Buchachenko, A. (2016). Why magnetic and electromagnetic effects in biology are irreproducible and contradictory? Magnetic and electromagnetic effects in biology. *Bioelectromagnetics* 37, 1–13.
[3] Radil, R., Barabas, J., Janousek L., Bereta, M. (2020). Frequency dependent alterations of S. Cerevisiae proliferation due to LF EMF exposure. *Advances in Electrical and Electronic Engineering*, 2020, 18(2), p. 99-103.
[4] Soley A., et al. (2005). On-line monitoring of yeast cell growth by impedance spectroscopy. *Journal of biotechnology*, 118(4): 398-405.

# *Measurement of Physical Quantities II*

# Modeling the Process of Determination of the Instantaneous Error of the Thermocouple During Operation

**[1]Wei Siwei, [2,3]Orest Kochan, [4]Krzysztof Przystupa, [3]Mykola Beshley, [2]Jun Su, [2,5]Mariana Levkiv, [3]Viktor Kuts, [3]Iryna Petrovska**

[1]CCCC Second Highway Consultants Co., Ltd., Wuhan, China
[2]School of Computer Science, Hubei University of Technology, Wuhan, China
[3]Lviv Polytechnic National University, Lviv, Ukraine
[4]Lublin University of Technology, Lublin, Poland
[5]I. Horbachevsky Ternopil National Medical University, Ternopil, Ukraine
Email: orestvk@gmail.com

***Abstract.*** *The technique for simulating the process of developing thermoelectromotive force by the inhomogeneous thermocouple during the change of the temperature field along its legs is proposed in this paper. This allows determining the instantaneous error of the thermocouple during their operation without the use of working standards. There were revealed new relationships between the maximum and instantaneous errors due to drift and inhomogeneity. The sum of absolute values of these errors is constant, and this relationship holds in any temperature field.*

*Keywords: Thermocouple, Drift, Inhomogeneity, Thermocouple with Controlled Temperature Field, Error Determination*

## 1. Introduction

The thermocouple (TC) is the most common sensor when measuring temperatures within the range of 500 - 1100ºC [1]. Its disadvantage is the degradation of its legs during operation, which manifests itself as: a) drift of the conversion characteristics (CC) (for the type K TC it can be up to 6.5ºC for 1000 hours of operation at 800ºC [2]); b) error due to acquired thermoelectric inhomogeneity [2-4] in changeable temperature field (for the type K TC up to 11ºC for 1000 hours of operation at 800ºC [4]). The methods of TC error correction [2, 6] require calibration either in a laboratory [1], however, it requires the use of a working standard at the operation place (which is undesirable [1]) or at the place of operation [2] by the temperature fixed point cell [5] (it is not in mass production). The method proposed in [7] does not require working standards. It only requires constant temperatures of the measuring and reference junctions during the procedure. This method: a) does not allow error due to thermoelectric inhomogeneity of TC to appear [7] due to the stabilization of its temperature field; b) provides determination of the instantaneous TC error in situ. To study the errors of the method [7], its mathematical model should be constructed. The aim of the work is to study the error of the method [7] due to the shift of the zone of temperature gradient along the TC legs.

## 2. The Method for Determining the Instantaneous Error of the TC

There was proposed a method for determining the instantaneous TC error during operation [8] by changing the temperature field along TC legs (see Fig. 1). The method is based on the thermocouple with a controlled temperature field (TCTF) [8, 9]. The TCTF consist of main TC 1 and multi-zone furnace 2 [8, 9]. Furnace 2 consists of heaters and temperature sensors located along main TC 1. They set the temperature field A (the field of operation) along TC 1 and maintain it constant. Then the error due to acquired thermoelectric inhomogeneity [3] cannot appear. According to the fundamental law of thermoelectric thermometry [1], thermoelectromotive force (thermo-e.m.f.) developed by a TC section is proportional to the temperature difference at its ends. Therefore, during the operation, the thermo-e.m.f. of TC 1 is developed by sections l1 - l2. When determining the instantaneous error of TC 1, the heaters of the TCTF form the field B. In the field B the thermo-e.m.f. is developed by sections l3 - l4. But these sections are operated at the temperature close to that of the reference junction and thus do not undergo degradation [10]. Therefore, the difference between thermo-e.m.f. of TC 1 in temperature fields A and B equals the error due to drift of TP 1. If TC 1 was calibrated in the temperature field B (for example, using a working standard) prior to operation, the sum of the initial error and error due to drift of TP 1 equals its instantaneous error.

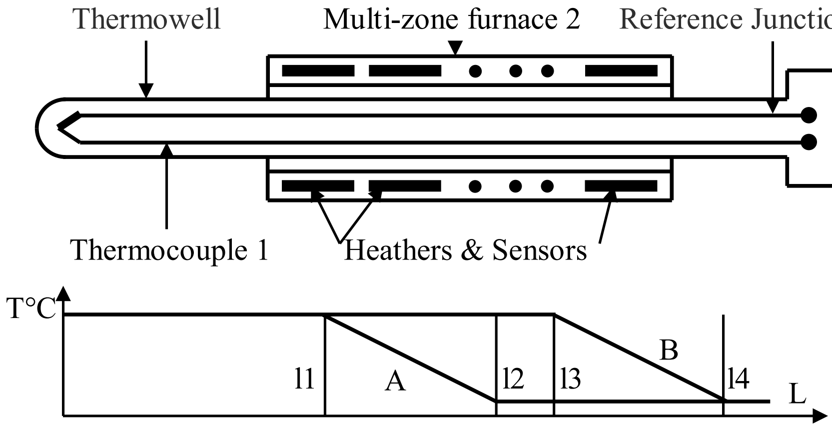


Fig. 1. Determination of the instantaneous error of the TC during operation by changing its temperature field.

## 3. Modeling the Determination of the Instantaneous Error of the Thermocouple

The research is carried out by modeling in a spreadsheet. The technique of modelling is as follows:

1. Split the TC into $i = 100$ sections, $i = 0$ corresponds to the reference junction (temperature of 0ºC), $i = 100$ corresponds to the measuring junction (temperature of 800ºC).
2. Set the temperature fields of the TC in the form of the sigmoids (the left hand side formula) and line segments (the right hand side formula)

$$T = \frac{800}{1 + e^{-3(N/10 - C)}}, \qquad \begin{cases} T = 0 \\ T = km + b,\ if\ T < 800 \\ T = 800 \end{cases} \tag{1}$$

where $T$ is the instantaneous temperature of the temperature field; $N$ is the current number of the temperature field; *C=7* is the coordinate of the point with the temperature of 400ºC for the field of operation (see the left hand side of (1)), for each subsequent field C decreases on 0.5. The total number of similar fields is 4 (see the right hand side of Fig. 2). The line segments fields are given on the left hand side of Fig. 2.

3. Carry out the analysis of the influence of changes in the temperature field from the sigmoids of the operation field to straight line segments of lines with different parameters for the sections are in operation at the close to that of the reference junction (see Fig. 2 left) on errors due to drift and due to acquired thermoelectric inhomogeneity. For the type

K TC, the relative Seebeck coefficient is chosen of $e=40\ \mu V/°C$. The drift of the Seebeck coefficient of each section is calculated according to the formula

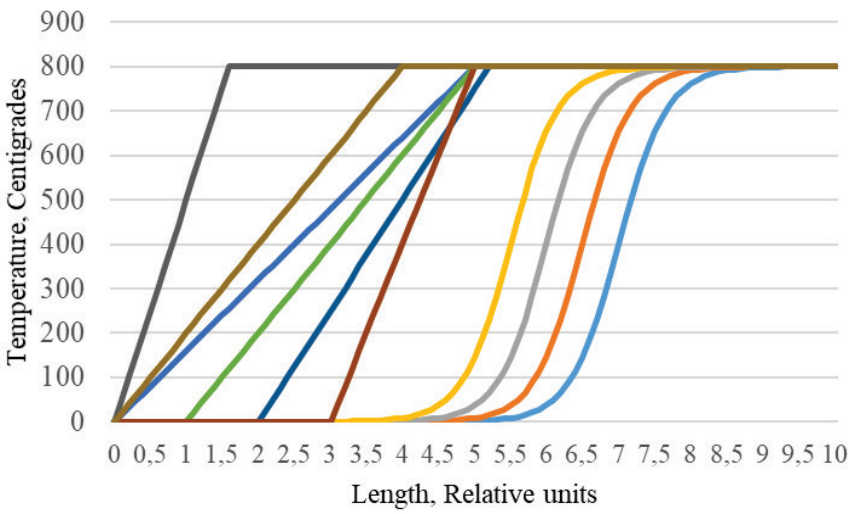


Fig. 2. Temperature fields profile in the form of sigmoids and in line segments with different parameters

$$\Delta e_i = AT_{EKSi} + BT_{EKSi}^2 \quad (2)$$

where $T_{EKSi}$ is the temperature of operation of the certain TC section (the rightmost sigmoid in Fig. 2); $A=0,0025\ K^{-1}$, $B=2\times10^{-6}K^{-2}$ are the coefficients adjusted match the total error of the TC with the experimental data ≈11°C [4].

4. Calculate the nominal and actual thermo-e.m.f., developed by each TC section in all 10 temperature fields according to the formulae

$$E_i^{NOM} = e\left(T_{i+1} - T_i\right), \qquad E_i^{REAL} = \left(e + \Delta e_i\right)\cdot\left(T_{i+1} - T_i\right), \quad (3)$$

where $E_i^{NOM}$, $E_i^{REAL}$ are the nominal and actual thermo-e.m.f. of each section; $T_{i+1}$, $T_i$ are the temperatures at the ends of each section.

3. Calculate the nominal and actual thermo-e.m.f., by the whole TC in all 10 fields

$$E_j^{NOM} = \sum_{i=0}^{100} E_i^{NOM}, \qquad E_j^{REAL} = \sum_{i=0}^{100} E_i^{REAL}, \quad (4)$$

where $E^{NOM}$, $E^{REAL}$ are the nominal and actual thermo-e.m.f. of the TC.

4. Calculate the errors due to drift $\Delta E_j^{DR}$ of the TC CC as the difference between the actual thermo-e.m.f. developed by the TC, in each $j$-th temperature field and the nominal one

$$\Delta E_j^{DR} = E_j^{REAL} - E_j^{NOM}, \quad (5)$$

5. Calculate the errors due to acquired thermoelectric inhomogeneity $\Delta E_j^{NEOD}$ as the difference between the thermo-e.m.f. developed in the temperature field of operation $E_{EXP}^{REAL}$ and in those developed in other fields $E_j^{REAL}$

$$\Delta E_j^{NEOD} = E_j^{REAL} - E_{EXP}^{REAL}, \quad (6)$$

6. Calculate the sum of absolute values of errors due to acquired inhomogeneity and due to drift of TC CC for each temperature field. The results of the study are presented in Fig. 3.

## 4. Conclusions

The following conclusions can be drawn: (i) when the zone of the temperature gradient is shifted toward the reference junction (see Fig. 1), there is a gradual "displacement" of the error due to drift (starts at 452 μV in Fig. 3) by error due to inhomogeneity (starts at zero in Fig. 3); (ii) the sum of the absolute values of these errors remains constant for any field (dashed line in Fig. 3); (iii) the maximum absolute values of errors due to drift and due to inhomogeneity are also equal;

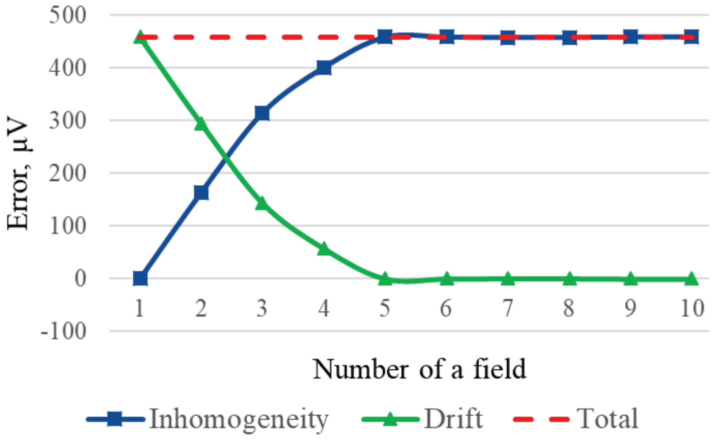


Fig. 3. Errors due to acquired thermoelectric inhomogeneity and due to drift of TC CC versus temperature field

(iv) the sum of the absolute values of errors due to drift and due to inhomogeneity is equal to this maximum value in any temperature field; (v) the result of determining the instantaneous TC error does not depend on the shape of the temperature field across the reference section. The study showed that the method of determining the instantaneous error of the TC during operation by purposefully changing the temperature field along its legs, proposed in [8, 9], has no error of method and can significantly improve the measurement accuracy. This paper develops the studies carried out in [7, 11, 12].

**Acknowledgements**

This work was support by the Technological innovation project of Hubei Province 2019(2019AAA047).

**References**

[1] Park, R. M. (ed.) (1993). *Manual on the use of thermocouples in temperature measurement*. ASTM International.

[2] Körtvélyessy, L. (1998). *Thermoelement-Praxis: neue theoretische grundlagen und deren umsetzung*. Vulkan-Verlag GmbH.

[3] Jun, S., Kochan, O. (2015). The mechanism of the occurrence of acquired thermoelectric inhomogeneity of thermocouples and its effect on the result of temperature measurement. *Measurement Techniques*, 57(10), 1160-1166.

[4] Sloneker, K. (2009). Thermocouple inhomogeneity. Ceramic Industry, 159 (4), 13-18.

[5] Ďuriš, S., Ranostaj, J., Palenčár, R. (2008). Development of fixed-point cells at the SMU. *International Journal of Thermophysics*, 29(3), 861-870.

[6] Sachenko, A., Kochan, V., Turchenko, V. (2003). Instrumentation for gathering data [DAQ systems]. *IEEE instrumentation & measurement magazine*, *6*(3), 34-40.

[7] Shu, C., Kochan, O. (2013). Method of thermocouples self verification on operation place. Sensors & Transducers, 160(12), 55-61.

[8] Jun, S., Kochan, O., Kochan, V., et al. (2016). Development and investigation of the method for compensating thermoelectric inhomogeneity error. *International Journal of Thermophysics*, 37(1), 10.

[9] Wang, J., Kochan, O., Przystupa, K., Su, J. (2019). Information-measuring system to study the thermocouple with controlled temperature field. *Meas. Sci. Rev.*, 19(4), 161-169.

[10] Webster, E. S. (2014). Low-temperature drift in MIMS base-metal thermocouples. *International Journal of Thermophysics*, 35(3-4), 574-595.

[11] Chen, J., Su, J., Kochan, O., Levkiv, M. (2018). Metrological Software Test for Simulating the Method of Determining the Thermocouple Error in Situ During Operation. *Measurement Science Review*, 18(2), 52-58.

[12] Jun, S., Kochan, O., Levkiv, M. (2017). Metrological software test for studying the method of thermocouple error determination during operation. In *2017 11th International Conference on Measurement*. IEEE, 171-174.

# An IoT-Based Datalogger of Environmental Values

**Petr Raichl, Petr Marcon**

Department of Theoretical and Experimental Electrical Engineering,
Brno University of Technology, Czech Republic
Email: xraich02@vutbr.cz

***Abstract.*** *The paper characterizes the architecture of an IoT system for measuring and visualizing environmental data. The first part describes the construction of a solar panel powered, IoT-based datalogger of environmental values such as temperature, humidity, and pressure. The second part then outlines a solution to the related cloud system. The datalogger is built as a setup driven by a microcontroller. The program for the microcontroller was written in the C language. Functionally, the microcontroller communicates with the sensors through an I2C bus; the configuration and control of the measurement are performed via a PC application compiled in C# and connected to the device over a USB bus. The measured data are stored in a Micro SD card and transmitted by means of the LoRa technology to the local LoRa cloud provider. The data are then resent from this local provider to a cloud-based Amazon MySQL database and can be visualized through a web application coded in the ASP.NET Core framework. This paper presents the entire, ready-to-use system.*

*Keywords: IoT, LoRa, Cloud, Environmental Sensors, Climate Datalogger, Microcontroller*

## 1. Introduction

Monitoring environmental values such as temperature, humidity, and pressure plays an important role in human life. It is sometimes difficult and time-consuming to measure environmental values at distant or poorly accessible places. As the Internet of things (IoT) is becoming a part of life, there are new Low-Power Wide-Area Networks (LPWAN), such as SigFox or LoRa, that could be used in dataloggers, including in particular those that record environmental values to make human life easier.

Most studies relevant to the topic, such as [1]-[3], typically do not offer the whole solution, i.e., the solution with the whole architecture (comprising the data storage and visualization); usually, only a ready-to-use solution, for example, ThingSpeak.com [4], is presented.

In view of these facts, our paper describes the entire solution for the measurement of environmental values at multiple distant or poorly accessible places, with almost real-time visualization of the measured values.

*Requirements*

The requirements for the datalogger were determined and resolved. The datalogger is powered by a Lithiumtitanate-oxide (LTO) battery, as this type of battery exhibits better behaviour in cold conditions [5]. This battery is charged by a solar panel. The heart of the datalogger is a microcontroller that controls other peripherals and communicates with the external world. The datalogger collects environmental values of temperature, humidity, and pressure at least once per minute. The measured data are sent to the cloud via one of LPWAN technologies. The measured data are also stored in a micro SD card to remain reachable when IoT services cannot be accessed. The device is configured via a PC through a USB bus. Visualisation of the measured data is needed.

## 2. Design of Datalogger

This section describes the actual concept of the system; applied technologies; architecture; and HW/SW implementation.

*IoT*

Figure 1 interprets the suitability of LPWAN technologies. Considering the use case of the device presented in this paper, the LoRa technology was chosen: It is perfectly convenient in use cases where the requirements for long-range communication and low-power management are met. Lora utilizes license-free radio frequency bands like 433 MHz, 868 MHz (Europe), and 915 MHz [6]. The LoRa protocol is designed specifically for lower power consumption and can connect areas up to 15 km apart. To employ the LoRa technology, users need to rely on some LoRa providers, such as Loriot, or The Things Network. In our case, an offer by the local provider Czech Radiocommunications was accepted because of their signal coverage in the Czech republic.

*Concept of Datalogger*

After analyzing the requirements, we materialized the concept of the datalogger (Figure 2). The core of the device is an STM32L151 microcontroller, which was chosen thanks to its support of low power modes and offer of peripheral communication interfaces. The datalogger is powered by an LTO battery. This battery is charged from a solar panel when the voltage drops below 2.5 V; otherwise, the charger is disconnected. The voltage is measured by an AD converter, embedded in the microcontroller. For the temperature and humidity sensing, an SHT-85 [7] was chosen, and the pressure sensing is facilitated by a BMP280 [8]. The main parameters of the sensors are listed in Table 1. Both of the sensors are connected to the microcontroller via an I2C bus. The micro SD card is connected to the microcontroller over an SPI bus. The configuration and control of the datalogger are executed by a PC application. The PC application is connected over a USB bus. An FT232 serves as a bridge between the USB on the PC side and the UART on the datalogger side. The FT232 allows the device to behave like a virtual COM port in the PC, making the implementation easier on both the PC and the device sides. The LoRa technology is enabled by an RN2483. This circuit is used as a modem, meaning that the circuit is connected to the microcontroller over a UART bus, and the communication is based on defined UART messages. In the microcontroller, the LoRaWAN stack or RF design do not need to be implemented.

Table 1: Main parameters of used sensors

| Sensor | Interface | Power Supply | Current consumption | Operating temperature | Accuracy (%) | Price (Eur) |
|---|---|---|---|---|---|---|
| SHT85 | I2C | 2.15-5.5 | 1.7uA | -40 - 125 | 0.4°C, 1.8%RH | 24 |
| BMP280 | I2C | 1.71-3.6 | 2.8uA | -40 - 85 | +-0.12hPa | 3.9 |

*Architecture*

Figure 3 shows the data flow from the datalogger to the visualization. The datalogger sends the measured data over the LoRaWAN network to the cloud of the local LoRa provider. As it is not possible to visualize the data in this cloud, they are resent to Amazon API Gateway. Then, the data are moved to a lambda function, which saves them in a MySQL database. The data measurement and sending periods are 1 min and 5 min, respectively; this means that, in the latter case, one packet sent contains 5 frames of measured values.

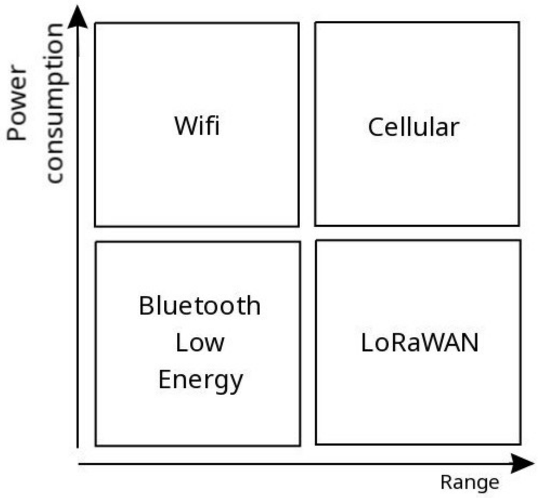


Fig. 1: Suitability of LPWAN technologies [6]

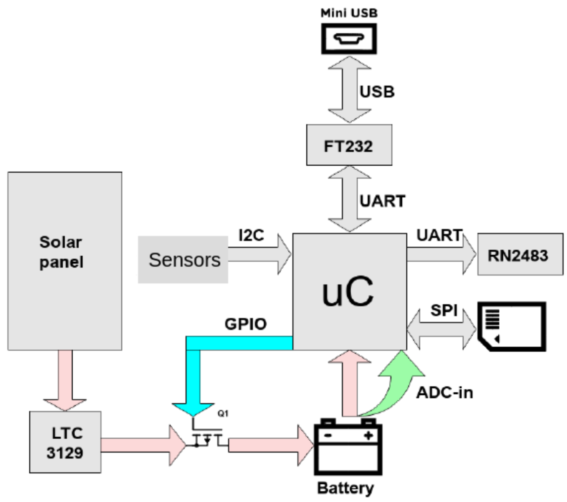


Fig. 2: Concept of datalogger

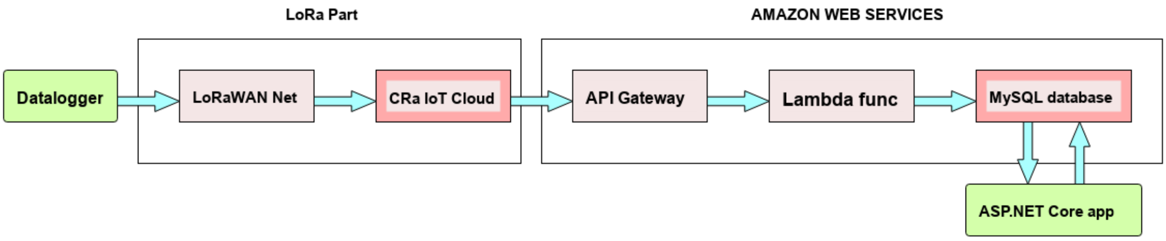


Fig. 3: Architecture of system.

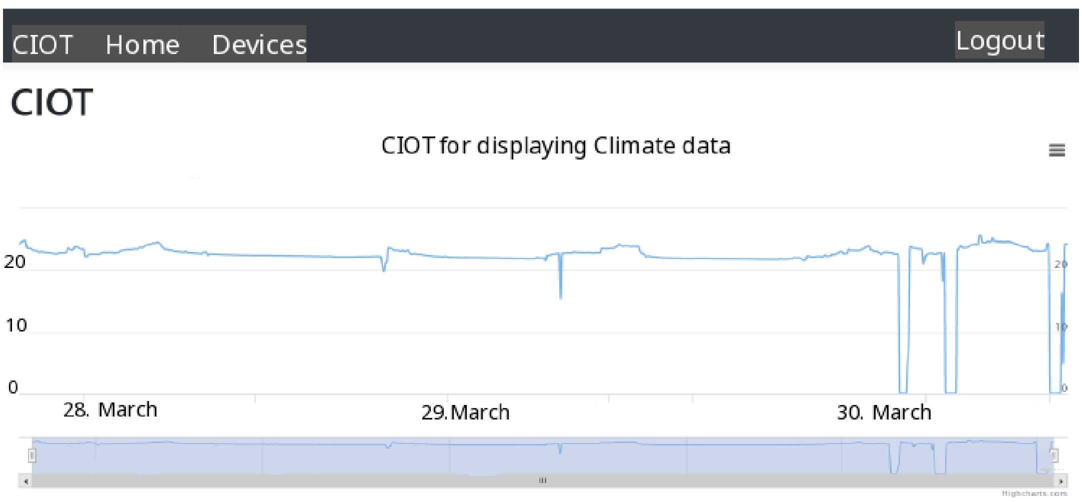


Fig. 4: Visualization of measured data.

*Visualization of Measured Data*

To visualize the measured data, we created a web database application in ASP.NET Core. This application connects to the MySQL database and enables the visualization of the measured data from devices registered by the user. An example of the measured data visualization is shown in Figure 4. In this application, 2 roles exist: that of the admin and that of the user. The admin role manages the registrations and permissions of the users, while the user role facilitates the registration of individual devices identified by unique id numbers. These devices can be added/removed, and their data are visualizable in graphs.

## 3. Conclusion

We introduced the concept of an IoT-based datalogger of environmental values, the device is powered by a solar panel and using the LoRa technology to ensure real-time visualization of the measured data. At one of the initial stages, the device and its electronics were designed. We also characterized the architecture of the whole IoT solution; this architecture utilizes the local LoRa provider's network and cloud. The measured data are resent from the LoRa provider to the MySQL database, which runs under Amazon Web Services. For the visualisation, a web application in ASP.NET Core was built; the application loads the data from the MySQL database and visualizes them in graphs, which are zoomable. The whole, ready-to-use system is described and implemented.

## 4. Acknowledgment

This paper was funded from the general student development project at Brno University of Technology.

## References

[1] Tzortzakis, K., Papafotis, K., Sotiriadis, P.P. (2017). Wireless self powered environmental monitoring system for smart cities based on LoRa. *Panhellenic Conference on Electronics and Telecommunications (PACET)*, 1–4.

[2] Puneet Kalia, K., Ansari, M.A. (2020). IOT based air quality and particulate matter concentration monitoring system. *Materials Today: Proceedings*, 32(3), 468–475.

[3] Pathak, A., AmazUddin, M., Abedin, M.J., Andersson, K., Mustafa, R., Hossain, M.S. (2019). IoT based smart system to support agricultural parameters: A case study. *Procedia Computer Science*, 155, 648–653.

[4] IoT Analytics - ThingSpeak Internet of Things. [cit. 19. 02. 2021]. Available from URL: `https://thingspeak.com/`.

[5] Wu, X., Mei, Z., Hu, C., Zhu, C., Sun, J. (2016). Temperature performance comparative analysis of different power batteries. *IEEE Vehicle Power and Propulsion Conference (VPPC)*, Hangzhou, 1–6.

[6] Orange Connected Objects & Partnerships: *LoRa Device Developer Guide*. [cit. 19. 02. 2021]. Available from URL: `https://developer.orange.com/wp-content/uploads/LoRa-Device-Developer-Guide-Orange.pdf`.

[7] Sensirion: *SHT85 [online datasheet]*. [cit. 19. 02. 2021]. Available from URL: `https://cdn.sos.sk/productdata/8d/94/c6c9b77b/sht-85.pdf`.

[8] Bosch: *BMP280 [online datasheet]*. [cit. 19. 02. 2021]. Available from URL: `https://cz.mouser.com/datasheet/2/783/BST-BMP280-DS001-1509562.pdf`.

# A Precision Coaxial Low-Current Shunt with Improved Mathematical Model

Maciej Malinowski, Krzysztof Kubiczek, Marian Kampik,

Krzysztof Musioł, Michał Grzenik, Kordian Dudzik and Wiesław Domański

Silesian University of Technology (SUT)
Department of Measurement Science, Electronics and Control, Gliwice, Poland
Email: Maciej.Malinowski@polsl.pl

***Abstract.*** *The article presents the construction and mathematical model of a precision coaxial wideband low-current shunt developed at the Silesian University of Technology (SUT) in Gliwice, Poland. Results of experimental validation of the calculated AC-DC transfer differences are also presented, revealing a good agreement between calculated and measured values.*

*Keywords: AC-DC Difference, Current Shunt, Mathematical Model, Numerical Simulation*

## 1. Introduction

In high precision measurements of alternate current (AC) and direct current (DC), resistive current shunts are used. The principle of operation of such a shunt is well known: the current flowing through it is converted to a proportional voltage drop. The voltage drop is usually measured with a high precision voltmeter or sampler. To obtain higher precision of AC current measurement, the voltage drop is measured using a thermal voltage converter (TVC).

In this article, we describe the construction and mathematical model of the precision coaxial 50 mA current shunt developed at SUT. We also present experimental validation of AC-DC transfer difference calculated using the developed mathematical model.

## 2. Design Precautions

When designing a resistive current shunt, two contradictory requirements shall be met: to limit power losses in the shunt, its resistance should be as small as possible, but from the other hand, the highest precision in voltage measurement is achieved when the value of voltage drop is relatively high (around 1 V). In the case of precision current shunts, the second requirement is a priority. One of the most critical parameters of a current shunt is its transimpedance. The use of this parameter (instead of resistance or impedance) is justified because, due to its structure, the shunt should be analyzed as a four-terminal network. When the shunt is used, e.g. for calibration of ammeters, multimeters or calibrators, then the determination of the module of the shunt transimpedance is sufficient. However, in some other applications like AC power or energy measurements, the phase error of the shunt must also be determined. Another important metrological parameter of the current shunt used in AC measurements systems is its AC-DC transfer difference, which should be small as possible [1]. The AC-DC transfer difference is caused mainly by residual parameters of the shunt (inductance and capacitance). Values of these residual parameters depend on the construction (geometry) of the shunt and properties (impedance) of resistors used [1],[2],[3]. The desired property of the current shunt is the stability of its transimpedance in time and environmental conditions (temperature, humidity) as well as its linearity, i.e. independence of resistance (transimpedance) from the magnitude of the current flowing through it. Precision low-current wideband shunts designed for low currents (below approximately 0.2 A) usually have coaxial, radial construction [4].

## 3. Description of the Prototype of the Shunt

The cross section of the precision current shunt developed at SUT is presented in Fig. 1. The resistance of the shunt equals 16 Ω, and the voltage drop at nominal input current is 0.8 V. The main part of the shunt is formed from twelve 192 Ω Z-foil SMD (surface mount devices) resistors connected in parallel. The temperature coefficient of resistance of these resistors is approximately 0.05 μΩ/(Ω·K). The resistors are mounted on a round 1.6 mm thick printed circuit board (PCB) made from glass-reinforced epoxy (FR-4) substrate laminated with a 35 μm thick copper layer. The PCB was attached to an N-type output male connector. To separate the input circuit from the output, a coaxial waveguide was placed between the input N-type connector and the PCB. The separation is required to reduce the inductive coupling between the input and the output. The inner wire is made from a 1.8 mm thick solid copper.

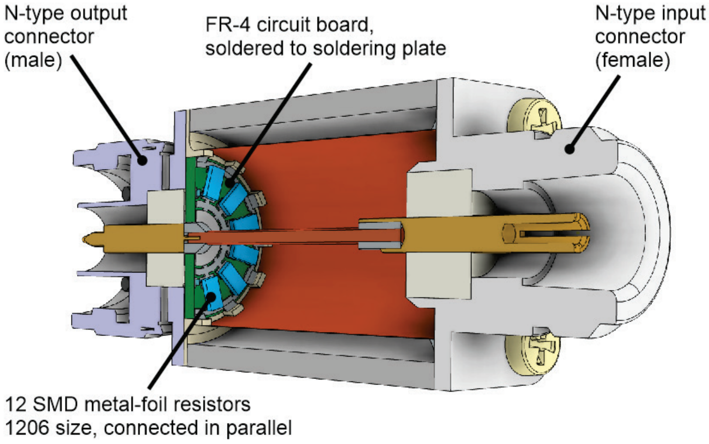


Fig. 1. The cross section of the resistive current shunt developed at SUT.

The outer part of the waveguide is made from 80 μm thick foil, rolled up to get a tube. The diameter of this tube is 20 mm, and its length is 35 mm. The enclosure of the shunt was printed from polylactide (PLA) using a 3D printing technology. The housing is screwed to both connectors with eight polyamide M3 screws.

## 4. Mathematical Model of the Shunt

In [5], a mathematical model of the shunt was presented, where the effect of the waveguide was modelled using lumped parasitic parameters. However, the distributed parameters model presented in [6] shows a significant influence on the AC-DC transfer difference of the shunt. The model allowed to calculate the AC-DC transfer difference of the prototype construction of the current shunt. The drawback of that model is that the waveguide and both connectors were modelled using a simplified lumped-element equivalent circuit. Hence the shunt transimpedance calculated using that model did not reflect the real impedance of the device. Therefore, another attempt was made to model the shunt correctly. The improved equivalent circuit of the shunt is presented in Fig.2.

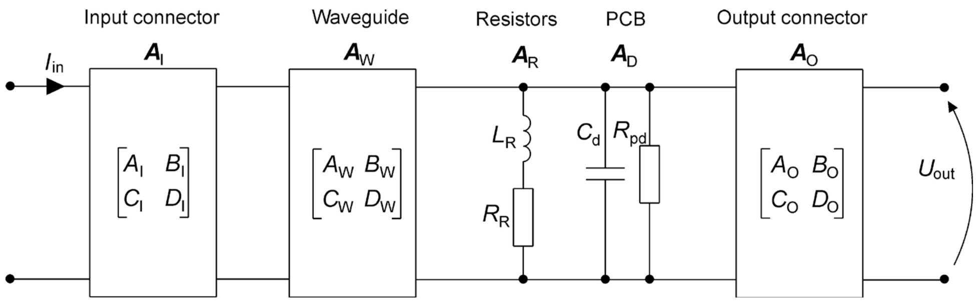


Fig. 2. Equivalent circuit of the 50 mA shunt developed at SUT.

The circuit shown in Fig. 2 contains an improved model of the waveguide represented by the chain matrix $\mathbf{A}_W$, $\mathbf{A}_I$ and $\mathbf{A}_O$. The waveguide and both connectors were modelled based on equations of a distributed parameter transmission line. The model is composed of a serial connection of five two-port networks [1], representing the input female N connector, the waveguide, resistors, the PCB and the output male N connector. The two-port network matrixes of the input and the output connectors, as well as the waveguide and the PCB are computed mathematically from their geometry dimensions and material properties [6]. Resistance of the precision resistors was measured with Keysight E4980A high-precision LCR meter [7]. Due to difficulties with the precise measurement of small values of inductance and capacitance of these resistors, their residual parameters were taken from the datasheet [8]. The shunt may be described by the matrix $\mathbf{A}_S$:

$$\boldsymbol{A}_S = \boldsymbol{A}_I \boldsymbol{A}_W \boldsymbol{A}_R \boldsymbol{A}_D \boldsymbol{A}_O \tag{1}$$

Matrix $\mathbf{A}_S$ has 4 components:

$$\boldsymbol{A}_S = \begin{bmatrix} a_{11} & a_{12} \\ a_{21} & a_{22} \end{bmatrix} \tag{2}$$

The $a_{21}$ element describes the transimpedance $Z_T$ of the shunt:

$$Z_S = \frac{1}{a_{21}} \tag{3}$$

To improve the accuracy of the mathematical model, the matrix $A_w$ representing the waveguide must contain distributed parameters of the transmission line, such as: resistance, capacitance and inductance. Because the dielectric placed between conductors is dry air, its conductance can be neglected. Additionally, because of the assumed concentricity of the two waveguide elements (its internal wire and the outer copper pipe), their electric and magnetic fields can be analyzed separately. The magnetic and electric fields are computed from the solution of the second order differential equation for magnetic vector potential using Bessel functions of the first and the second kind. The model also takes the skin effect into account. The obtained residual parameters of the conductors allow computation of characteristic impedance of the waveguide. To take into account the wave phenomena, such as interference and reflection, it was necessary to apply hyperbolic functions to provide the distribution of residual parameters along with the guide. The more detailed model description with its mathematical equivalence can be found in [6].

Finally, the AC-DC transfer difference of the current shunt is given by [1]:

$$\delta_{AC-DC} = \frac{Z_{Tm}(f) - Z_{Tm}(0)}{Z_{Tm}(0)} \tag{4}$$

where $Z_{\mathrm{Tm}}$ is a module of the shunt transimpedance.

The uncertainty of the calculated AC-DC transfer difference was computed using the Monte Carlo method assuming tolerances of geometrical dimensions and uncertainties of material constants.

## 5. Validation of the Mathematical Model of the Shunt

To validate the correctness of the calculated AC-DC transfer difference, the prototype of the shunt was sent for calibration to Swedish National Metrology Institute (NMI) RiSE. The comparison between measured and calculated AC-DC transfer differences and their uncertainties is presented in Fig.3.

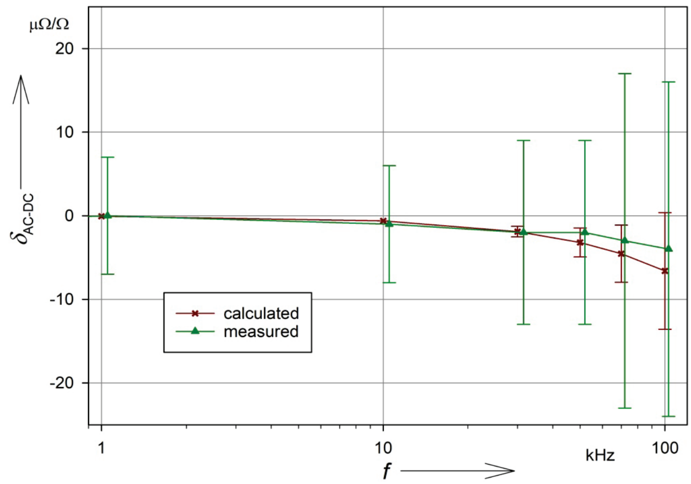


Fig. 3. The comparison between the measured and the calculated AC-DC transfer differences and their uncertainties.

## 6. Conclusions and Future Work

The calculated AC-DC transfer differences are in good agreement with the measured results, confirming the correctness of the improved mathematical model of the shunt. Moreover, the calculated results are closer to measured values than in the case of the earlier developed mathematical model using lumped elements. The model will be used in further design and optimization of the set of current shunts of nominal currents 10, 20, 100 and 200 mA. The developed shunt will be used in conjunction with thermal voltage converters serving as a high-grade precision standard of the AC current.

### Acknowledgement

This work was supported by the Polish National Science Center (NCN) under Project 2020/37/B/ST7/00057

### References

[1] Zachovalova V. (2014). On the Current Shunts Modeling. *IEEE Trans. Instrum. Meas.*, vol. 63, no. 6, pp. 1620–1627.

[2] Funck T., Spiegel T. (2017). AC – DC Disk Resistors Made of Surface Mount Components. *IEEE Trans. Instrum. Meas.,* vol. 66, no. 6, pp. 1454–1458.

[3] Ouameur M., Ziadé F., Le Bihan Y. (2018). Design and Modelling of a Shunt for Current Measurements at 10 A and up to 1 MHz: a theoretical approach. *CPEM 2018 Conf. Digest*, no. 1, pp. 0–1.

[4] Filipski P.S., Boecker M. (2006). AC-DC current shunts and system for extended current and frequency ranges. *IEEE Trans. Instrum. Meas.,* vol. 55, no. 4, pp. 1222–1227.

[5] Malinowski M., Kampik M., Grzenik M., Kubiczek K. and Dudzik K. (2020). A Wideband Current Shunt. *2020 Conference on Precision Electromagnetic Measurements (CPEM)*, Denver, CO, USA, pp. 1-2.

[6] Malinowski M., Kubiczek K., Kampik M. (2021). A precision coaxial current shunt for current AC-DC transfer. *Measurement*, vol. 176, 109126.

[7] Malinowski M., Kampik M., Musioł K. (2020). Software for automation of measurements with Keysight E4980A LCR meter. *Measurement systems in research and in industry. 13th Scientific conference*, Zielona Góra.

[8] Vishay Precision Group Inc. (2020). *Ultra High Precision Foil Wraparound Surface Mount Chip Resistor Datasheet 4128-EN. Rev. 04-Mar-2020.*

# Use of a Virtual Instrument for Measurements of Direct Voltages in the Presence of Interferences

**[1]Przemysław Otomański, [2]Eligiusz Pawłowski, [3]Anna Szlachta**

[1]Poznan University of Technology, Institute of Electrical Engineering and Electronics, Piotrowo street 3A, 60-965 Poznań, Poland,
[2] Lublin University of Technology, Faculty of Electrical Engineering and Computer Science, Nadbystrzycka street 38A, 20-618 Lublin, Poland,
[3]Rzeszow University of Technology, Department of Metrology and Measurement Systems, W. Pola street 2, Rzeszow, 35-959, Poland
Email: przemyslaw.otomanski@put.poznan.pl

***Abstract.*** *The paper discusses the topic of measurement of direct voltages in the presence of strong electromagnetic interferences. It presents a suitable measuring system, a virtual measuring instrument created in the LabVIEW environment, and the results of tests carried out, such as NI PCI-6221 data acquisition board. The described approach can also be applied in other measurement situations.*

*Keywords: Probability Distribution, Virtual Instrument, Electromagnetic Interference*

## 1. Introduction

In industrial conditions, measuring systems can be exposed to various interferences. Interferences that infiltrate into the measuring system are the source of additional measurement errors, which increase the uncertainties of the final measurement result. Interferences may infiltrate into the measuring system by conduction, capacitive and magnetic coupling, and an electromagnetic wave. Conducted interferences occur in systems in which the measuring circuit's ground points that are distant from each other have different potentials. This causes a flow of equalizing currents in the ground conductors, and the formation of additional voltage decreases that sum up with the signal being measured. Interferences infiltrating through magnetic coupling occur when a conductor conducting alternating current is near the measuring system forming a closed loop. An alternating magnetic field is formed around such a conductor, and infiltrating into the measuring circuit, it induces a current being a source of errors. This effect is compounded if there are ferromagnetic components nearby, which form a magnetic circuit increasing this impact. Infiltration of interferences through an electromagnetic wave occurs when an appliance is a source of radio waves near the measuring system. The conductive components of the measuring system act as antennae, in which currents being the source of measurement errors are induced.

## 2. Experimental Research

The diagram of the measuring system applied in the tests is presented in Fig. 1. It is composed of a personal computer (PC) with an installed PCI 6221 data acquisition board by National Instruments and with the LabVIEW environment, of a stable source of reference voltage $V_{REF}$, and of a ferromagnetic core *FC* ensuring the magnetic coupling of the measuring circuit with the source of interferences being the L-N-PE line powering the computer. The PC is powered from the 230 V 50 Hz grid through a system that ensures a magnetic coupling with the measuring circuit. The L-N powering conductors are coiled on the toroidal ferromagnetic core *FC* so that the created magnetic fluxes sum up. A conductor being a component of the measuring system, can be passed through the opening in the *FC*. The current powering the computer contains a range of higher harmonics being a source of strong interferences, which infiltrate into the measuring system through magnetic coupling in the form of interference voltage $V_{NOISE}$. The data acquisition board is connected to the computer via the PCI bus. A source of stable reference voltage $V_{REF}$=+5V was connected to the AI0 analog input of the board. Measurements with a low level of interferences require placing the conductors that form the measuring circuit at least 1 m away from the conductors that power the computer. Measurements with a high level of interferences are achieved by passing the measuring circuit conductor through the opening in the *FC*. This causes an increase in the level of interferences in the form of a circa 300-times increase in the type A uncertainty.

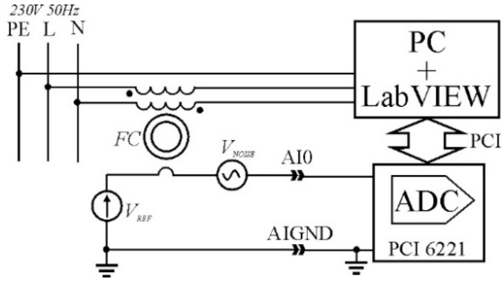


Fig. 1. Diagram of the measuring system applied in the tests.

## 3. Uncertainty of Measurement

The cause of the uncertainty of measurement result is that we do not know the exact value of the measurand [1]. This is because the results obtained in the process of direct measurement reveal errors in both the uncertainties of type A, which are the result of random effects and the uncertainties of type B, caused by systematic effects. According to the recommendations of an international document [1], the following notations and symbols will be adopted, corresponding to the parameters of probability distributions:

- standard uncertainty of type A, calculated on the basis of observed scatter of the results of a series of measurements, which is equal to the estimator of the standard deviation for average:

$$u_A = \sqrt{\frac{1}{n(n-1)}\sum_{i=1}^{n}(x_i - \bar{x})^2} = \bar{S}_{\bar{x}} \tag{1}$$

- standard uncertainty of type B, equal to the standard deviation of the assumed distribution of apparatus errors. With the assumption that the apparatus errors have rectangular distribution within the limits of maximum error $\pm\Delta_g$ :

$$u_B = \frac{\Delta_g}{\sqrt{3}} = \sigma_J \tag{2}$$

- combined standard uncertainty for a directly measured value, when the standard uncertainties of type A and type B are taken into consideration:

$$u_c = \sqrt{u_A^2 + u_B^2} \tag{3}$$

- expanded uncertainty:

$$U = k(\alpha)\cdot u_c \tag{4}$$

- $k(\alpha)$ is the coverage factor corresponding to the standardized variable of a given distribution.

## 4. *Virtual Instrument*

In practice, virtual measuring instruments are often used for determining the value of measurement errors. Examples of such instruments are presented in the papers [2, 3, 4]. To determine errors and uncertainties of measurements in the system shown in Fig. 1, a virtual instrument was prepared in the LabVIEW environment, the front panel of which is presented in Fig. 2. The created application enables measurements of direct voltage in a series of a preset number $n$ of samples, calculates the average value $\bar{x}$, the measurement uncertainties $u_A$, $u_B$, $u_c$, $U$, the board's maximum error $\Delta_g$ and performs additional statistical analysis of results [5]. Configuration parameters of the data acquisition board are indicated in the upper part of the panel. Actual values of the completed measurements are indicated in the middle part of the panel on the left side. Next to them, on the right side, the series of measurements used at the moment for averaging and determining all the other parameters is indicated. In the right window, average values of successive series of measurements are marked red in the chart, the range with the width of $\pm U$ is marked purple, and the range with the width of $\pm 3\sigma$ is marked blue.

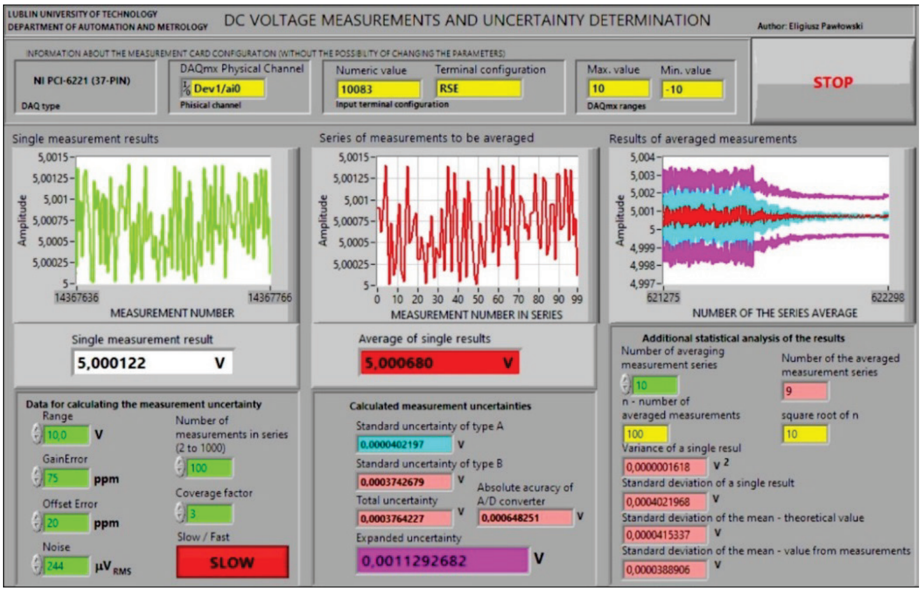


Fig. 2. The panel of the virtual instrument prepared for the purposes of tests.

The data enabling the calculation of the measurement uncertainties are entered to the software in the left bottom part of the panel in the green windows. The calculation results are indicated next to them in the middle part of the panel: average value (red field), the uncertainty of type A (blue field), the uncertainty of type B, combined uncertainty and maximum error of the ADC (pink colour) and expanded uncertainty (purple colour). The right part of the panel contains a chart presenting averaged results of measurements from successive series and additional statistical analysis of the results. The number of measurement series $N$, which will be subject to additional analysis, can be entered in the green field. Above all, the standard deviation for a single result $s(x_i)$ and the standard deviation of the average value $s(\bar{x})$ from successive measurement series are calculated. Theoretically, the ratio of these two values should be equal to the root of $n$ of the averaged measurements [6]. The software makes it possible to verify this theoretical correlation based on measurements carried out in an actual system.

## 5. Results

Measurements were carried out with a low and a high level of interferences, each time for an increased number of measurements in the series with $n = 2, 5, 10, 20, 50, 100, 200, 500, 1000$. For each completed series of measurements, the software calculated type A uncertainty, type B uncertainty and expanded uncertainty $U$. The obtained results are presented in charts in Fig. 3. In the case of measurements with a low level of interferences (Fig. 3a) and a low $n$ value, type B uncertainty prevails but type A uncertainty is slightly lower, and its value is similar. However, type A uncertainty decreases much faster in line with the increase in $n$ and constitutes merely circa 4% of type B uncertainty for $n$=1000. At the same time, however, expanded uncertainty $U$ virtually does not change already for $n$≥200, so series of measurements that are longer than 200 measurements does not have a metrological justification. In the case of measurements with a high level of interferences (Fig. 3b), expanded uncertainty $U$ increased circa 100-times. Type A uncertainty prevails in these measurements, and it is higher than type B uncertainty for low $n$ by two orders of magnitude. This discrepancy decreases for higher $n$ values but even for $n$=1000, type A uncertainty is higher than type B uncertainty by one order of magnitude. All uncertainties decrease in line with the increase in $n$ and even with the change from $n$=500 to 1000 expanded uncertainty $U$ decreases by 30% more. However, it is impossible to achieve an uncertainty that is comparable to the measurements with a low level of interferences.

a)

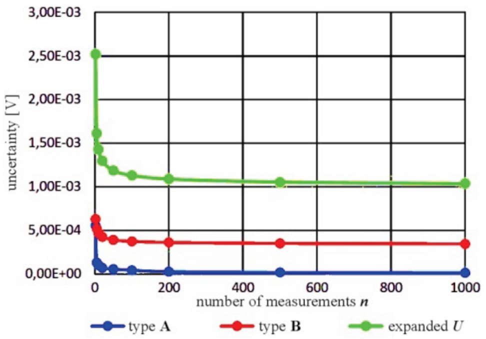


b)

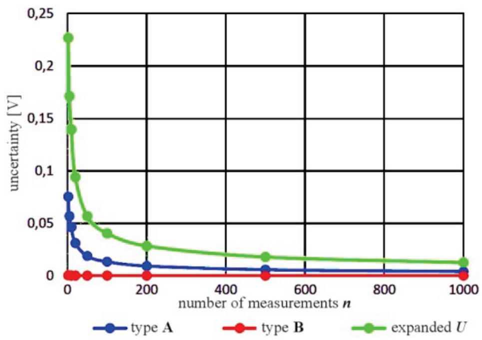


Fig. 3. Type A uncertainty (blue), type B uncertainty (red) and expanded uncertainty $U$ (green) as a function of the number of measurements $n$ in a series for a low level of interferences (a) and a high level of interferences (b).

## 6. Conclusions

The tests reveal that in the case of a low level of interferences, type B uncertainty, arising from the data acquisition board accuracy, is the primary component of expanded uncertainty $U$. Type A uncertainty is considerably lower, and the tests confirm that it decreases in line with the theoretical correlation in proportion to the root of $n$ of the averaged measurements, with series longer than $n$=200 not being justifiable. In the case of a high level of interferences, type A uncertainty becomes the primary component, while type B uncertainty remains virtually at the same level. In the case of a high level of interferences, an effective way to decrease uncertainty is also to increase the number of averaged measurements, even for $n$≥1000.

## References

[1] JCGM 100:2008 Evaluation of measurement data—Guide to the expression of uncertainty in measurement Joint Committee for Guides in Metrology.

[2] Otomański P., Szlachta A. (2008). The evaluation of expanded uncertainty of measurement results in direct measurements using the LabVIEW environment, *Measurement Science Review*, 8 (6), 147-150.

[3] Otomański P., Krawiecki Z., Odon A. (2010). The application of the LabVIEW environment to evaluate the accuracy of alternating voltage measurements, *Journal of Physics: Conference Series*, 238, 1-6.

[4] Pawłowski, E. (2017). Design and evaluation of a flow-to-frequency converter circuit with thermal feedback. *Measurement Science & Technology*, 28 (5), 054004-054013.

[5] Dorozhovets M., Szlachta A. (2020). Uncertainties of the estimators and parameters of distribution in measurements with multiply observations, *Measuring Technology and Metrology* ISTCMTM, 81 (4), 3-9.

# Combination of 3 Different Measurements: Branching Fractions, Radiative Lifetimes, and Absorption Oscillator Strengths- a Good Opportunity for the Analysis of the Presence of Elements in Astrophysical Objects

**Uldis Bērziņš**

[1]Institute of Atomic Physics and Spectroscopy, University of Latvia, Riga, Latvia,
[2]Nationa Science Platform “Fotonika”, University of Latvia, Latvia
Email: uldis.berzins@lu.lv

***Abstract.*** *We present the method and setup for determination and self-testing of atomic radiative constants: transition probabilities, oscillator strengths and natural lifetimes. We describe how it works in simple 4 level scheme, present our experimental setup, and preliminary results for As I branching fractions, and discuss some aspects of future development. This method can be valuable for analyzing the results from different experiments performed by various authors and methods without directly re-measuring them. For example, in astrophysics is very important to select correct oscillator strengths for evaluation element abundances in stars and interstellar media since inaccurate data lead to uncertainties in discrimination between different evaluation models.*

*Keywords: Atomic Spectra, Emission, Absorption, Lifetimes, Experimental Methods.*

## 1. Introduction

The applications which require accurate knowledge of oscillator strengths and lifetimes are the interpretation of astrophysical data, atmospheric physics, combustion, the modelling and diagnosis of thermonuclear plasmas, nonlinear optics, isotope separation and the development of new types of lasers. Precision measurements of oscillator strengths and lifetimes also provide stringent tests of atomic structure calculations. These quantities are very sensitive to the wave functions and the approximations used, particularly in cases where electron correlations and relativistic effects are significant. They provide experimental tests of fundamental theory, such as quantum electrodynamic corrections and the non-conservation of parity predicted. Despite the wide range of interests, only very few oscillator strengths and lifetimes are known for the highest accuracy. [1]

In astrophysics, the need for atomic line data from the ultraviolet (UV) to the infrared (IR) regions is greater now than ever. In the past twenty years, since the Hubble Space Telescope launch, significant progress has been made in acquiring atomic data for UV transitions. The optical wavelength region, now expanded by progress in detector technology, continues to motivate new atomic data. In addition, investments in new instrumentation for ground-based and space observatories have led to the availability of high-quality infrared spectra, where the need for atomic data is most critical. [2]

## 2. Subject and Methods

***The method*** where relative atomic oscillator strengths **f**, and transition probabilities **A** are measured in absorption and emission and combined in one set was already introduced by Ladenburg in 1933 [3]. The absolute scale was obtained from absorption data, and lifetime $\boldsymbol{\tau}$ was calculated as an inverse result from all transition probabilities for all lines from this excited state. This method is demonstrated in Fig. 1. In the atom with two excited levels, **u** and **v**, and two levels **l** and **i**, with ground electron configuration, only 4 transitions can

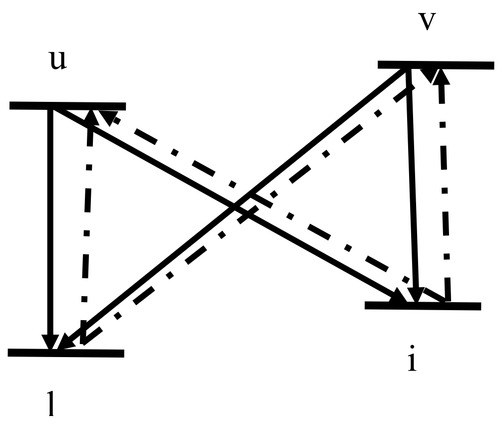


$f_{lu} = 1.5 \times (g_u/g_u)\ \lambda^2 A_{ul} \times 10^{-18}$
$\lambda$ is the wavelength in nanometers
$g_u$ and $g_l$ are the statistical weights

$A_{ul} + A_{ui} = 1/\ \tau_u$ lifetime measurement for **u**
$A_{vl} + A_{vi} = 1/\ \tau_v$ lifetime measurement for **v**
$A_{ul}\ /\ A_{ui}$ = branching factors for **u**
$A_{vl}\ /\ A_{vi}$ = branching factors for **v**
$A_{ul}\ /\ A_{vl}$ = absorption ratio for **l**
$A_{ui}\ /\ A_{vi}$ = absorption ratio for **i**

Fig. 1. 4 level scheme and the corresponding equations for the relative absorption and emission and lifetime measurements.

be observed in emission and absorption spectra. All equations between different transition probabilities oscillator strengths and lifetimes are given in frame on the right side. The first four equations describe the lifetime and branching fraction measurements. From them, four transition probabilities can be calculated. The last four equations describe the "bow ties" experiment, and four relative transition probabilities can be calculated. As a result, we have two independent systems of equations with two independent solutions for four transition probabilities. The solutions have to be the same for both systems. If it not so, then some of the experiment has not performed correctly. It is the internal test for the method.

Absorption measurements have been discontinued for the last few decades despite the available method developed and demonstrated on Ti II [4]. We have developed lifetime measurement techniques and applied them by using selective laser excitation on S I [5,6].

***Experimental sett-up***. We use the slightly modified setup from one used in our bow ties measurements for Te I [8]. The key element in our experiment is the source atomic spectral lines is radio frequency inductively coupled plasma (RF-ICP) discharge, see Fig. 2. The lamp bulb was placed inside the coil of the generator, and the plasma discharge was powered by 50 MHz frequency of RF generator with an external voltage supply. Both: a lamp and a generator are manufactured in our lab. The light from the (RF-ICP) lamp is collected on the entrance slit of monochromator SPM-2 (Carl-Zeiss Jena), allowing high spectral resolution in the 200-300 nm range. The application of this SPM-2 allows us to work using a reasonably opened slit in the case of very weak signals from the light source. Intensity of individual

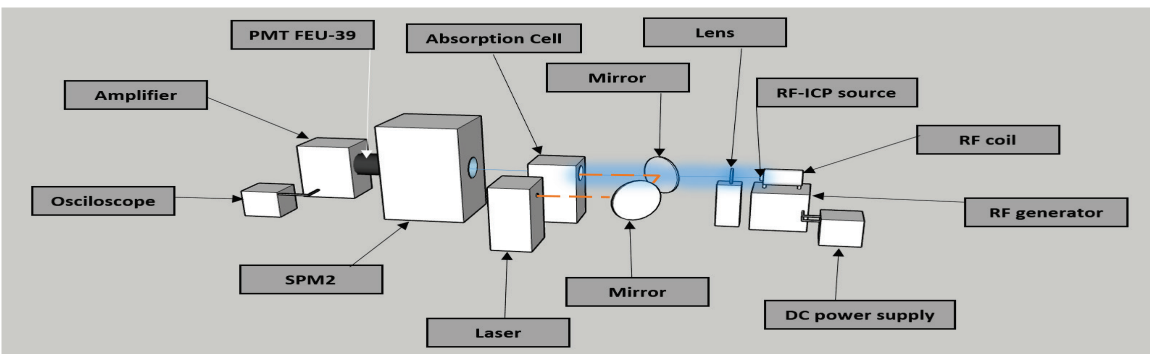


Fig. 2. Schematic of the experimental setup for emission and absorption measurements of relative oscillator strengths.

spectral lines was detected using photomultiplier tube PMT 39A attached at the exit slit of the monochromator. The photocurrent was amplified and measured using the voltmeter. The calibration of the spectral response of this system was performed using both: a hydrogen lamp and a deuterium lamp. The calibration error has estimated not to exceed 15% in area 190-300 nm. The above described part is used for branching ratio measurements.

For absorption measurements, the equipment is supplemented with an absorption cell, which is placed in between SPM-2 and RF-ICP source. The absorption cell is placed in a furnace as many elements need to be heated up to reach the concentrations of atoms or molecules required for absorption. For the population of the atomic metastable states with the ground electron configuration, the photo-dissociation of molecules rather than heating gives more relevant results. Excimer laser 248 nm pulse can be sent into absorption cell

with the help of special mirror coated for 248 nm reflection at 45-degree angle. If absorption for metastable states is investigated in pulse mode, the records must be performed on oscilloscope in few milisecond time frame.

## 3. Results and Discussion

We have demonstrated experimental setup for bow ties measurements in UV spectral region. And we are presenting the branching fraction measurements for 21 As I spectral line between 7 levels of $4p^25s$ electron configuration and 5 levels of ground $4p^3$ electron configuration.

Tab.1 Branching fractions for Arsenic $4p^25s$-$4p^3$ transitions

| Transition | Λ, nm | Our data | [8] | [9] DV | [9] DL |
|---|---|---|---|---|---|
| $^4P_{1/2}$ -$^4S^o_{3/2}$ | 197.262 | 0.94 (1)* | 0.907 | 0.904 | 0.939 |
| -$^2D^o_{3/2}$ | 249.294 | 0.057 (6) | 0.0538 | 0.0815 | 0.0552 |
| -$^2P^o_{1/2}$ | 307.531 | 0.0016 (2) | 0.0342 | 0.00831 | 0.00208 |
| -$^2P^o_{3/2}$ | 311.959 | 0.0024 (3) | 0.0049 | 0.00676 | 0.00330 |
| $^4P_{3/2}$ -$^4S^o_{3/2}$ | 193.759 | 0.94 (1) | 0.941 | 0.926 | 0.950 |
| -$^2D^o_{3/2}$ | 243.723 | 0.010 (1) | 0.00722 | 0.00893 | 0.00892 |
| -$^2D^o_{5/2}$ | 245.653 | 0.043 (5) | 0.0314 | 0.0488 | 0.0346 |
| -$^2P^o_{1/2}$ | 299.098 | 0.00093 (10) | 0.0046 | 0.00297 | 0.00132 |
| -$^2P^o_{3/2}$ | 303.285 | 0.0039 (4) | 0.015 | 0.0136 | 0.00460 |
| $^4P_{5/2}$ -$^4S^o_{3/2}$ | 189.043 | 0.98 (1) | 0.985 | 0.975 | 0.977 |
| -$^2D^o_{3/2}$ | 236.304 | 0.00077 (15) | 0.00077 | 0.00109 | 0.000742 |
| -$^2D^o_{5/2}$ | 238.118 | 0.020 (2) | 0.013 | 0.0236 | 0.0222 |
| -$^2P^o_{3/2}$ | 291.882 | 0.00005 (1) | . | 0.000082 | 0.000028 |
| $^2P_{1/2}$ -$^4S^o_{3/2}$ | 188.196 | 0.015 (5) | 0.025 | 0.0057 | 0.0142 |
| -$^2D^o_{3/2}$ | 234.984 | 0.87 (4) | 0.804 | 0.757 | 0.816 |
| -$^2P^o_{1/2}$ | 286.043 | 0.095 (10) | 0.143 | 0.197 | 0.145 |
| -$^2P^o_{3/2}$ | 289.870 | 0.017 (3) | 0.0275 | 0.0403 | 0.0260 |
| $^2P_{3/2}$ -$^4S^o_{3/2}$ | 183.174 | 0.011 (3) | 0.0164 | 0.00305 | 0.00984 |
| -$^2D^o_{3/2}$ | 227.136 | 0.0051 (5) | 0.00342 | 0.00104 | 0.00157 |
| -$^2D^o_{5/2}$ | 228.812 | 0.79 (4) | 0.684 | 0.627 | 0.718 |
| -$^2P^o_{1/2}$ | 274.500 | 0.046 (5) | 0.059 | 0.0815 | 0.0679 |
| -$^2P^o_{3/2}$ | 278.022 | 0.15(2) | 0.236 | 0.260 | 0.204 |
| $^2D_{5/2}$ -$^4S^o_{3/2}$ | 164.432 | /0.0053/ | | 0.00430 | 0.00664 |
| -$^2D^o_{3/2}$ | 199.113 | 0.11(2) | 0.090 | 0.1046 | 0.0973 |
| -$^2D^o_{5/2}$ | 200.335 | 0.79 (6) | 0.813 | 0.716 | 0.765 |
| -$^2P^o_{3/2}$ | 237.077 | 0.10 (1) | 0.0964 | 0.175 | 0.133 |
| $^2D_{3/2}$ -$^4S^o_{3/2}$ | 164.379 | /0.0013/ | | 0.00086 | 0.00171 |
| -$^2D^o_{3/2}$ | 199.035 | 0.78 (4) | 0.778 | 0.632 | 0.686 |

| | | | | | |
|---|---|---|---|---|---|
| $-^2D^o_{5/2}$ | 200.255 | 0.016 (2) | 0.142 | 0.00921 | 0.0172 |
| $-^2P^o_{1/2}$ | 234.402 | 0.061 (7) | 0.0668 | 0.134 | 0.110 |
| $-^2P^o_{3/2}$ | 236.966 | 0.14 (2) | 0.141 | 0.225 | 0.186 |

* 0.94 (1) means 0.94 ± 0.01

There is difference in between branching fraction data especially to the higher metastable states $4p^3\ ^2P^o_{1/2}$ and $^2P^o_{3/2}$. Two independent lifetime measurements has been performed for As I $4p^25s$ excited states with beam foil [10] and laser [11] excitation. We see that absorption measurements and realization of ”bow ties” could give us more clearance in oscillator strengths and lifetime data for neutral arsenic.

**Acknowledgements**

This work was supported by ERDF project No. 1.1.1.5/19/A/003.

**References**

[1] Curtis L. J., (1996), Precision Oscillator Strength and Lifetime Measurements, *in Atomic, Molecular, & Optical Physics Handbook*, edited by G. W. F. Drake, AIP Press, New York p 261-268

[2] Wahlgren, G. M. (2011). Atomic data for stellar astrophysics: from the UV to the IR, Canadian Journal of Physics, 89(4), 345–356. doi:10.1139/p10-125

[3] Ladenburg R., (1933) Dispersion in Electrically Excited Gases Rev.Mod.Phys. **5**, 243-256

[4] Whallgreen G.M., (2010), Oscilator strengths and their uncertainties, in: Non-LTE Line Formation for Trace Elements in Stellar Atmospheres, R. Monier, B. Smalley, G. Wahlgren and Ph. Steel (eds) EAS Publications Series, **43** 91-114

[5] Berzinsh U., Caiyan L., Zerne R.,Svanberg S., Biémont E., (1997) Determination of radiative lifetimes of neutral sulfur by time-resolved vacuum-ultraviolet laser spectroscopy, Phys. Rev. **A 55,** 1836-.

[6] Zerne R., Caiyan L., Berzinsh U., S Svanberg S., (1997), Oscillator strengths of sulphur 3s23p34s $3S^o$-$3s^23p^34p\ ^3P$ transitions measured by time resolved two-photon laser spectroscopy, Physica Scripta **56**, 459-,

[7] Ubelis A.P., Berzinsh U.V., (1983), Transition probability measurements of Te I spectral lines by methods of emission and absorption of radiation Physica Scripta 28 (2), 171-,

[8] Lotrian J., Guern Y., Cariou J., (1980), Experimentally determined transition probabilities of the system $4p^3$ to $4p^25s$ of neutral arsenic. J. Phys. B 13, 685-

[9] Holmgreen L., (1975), Theoretically calculated transition probabilities and lifetimes for the first excited configuration $4p^25s$ in the neutral As, Sb, and Bi atoms. Phys Scr. **11**, 15-

[10] T. Andersen, S. Worre Jørgensen, and G. Sørensen, (1974), Radiative lifetimes of As I and Sb I, JOSA, 64, 891-892.

[11] Bengtsson G.J., Berzinsh U., Larsson J, Svanberg S., (1992), Determination of radiative lifetimes in neutral arsenic using time-resolved laser spectroscopy in the VUV region, Astronomy and Astrophysics 263, 440-44.

# *Measurement of Physical Quantities III*

# Potentially Achievable Levels of Lateral Radiation of an Equal-Amplitude Nonuniformly-Filled Array

**[1]Aleksandr Ostankov, [2]Kaung Myat San, [2,3,4]Oleg Chernoyarov, [5]Serguei Pergamenchtchikov**

[1]Voronezh State Technical University, Voronezh, Russia,
[2]National Research University "MPEI", Moscow, Russia,
[3]National Research Tomsk State University, Tomsk, Russia,
[4]Maikop State Technological University, Maikop, Russia,
[5]University of Rouen, Rouen, France,
Email: chernoyarovov@mpei.ru

***Abstract.*** *The task of minimizing the lateral radiation level of a linear uniform amplitude array with a uniform amplitude distribution using the space-tapered allocation of its elements is considered. It is demonstrated that the use of the evolutionary method of parametric optimization makes it possible to find the coordinates of isotropic elements of the array providing the minimum values of the maximum level of the side lobes in the radiation pattern. The search for the different values of the number of elements as well as for the length of the array is performed. The dependences of the potentially attainable side lobe level upon the number of array elements are obtained for the different values of the array sparseness.*

*Keywords: Nonuniformly-Filled Array, Sparseness, Optimization, Lateral Radiation, Side Lobe Level, Beam Expansion Factor*

## 1. Introduction

Increasing the directivity of the antenna array by reducing the lateral radiation level is an urgent task of antenna technology since it can lead to the improved noise immunity of the radio system. With a decrease in the side lobe level (SLL) of the directional pattern with respect to the main beam, the antenna becomes less sensitive to the interferences arriving in directions outside the main beam of the directional pattern. Reducing the level of interferences, in turn, helps to increase the radio system capacity.

The drop of the side lobes of the directional pattern in the case when the width of the main beam is specified can be achieved not only by implementing a special amplitude distribution over the uniformly-spaced array mouth, but also by the optimal allocation of the elements within a nonuniformly-filled array [1]. Of particular interest is the SLL minimization under a uniform amplitude distribution of the field over the array mouth, that is, when the array includes the emitter elements with the same gain, and the variation of their gain is extremely undesirable. The task of minimizing the lateral radiation of arrays by means of space-tapered allocation of elements has been considered in many studies (see, for example, [2], [3]). Most of the researches focus on the new algorithms or their high-speed modifications designed to optimize the directional pattern of nonuniformly-filled arrays. At the same time, there are very little data in the prominent papers on the limit values of the lateral radiation levels of nonuniformly-filled arrays, including those with an equal-amplitude field distribution over the mouth.

The purpose of the paper is to find the minimum possible values for the maximum levels of the side lobes of the linear nonuniformly-filled array directional pattern for the case when the number of the isotropic elements of such array varies as well as its length. At the same time, the amplitude field distribution over the mouth remains uniform.

## 2. The Problem Statement and Mathematical Formalization

One begins with presupposing that the elements of the linear array are isotropic and the total number of array elements is equal to $N$. The space between $k$-th and $(k+1)$ -th elements is assumed to be equal to $d_k$ (Fig. 1). Then the coordinate of the $k$-th array element is determined as

$$x_k = \sum_{i=1}^{k-1} d_i , \qquad k = \overline{1, N} . \tag{1}$$

In addition, one considers that the elements are allocated strictly symmetrically relative to the array center. Under this condition, the ranges between the emitters with the numbers $k = N/2+1, \ldots, N-1$ allocated to the right of the array center are identical to the ranges between the emitters with the numbers $k = 1, \ldots, N/2-1$ allocated to the left of the center (Fig. 1) so that

$$d_k = d_{N-k} , \qquad k = \overline{1, N/2-1} .$$

The minimum range between elements is limited by the initially set value $d_{\min}$. The limitation of the ranges $d_k$ is related to the need for the technical implementation of the power supply circuit of the elements, as well as for the reduction of the electromagnetic interaction of the elements.

Let the array length be fixed and equal to $L = \mu\lambda(N-1)$, where μ is a specified array sparseness coefficient that is equal to the ratio of the spacing $d_e$ of the uniformly-spaced array of the same length $L = d_e(N-1)$ to the wavelength λ.

The unknown quantities are the ranges $d_k$, $k = \overline{1, N/2}$ between the elements of the array. It should be noted that only such ranges as $d_k$, $k = \overline{1, N/2}$ satisfy the solution of the task under which the maximum SLL of the amplitude directional pattern of the array takes a minimum value.

Since the emitting elements of the array are isotropic, then, to calculate the complex directional pattern of the array $f(\Theta)$, the following formula for the array factor should be applied [1]:

$$f(\Theta) = \sum_{k=1}^{N} A_k \exp(-j\Phi_k)\exp(jkx_k \sin\Theta). \tag{2}$$

It is considered that the emission wavelength λ is set and determines the wave number of the free space $k = 2\pi/\lambda$. The observation angle Θ is measured from the normal to the array mouth clockwise (Fig. 1). The amplitude and phase field distributions over the mouth are uniform so that the amplitudes $A_k$ and the initial phases $\Phi_k$ of the currents (fields) at any of the $k$-th array element are the same ( $A_k = A$, $\Phi_k = \Phi$ ).

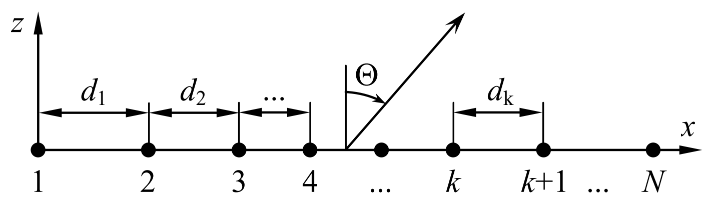


Fig. 1. Model geometry of the nonuniformly-filled array.

As an objective function, the minimum of which must be achieved during optimization, the dependence of the maximum level of the side lobes of the normalized directional pattern in dB upon the ranges $d_k$ between the array elements is taken. When calculating the current value of the objective function, the coordinates of the array elements are determined according to (1), and then the complex directional pattern $f(\Theta)$ of the array is calculated using (2). At the next step, the amplitude directional pattern $|f(\Theta)|$ is determined and then normalized ($F(\Theta) = |f(\Theta)| / \max|f(\Theta)|$). The maximum SLL $\xi$ is determined in dB by the normalized amplitude directional pattern $F(\Theta)$.

It is important that in the process of searching for the desired ranges $d_k$ that provide the minimum value of the maximum SLL, the values $x_k$ of the coordinates of the elements do not go beyond the limits of the physically realizable values. For this purpose, a penalty function of the exponential type is introduced. If the coordinate of any element leaves the area of the positive values or exceeds the array length, then the penalty function takes a positive value and it is the greater the more the coordinate is deviating from the realizable values. In a similar way, the restriction on the minimum value $d_{\min}$ for the ranges $d_k$ ($d_{\min} \le d_k$) is imposed. The final objective function is formed, taking into account the penalty functions. During the numerical implementation of the parametric optimization, a modification of the genetic algorithm is used, as it provides a confirmed efficiency in solving optimization problems involving a large number of variables [4].

## 3. The Results of the Problem Solution

Below there are presented the minimum values of the maximum SLL of the directional pattern for the nonuniformly-filled arrays with the different values of the sparseness coefficient ($\mu = 0.5, 0.6, 0.7$) and the number of elements ($N = 4, 6, \ldots, 20$) obtained as a result of the numerical optimization under the minimum range between the emitters set equal to $d_{\min} = \lambda/4$.

In Fig. 2, one can see the found minimum values of the maximum SLL $\xi$ in dB provided by the optimization of the allocation of the array elements. These values are presented as a family of dependences upon the number *N* of elements. The dashed line shows the dependence of the maximum SLL upon *N* for the case of a uniformly-spaced array. It follows from Fig. 2 that the gain in the level of lateral radiation due to the nonuniform allocation of elements increases with their number *N*, and it becomes even greater the lower is the sparseness coefficient $\mu$. In particular, if $N = 10$, then the gain is 4.7 dB (for $\mu = 0.7$), 6.0 dB (for $\mu = 0.6$) and 6.7 dB (for $\mu = 0.5$), while if $N = 20$, then one gets 6.6, 8.9 and 10.5 dB, respectively. It should be noted that the obtained dependences $\xi(N)$ generally have an oscillating form, and the larger is the array sparseness, the smaller is the characteristic oscillation interval of $\xi(N)$.

It is revealed that when minimizing the lateral radiation of the nonuniformly-filled array, the main beam of its directional pattern expands in comparison with the directional pattern of a uniformly-spaced array of equal length. The relative values of the expansion coefficient of the directional pattern main beam ($K_{\text{eb}}$) determined by the "minus" 3 dB level, while the arrays are optimized by minimizing SLL, are shown in Fig. 3. It follows from Fig. 3 that the more elements are included in the array and, accordingly, the greater is the gain in SLL, the greater does appear the expansion of the main beam. However, for all the cases that are considered in our study ($\mu \geq 0.5$, $N \leq 20$), the value of $K_{\text{eb}}$ does not exceed 13%, as it can be seen from Fig. 3.

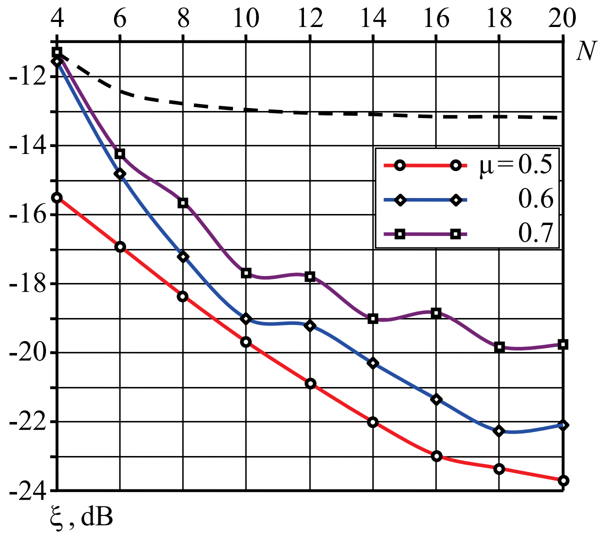


Fig. 2. Potentially attainable levels of lateral radiation of the equal-amplitude non-uniformly-filled array with $d_{\min} = \lambda/4$ and different degrees of sparseness.

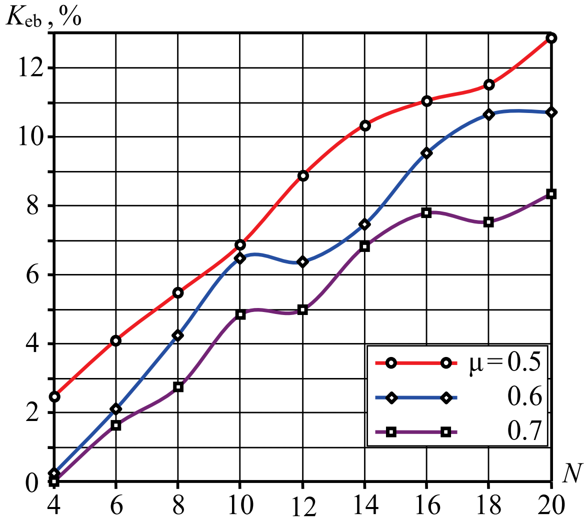


Fig. 3. Expansion coefficient of the directional pattern main beam of the nonuniformly-filled array with a potentially attainable level of lateral radiation.

It is also important that the value of $K_{\text{eb}}$ can be reduced by introducing an additional restrictive condition for the $d_k$ search. And that would obviously lead to some increase in the minimum values of the maximum SLL.

## 4. Conclusion

Using the above results, for different values of the number of elements and the degree of sparseness, the maximum achievable levels of lateral radiation of a linear equal-amplitude nonuniformly-filled array can be found analytically. The obtained data can be used for potential estimation of the directional properties of the designed equal-amplitude arrays.

## Acknowledgements

This study was financially supported by the Ministry of Science and Higher Education of the Russian Federation (research project No. FSWF-2020-0022) as well as RFBR and CNRS (research project number 20-51-15001).

## References

[1] Hansen, R.S. (2009). *Phased Antenna Arrays*. Wiley.

[2] Fuchs, B.A., Skrivervik, J.R., Mosig, J.R. (2012). Synthesis of uniform amplitude focused beam arrays. *IEEE Antennas and Wireless Propagation Letters*, 11, 1178-1181.

[3] Saxena, P., Kothari, A. (2016). Optimal pattern synthesis of linear antenna array using grey wolf optimization algorithm. *International Journal of Antennas and Propagation*, 2016, 1-11.

[4] Chernoyarov, O.V., Salnikova, A.V., Kirpicheva, I.A., Ostankov, A.V. (2019). A simple method for increasing the equal-amplitude non-uniform linear thinned array directivity. In *5th International Conference on Frontiers of Signal Processing*. IEEE, 117-120.

# Minimalization of a TEM CELL

**Martin Mierka, Rene Hartansky**

Institute of Electrical Engineering, FEI STU, Bratislava, Slovakia,
Email: martin.mierka@stuba.sk

***Abstract.*** *Several papers have been published by the team of authors from the Institute of Electrical Engineering, FEI STU, about designing a TEM CELL for measuring purposes. In this paper, you can find a description of designing a TEM CELL for a specified frequency range based on the formulas specified in the middle 90's. Afterwards, it will be described how you can minimize the design if you need just one port and you have specified absolute dimensions of the object placed into the TEM CELL. The frequency-dependent results of CADFEKO simulations of VSWR and characteristic impedance can be found in this paper too.*

*Keywords: TEM CELL, EM Field Generator, MEMS Sensor Case*

## 1. Introduction

The TEM CELL is a device, which creates a homogeneous EM field inside of the TEM CELL. It can be used for measuring the EM properties of the object placed into the cell. In our case, we use a TEM CELL for measuring physical quantities (e.g. force, distance, pressure) by placing a MEMS structure into the cell. To design a suitable TEM CELL, we must define all necessary input values and criterion. After the first design and its simulation in CADFEKO, we continue with minimalization of TEM CELL by reshaping its box and microstrip.

## 2. Theoretical Design of a TEM CELL

Firstly, we need to inspect the MEMS structure and its characteristic properties. To assure non-connection of conductive parts between MEMS and conductive parts of TEM CELL, we have set adapted MEMS dimensions (real value with reserve) for the calculations (length

$l_{LC}$ = 60 mm, height $h_{LC}$ = 12,5 mm and width $w_{LC}$ = 6 mm). The working frequency of MEMS is from 115 MHz up to 155 MHz [1]. We decided to set the working frequency range of TEM CELL $f_{TC}$ from 100 MHz to 170 MHz (MEMS frequency range with reserve). The characteristic impedance of TEM CELL $Z_{TC}$ must be adapted to the characteristic impedance of feeder (in our case a voltage-controlled oscillator – VCO). Therefore we set the characteristic impedance of TEM CELL $Z_{TC}$ = 50 Ω.

All of the necessary values for the design are known, we can continue with the calculations of TEM CELL dimensions. TEM CELL consists of a box and a microstrip. The length of the microstrip is set by the designer (in our case $L = l_{LC}$ = 60 mm), but width is calculated. For calculation of the width dimension, we will use formula (1) (firstly presented in the US Patented paper – Transverse Electromagnetic Cell) [2]. In this formula, we can find value $b$, which represents the height and width of the box. The microstrip is in the middle of TEM CELL.

We are placing our MEMS structure on a plastic foil, which is placed directly on the microstrip. Therefore, the height of TEM CELL is twice the height of the MEMS structure ($b$ = 25 mm). The inside environment of TEM CELL is air, which relative permittivity is defined by $\varepsilon_r$ = 1,00054. Boundary capacity for a square-shaped TEM CELL is defined $C_f'$ = 0,087 pF/cm (1). The last value needed is the thickness of the microstrip. The easiest way to construct a microstrip is by CNC drilling into a printed circuit board (PCB). The thickness of the copper layer in PCB is $t = 35$ µm, and the thickness of cuprexide is $h_{PCB} = 1{,}4$ mm. Adding all necessary values into formula 1, we get the width of the microstrip.

$$w = \frac{\left(94{,}15 - Z_{TC} * \sqrt{\varepsilon_r} * \frac{C_f{}'}{0{,}0885 * \varepsilon_r}\right) * b * \left(1 - \frac{t}{b}\right)}{Z_{TC} * \sqrt{\varepsilon_r}} = 22{,}467\ mm \qquad (1)$$

Before we can construct our cell, we need to set some more dimensions. As we know, both ends of a TEM CELL have a pyramidal shape. The cell will be connected to the generator by an SMA cable. The width dimension of the top square of the pyramidal shape is defined by the SMA connector $w_{SMA} = 12{,}7$ mm. The height of this pyramidal shape is the same as the calculated width of microstrip $w = 22{,}467$ mm. The gap between the microstrip and the box is set to M = 1 mm.

The final device consists of TEM CELL and MEMS structure, which will be influenced by measured force. The microstrip must be stable without any movement. Therefore, we have decided to place under strip solid PVC material. The height of this material is defined by formula (2). The final dimensioned shape is presented in Fig. 1.

$$H_{PVC} = \frac{b}{2} - h_{DPS} = \frac{25 * 10^{-3}}{2} - 1{,}4 * 10^{-3}\ m = 11{,}1\ mm \qquad (2)$$

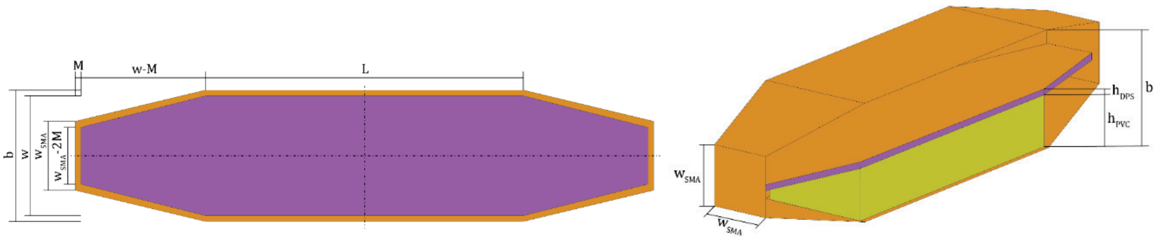


Fig. 1 Dimensioned shape of TEM CELL design no.1, left– top view of TEM CELL; right – side view of TEM CELL (purple – cuprexide, orange – copper, yellow – PVC).

After designing the shape, we can continue with the numerical simulation in CADFEKO environment. We will inspect the voltage standing wave ratio (VSWR) and characteristic impedance $Z_{TC}$ frequency dependence of TEM CELL. We will feed the cell from the port located on one side and to the port on the other side, we will place a resistant load. The load is defined by the characteristic impedance $Z_{TC}$ of the whole design $R_0 = 50\ \Omega$. The frequency range for the simulation was already mentioned, and it is $f_{TC} = 100 - 170$ MHz.

Based on the results of design 1, we can conclude that the designed shape has very good properties (see Fig. 5). The deviation in the characteristic impedance of TEM CELL is around 3 Ω, and the deviation in VSWR is around 0,07. These results tell us that the cell with designed dimensions is almost frequency independent in our frequency range.

This paper aims to design a TEM CELL with very similar properties but with extraordinary shape.

## 3. Minimalization of Symmetric TEM CELL

To minimalize the design, we need to find any possible optimizations. On one side of the TEM CELL, we are placing an SMA resistant load. If we solder at the end of the microstrip an SMD resistor, we don't need the whole pyramidal shape with an SMA connector on one side of the cell. We just need to add free space between the edge of TEM CELL and microstrip. The free space $M_{SMD}$ is defined by the dimensions of an SMD1206 package and some reserve to $M_{SMD} = 3$ mm.

Another minimalization can be done by lowering the microstrip from the middle position. It can be done by lowering the height of the solid PVC material. Firstly, we need to find out what is the maximal value $x$, that we can lower the height of PVC. In symmetric shape, we know that the SMA connector is placed directly in the middle of the pyramidal shape. The space between the bottom edge of the SMA connector and the bottom of TEM CELL is the maximal height $x$, that we can lower the PVC layer. It is defined by formula (3).

$$x = \frac{b - h_{SMA}}{2} = \frac{25 * 10^{-3} - 12{,}7 * 10^{-3}}{2} m = 6{,}15\, mm \tag{3}$$

Because we are lowering not only the PVC layer but also the height of TEM CELL, the minimized height $b$ is following:

$$b = 25 * 10^{-3} - 6{,}15 * 10^{-3}\, m = 18{,}85\, mm \tag{4}$$

We have changed the height of TEM CELL, but the space over the microstrip is still wide enough for inserting the MEMS structure. Because we have changed the $b$ parameter (height and width of TEM CELL), recalculating the width parameter of microstrip with formula (1) we get

$w = 16{,}93$ mm. The redesigned dimensioned shape can be found in Fig. 2. The results of the simulation of VSWR and $Z_{TC}$ dependence can be found in Fig. 5.

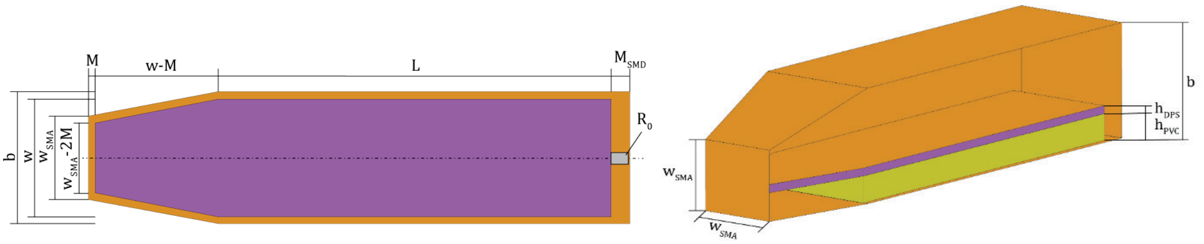


Fig. 2 Redesigned dimensioned shape of TEM CELL design no. 2; left– top view of TEM CELL; right – side view of TEM CELL (purple – cuprexide, orange – copper, yellow – PVC).

As we can see, the results are different comparing to the first design. The characteristic impedance is shifted higher for about 17 Ω, and the VSWR curve shape is more linear, however more distant from the ideal value ($VSWR = 1$). Based on this conclusion, we decided to reduce the value of resistor $R_0$ from 50 Ω to 33 Ω. The results of simulation no. 2 with 33 Ω load $R_0$ are presented in Fig. 5.

The results are still not appropriate comparing to the first symmetric design. To find out where are other possible options for minimalization, we decided to simulate the current distribution through the microstrip and the nearfield in TEM CELL.

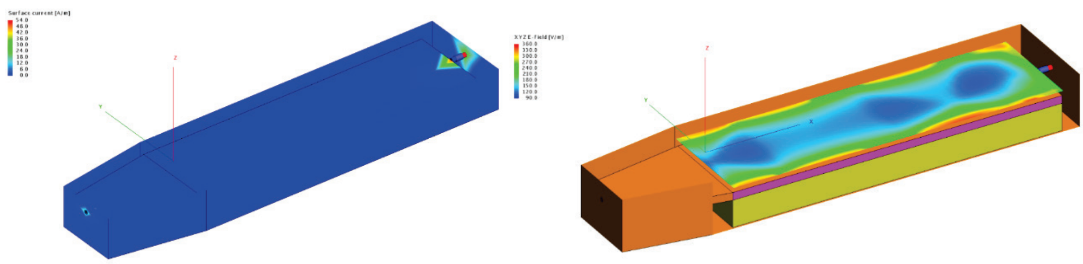

Fig. 3 Simulation of design no. 2 with changed load; left – current distribution in TEM CELL; right – nearfield 1 mm over the microstrip.

Based on the results, we decided to cut the microstrip into 5 different strips leaving the same width $w = 16{,}93$ mm. The boundary strips (1,5) are $W_{1,5} = 1$ mm wide, center strip (3) is $W_3 = 3$ mm wide and middle strips (2,4) are $w_{2,4} = 2$ mm wide. Gaps $M_P$ between strips are evenly distributed.

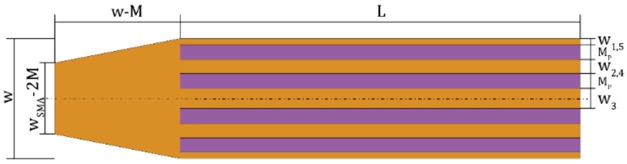


Fig. 4 Design of microstrip placed into TEM CELL, design no. 3.

To spread current into every strip, we need to place the load at the end of every strip without changing the 50 Ω characteristic impedance. Placing 5 separate SMD resistors at the ends of strips creates a parallel resistor connection (defined by formula (5). To spread current equally, we decided to set every load to the same value. By adjusting formula (5), we get the value for all 5 resistors $R_{1-5} = 250\ \Omega$ (6). As we can see in Fig. 5, the last design no. 3 has almost the same properties as the first one.

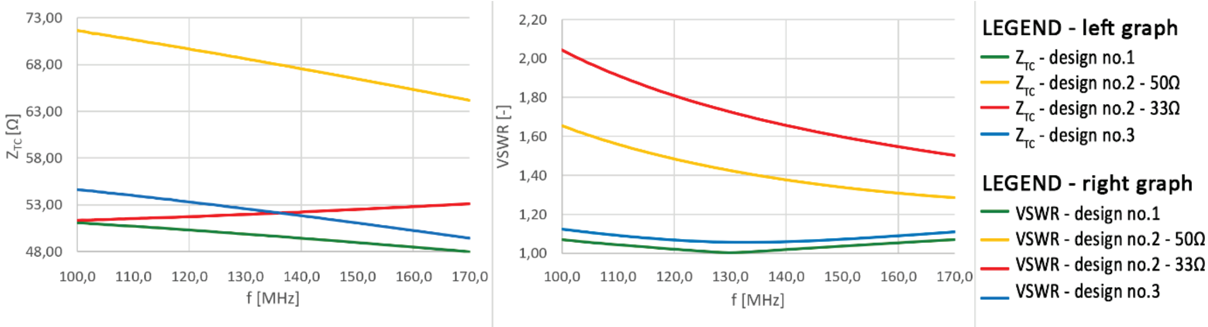


Fig. 5 Simulation results of characteristic impedance $Z_{TC}$ (left) and VSWR (right) of all TEM CELL designs.

$$R_0 = \frac{R_1 + R_2 + R_3 + R_4 + R_5}{5} \tag{5}$$

$$R_{1-5} = R_0 * 5 = 50 * 5 = 250\ \Omega \tag{6}$$

## 4. Conclusions

To create a competitive sensor for the industry segment, we need to follow current trends. One of them is minimalization with the preservation of previous characteristic properties. We created a final design with very common results by continuous adjustments, compared to the first design, which was created by a patented template. With the last design, our team will continue in research by constructing it and measuring its properties.

**Acknowledgement**

This work was supported by the projects APVV 14-0076 "MEMS structures based on load cell".

## References

[1] Harťanský, R, et al. (2020). MEMS Sensor of Force. *Russian Journal of Nonlinear Dynamics.* 16 (1), 87 - 94.

[2] Fischer, Joseph F. (1993). *Transverse electromagnetic cell. 5,436,603* USA.

# UHF DTV Antenna System diagnostics by radiation pattern measuring

[1]Jakub Krchnak, [2]Rene Hartansky, [3]Norbert Grilli

[1]MWTC s.r.o., S. Straku 46, 914 01 Trencianska Tepla, Slovakia
[2]FEI STU, Ilkovicova 3, 812 19 Bratislava, Slovakia
[3]Towercom, a.s., Cesta na Kamzík 14, 831 01 Bratislava, Slovakia
Email: mwtc@mwtc.tech

***Abstract.*** *The article deals with the new Large Antenna System (AS) diagnostics method at VHF / UHF range in the air during scattering from the AS. This method is based on comparing the calculated radiation pattern of AS, as an array of unified segments, in the fully functional state with the calculated radiation pattern of AS generated in a state of malfunction caused by faulty segments. Based on results, it is possible to determine a faulty segment by doing a single measurement of the horizontal radiation pattern of AS.*

*Keywords: Numerical Modeling, Large Antenna Systems Diagnostics, FEKO, Radiation Pattern.*

## 1. Introduction

Radiation pattern measurements of large antenna systems in VHF/UHF ranges are key measurements in determining a satisfactory functionality of said AS. These measurements can be performed in many ways. However, the most popular technique is the measurement using an aerial vehicle. A helicopter or a UAV (Unmanned aerial vehicle) is best suited for the successful accomplishment of necessary measurements. A few different flights have to be performed in order to determine a suitable distance and height for sufficient data collection. After conditions have been met, the horizontal and vertical flight patterns are performed to obtain data for determining horizontal and vertical radiation pattern. The minimum flight distance requirements have to be maintained. The minimum distance where AS appears as a single antenna is one such requirement. Therefore it is difficult to determine defective segments if AS consists of multiple segments. Another measurement has to be performed in order to determine faulty segments. Segments are methodically being turned off, and *VSWR(Voltage Standing Wave Ratio)* of AS is being measured to determine which segment is not working properly. This procedure is very time and resource consuming, given that the outage has to be planned in advance, and for the duration of the diagnostic measurement, the AS disconnected. This paper proposes a simplification of faulty segment diagnostics. By comparing a simulated radiation pattern with the one given by measurements, the faulty segment can be identified and subsequently replaced with a new one. This significantly lowers the time AS is in an outage state since this new diagnostic method can be performed while the AS is radiating and has to be outed only during maintenance.

## 2. Subject and Methods

*Segment evaluation*

Currently, most antenna systems are consisting of a number of unified segments, creating an antenna array. These segments are supplied in a way to create a desired radiation pattern of the system. Chosen UHF DTV antenna system is consisting of vertically polarised sector antennas designed specifically for this use. Every segment has to meet the requirements set by technical documentation for an array to work correctly. Evaluation of these segments is key for proper simulation in the simulation tool. Few measurements have been performed to set the basis for the simulation model and verify parameters stated in technical documentation. Measurements of impedance and *VSWR* have been performed in an outside environment. Measurements of radiation pattern have been performed in a semi-anechoic chamber.

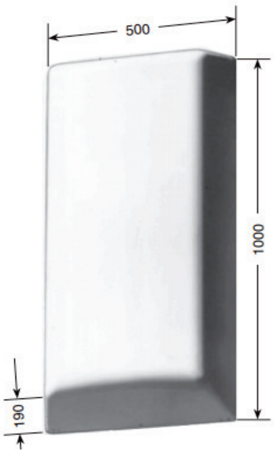


Fig. 1. Sector antenna as a single segment [1].

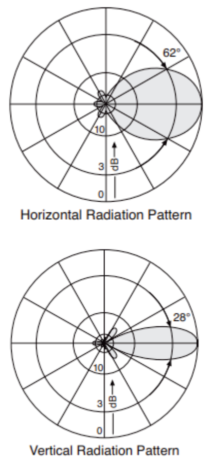


Fig. 2. Horizontal and vertical radiation pattern of the segment at mid band [1].

*Evaluated Antenna System*

Antenna System chosen for evaluation consists of twelve segments mentioned above. Segments are connected via a phased feeder line and mounted on a column in sets of fours, called bays, in such a way that they cover four sectors - effectively creating an all directional AS.

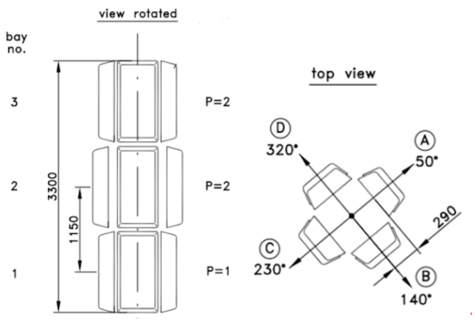


Fig. 3. Position of segments on AS [1].

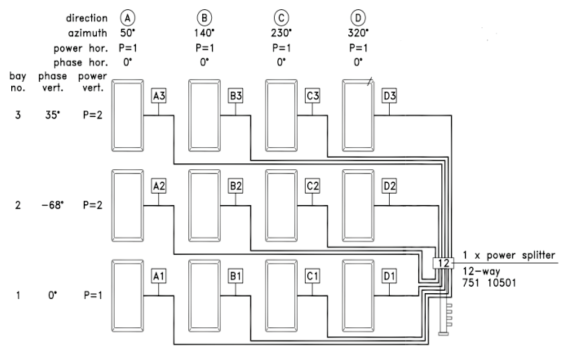


Fig. 4. Phase and amplitude distribution among segments [1].

As we can see in Figure 3, segments in a bay are supplied by signal of the same amplitude and phase, however, different bays differ in phase and amplitude amongst each bay. This accomplishes desired radiation pattern of the AS as a whole.

*Simulation and Diagnostics*

In this section, we will try to describe a simulation of the radiation pattern of chosen AS. The simulation tool used in this article is the licenced 32-bit version Altair FEKO. It is a software suite intended for the analysis of a wide range of electromagnetic problems, mainly antennas, using Method of Moments (MOM). During simulation, we will rely on the fact that any change in segment configuration, physical or electrical, will result in a change of radiation pattern of the array. First, a fully functional system of unified segments was simulated. To simulate a segment failure, the phased 3D model of the segment in AS was left out, and results were evaluated to detect any changes in the radiation pattern of the AS.

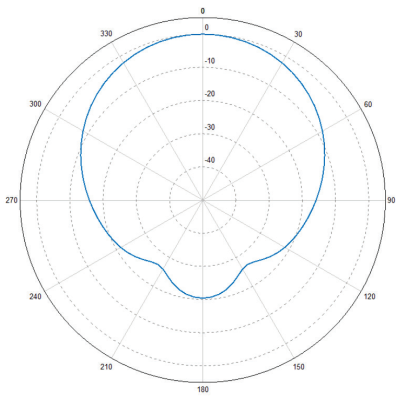

Fig. 5. Horizontal pattern of the unified segment.

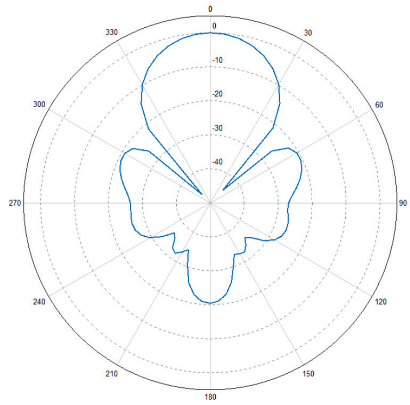

Fig. 6. Vertical pattern of the unified segment.

The unified segment has been simulated at a frequency of 506 MHz, as it is one of the suggested operating frequencies of the AS. With the data from the simulation, the AS was designed accordingly to the topology described in *Fig 3* and *Fig* 4, so the behaviour of a fully functional system can be observed. Once the radiation pattern of fully functional AS has been obtained to use as a reference, segments can be turned off to simulate a failure.

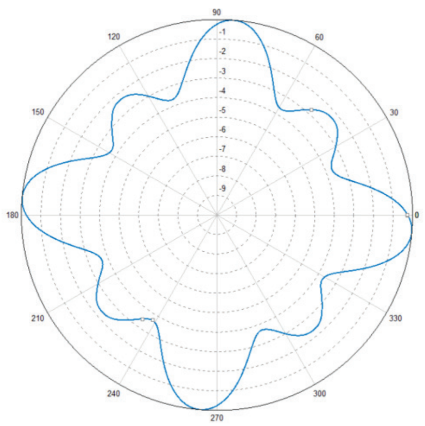

Fig. 7. Radiation pattern of fully functional antenna system.

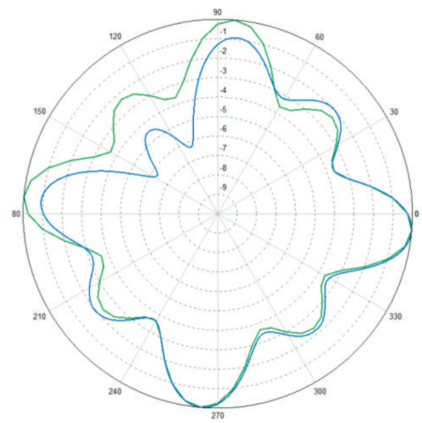

Fig. 8. Radiation pattern of antenna system with faulty segment D1.

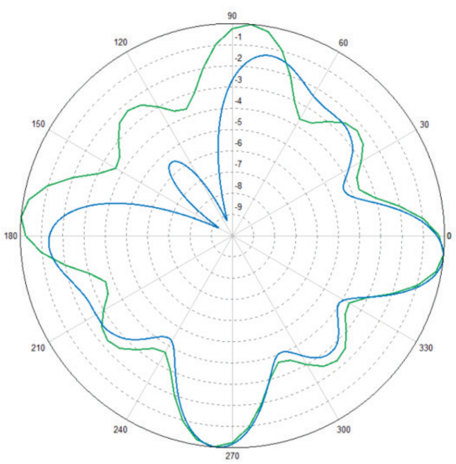

Fig. 9. Radiation pattern of antenna system with faulty segment D2.

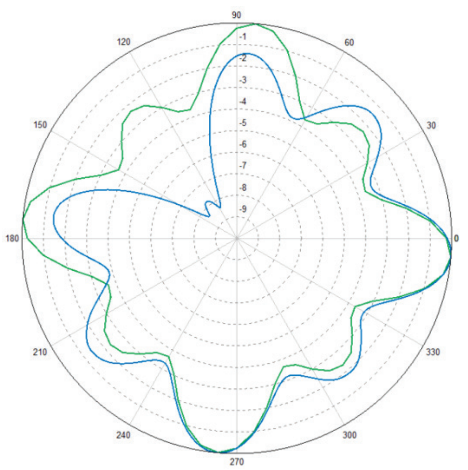

Fig. 10. Radiation pattern of antenna system with faulty segment D3.

The segments were being turned off one by one to see any changes in the radiation pattern. As we can see *in Fig.* 8 – 10, as each of the segments in a branch is being turned off, the radiation pattern changes significantly. The radiation pattern of the AS changes accordingly to what segment has been turned off. Therefore it is possible to tell exactly which segment is experiencing a failure without any additional measurements, or in this case simulations. Since the AS is symmetrical to all four quadrants, changes in remaining branches A, B, C respectively will result in similar changes in radiation pattern angled accordingly to which branch is experiencing a failure.

## 3. Results

By simulating the AS consisted of specialized unified segments, it has been prooved that diagnostics of faulty segments using only radiation pattern measurements is possible and with sufficient equipment realizable.

## 4. Conclusions

We have proposed a method of faulty segment diagnostics using only radiation pattern measurements. Thanks to this method, it is possible to merge faulty segment diagnostics and radiation pattern measurement, eliminating faulty segment diagnostics using VSWR measurement, during which the antenna cannot be radiating. Therefore it is possible to limit the time AS is in an outage state only to the time needed for maintenance/faulty segment replacements. This method is appliable to AS of any size with any number of segments, making this method versatile for many scattering systems. However, radiation patterns used as a reference have to be simulated in advance and thorough knowledge of unified segments and AS is needed for simulation to be accurate. Moreover, sufficient and accurate equipment operated by properly educated or trained personnel is necessary for measurements to be performed successfully.

## Acknowledgements

This work was supported by the national scientific grant agency VEGA under the project No.: 2/0155/19 "Processing sensoric data via Artificial Intelligence methods", projects APVV 14-0076 "MEMS structures based on load cell", APVV 15-00624 "Electromagnetic compatibility ensuring of monitoring systems of the abnormal operating condition of the nuclear power plant".

## References

[1] Towercom a.s. Technical documentation UHF DTV Antenna. KATHREIN-Werke KG, Broadcast Antennas, P.O.Box 100 444, D-83004 Rosenheim, Germany.

[2] Halenar I., Nikitin Yu. R. The Dependability of Wireless Sensor Network. Technological Forum 2014: 5 *International technical conference: Book of proceeding (Kouty, Czech Republic, 17-19.06.2014).* Czech technical university in Prague. Pp. 195–198. ISBN 978-80-87583-10-4.

[3] Pivarčiová E., Sobrino D.R.D., Nikitin Yu.R., Holubek R., Ružarovský R. Measuring and Evaluating the Differences of Compared Images for a Correct Car Silhouette Categorization using Integral Transforms. *MEASUREMENT SCIENCE REVIEW, vol. 18*, No. 4, 2018. pp. 168-174. DOI: 10.1515/msr-2018-0024.

[4] Balanis C.A. Advanced Engineering Electromagnetics, John Wiley & Sons, Inc. 1989. Arizona State University. ISBN0-471-62194-3.

[5] Kraus J.D. Antennas 2nd edition, McGraw-Hill International editions. 1988. ISBN 0-07-100482-2.

# Hysteresis Loop Measurement for Small Closed Material Samples

**Tomáš Hejtmánek, Zdeněk Roubal**

Department of Theoretical and Experimental Electrical Engineering, FEEC, BUT,
Technická 3082/12, 616 00 Brno; Czech Republic,
Email: xhejtm07@stud.feec.vutbr.cz

***Abstract.*** *The current workplace for measuring magnetization curves uses an analog fluxmeter in which small closed samples have an undesirable effect on its lowest input resistance at the lowest ranges. When measuring a quasi-static hysteresis loop, this small input resistance limits our maximum sensitivity because the measuring winding resistance affects the constant of the analog fluxmeter. At higher frequencies, the inherent inductance of the measuring winding is signifying, which limits the area of integration of the fluxmeter into the order of kHz units. Both of these undesirable properties can be eliminated with a high-quality automatic-zero separator amplifier.*

*Keywords: Hysteresis Loop, Analog Fluxmeter, Automatic Zero Operational Amplifier, Input Noise Measurement*

## 1. Introduction

Standard methods of measuring material magnetic properties provide the best results with a toroidal coil [1], [2], [5]. This coil has two windings: The first winding $N_1$ is used for magnetization, and the second winding $N_2$ for measurement. Both the windings are wound around the entire core, [3]. For the measurement, the applied winding is placed close to the core of the coil (see Fig. 2).

The magnetization winding produces the requested magnetic field strength $H$ in the core of the coil. Consequently, the voltage obtained from the measurement winding is given by the following equation:

$$u_2(t) = N_2 \cdot \left( -\frac{d\Phi}{dt} \right) = N_2 \cdot S_Z \cdot \left( -\frac{dB}{dt} \right), \tag{1}$$

Fig. 1 shows a diagram of the measurement workspace of the static and dynamic hysteresis loops. Voltage $u_4(t)$ represents the current through winding $N_1$ and is connected to the oscilloscope together with the electronic fluxmeter output voltage $u_3(t)$. The static and dynamic hysteresis loop is measured by means of oscilloscope PicoScope 5242A.

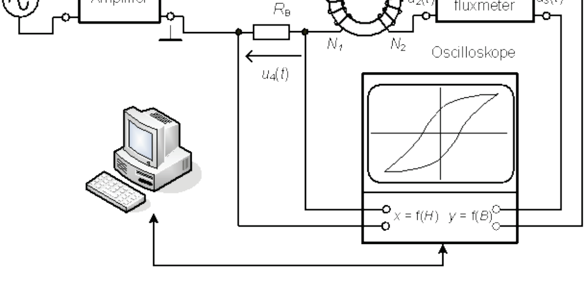


Fig. 1. A block scheme of the measurement method.

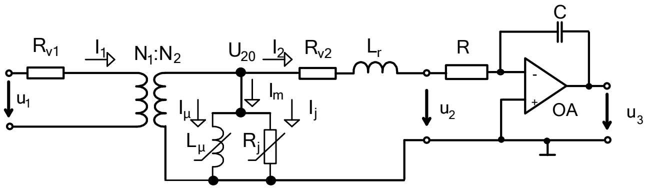


Fig. 2. An equivalent schematic of the toroidal coil with the inverting integrator [1].

In work [1], it was derived that the UTEE fluxmeter in common samples without a separation amplifier works up to 4 kHz. However, if we use an isolation amplifier and eliminate the influence of the inductance $L_r$ of the measuring winding, then with the UTEE fluxmeter we will be able to measure up to 100 kHz.

## 2. The Block Design of the Amplifier

As shown in Fig. 3, the entire preamplifier will consist of three main blocks. The first part will be the discrete instrumentation amplifier "A". Discrete instrumentation amplifier contains two voltage followers and a differential amplifier. It will serve for impedance separation of measuring coils. This will not affect the gain of the input amplifier due to the change in impedance of the measuring coil with frequency. The input also boosts the voltage to reduce noise in other parts of the preamplifier. Letter A in every block and numbers in brackets denotes largeness of amplification.

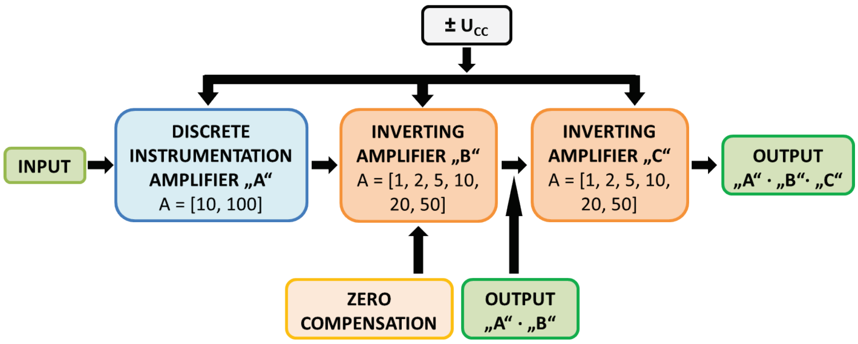


Fig. 3. Block diagram of the device.

The following two amplifiers, "B" and "C", are the main part of the device and amplify the voltage from the instrument input. Another block is a differential amplifier. The use of a differential amplifier is very advantageous here since this connection allows suppression of common interference. The output voltage is equal to the input voltage difference. The differential gain will be ten. The following two blocks are the same. Both amplifiers are inverting and can be individually adjusted for each amplification step. The voltage offset can be manually reset because neither automatic zero-compensation is not perfect, and the soldered connections can generate thermoelectric voltages, which must also be compensated. If the amplification of the amplifier "B" is sufficient, it is possible to take the amplified signal directly from the output "A" • "B". For very low voltages, the resulting gain is given by the amplification product of amplifiers "A", "B" and "C". In order to be able to control the amplifier by means of a control panel, the switching relays are connected via a transistor array to the rear connector of the amplifier. By applying a control voltage to a given pin of the connector, it is possible to switch the corresponding relay [4]. The whole device is powered by batteries to reduce the effects of line interference.

## 3. Choose Operational Amplifier

The main component of the preamplifier is an operational amplifier. Depending on the requirements, it was necessary to select suitable OA's. The most important criteria were the lowest offset and temperature drift. From a plethora of manufacturers were selected several OA's, which had very good parameters. All selected operational amplifiers have automatic-zero offset compensation, but the disadvantage is the higher noise voltage. However, zero offset was the main requirement for selection. The OA LMP2021 was used in the construction. In Table 1 selected types are listed, all parameters are from datasheets.

Table 1. Suitable auto-zero operational amplifiers, where is $A_0$ open loop gain, GPB Gain-bandwidth product, $S$ slew-rate, $U_{OS}$ input offset voltage, $\Delta U_{OS}/\Delta T$ offset voltage drift with temperature, $I_B$ input bias current, $R_D$ input resistance in differential mode, $u_N$ voltage noise density.

| | $A_0$ | GBP | S | $U_{OS}$ | $\frac{\Delta U_{OS}}{\Delta T}$ | $I_B$ | $R_D$ | $u_N$ |
|---|---|---|---|---|---|---|---|---|
| | [dB] | [MHz] | [V/µs] | [µV] | [µV/°C] | [pA] | [MΩ] | [nV/√Hz] |
| **LMP2021** | 150 | 5 | 2,5 | -0,9 | 0,001 | 23 | - | 11 |
| **OPA735** | 130 | 1,6 | 1,5 | 1 | 0,05 | 100 | - | 135 |
| **ADA4528** | 140 | 3 | 0,45 | 0,3 | 0,002 | 220 | 0,225 | 5,5 |
| **LTC2051** | 140 | 3 | 2 | 0,5 | 0,01 | 8 | - | - |
| **ISL28134** | 174 | 3,5 | 1,5 | -0,2 | -0,0005 | 120 | - | 8 |

## 4. Noise Measuring of Amplifier

The measured parameter of the amplifier was input noise. The HP 35660A FFT Spectrum Analyzer was used for this measurement, allowing a wide range of measurements in the low-frequency range. The frequency range of the analyzer extends to 100 kHz. The completed measuring amplifier is shown in Fig. 4.


Fig. 4. The front panel of the device.

The measurement was carried out with a short-circuited amplifier input, and its output was connected to one channel of the spectrum analyzer. Averaging 100 values was used. Graphs of the total input noise per unit bandwidth were constructed from the readings for two different gain combinations.

The total input noise voltage, see Fig. 5. It is obvious from the measured dependence that noise is very similar to white noise in its nature. Only large frequencies of noise voltage are visible at frequencies around 26 to 30 kHz. This interference causes the automatic amplifier to reset the clock frequency. To suppress this interference, we would have to limit the amplifier's bandwidth to less than 26 kHz or use another type of amplifier that works at higher clock frequencies. This measurement was unique in terms of determining the exact clock frequency of the auto-zero OA, as the manufacturer does not provide this information. The measured input noise voltage in the range of 1 to 26 kHz corresponds to the manufacturer's data of the operational amplifier and the simulations in the PSpice program. In this frequency range, the amplifier meets the requirements for very low voltage amplification. At very high gains, even on the harmonic signal, the interference from the clocking frequency of OA auto-zeroing is more pronounced. Input voltages lower than approx. 30 nV cannot be measured as they are drowned in noise.

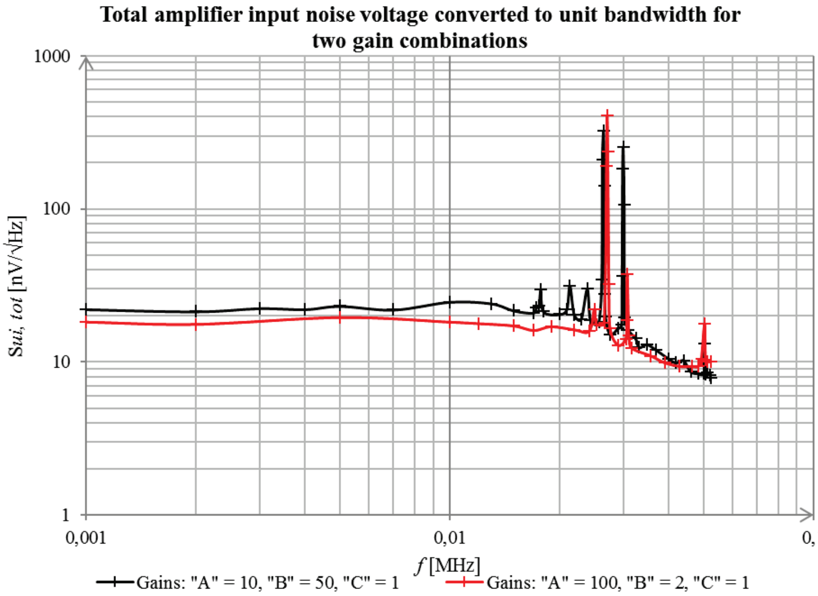


Fig. 5. Input noise characteristic, gain description corresponds with the marking of amplifiers in block diagram on Fig. 1.

## 5. Conclusions

The designed isolation amplifier made it possible to significantly expand the frequency band of the analog fluxmeter UTEE and also eliminated the effect of the resistance of the measuring winding on the required sensitivity. It turned out that OZ LMP2021 contains unwanted zeroing products at its output. Therefore, a variant with ADA4528 will be proposed where the zeroing currents are above 1 MHz.

## Acknowledgements

The preparation of this paper was assisted by the general student development project BD FEKT-S-20-6360 in progress at Brno University of Technology.

## References

[1] Roubal, Z., Marcon, P., Cap, M. (2012). Analysis of magnetic properties measurement in closed samples. In: 2012 *ELEKTRO*. IEEE, 460-464.

[2] Roubal, Z., Smejkal, V. (2013). Determination of parameters in the Jiles–Atherton model for measured hysteresis loops. In 9th International Conference Measurement.

[3] Košek, M., Novák, M., Eichler, J. (2019). Magnetic Viscosity Measurement on Grain Oriented Steel. In 2019 12th International Conference on Measurement, 327-330. IEEE.

[4] Hejtmánek, T. (2016). *Návrh měřicích zesilovačů pro magnetické měření*. Bachelor Thesis.

[5] Tumański, S. (2011) *Handbook of magnetic measurements*. Boca Raton: Taylor & Fracis.

# Longer Parts Coefficient of Thermal Expansion Measurement Method

**Norbert Pomp, Pavel Klouček**

VÚTS, a.s., Liberec, Czech Republic
Email: norbert.pomp@vuts.cz

***Abstract.*** *Thermal expansion is well-known phenomena in which technical quantification is based on the coefficient of thermal expansion acquaintance. Laboratory instruments for thermal expansion coefficient measurement with high precision exist. However, they can test only short and homogenous samples. Advanced technology enforces the rigorous prediction of thermal dimension changes of a complex part where models may be too complicated or have to be verified.*

*Keywords: Thermal Expansion, Coefficient of Thermal Expansion, Composite Materials*

## 1. Introduction

The exact knowledge of real parts dimensions should be very important in plenty of applications where the temperature of the parts is changing. In some cases, the needs of unchanging part dimensions under the changing temperature are crucial.

Several methods and laboratory devices for the coefficient of thermal expansion measurement exist and are commonly used. All of them are focused on the small, homogenous sample measurement. The thermal expansion of the parts and assemblies consisting of different materials is hard to predict. So the only way to find the parts thermal expansion behaviour is by measuring.

## 2. Subject and Methods

The method for long parts linearized coefficient of the thermal expansion measurement with resolution better than $0.3 \times 10^{-6}$ K$^{-1}$ was developed and verified. The aim of the method is a measurement of thermal expansion coefficient of longish, about one meter long real parts with high resolution. The method is based on the measurement of elongation of the sample, while the sample temperature is changed from start level to terminal one using climatic chamber and measured as well. The measured sample and elongation transducer are both fixed to a massive solid steel frame. It is hard to ensure elongation transducer stability when its temperature is changed, so the transducer has to be placed out of the heated area, while the only contact transducer is suitable because of resolution of at least 0.1 µm and long term stability. It enforces to put some extension element between the heated sample and the elongation transducer. Unfortunately, the unknown thermal profile of the extension elements and their thermal elongation introduce the systematic measurement error to the measurement results.

To the systematic error determination, the reference sample measurement was realized. The reference sample was made from a homogenous material. The reference sample has to be as similar to the measured sample as possible in dimensions and thermal expansion coefficient, too. The elongation $\Delta L$ found during the measurement consists of the sample elongation component $\Delta L_{Sample}$, the frame component $\Delta L_{Frame}$ and the systematic error component signed as $\Delta L_{Mount}$, where the biggest part represents the mounting fixture expansion. The frame expansion is evaluated from measured frame temperature and known expansion coefficient of steel. Introducing the known reference sample elongation (2) into the eq. (1) as the sample elongation ($\Delta L_{Sample} = \Delta L_{Ref}$) leads to the $\Delta L_{Mount}$ evaluation. The reference sample expansion coefficient $\alpha_{Ref}$ can be measured by a proven laboratory device on a small sample made from the same semi-product as the reference sample.

The $\Delta L_{Mount}$, which has the same behaviour in all similar measurements, can measure systematic error compensation and evaluation of $\Delta L_{Sample}$ for tested samples.

$$\Delta L = \Delta L_{Sample} + \Delta L_{Mount} - \Delta L_{Frame} \tag{1}$$

$$\Delta L_{Ref} = \alpha_{Ref}\, L_0\, \Delta T_{Ref} \tag{2}$$

The Invar alloy was chosen as the reference sample material, especially because of its low thermal expansion coefficient.

## 3. Laboratory Small Sample Measurement

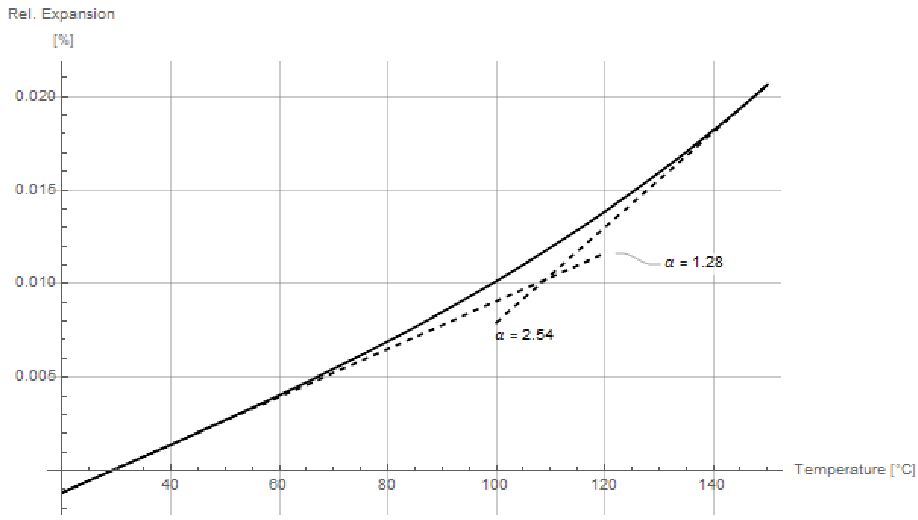


Fig. 1. Thermal expansion laboratory measurement of Invar alloy sample.

The reference rod material small sample thermal elongation measurement was carried out. The sample elongation depending on its temperature, is shown in Fig. 1. It is evident that the Invar thermal elongation function is not linear. The thermal expansion coefficient ranges from 1.28 to 2.54 × $10^{-6}$ $K^{-1}$ in the measured temperature range of 20 - 150°C. The mean value of the thermal coefficient in this range is 1,67 × $10^{-6}$ $K^{-1}$.

The measured curve can be interpolated by the polynomial. Evaluation of the relative elongation function is more useful for next work than the relative elongation coefficient function; the reference point $T_0$ = 20°C:

$$\varepsilon_{Ref} = 2.76 \times 10^{-11}\, \Delta T_{Ref}{}^{3} - 2.18 \times 10^{-9}\, \Delta T_{Ref}{}^{2} + 1.33 \times 10^{-6}\, \Delta T_{Ref} - 3.78 \times 10^{-5} \tag{3}$$

## 4. Systematic Errors Compensation

The reference measurement was done in two procedures. The first one was a standard two-points measurement considering linear thermal expansion. The temperature for each of the start and the endpoint was kept for one hour. The temperature between these two points was forced to rise fluently. When the coefficient of thermal expansion was studied as temperature depending, the temperature rose in several steps with given stabilization time, see Fig. 2. Temperature dependency for the $\Delta L_{Mount}$ function was evaluated from each stable state, and the interpolation function was found as:

$$\Delta L_{Mount} = 9.14 \times 10^{-8}\, T_{Mount}{}^{3} - 6.43 \times 10^{-6}\, T_{Mount}{}^{2} + \\ +2.20 \times 10^{-4}\, T_{Mount} - 7.09 \times 10^{-4} \quad (1)$$

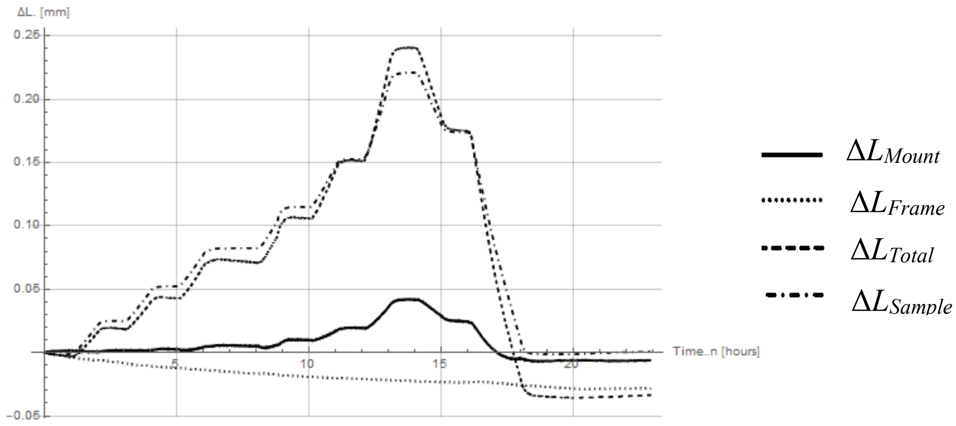


Fig. 2. Reference measurement for non-linear compensation evaluation.

## 5. Evaluation and Results

Several samples of different materials were measured by the described method. The laboratory measurement of the short sample was carried out when it was possible, and its values were compared. The difference of measured thermal expansion coefficient obtained by laboratory measurement and by longish samples method was smaller than the method requirement. The interesting results were found for the composite sample measurement, see Fig. 3. Its expansion coefficient is very low and strongly dependent on temperature. The non-linear extension of the Invar alloy parts significantly influenced measured elongation values in this case. Fig. 3 demonstrates the differences between the two-point (dotted line) and multiple-point (continuous line) systematic error compensation, where the upper two curves represent the sample elongation after compensation and the lower two curves correspond to the systematic error elongation component. This comparison is slightly incorrect because the reference measurement was done under different conditions than composite sample measurement (stair-step vs. constant ramp temperature changes)

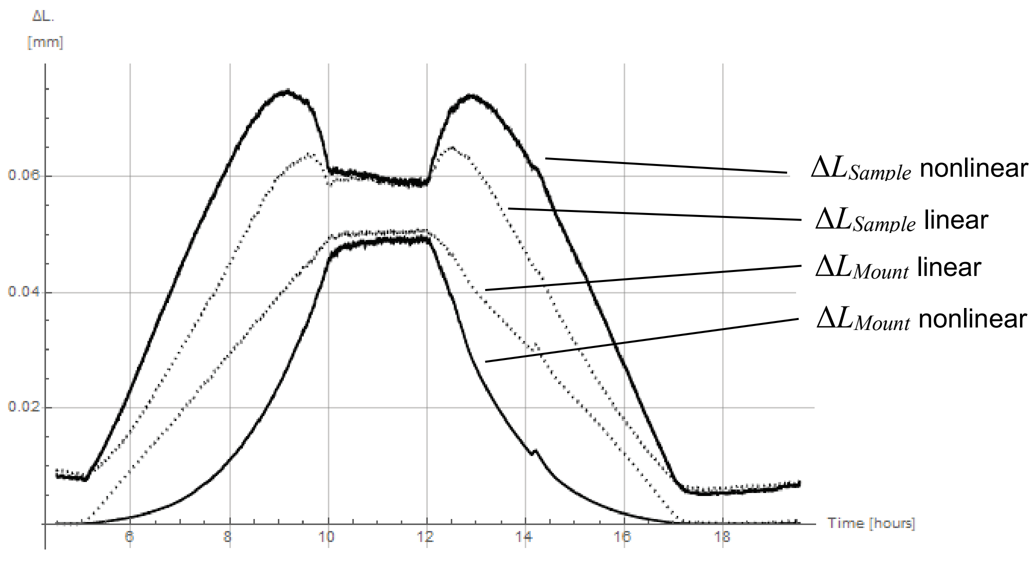


Fig. 3. Comparison of linear and non-linear measurement evaluation.

## 6. Conclusions

The rising requirement of exact dimensions knowledge ingoing together with rising usage of composite parts enforces the development of the real part thermal elongation measurement methods. The developed method is based on the precise measurement of the real part elongation during controlled temperature changes. Because of the measurement design, the parasite influence of the fixtures has to be compensated. The reference sample was made from Invar alloy, which has a small, but not constant thermal expansion coefficient, so the error compensation is temperature depending. When all known influences are taken into account, the reproducibility of thermal expansion coefficient measurement was found better than $1 \times 10^{-7}$ m/m $K^{-1}$.

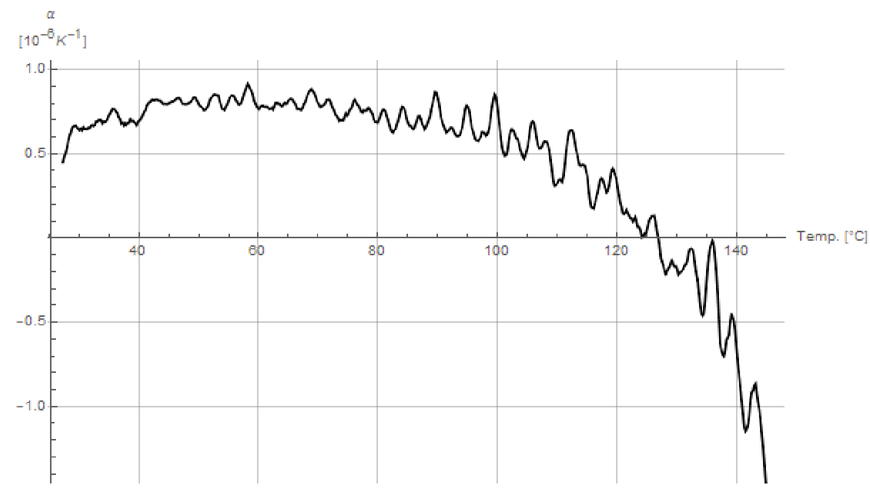


Fig. 4. Composite sample thermal coefficient changing in temperature.

The measured special low expansion rod coefficient of thermal expansion depends on temperature and varies from +0.6 to $-1.3 \times 10^{-6}$ m/m $K^{-1}$ in temperature range 20 to 150°C. The presented non-linear evaluation is still vitiated by an error of different measurement conditions mentioned above (stair-step vs. constant ramp temperature changes) because the composite sample was not available for repetitive stair-step measurement. The mounting fixtures temperature change is slower than for the measured sample due to its mass, so the resulting curve of thermal coefficient of the measured sample should be actually more flat than the presented one. Nevertheless, the non-linear evaluation is much more correct than the linear one, even when the temperature stabilization was ignored.

## Acknowledgements

This work was supported by the Czech Ministry of Industry and Trade in Institutional Support.

## References

[1] Linseis L75 PT, user manual. Linseis Messgeraete GmbH, Germany

[2] Maglic, K. D., Cezairliyan, A., Peletsky, V. E. (1992). *Compendium of Thermophysical Property Measurement Methods.* Springer, Boston, MA, ISBN 978-0-306-43854-7.

[3] Arbogast, A., Roy, S., Nycz, A., Noakes, M. W., Masuo, C., Babu, S. S. (2020). Investigating the Linear Thermal Expansion of Additively Manufactured Multi-Material Joining between Invar and Steel. Materials Volume 13. ISSN 1996-1944. MDPI Basel

[4] El Asamai, S., Hennebelle, F., Coorevits, T., Fontaine J. (2019). Determination of the Coefficient of Expansion of a Carbon Tube and its Assemblz for Thermal Compensation of Metrological Structures. *19th International Congress of Metrology*, Paris.

# AUTHORS INDEX

## S



## T



## U



## V



## W



## Z

ISBN 978-80-972629-4-5

9 788097 262945

Institute of Measurement Science
Slovak Academy of Sciences
Dúbravská cesta 9
841 04 Bratislava, Slovakia